NUMERICAL EXPERIMENTS ON THE AERODYNAMICS OF WAVERIDERS

by

SAJID RAZA CHAUDHRY BSc.

Thesis submitted to the Faculty of Engineering,
the University of Glasgow for the degree of Doctor of Philosophy.

March 1994

ProQuest LLC.
789 East Eisenhower Parkway
P.O. Box 1346
Ann Arbor, MI 48106 – 1346

To my father (late)
and mother

ACKNOWLEDGEMENTS

I would like to express my sincere gratitude to Professor B.E. Richards for his supervision, help and guidance throughout the research described in this dissertation.

I thank also to Dr. Qin Ning for his invaluable and sincere help and encouragement during this research. Thanks are also due to Dr. Jiang Dachun, Dr. Wang and Dr. B.Batsuno for many valuable discussions.

I would also wish to express many thanks to the staff of computing services for their kind help and the excellent service they provided.

Finally I thank my parents and my family for their continuous support. I also gratefully acknowledges the assistance of my friends and all those who helped me during my stay in Glasgow.

The author gratefully acknowledges the financial assistance provided by the Government of Pakistan during this research.

ABSTRACT

Because of a high level of activity in manned space missions and hypersonic transport the ideas on waveriders are currently of great interest. Waveriders have been regarded as the best shapes for space planes. This derives from their high lift capability which will enable the vehicle to slow down at high altitude thus helping it alleviate the kinetic heating problem. The present study reports on the advantages of waveriders for their application to space plane shapes. The advantages of selecting waveriders as lifting shapes is attributed to their flow simplicity by using shapes defined inversely from a two dimensional flow as a basis of their construction. For these deceptively simple shapes initial estimates of the aerodynamic properties can be made through inviscid flow calculations. A historical preview of waveriders suggests that viscous effects are very important for accurate prediction of flowfield around these shapes. However, these effects were not included in the course of development of these shapes. In this study along with the classical theory of waveriders viscosity effects on the waverider design are highlighted. Also emphasised are the important relevant factors in hypersonic flow and the advantages of applying computational fluid dynamics (CFD) for simulation of the flowfield as compared to analytic and experimentation method.

In the past, work has been reported on the inclusion of viscous effects by using the boundary layer for the viscous correction. The present study shows that, in the presence of strong viscous-inviscid interaction, viscous effects from these applications can only be reliably predicted using solutions of the Navier-Stokes equations. Based on this strategy numerical solutions of the Navier-Stokes Equations were applied to different waverider shapes to highlight the importance of viscous effects. Since the flow on typical waverider shapes is near conical, then a locally conical approximation was used for two reasons: it simplifies the problem from a 3-D to a 2-D one without compromising significantly accuracy ; it reduces the requirement of computing resources in terms of processor time and storage.

Application of the Navier Stokes equations in locally conical form (LCNS) to simulate the flow around idealised waverider shapes revealed interesting off-design flow behaviour for on-design flow conditions.

Sensitive effects on performance due to off-design behaviour are observed for caret wings. Results are obtained for 4 cases of caret wings optimised for free stream Mach numbers of 1.44, 1.74, 2.51 and 4.93 and 3 cases of a cone-wing configuration at Mach 10 with angles of attack of 5°, 10° and 15°. For caret wings results show how viscous effects have significant influence even at low Mach numbers. Flow simulation of these cases illustrates the advantage of using CFD on these shapes and shows how incorporating the NS equations provides a powerful tool to explore in detail waverider aerodynamics in on-design and off-design operation. Results also show how suitably it can deal with shock-shock, shock-boundary layer and shock vortex interactions, simultaneously. Also predicted was the effect on heat transfer due to the change in angle of attack of the shape.

As caret wing and wing-cone combinations are thought to have limited applicability for practical aircraft shape the studies were extended to more general shapes. This study is the first to deal simultaneously with general shapes derived from both conical and wedge flowfields. General conical-derived shapes were constructed through a numerical approach based on flow around a cone using the Taylor Maccoll theory. For a general wedge-derived shape the base flow was the flow behind wedge induced oblique shock waves. Comparisons were made to evaluate the advantages and disadvantages of each type of configuration generated. Results were discussed in the light of numerical prediction and experimental results published in the literature. It was recognized that if volume constraints are relaxed, then, there are some considerable advantages in using wedge flow as a basis, instead of conical flow. Also it was shown that a change in only the leading edge shape can considerably improve the performance characteristics of waveriders. Furthermore a wedge-derived waverider provides a higher lift than an equivalent cone-derived one and also at off-design conditions a wedge-derived shape shows less sensitivity than its conical counterpart.

NOMENCLATURE

A,S	=area.
A_p,S_p	=planform area.
A_b,S_b	=base area.
c_f	=coefficient of friction.
C_D	=coefficient of drag.
C_L	=coefficient of lift.
c_p	=coefficient of pressure.
e	=total internal energy.
D	=drag.
e_x,e_y,e_z	=basis unit vectors in Cartesian co-ordinates.
e_r,e_θ,e_ϕ	=basis unit vectors in spherical co-ordinates.
F	=flux vector in θ direction.
G	=flux vector in φ direction.
H	=source term vector.
K_θ	=Hypersonic similarity parameter.
k	=thermal conductivity.
L	=lift.
L/D	=lift to drag ratio.
M	=Mach number.
N	=Normal force.
p	=pressure.
Pr	=Prandtl number, $c_p\mu/k$.
q	=rate of heat transfer.
R	=gas constant.
$Re_{\infty,r}$	=Reynolds number = $\rho_\infty V_\infty r/\mu_\infty$.
r	=radial coordinate.
s/l	=semi span to length ratio.
T	=temperature.
t	=time.
U	=conservative vector.
u	=velocity.
u_r,V_r	=velocity in radial direction.
u_θ,V_θ	=velocity in θ direction.
u_φ,V_φ	=velocity in φ direction.

$\bar{\omega}$	=mean molecular speed.
α	=angle of attack.
β,σ	=shock deflection angle.
$\beta^{'},\beta_l$	= ref fig(2.3).
γ	=ratio of specific heats = C_p/C_v = 1.4
Δ,δ	=increment.
δ	=boundary layer thickness.
Δ_+,Δ_-	=forward and backward difference operator.
θ	=cone angle, coordinate or wedge and body angle (θ_b).
Λ	=sweep back angle.
μ	=viscosity.
μ	=Mach angle.
ρ	=density.
τ	=stress tensor.
τ	=volume parameter (τ=V/F), $F=S^{3/2}$
ϕ	=coordinate.
χ	=viscous interaction parameter=$M_\infty^3\left[\frac{C}{Re_\infty}\right]^{1/2}$, where, $C=\frac{\rho_w \mu_w}{\rho_e \mu_e}$.
ω	=design value of (β-θ).

Subscripts

b	=values on the body.
c	=values on cone surface or on compression surface.
e	=values outside boundary layer w.r.t. reference condition.
fs	=stream line value.
i,j	=values at (r,θ_i,φ_j).
le	=leading edge
max	=maximum value.
s	=values at the shock.
w	=conditions on the wall.
∞	=free stream conditions.
$^\circ$	=stagnation value.

Superscript

n	=time level.
*	=value at reference point.

CONTENTS

INTRODUCTION

1.1 Space Planes

With the success of man's dream towards conquering space and the prospect of manned orbital operation by Space Shuttle, the interest in developing hypersonic aerospace vehicles has grown and now terms and concepts such as AOTV's (Aeroassisted transfer vehicles), US Space Station, SDI, Orient Express, ICBM's, NASP have become accepted because with present day technology, achievement of these goals may seems difficult but are no longer impossible. Today it is a matter of time for space scientists to overcome these challenges and they are very near to demonstrating their ability to reach into orbit or space in a single stage by taking off and landing from a conventional runway. Two of the important programs of this kind are the US National Aerospace Plane (NASP)[1] and the British HOrizontal Take Off and Landing Space Shuttle (HOTOL)(fig(1.1))[2]. NASP is an ambitious attempt to fly 25 times faster than the speed of sound and to demonstrate single-stage-to-orbit operation.

Hypersonic programs in the broadly defined environment can be classified into different engineering systems. All these systems can be classified under different envelopes of the hypersonic regime from M>5 to M=∞ and are affected by the vehicle scale and angle of attack. This is because the angle of attack defines the fundamental relationships between the levels of pressure drag and viscous drag forces. Systems designed for high lift to drag ratio (L/D), normally operate at lower angle of attack where viscous effects are dominant. Whereas, low L/D systems are pressure dominant and operate at high angle of attack. Also, α along with vehicle scale determines effect on boundary layer transition.

The angle of attack also impacts on the relative importance of real gas effects on both the aerodynamics and material aspects of the configuration. For an equilibrium flow a significant loss in static pressure and C_L would result due to dissociation of molecules (during re-entry Oxygen dissociates at M=7 and Nitrogen at M=12). This dissociation could partly be prevented by flying at high altitudes where this reaction occurs so slowly that flow is

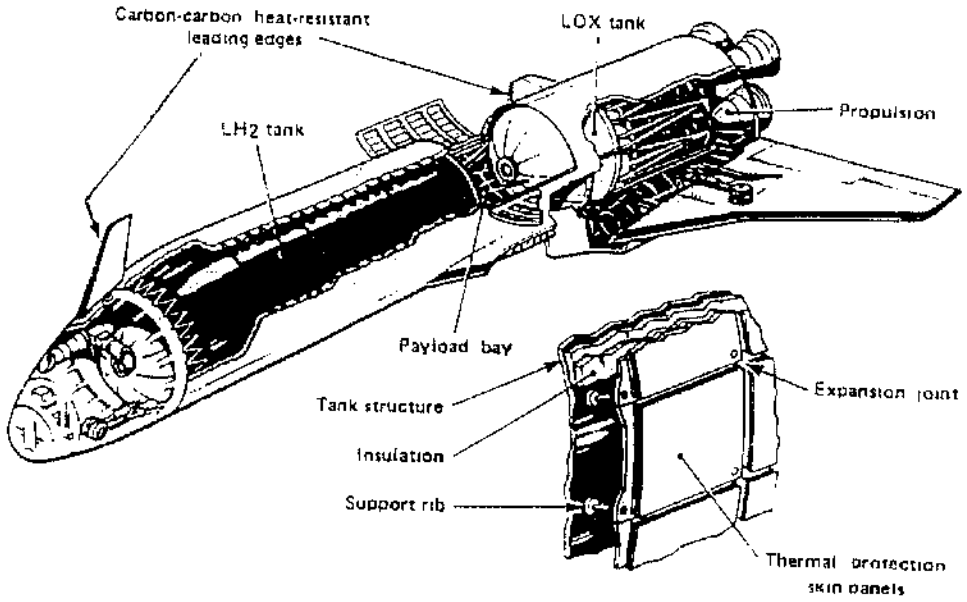

Fig. 1.1 British Space Plane (HOTOL). [2]

effectively frozen. But, partial lift can also be regained by increasing α, because for a real gas, plane shocks remain attached at larger incidences than for a perfect gas.

Several fundamentally different hypersonic systems operating within this environment are categorised as follows[3].

Ballistic Systems employed by the Departments of Defense.

These are generally dominated by turbulent flow and high degree of interaction between the imposed heating and materials response. Although they have generally geometrically simple configurations, three dimensional effects are strong.

Manoeuvring re-entry vehicles.

These integrate the features of a ballistic system with the manoeuvrability of a lifting body. Manoeuvring is employed for both terminal evasion and as a means of improving overall system accuracy.

a. Terminal evasion may be required to enhance penetration against a potential adversary system.
b. System accuracy can be improved by performing navigation updates, either prior to or during re-entry and their manoeuvring to correct for trajectory errors experienced during the earlier flight phase.

Low lift to drag lifting systems.

These systems are typified by a small contribution of viscous effects on the aerodynamics and aerodynamic heating of the vehicle.

The L/D of a system is directly related to the angle of attack of the configuration. For example low L/D shapes operate at high angle of attack. A typical example of this is shown in fig(1.2). The Space Shuttle operates at 40^0 angle of attack during the majority of the re-entry trajectory. At these high incidences, and at velocities of orbital entry, chemical activity

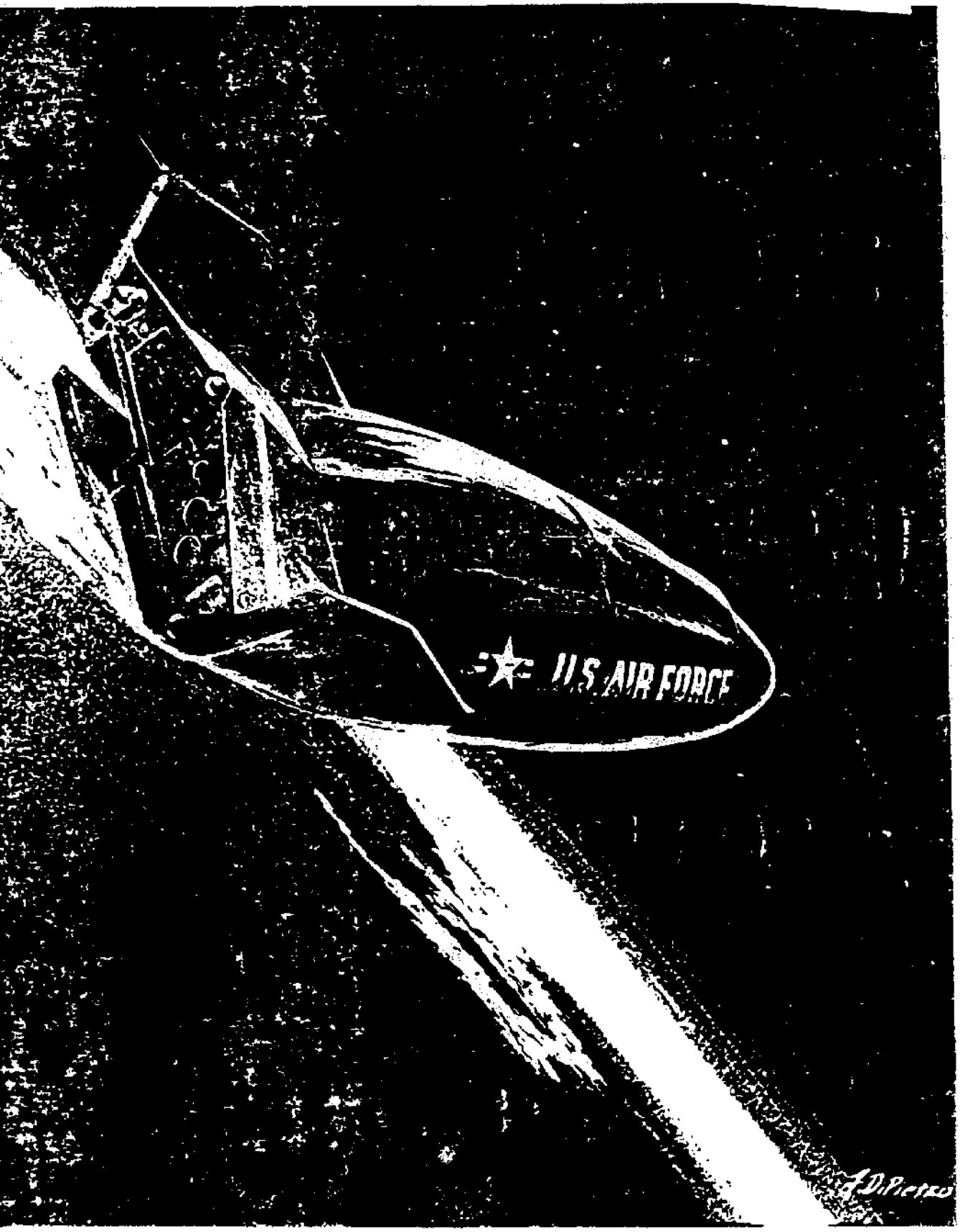

Fig. 1.2 SV5-D, Low lift to drag lifting system. [3]

within the local flow field is created on the large blunt nose of the configuration and sustained by the lower surface of that class of configurations. Chemical effects are important in this class.

High lift to drag lifting systems.

High L/D lifting systems operate at lower angles of attack and are dominated by viscous contributions to the overall drag equal to or higher than the corresponding pressure contributions. As a result, developmental wind tunnel testing requires a higher accuracy of flight simulation.

High L/D configurations demand very small blunt nose shapes in order to reduce the drag and thus generate the required aerodynamic characteristics. The result is that the amount of high energy, chemically active flow processed is very small and the degree of chemical activity cannot be sustained by the very low angle of attack surfaces of the configuration. Fig(1.3) and fig(1.4) indicate designs of hypersonic high L/D vehicles.

Aerodynamic Orbital Transfer Vehicles (AOTV's)

These operate in a confined velocity range bounded by the orbital velocities of the initial state (normally a high energy stationary orbit) and a low energy low earth orbit. Examples of this kind are shown in fig (1.5) and fig (1.6). These are low L/D configurations with substantial chemical activity and that chemical activity consists both of chemical dissociation (indicative of orbital entry conditions) and ionization which is indicative of higher temperature reactions at velocities in excess of those for low earth orbit.

1.2 Importance Of Lift & L/D Ratio in Space Plane Shapes.

Common to all the above space mission concepts it is identified that for practical hypersonic flight, although all the subsystems of the vehicle e.g., propulsion, structural, flight control and thermal protection system, contribute towards its performance, a major part is played by an optimum aerodynamic shape to obtain the best aerodynamic results (i.e., a shape which could give high lift to drag ratio at high C_L). Such a shape can be

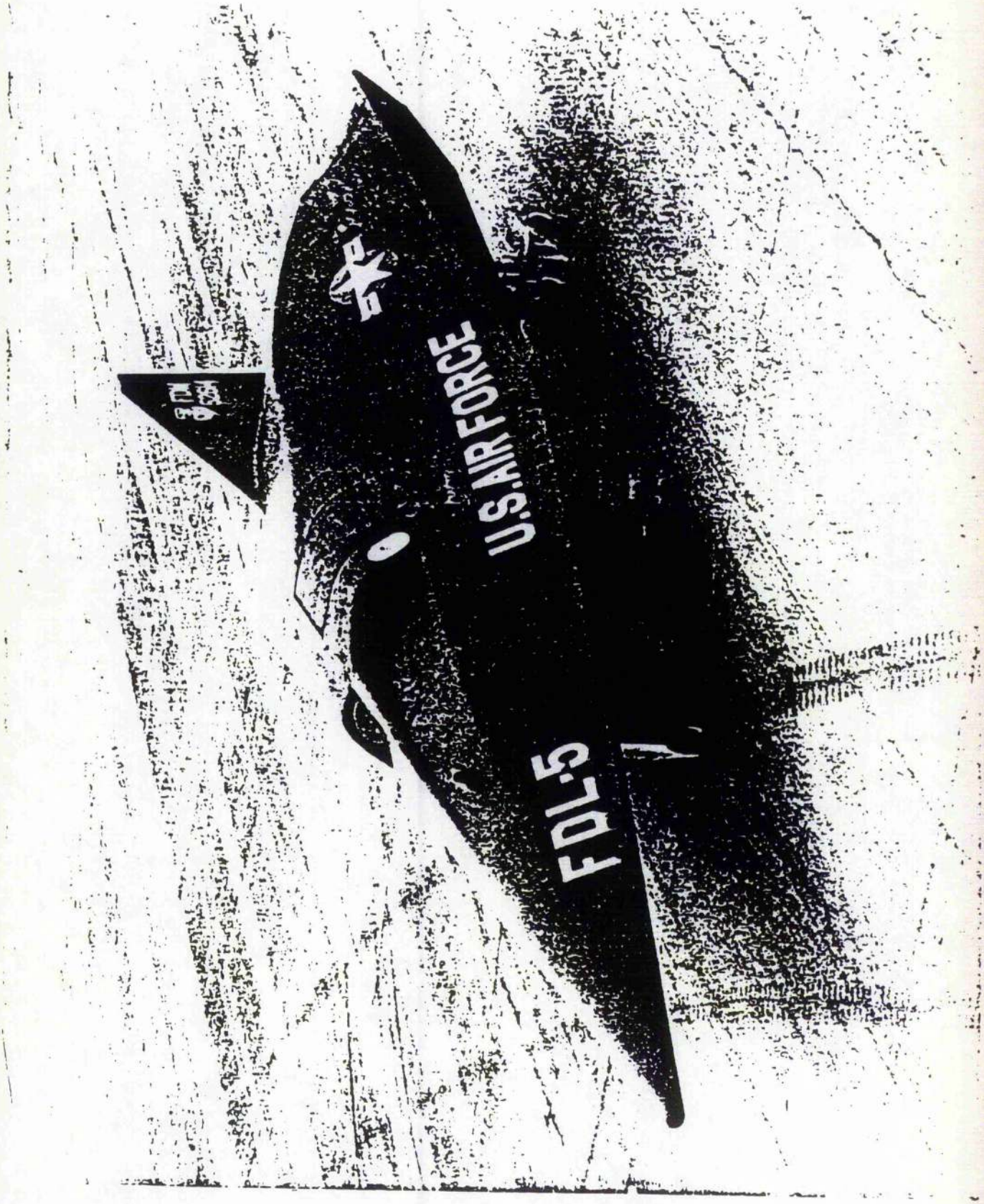

Fig. 1.3 High L/D lifting system.[3]

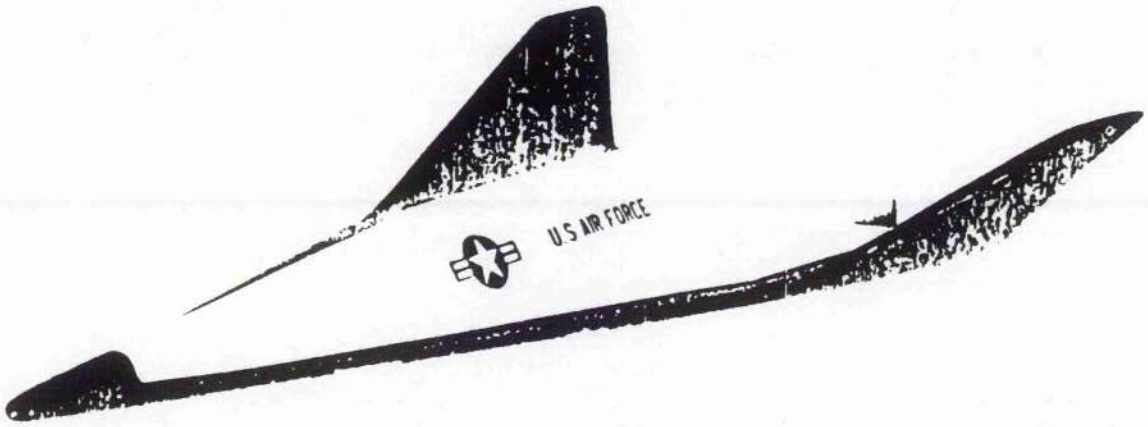

Fig. 1.4 Boost Glide Vehicle ; High L/D sytem. [3]

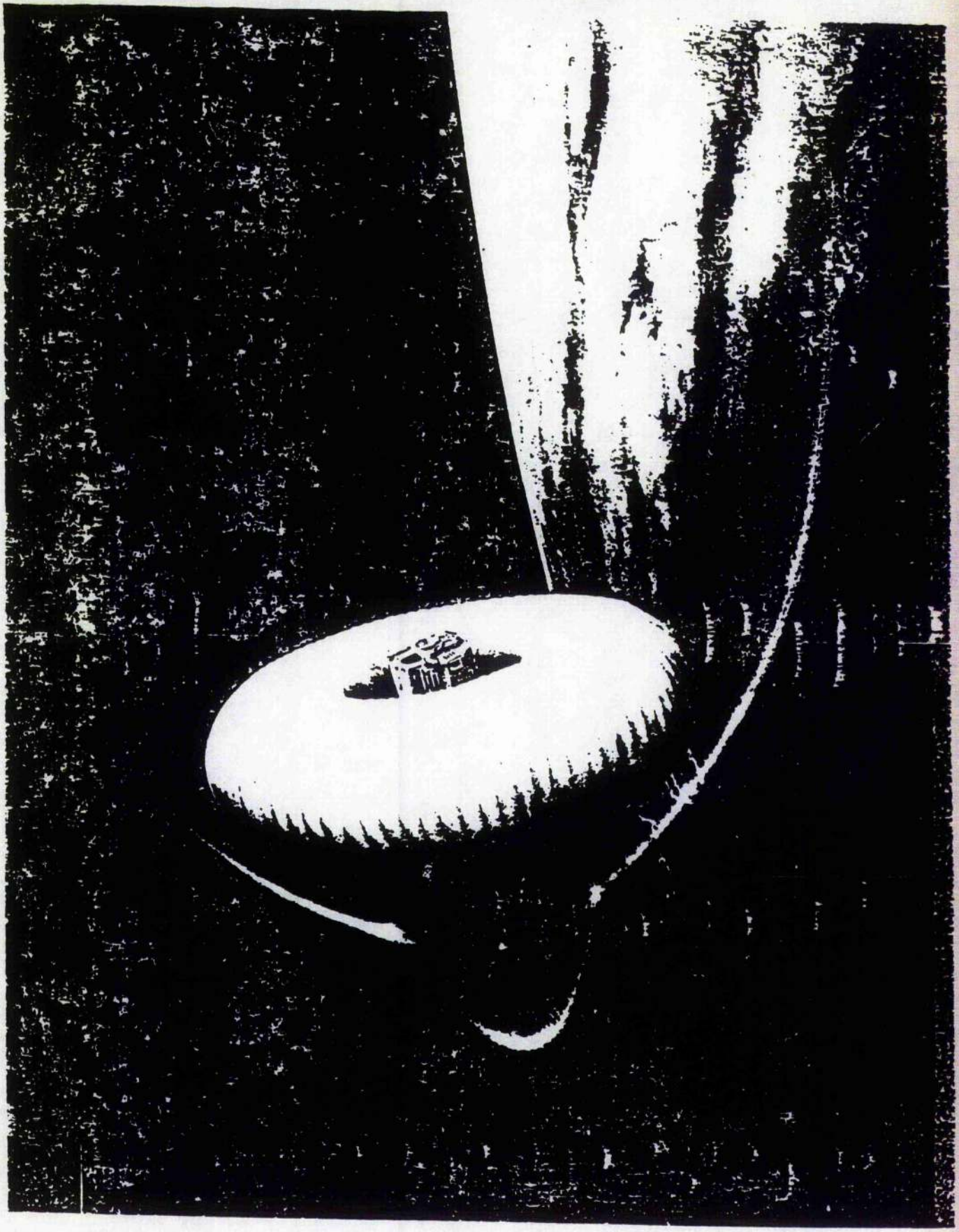

Fig. 1.5 AOTV (Aero Orbital Transfer Vehicle)[3].

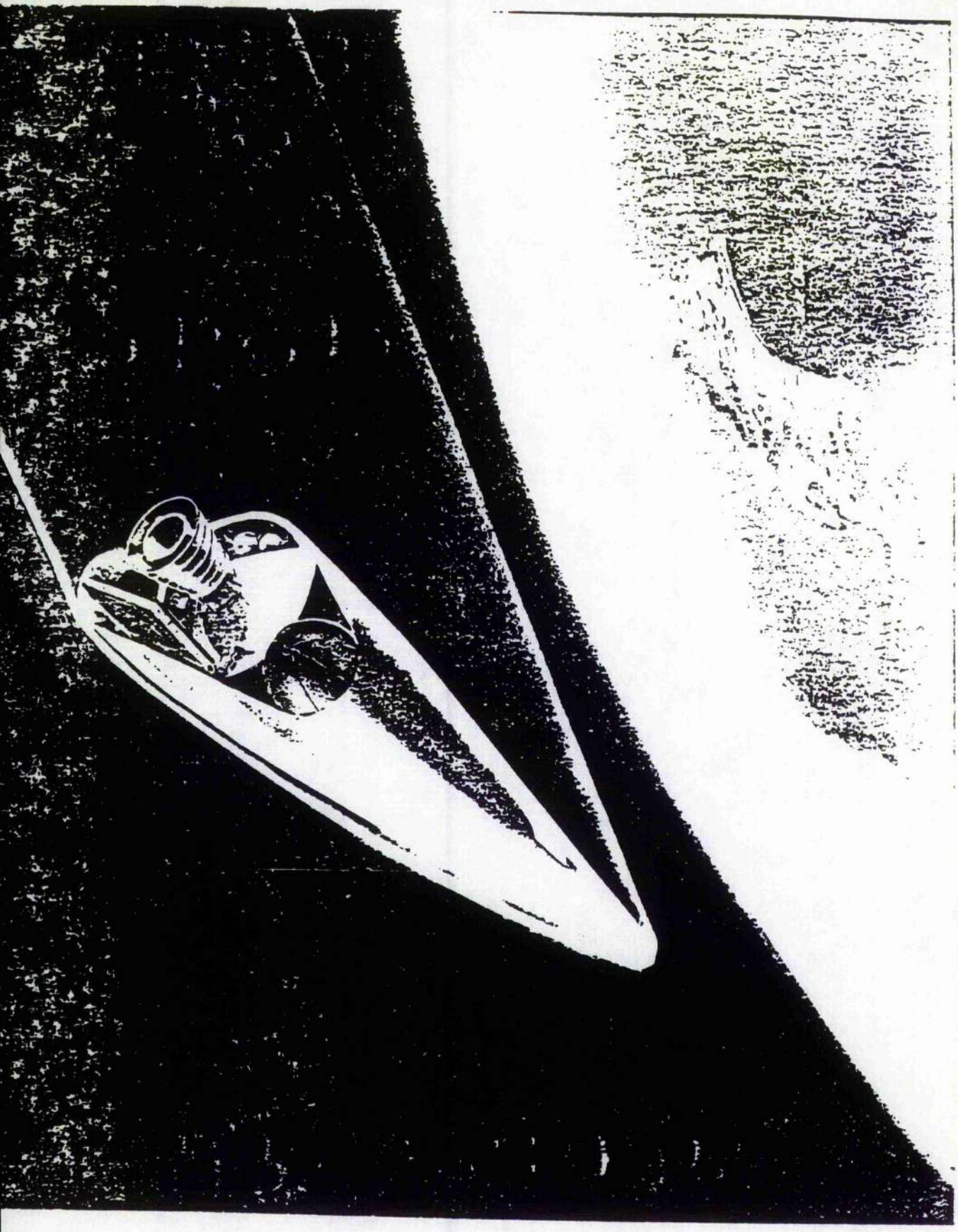

Fig. 1.6 AOTV (Aero Orbital Transfer Vehicle)[3].

advantageous in hypersonic flight because it gives long range, good manoeuverability, high cross range for re-entry and, most important, potentially lower heating.

In general most space planes are designed for high lift and low drag. High lift provides a vital advantage to supersonic vehicles because if the amount of aerodynamic lift is sufficient to overcome the gravitational force then thrust is required only to overcome the drag. Secondly high lift, as opposed to high L/D ratio, allows the configuration to decelerate at a higher altitude for the same velocity.

1.3 Why Waveriders ?

For Space Plane shapes, besides high lift and low drag, it is also desirable to provide some useful volume for payload, fuel and equipment. The advantages of achieving high lift are discussed in the previous section. Since the late sixties much of the work in the context of hypersonic re-entry vehicles in America [4],[5] can be related to the modification of the present shape of the Space Shuttle orbiter. In studies in Europe, more emphasis has been placed on providing concavity on the lower surface instead of convex or flat bottomed space craft. In this context Nonweiler first gave the concept of a delta wing whose under surface is not planar but has an inverted V or anhedral cross-section of such a form that at the design Mach number and incidence the shock waves formed are plane[6],[7].

The disadvantage of flat bottomed or convex wings over anhedral wings (fig(1.7)) is that for the former case there is a considerable cross flow beneath the wing and the streamlines are curved away from the center line where pressure is maximum which results in spillage around the leading edges.

Hence if a wing can be made in which diverging flow or spillage can be avoided, by having the shock wave attached to its leading edge then at the design Mach number it will have an isobaric under-surface. Furthermore the prediction of the flow will be simple to handle through shock expansion theory. Construction of such a wing in its simplest shape is known as the Caret Wing or simple waverider and in this form it can be constructed by

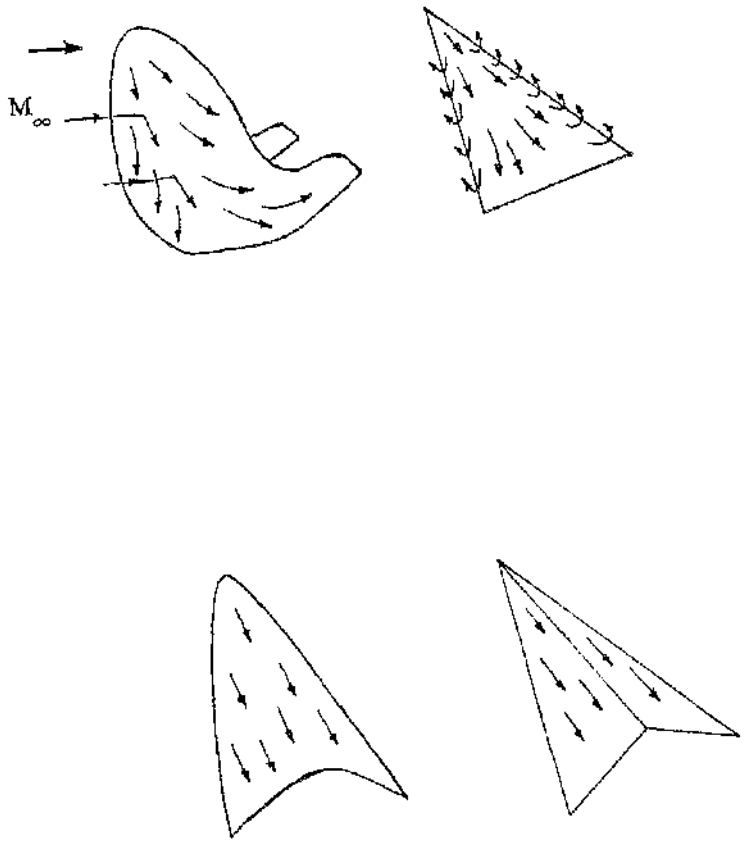

Fig. 1.7 Disadvantage of flat bottom or convex wings over anhedral wings.
(flow spillage from convex and flat bottomed vehicles.)

defining[6] a shape composed of streamlines put together from known exact solutions of inviscid flow equations.

Broadly speaking the term waverider is not restricted to the caret wing but can be used for all such optimum shapes derived on the above principles whether the basic flow is wedge or cone derived. Also, it is observed that the vehicle having recessed lower surfaces can provide, at a given incidence and Mach number, values of C_L substantially higher than convex or flat bottomed surfaces. The explanation for this is that at their design conditions they produce a stronger shock attached to the leading edge with full containment of flow thus resulting in high lift and less spillage.

As pointed out earlier besides the advantageous requirements of achieving high lift, lower drag and high lift-to-drag ratio another requirement for high speed vehicles is to overcome the problem of heat transfer. An important aspect of waverider application is the overall reduction in heat transfer

a: At the stagnation point, since, at a given wing loading, flight speed and L/D ratio, deceleration will occur at high altitudes and, hence, at given flight speed ambient air density is reduced.

b: On the lower surface since, at given flight speed local flow velocities will have been reduced by the stronger shock, in comparison to that on a conventional body, hence, low convective heat transfer.

c: Since, heating which is directly proportional to the square root of density can be minimized by reducing the wing loading (W/A) and increasing C_L (as long as the C_L increase does not decrease the heating at a rate greater than corresponding decrease in density).

1.4 General features of Hypersonic Flow.

Problems for hypersonic flow differ in many aspects from normal flow problems due to the flow complexities involved. These complexities are caused due to the variation of properties for different parameters at high velocity and at high altitude where the density hence Reynolds Number is low, therefore the boundary layers are thick.

One of the basic properties of hypersonic flow is that it is nonlinear, different from subsonic flow. Some of the basic differences are highlighted in fig(1.8-1.10). Fig(1.8) shows the contrast between the random energy (K.E. due to molecular motion of a gas = $\frac{1}{2}ma^2$, since, $\bar{v} \cong a$, the mean molecular speed) and ordered energy $\frac{1}{2}mV^2$ (due to mass flow rate). It reveals that for subsonic flow random energy ($a^2 >> V^2$) dominates whereas for hypersonic speed ordered energy ($V^2 >> a^2$) is higher. The ratio of 'ordered energy/random energy' is obtained from energy equation

$$C_p T + \frac{V^2}{2} = \text{const.}$$

which on re-arrangement gives $\frac{a^2}{\gamma - 1} + \frac{V^2}{2} = \text{const.}$ The ratio of these two terms is then

$$\frac{V^2}{a^2} \cdot \frac{\gamma - 1}{2} = \frac{M^2}{5} \text{ for } \gamma = 1.4.$$

Also in subsonic flow it is the size of the wake which determines drag whereas for hypersonic flow it is the size of stagnation region which determines drag (fig(1.9)). And to generate lift for subsonic flow it is the upper surface which is important whereas in hypersonics the high lower surface pressure produces the lift and the upper surface is of little significance(fig(1.10)).

To have a good picture of hypersonic flow theory it is useful to examine the flow fields qualitatively as they appear in observed flows. The distinction between the flow around a blunt body and slender body is shown in fig(1.11) and fig(1.12). Whatever the shape of the body, it has been observed that there is a strong fore and aft symmetry in the flow pattern, and the flow field is always completely undisturbed upstream of the body to within a very short distance of the surface of the body.

The front of the body is enveloped by a shock wave which diverges as it extends downstream. The flow in front of this shock is undisturbed and the flow field of interest lies entirely behind the shock. The important field of interest is the flow field between the shock and the body. One thing that can be noticed from the figures is that the degree of inclination of surfaces in the flow field to the oncoming stream is very significant. The

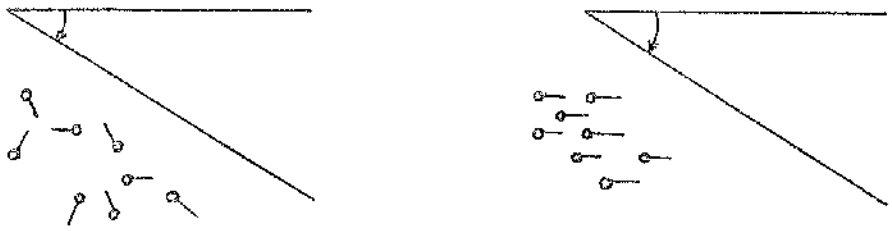

a. Subsonic ($a^2 >> V^2$) random energy extremes. b. Supersonic ($V^2 >> a^2$) Ordered energy higher.

Fig. 1.8 Impact theory for subsonic and hypersonic cases.

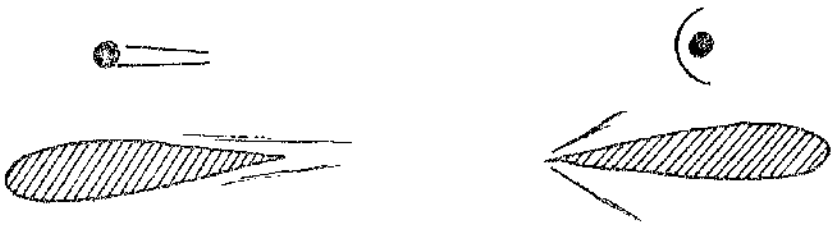

a. Subsonic ($M << 1$) :

rearward fairing, size of the wake determines the drag.

b. Hypersonic ($M >> 1$) :

forward fairing, size of the stagnation region determines the drag.

Fig. 1.9 Comparison of aerodynamic drag.

a. Subsonic ($M << 1$) :

Upper surface produces lift.

b. Hypersonic ($M >> 1$) :

Lower surface produces the lift.

Fig. 1.10 Aerodynamic lift

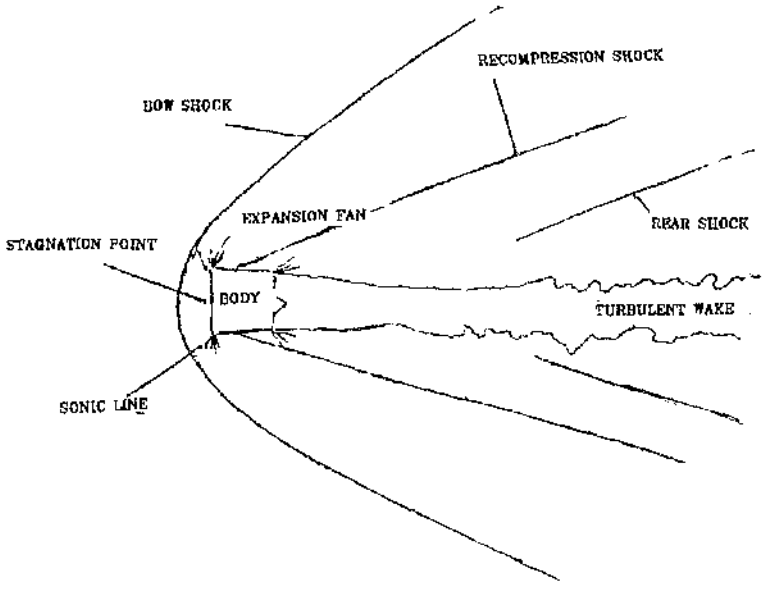

Fig. 1.11 Circular cylinder with flat face forward in air at $M_\infty = 3$

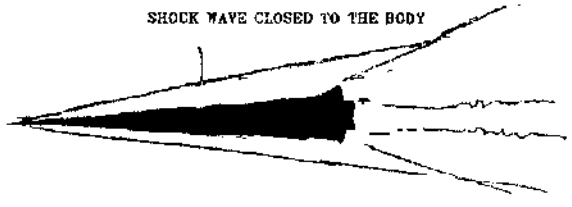

Fig. 1.12 Flow around slender body at high Mach number $M_\infty = 9.6$

enveloping shock lies very close to body surfaces which has a sufficiently large positive inclination to the free stream direction. The region between the body and the shock is termed the shock layer. No shock lies near body surfaces which have an appreciable negative inclination. The pressure on such surfaces are much less than those found in the thin shock layer, although usually greater than the pressure in the free stream. Far downstream of the body the shock wave becomes weak. A wake is observed directly downstream of the body. The diverging shaped relatively weak shock far downstream is termed the shock tail.

Within the shock layer the pressure and temperature are very much greater than in the free stream, with no limit on ratios of these quantities across the shock with increase of Mach number. And although the density is appreciably greater than in the free stream, the density ratio across the shock is limited to finite values with increasing Mach number. If the temperature of the freestream is of the order of the body, at high Mach numbers, the recovery temperature or enthalpy will be very high resulting in a heat transfer from gas to body.

Hypersonic vehicles generally fly at high altitudes where densities and hence the Reynolds Number is low, and therefore boundary layers are thick. Moreover the boundary layer thickness on slender bodies is approximately proportional to M_∞^2, hence the high Mach number further contributes to the thickening of the boundary layer. In many cases, the boundary layer thickness is of the same magnitude as the shock layer thickness as shown in fig(1.13) at M_∞=36. Here the shock layer is fully viscous, and the shock wave shape and surface pressure distribution are affected by such viscous behaviour —— this phenomena is also known as viscous interaction. This can be clearly observed in fig(1.14) where viscous interaction occurs on a flat plate. For comparison see fig(1.14a) which shows no viscous interaction and the pressure remains constant over the whole surface of the body. For inviscid flow assumptions this may be true but in reality there is a boundary layer which deflects the external inviscid flow, creating a comparably strong curved shock wave which curves downstream from the leading edge (fig(1.14b)). Thus in addition to influencing the aerodynamic force, such high pressure increases the aerodynamic heating at the leading edge.

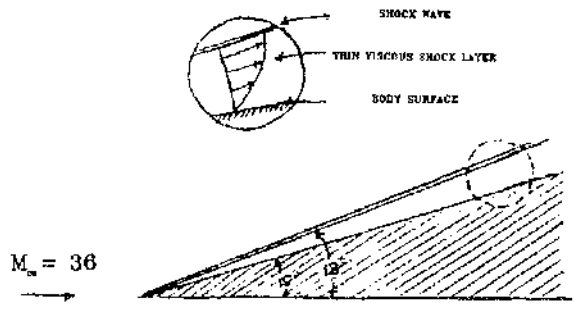

Fig. 1.13 For very high Mach number Hypersonic flow, shock layer thickness will tend to equal to boundary layer thickness.

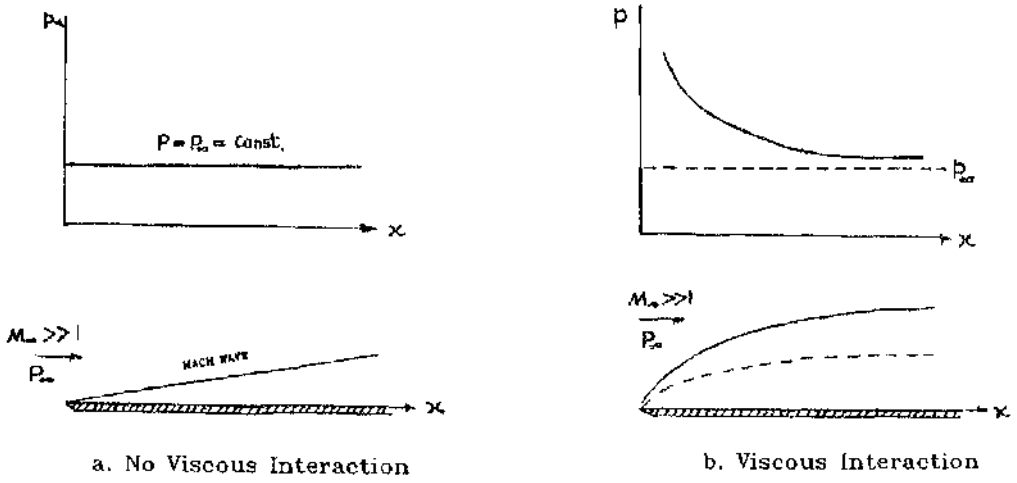

a. No Viscous Interaction

b. Viscous Interaction

Fig. 1.14 Viscous interaction on a flat plate at Hypersonic Speed.

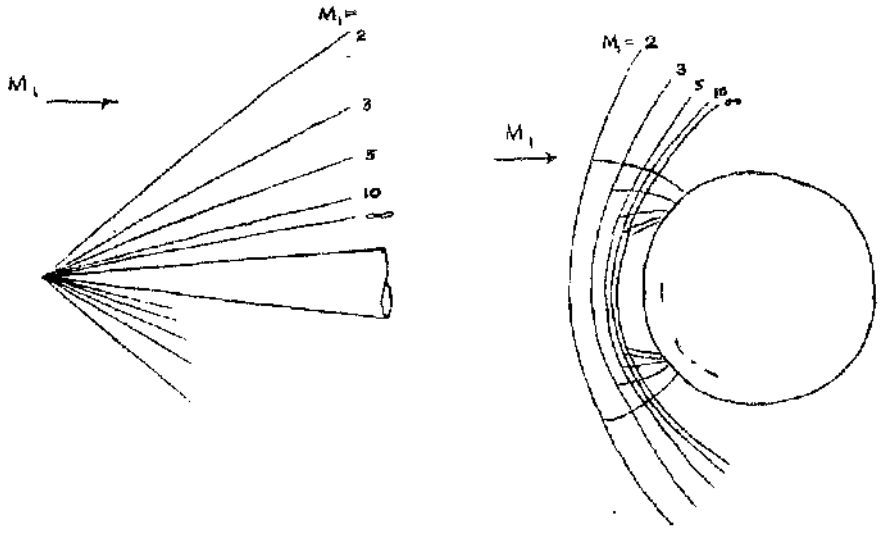

Fig. 1.15 Shock positions for flow past slender cones and sphere at different Mach numbers ($\gamma = 1.4$)

1.5 Hypersonic methodology and CFD.

From the dawn of manned flight, aerodynamic testing played an important role in the development of aircraft, missiles and space crafts. The significance of aerodynamic testing and acquisition of aerodynamic data for design purposes played a key role in further development and modification of these shapes.

The history of testing goes back to the Wright Brothers who after performing tethered and gliding flights developed wind tunnels and completed their wind tunnel program before constructing the prototype. Testing for high speed or supersonic flow can be traced to the Germans who during World War II used supersonic wind tunnels to design V2 Missiles. But at that time these facilities were barely adequate to provide the aerodynamic inputs needed to design these missiles. For developing very high speed (hypersonic) flight, even until the launch of first Russian Satellite Sputnik in October 1957 and first Atlas booster by USA in December 1957, wind tunnels working in the range of Mach 20 were not available and most of the atmospheric re-entry heating data acquisition were dependent on small shock tubes and laboratory experiments.

Until the early fifties for hypersonic flow studies, scientist believed that there is no essential difference between M = 2 and M = 10, any more than there is between subsonic and lower subsonic (e.g., 50 ft/sec and 500 ft/sec).

Believing the said analogy and following supersonic designs for the development of hypersonic cases was probably responsible for some delay in the initial progress in this field. And as time progressed it became clear that hopes for objectives of high Mach number and hypersonic velocity duplication over a wide range of Reynolds number would be impossible to achieve. Besides this experimentation in this regime is time consuming and expensive, and thus development of several specialized devices was required. Moreover it was lately realized that hypersonic behaviour is different from subsonic and supersonic flow and more sophistication is required for this case as compared to traditional subsonic and supersonic testing. Also more

care is required in the interpretation of this data.

In the 60's with the start of the race to land a man on Moon (from May 25, 1961) interest in this field arose. During this decade different series of projects such as Mercury, Gemini and Apollo were carried out. The review of Gemini and Apollo data indicates that, in some cases, provided the measurements are carefully interpreted, hypersonic force and stability data (including viscous drag) may be obtained to good accuracy on the basis of Reynolds number, Mach number or other appropriate similitude up to a particular range. But in most cases all aerodynamic characteristics are necessarily susceptible to the particular simulation environment, e.g., the production and scaling of real gas phenomenon, such as dissociation and ionization in the model flow field including wake, may require duplication of actual flight conditions. For heat transfer coefficients, comprising convective and radiative components, which are a function of thermodynamic equilibrium and temperature, may strongly depend on actual flow enthalpy and density. The sensitivity of base pressure to real gas effects under thermodynamic equilibrium indicates that, at M = 20, and 80,000 ft altitude, base pressure was estimated to be 2.3 times larger than for ideal air flow where γ=1.4.

Other complex flight phenomena required to be simulated include roll-pitch or spin-yaw which demand the duplication of the ablation effect and model dynamics at hypersonic speed and calls for high sophistication in design of experimentation and instrumentation.

Although ground test facilities are in their evolutionary mode and there is a consistent development of wind tunnel facilities, still each type of facility carries a number of limitations. Some of the conventional and high performance wind tunnels used in this regard are

a: Conventional (conventional continuous, blow-down wind tunnels, nitrogen, arc jet wind tunnels, helium wind tunnels).

b: High performance short duration tunnels (free piston compressor wind tunnel, gun tunnels, long-shot tunnels, slow piston compressor tunnels, shock tubes etc.)

Of these wind tunnels conventional hypersonic wind tunnels and free piston compressor tunnels are developed for relatively long duration operation, from continuous down to 0.1 sec and with air at condensation free conditions up to about Mach 15. The upper limit of their Mach number, Reynolds number and enthalpy or test section velocity performance are governed by factors such as:

(i) The capability of the heating technique to achieve high temperature;

(ii) The very large energy level required for long duration operation at a high enthalpy and pressure;

(iii) Excessive heat losses sustained over long period of time;

(iv) Difficulty in preventing nozzle throat erosion due to long flow duration; and

(v) Structural restraints on the maximum stagnation pressure.

Although it had been claimed that some of these limitations including Re-M duplication had been overcome by the development of shock tube and similar short duration facilities but still it failed to provide the velocity and high Reynolds number experienced in atmospheric re-entry. Also during re-entry, velocity characteristics of ballistic and space flight at 23,000 ft/sec, exhibit significant thermochemical kinetic effects such as (non-equilibrium) dissociation and ionization in the flow field, duplication of which is very difficult in ground tests.

Development of test facilities to improve its performance brought another constraint whereby the inverse relation between performance and test duration is expected. So, to resolve the attainment of high Mach numbers and Reynolds number, flow velocities and enthalpies meant increases in test flow energy flux, test section size, stagnation pressure and temperature. All this could only practically be realised through the reduction of test time because large test flow power levels could be achieved for only very short periods of time through the application of energy storage in thermal, chemical, kinetic or electrical form. Therefore the testing time for recently built wind tunnels is very small, (of the order of fractions of seconds). In all different hotshot, longshot and shock tunnels the operating period is from 100 to 1 msec range.

This high performance at very small testing time intervals poses another question —— **Is it feasible to compare the data acquired by wind tunnel to the actual flow ?**

Thus in view of above discussion there are difficulties in obtaining reliable hypersonic data from ground testing because the accuracy of results is related to the large number of similarity parameters which, ideally, should be satisfied, in simulation. So it appears that wind tunnel facilities have limitations for further development, and other techniques including free flight options may be required to reach the high velocity and low altitude characteristics of hypersonic vehicle trajectories of interest.

One such technique which has potential in making progress in the understanding of the physics of fluid follows from the advent of modern computers. This approach is called CFD (i.e., Computational Fluid Dynamics).

CFD can be defined[10] as the numerical solution of a set of partial differential equations which describe the fluid motion by applying the laws of conservation of mass, momentum and energy to evaluate the flow parameters of pressure, density, temperature and velocity vectors etc. These equations are non-linear in nature and are difficult to solve analytically. Numerically these are solved on a computer at a finite number of discrete points in the flow field by defining an arranged computational grid.

Until the start of the 60's computational methods were rarely used[11] in aerodynamic analysis. The primary design procedure for the development of aerodynamic configurations used to be through the use of the wind tunnel along with an analytical approach. Shapes were tested and modified in view of pressure and force measurements and flow visualization techniques.

During the last two decades revolutionary changes[12] in the power and performance of the computer (fig(1.16)) have been achieved and it is beginning to be realized that CFD can be used as a primary instead of a secondary source of data acquisition, to achieve accurate simulation of flow conditions in flight.

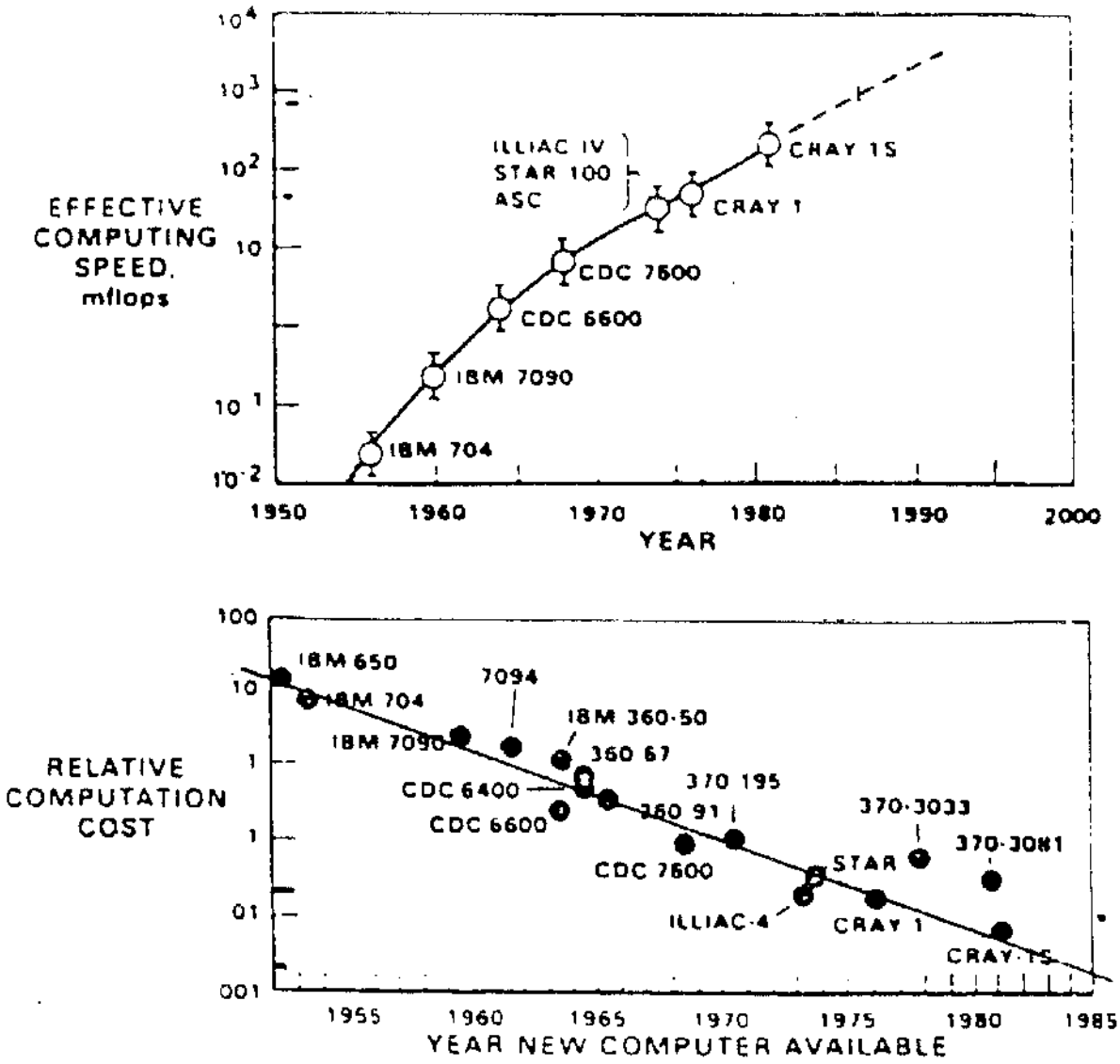

Fig. 1.16 Progress in digital computer capability and cost effectiveness.

Flow simulation in wind tunnel is limited, and is especially difficult at hypersonic speed (as discussed earlier) due to many factors like exact duplication of pressure, velocity, Reynolds number, model size and type of atmosphere in the wind tunnel whereas computers have none of these limitations. Computationally it is possible to achieve a simultaneous solution for air density, flight velocity and vehicle scale all at one time. For hypersonic flight, with the fundamental inability of wind tunnels and shock tubes to simulate high temperature real gas effects, computers are becoming the primary and wind tunnel/shock tubes the secondary provider of flow simulations.

Another objective for the application of CFD is to shorten the aerospace vehicle design cycle and to improve the potential performance of new vehicles. CFD methods can compress the design cycle by avoiding the time and expense associated with experimental design methods. To quote a few examples, results for a generic Mach 3 transport aircraft were obtained in just 2 hrs on a Cray 2 Supercomputer. Comparison of these results with wind tunnel data showed an impressive accuracy for lift and drag co-efficient at different angles of attack.

Contrary to all wind tunnel limitations, in the past, aerospace vehicle design has been considered as an evolutionary process and most progress has been based on the prior experience and data available from the wind tunnels. But now with the availability and emergence of CFD as a powerful tool, it has established its importance in aero design procedure. Therefore now analytical and experimentation are not the only tools used for design. Rather there are three basic tools[13] used for any flight vehicle design process. These are analytical methods, computational procedures and experimentation.

Amongst these, analytical methods give very quick and closed form solutions but they have limitations of restrictive assumptions and can deal with ideal cases of aerodynamics only. Similarly in the case of experimentation, representative or actual configuration can be tested and representative or complete aerodynamic data can be produced. But experimentation is costly both in terms of model and testing conditions.

Relative to these, computational procedures require very few restrictive assumptions and can be applied to very complicated configurations as well. Additional to this, they are beginning to have few limitations of Mach number or Reynolds number, so they result in a complete surface and exterior flow field definition. Also they are beginning to be far more cost effective than wind tunnel testing.

The principal application of computational simulation is towards the design of an aircraft. Many activities that take place in an aircraft design project can be summed up as being part of a basic process loop in three steps.

1. Configuration definition
2. Data acquisition
3. Evaluation.

Computational aerodynamics has affected this process loop by providing

1. A new means of data acquisition.
2. Executing the design loop in an inverse manner

through proper use of effective computational codes.

1.6 Historical Preview of Waveriders

The V2 rocket started the race to dominate space and with that came the need to tackle problems of hypersonic flow. Therefore to orbit the earth and to take man into space, different space plane shapes were considered. It was during this evolutionary period that a considerable emphasis was made on slender wing body combinations to achieve high lift with an optimum L/D ratio.

All this was based on a simple principle that in order to achieve a high lift the components of an aircraft should be individually and collectively arranged to impart the maximum downward and the minimum forward momentum to the surrounding air. This can be accomplished simply by adding[14] a delta wing to a cone and extending its leading edge forward to the shock wave to preserve momentum (fig 1.17). A further increase in lift

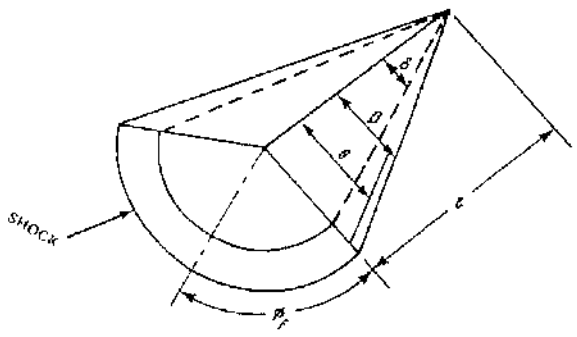

Fig. 1.17 Idealized conical waverider.

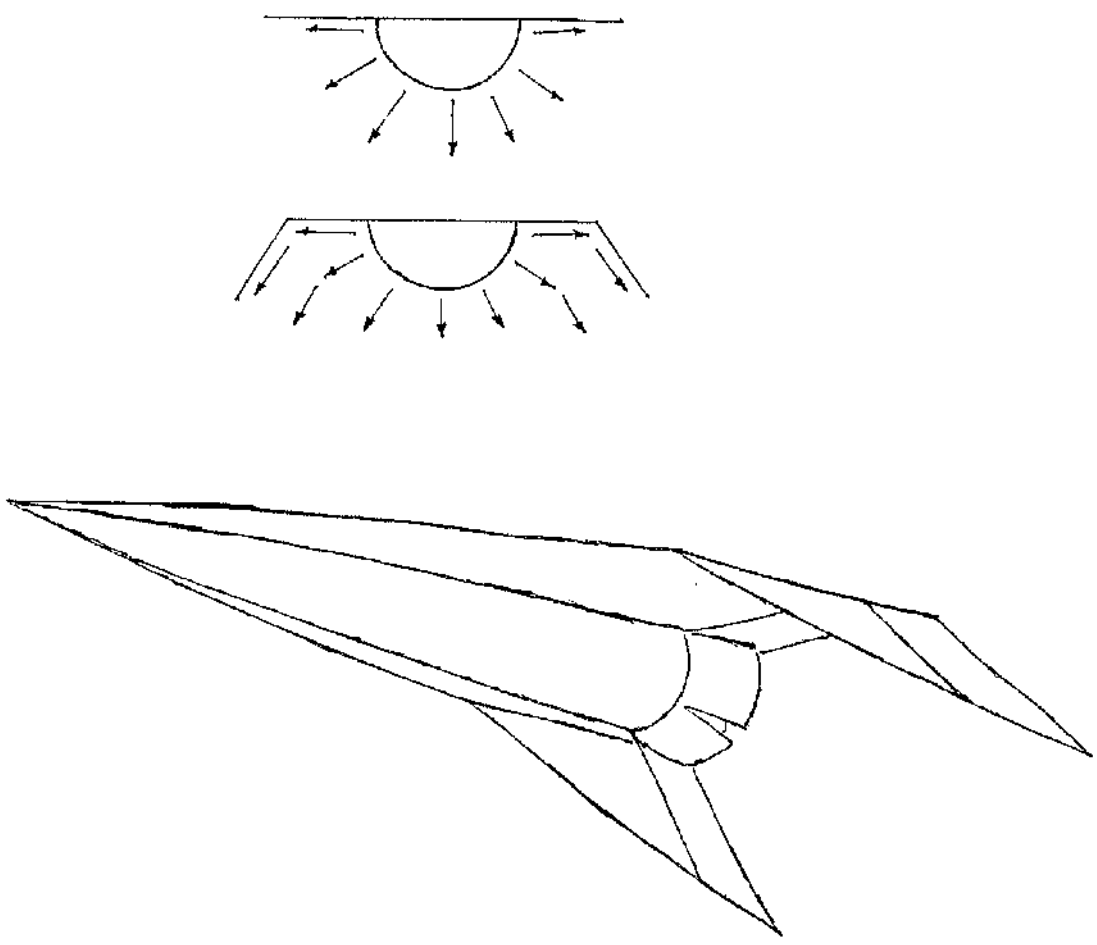

Fig. 1.18 Extra wing deflection for flat top waverider.

can be achieved by deflecting the wings downward (fig 1.18). The advantage of such drooping tips apart from high lift is directional stability and control.

The idea of achieving high lift was further refined by Nonweiler. For waveriders Nonweiler[6,7] considered first the idea of caret shaped wings for lifting bodies and showed that the flow around these can be calculated by simple 2-dimensional wedge flow. These delta or caret waverider wings whose upper surface is composed of a free stream surface and the lower surface has an inverted V or W, have a cross section of such a form that at the design Mach number and incidence any shock waves formed are planar (fig 1.19).

Criticisms were made about these shapes, such as the need for a long under carriage due to anhederal, increased wetted area and less volumetric efficiency. Flower[15] later tried to tackle some of these problems and extended Nonweiler's method for designing caret wings giving some considerations to defining the upper surface and free stream surfaces. In his study he deduced appropriate shapes by constructing the upper surface from a Prandtl Meyer expansion joined with the lower compression surface. Different shapes were yielded such as the X-Delta and Y-Delta shapes as shown in fig (1.20).

Some further research about this has been caried out by Roe[16,17] and Squire[18]. The Squire suggestion resulted after comparisons were made of the lift of flat delta wings and waveriders at high angles of incidence and high Mach number. He supported the case that for the lifting reentry situation caret wings have more favourable characteristic for producing high C_L than those for flat delta wings with the same ratio of lift to drag. Therefore at a given Mach number and wing loading, they can re-enter at higher altitudes resulting in a reduction in stagnation point heating rate. Also thin shock layer theory was advocated to have produced the exact prediction of the aerodynamics of caret wings at design conditions. Squire also pointed out some off design behaviour for caret wings.

Some relevant experimental data regarding caret wings can also be found in ref[18] and ref[19].

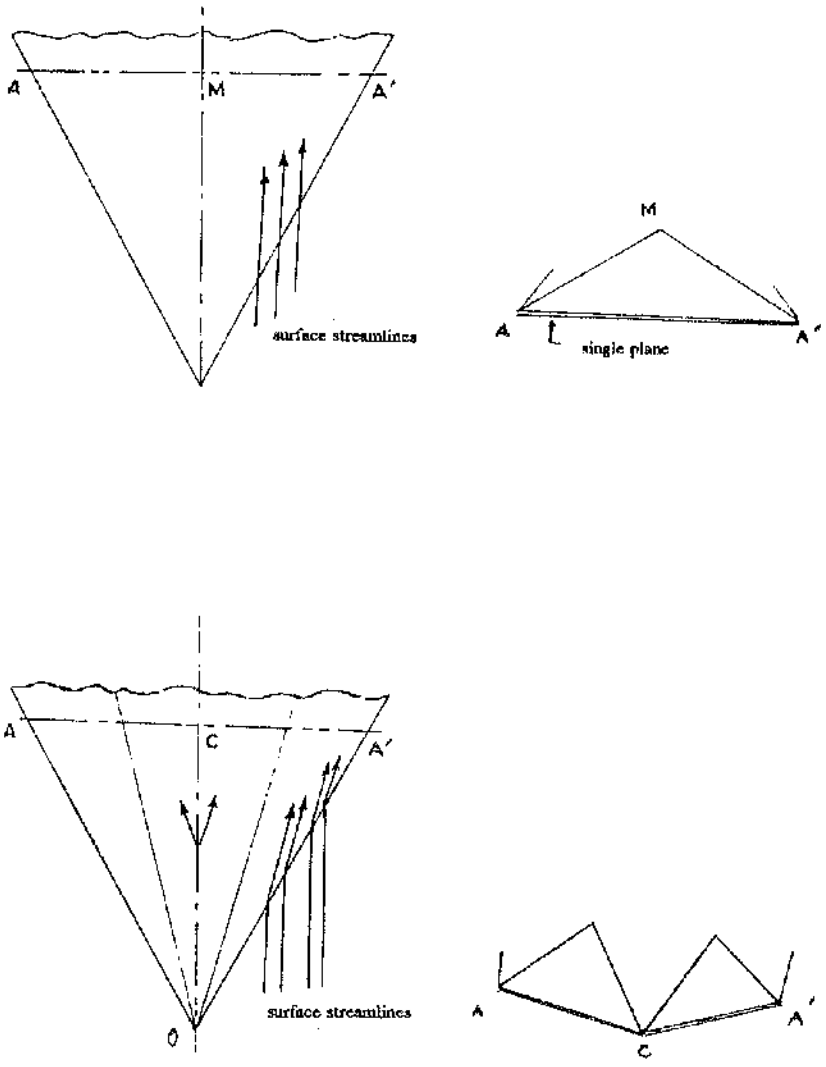

Fig. 1.19 Caret Wing (a. Inverted V shape, b. W Shape)

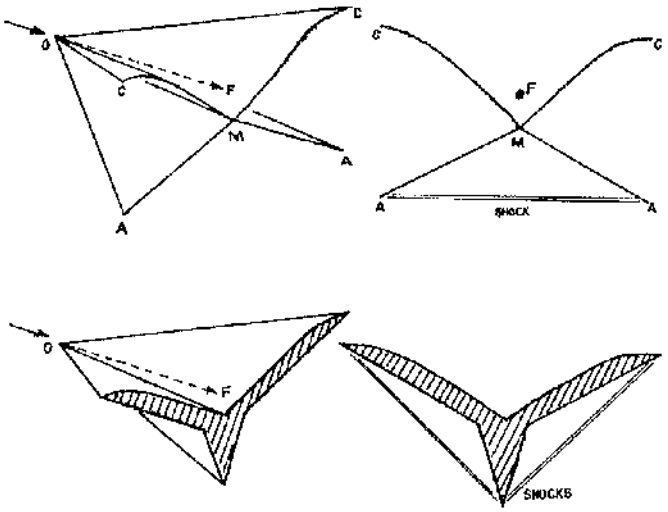

Y-Delta

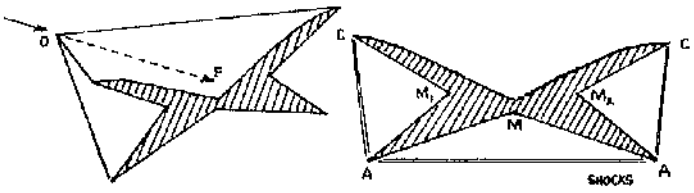

X-Delta

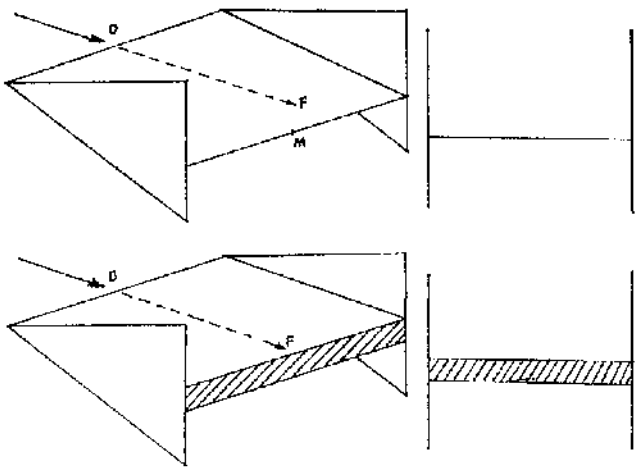

H Wings

Fig. 1.20 Shapes proposed by Flowerns 1.

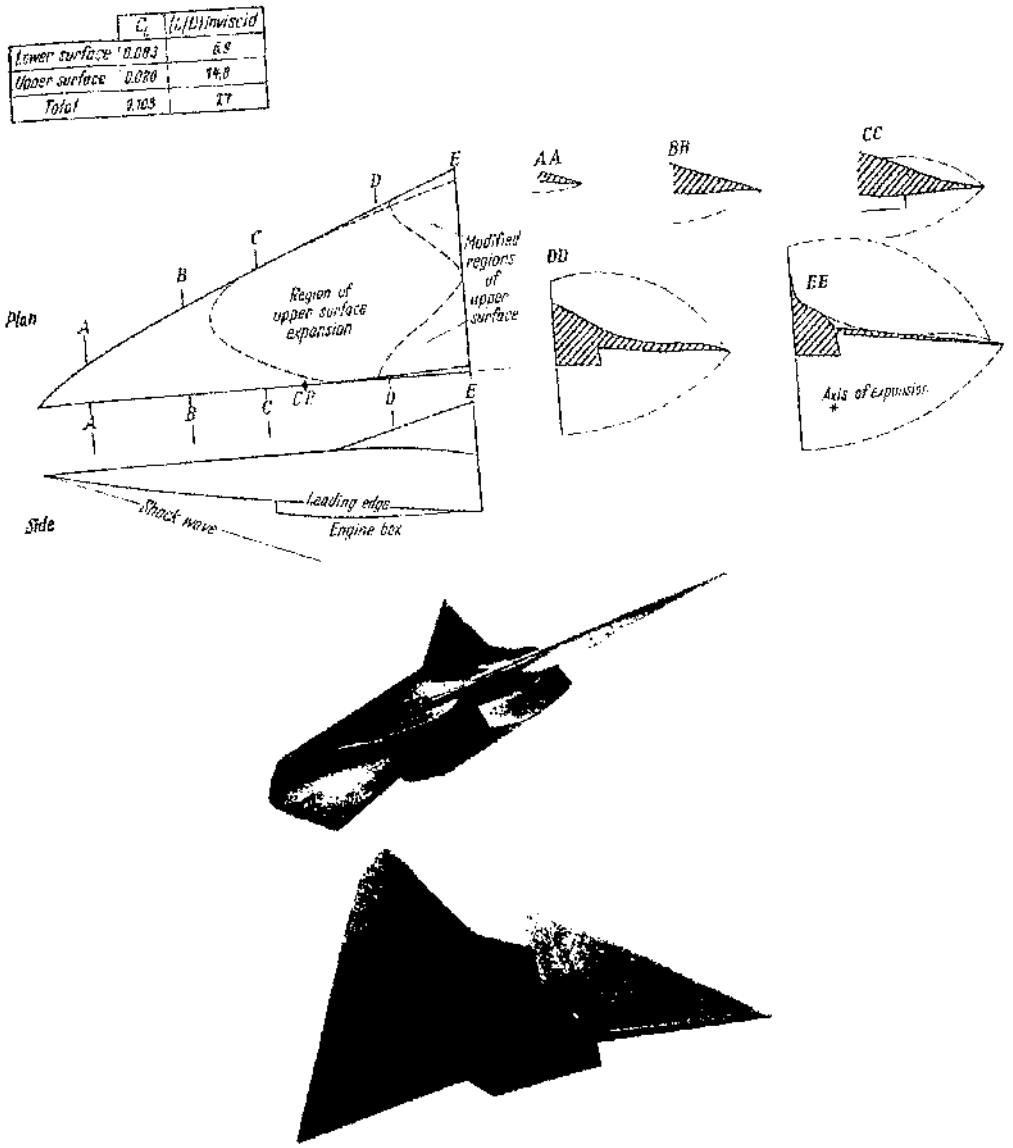

Fig. 1.21 Proposed lifting configuration by Jones et al[21].

But as all these shapes derived from 2-D flow generally have flat surfaces and sharp corners so criticism has become more severe when such differing factors as viscous and heating effects are considered. These are very influential on vehicle design at hypersonic speed. It was then considered that curved surfaces could be designed in a similar fashion to those utilized for flat surfaces generated by 2-D wedge flow, by using the stream surfaces in conical flow thus revealing features of more usable volume and less wetted area. Flow around such cone generated surfaces derive from studies by Jones and Wood[20], Jones, Roe and Pike[21], and L.C. Squire[22,23]. Also Rasmussen[24], Kim[25], Bowcutt and Anderson[26] carried out research on conical flow waveriders. Experimental data for conical flow waverides can be seen in ref[27,28]. Parallel to this work, attempts were also made to design these type of lifting configurations by considering axisymmetric flow field and power law bodies[29].

Jones, Moore, Pike and Roe[21] proposed to build a lifting configuration from an axisymmetric flow field by designing it exactly for inviscid flow and optimizing it further by replacing the stream surfaces with solid boundaries. A generic shape developed as a result of their work can be seen in fig (1.21), which was designed to cruise between M=4 to M = 7 and to produce an L/D of up to 7.7 assuming inviscid flow.

Jones and Wood[46] presented in 1963 a method for designing lifting configurations from flow around a non-lifting cone. Two different type of shapes were suggested. Where the leading edge extends to the apex of the basic conical shock the configuration was designated Type A and where the lifting surface apex lay behind the apex of the basic cone they called it Type B configuration. The difference between type A and B in their limiting form is that in the former case wing and cone can be seen separately where as in the latter the distinction between two is difficult to visualise. This designation is used later in the thesis.

An interesting case of optimum wing design is considered by Cole and Zien[29] where hypersonic small disturbance theory is used to define these shapes derived from axisymmetric flow. Here unlike wedge (planar) or conical shocks a power law ($r_s \sim x^n$) shock shape is assumed and results are obtained

from $n = \frac{1}{2}$ to $n = 10$ at γ=1.4.

Since the early seventies in the topic of waveriders derived out of conical flow, most work can be related to Rasmussen and his colleagues[24,25,27,28,30]. They did experimentation and optimization for different waverider configurations generated from axisymmetric conical flows. Different cases of study include waveriders from circular as well as elliptic cones from a zero lifting situation to yawed cones at incidence and yaw and with longitudinal curvature. Most of the group's work is based on hypersonic small disturbance theory with inviscid assumptions apart from ref[30] where viscous effects are included by means of a laminar boundary layer.

Other promising shapes have been reported by Bowcutt, Anderson & Capriotti[26] which have emphasised the importance of viscous effects and included them in their optimized hypersonic waverider shapes. Viscous effects were included by correcting for 2D laminar, transitional and turbulent boundary layer displacement thickness along inviscid streamlines. The upper surface was carved from the expansion flow and the lower compression surface by tracing stream lines in conical flow. A blunt leading edge with a certain radius was included to correspond to an acceptable leading edge temperature level.

1.7 Aim and Approach of the present study.

A review of the study so far regarding these waverider shapes suggests that in the process of designing these shapes, major features of hypersonic-like viscous effects and high temperatures have not been given proper consideration. Practical experience with the Space Shuttle suggest that viscous and high temperature effects are very critical with regard to accurately assessing different flow phenomenon such as aerothermal heating, shock/boundary layer interaction and separated flow. Only Bowcutt & Anderson [26] appear to have included viscous effects in their optimization procedure for waverider design.

Hypersonic flow differs fundamentally from subsonic flow due to the

variation of properties associated with high velocity at high altitude. Such factors as entropy layer, viscous interaction, high temperature, low density and real gas effects must then be considered when simulating the flow. For instance at high velocity the boundary layer becomes thick due to high kinetic energy dissipation within the boundary layer causing an increase in viscosity and temperature and a decrease in density. This thickening of the boundary layer introduces a viscous-inviscid interaction causing problems for boundary layer analysis which affects the surface pressure distribution.

For the viscous interaction parameter ($\chi = M_{\infty}^{3}\left[\frac{C}{Re_{\infty}}\right]^{1/2}$)>>1, the surface pressure distribution may differ significantly from the inviscid prediction. Contrary to this all previous waverider designs are based upon inviscid flow, even though χ is generally not below a value of 1. Because waverider configurations provide the basis for vehicles designed to fly at high altitudes where the Reynolds number is low and the Mach number high, hence, viscous effects become very important.

Much has been done however for improving viscous corrections [32-37] by treating the problem as a coupled one with a boundary layer displacement thickness correction and a general approximate calculation of the outer inviscid flow. But this is still a severe compromise due to the different constraints involved. Most viscous flow problems can be treated using boundary layer calculations. However, a number of very important viscous flow problems cannot be solved by this approach because the accompanying assumptions are not valid. An extreme example is that of when the inviscid flow is fully merged with the viscous flow, then the two flows cannot be solved independently as required by boundary layer theory. Boundary layer theory also fails when a large vortical flow region forms in the flow field, e.g., on the leeward side of the vehicle at a high angle of attack. Therefore it becomes necessary that it must be solved by a set of equations which are valid in both the inviscid and viscous regions. An obvious set of equations which can be used to solve strongly interactive flow fields are the Navier-Stokes equations. Based on this strategy numerical solutions of the Navier-Stokes Equations were applied to different waverider shapes to study viscous effects.

Recent high interest in space planes and the exploitation of the advantages of waveriders were the main motives for present study. Based on the above discussion the approach for the present study is developed as follows.

In this introductory chapter, after describing the different hypersonic systems used for space exploration, advantages of having high lift are reviewed and waveriders have been shown to be favourable shapes for such application. In the next few pages general features of hypersonic flow are discussed and comments are made on the advantages of CFD to simulate hypersonic flow as compared to analytic and experimentation methods. The role of each approach to space plane design is also discussed briefly. An historical review of waverider shapes is provided, pointing out the importance of inclusion of factors such as viscous effects in waverider design, which are usually not included in the course of development of these shapes. To highlight the importance of these forms a basis of this study.

The second chapter is devoted towards the classical theory of waveriders. The theory is given for both wedge derived and conical derived waveriders. The critical effects of viscosity and high temperature on waveriders is also studied in this chapter.

In the next chapter research efforts to simulate the flow around these shapes by applying the Navier Stokes solution is described. Interesting physical phenomenon revealed by simulation in this way is discussed. Off design behaviour and advantages of applying CFD on these shapes are pointed out.

Study of more general shapes is the topic for chapter four. Here more general shapes are derived numerically from conical and wedge flow. Comparison is made to reveal the advantage of waveriders derived from wedge flow with that derived from conical flow.

Finally general conclusions are drawn from the study and suggestions are made for future work.

CLASSICAL THEORY OF WAVERIDERS.

2.1 Introduction.

The considerable research in high speed vehicle design has suggested that the best aerodynamic shape is that called the waverider. The shapes are so named because under design conditions their lateral edges would ride on a captured shock wave. The advantages of this type of configuration are that it has

a. lower drag for the same lift
b. higher lift
c. higher lift to drag ratio

than conventional shapes especially in hypersonic flow. Also apart from their advantages of having good aerodynamic characteristics they can be designed inversely to fit a known flow field. In this way analysis becomes easy because in this process it is not the shape that is chosen in advance, but rather the flow field, which is usually then a simple one.

As waveriders have favourable characteristics for use as space plane shapes therefore

1. One can study systematic families of shapes and draw general conclusions as to effects of aspect ratio, payload volume, distribution of volume etc. on performance characteristics.
2. One can study more about their performance characteristics which could become the basis by which to judge the excellence of design achieved by other methods.
3. Although the flow about a waverider in its design condition has a deceptive simplicity, the flow in conditions slightly "off design" may provide a point of entry for the study of more general and more complex flows about wing like shapes.

In the present chapter along with the definition of waverider, a simplified theory and analytical method for the prediction of flow field around a caret and conical waverider shape is given. Also the method to

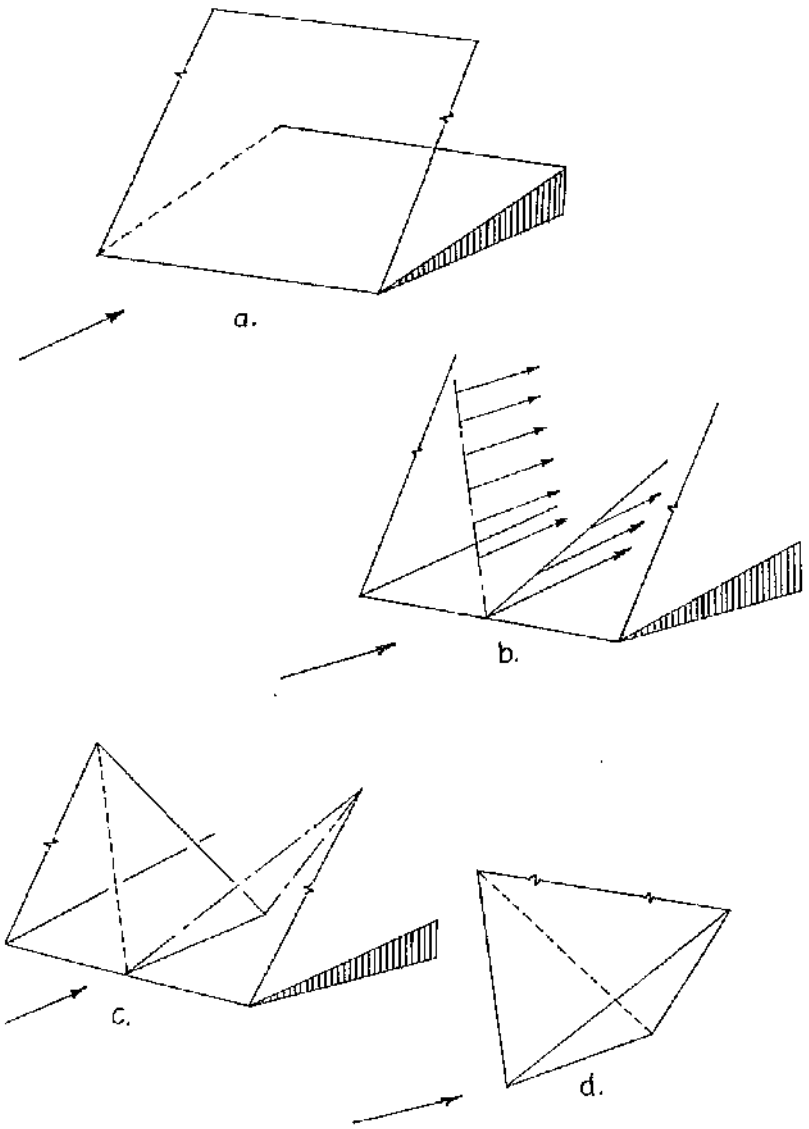

Fig. 2.1 Construction of simple caret wings.

predict the lift and drag co-efficients for any arbitrary shape waverider is explained. An historical review of the study of flow around waverider is made before pointing out the importance of inclusion of viscous and high temperature effects towards finalising waverider design shapes.

2.2 Definition of waveriders.

A waverider can be defined as a supersonic vehicle whose shape is composed of streamlines derived from known exact solutions of the inviscid flow equations. Nonweiler[6] first pointed out that a flow field determined by oblique shock relations forms a stream surface which defines the family of caret shapes (fig 2.1). In its simplest form Caret shapes can be designed by starting with the flow past a two dimensional wedge (fig 2.1a) and then drawing a pair of intersecting straight lines lying in the plane of the shock, and visualizing the stream surface which stems from them. Further if we place a body having exactly the shape of this surface and by introducing it carefully, on aligning it exactly with the flow direction the simplest caret wing (fig 1.19) can be designed. A more detailed discussion has been carried out in ref[38]. Interesting features of these wings are that the leading edge of these wings ride on the surface of a planar shock wave, which account for the term *"Waveriders"*. Thus a waverider can be defined as

" an inversely designed vehicle whose flow field (hypersonic or supersonic) is determined first and whose shape is derived afterwards"

As exact solutions are available for oblique shocks and circular cones in supersonic flow, they form the basis for inversely derived waveriders.

Instead of the literal definition stated above a more general definition is also commonly used where the characteristics of waveriders are applied to other configurations that indirectly exploit their advantageous properties.

2.3 Classification of Waveriders.

Depending on the final shape of the waveriders, whether they are caret, elliptical, conical or non conical, they can be classified under two main

groups : shapes which are derived from wedge flow; and waveriders constructed from conical flow.

2.3.1 Wedge Derived Waveriders (CARET WINGS)

2.3.1.a Theory

For the caret wing the flow beneath it can be considered equivalent to that on a 2-D wedge and can be predicted by oblique shock wave theory.

In its simplest approach for waveriders, consider a two dimensional flow about a wedge. Further assume that flow is parallel to the upper surface of the shape and it coincides with the freestream surface. The result is that there is no shock or expansion wave on the upper surface and the pressure on this surface is p_∞. On the lower surface there is an attached oblique shock wave, with a compressive pressure p_c, which can be evaluated by applying the oblique shock theory relationship for a 2-D wedge

$$\frac{p_c}{p_\infty} = \frac{2}{\gamma+1}\left[\gamma M_\infty^2 \sin^2\beta - \left(\frac{\gamma-1}{2}\right)\right] \qquad \text{——— (2.1)}$$

where, β is the shock angle and γ is the ratio of specific heats.

The flow in the base region, is confined between two Prandtl Mayer expansion waves but these are not considered. Although this is important, experiment shows that even at M_∞=5 the pressure at the base is closer to zero than p_∞. However the value of base pressure is Reynolds number and body configuration independent.

Lift and drag relations per unit span for an infinite wedge using shock expansion theory are

$$L = p_c \ell_c \cos\theta - p_\infty \ell \qquad \text{——— (2.2)}$$

$$D = p_c \ell_c \sin\theta - p_\infty \ell_b \qquad \text{——— (2.3)}$$

As, compression length; $\ell_c = \ell/\cos\theta$, and

base length; $\ell_b = \ell\tan\theta$

with ℓ = length of the caret wing (fig 2.2)

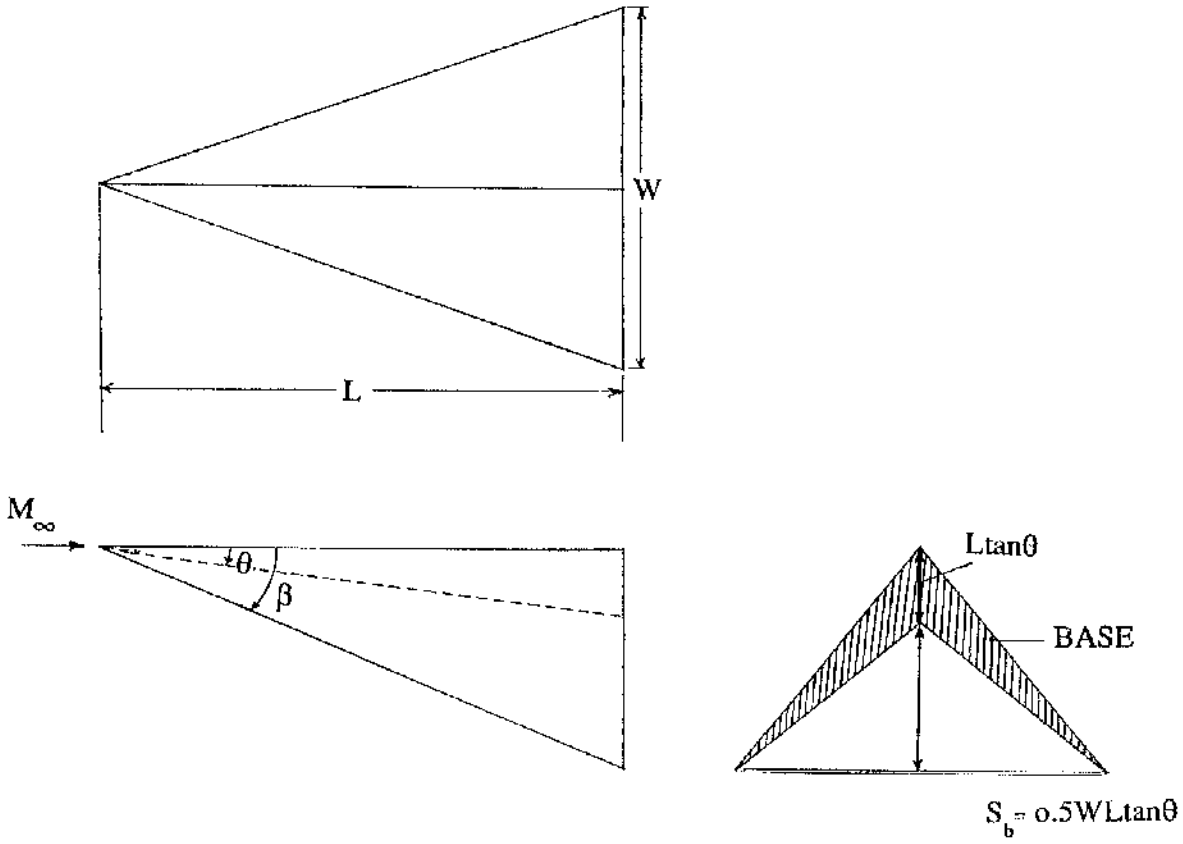

Fig. 2.2 Caret wing.

So,

$$L = (\frac{p_c}{p_\infty} - 1)p_\infty \ell \quad \text{and} \quad D = L\tan\theta$$

and lift and drag coefficients are

$$C_L = \frac{L}{0.5\gamma p_\infty M_\infty^2 \ell} = \frac{2}{\gamma M_\infty^2}(\frac{p_c}{p_\infty} - 1) \qquad \text{——— (2.4)}$$

$$C_D = C_L \tan\theta \qquad \text{——— (2.5)}$$

By using relation 2.1, to eliminate $\frac{p_c}{p_\infty}$,

$$C_L = \frac{4}{(\gamma+1)M_\infty^2}(M_\infty^2 \sin^2\beta - 1) \qquad \text{——— (2.6)}$$

Now, the dimensionless parameters governing the flow are γ and M_∞. The wedge angle θ can be solved in terms of β by using the relation.

$$\theta = \tan^{-1}\left[\cot\beta \frac{M_\infty^2 \sin^2\beta - 1}{1 + \{[(\gamma+1)/2] - \sin^2\beta\}M_\infty^2}\right] \qquad \text{——— (2.7)}$$

But as eqn(2.7) cannot be solved explicitly for β, therefore an approximate equation can be derived, valid for high speed flow, which can achieve this purpose by using scaling parameters as follows.

For $M_\infty^2 >> 1$ for the waveriders, the shock is attached, and for an attached shock, if θ is relatively large when $M_\infty^2 >> 1$, the heat transfer and drag become very high. Therefore in order to keep heat transfer and drag small at very high speeds θ must be very small and the body slender. To incorporate this a scaling parameter can be introduced as

$$K_\theta = M_\infty \sin\theta \qquad \text{——— (2.8)}$$

This is known as the Hypersonic Similarity Parameter.

Similarly a scaling parameter appropriate for the shock angle, K_β, can also be introduced

Where, $K_\beta = M_\infty \sin\beta$ ——— (2.9)

Eqn (2.7) can be written in similarity form as

$$\tan\theta \tan\beta = \frac{K_\beta^2 - 1}{[\frac{\gamma+1}{2}]M_\infty^2-(K_\beta^2-1)} \qquad \text{——————} \quad (2.10)$$

In equation(2.10) for K_θ, $K_\beta \longrightarrow$ of order unity, & $\theta,\beta \longrightarrow 0$, $M_\infty \longrightarrow \infty$, therefore, $[(\gamma+1)/2]K_\beta K_\theta = K_\beta^2-1$

Making substitution, $K_\theta(\frac{\gamma+1}{4})=K$

$$2KK_\beta = K_\beta^2-1$$

$$K_\beta = K + (K^2+1)^{1/2}$$

or $$K_\beta^2-1 = 2K\left[K+(K^2+1)^{1/2}\right] \qquad \text{——————} \quad (2.11)$$

Therefore by introducing similarity parameter for lift and drag co-efficients

$$C_L = \frac{\gamma+1}{2}\theta^2\left[1+(1+K^{-2})^{1/2}\right]$$

and $$C_D = C_L\theta$$

So, now as γ, M_∞ and θ are known, we can find lift and drag for caret shape waveriders.

i.e., $$\text{Lift} = L = (p_c-p_\infty)A_p = (\frac{p_c}{p_\infty}-1)p_\infty \times \frac{W\ell}{2} \qquad \text{——————} \quad (2.12)$$

$$\text{Drag} = D = (p_c-p_\infty)A_b = L\tan\theta \qquad \text{——————} \quad (2.13)$$

Where

A_p = planform area = $\frac{1}{2}W\ell$

A_b = Base area = $\frac{1}{2}W\ell\tan\theta$

and, W = Base width (ref. to fig.(2.2))

Therefore,

coefficients of lift and drag can be derived as

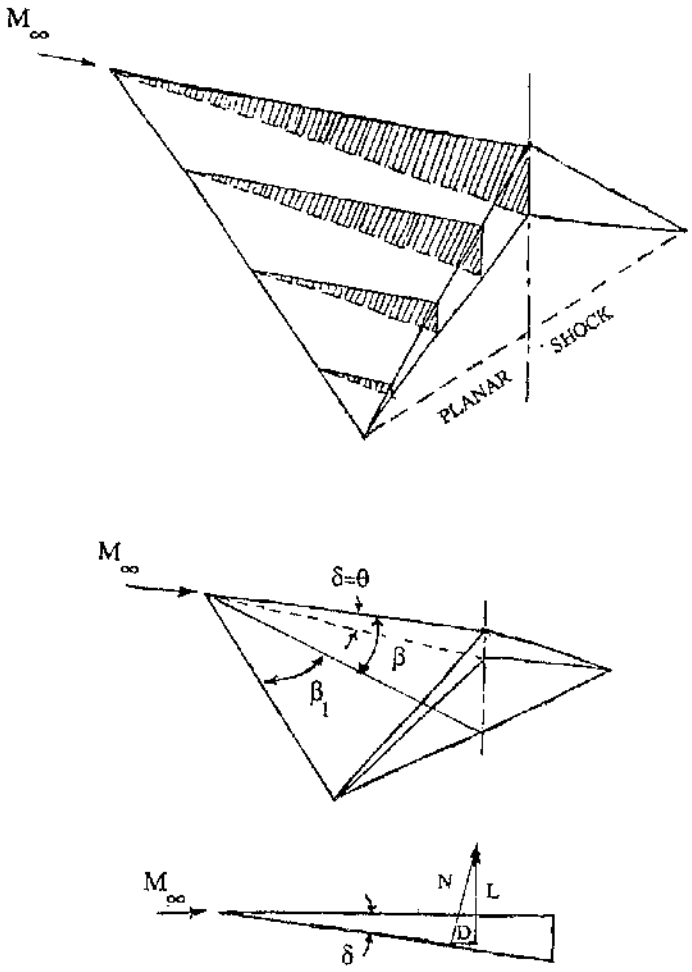

Fig. 2.3 Caret Shaped Waveriders

$$C_L = \frac{2L}{\rho V_\infty^2 \times Area)_{Plan}} = \frac{2L}{\rho M_\infty^2 \gamma RT \times \frac{1}{2} W \ell} = \frac{2}{\gamma M_\infty^2}\left[\frac{p_c}{p_\infty} - 1\right] \quad \text{—— (2.14)}$$

and,

$$C_D = C_L \tan\theta \quad \text{---------- (2.15)}$$

Equations (2.14) and (2.15) are same as (2.4) & (2.5) for two dimensional wedge flow.

Then the C_L and C_D for a waverider in scaling parameters can also be written as[34]

$$C_L = \frac{\gamma+1}{2}\theta^2\left[1+(1+K^{-2})^{0.5}\right]$$

$$C_D = C_L\theta$$

2.3.1.b Optimization of Drag for Caret Wings.

Relations for L/D derived earlier are true for inviscid flow. Neglecting also both base and friction drag, the L/D ratio increases without limit as $\theta \to 0$; but at the same time the configuration has no volume in the limiting case . Therefore to achieve a given volume, the surface area will need to be large when θ is small. Hence the friction drag (for small θ) will be large compared to the pressure drag. Consequently there will be some optimum deflection angle for a given skin friction coefficient (c_f). This optimum angle can be determined by assuming a constant c_f for the wetted surface of the caret wing (fig 2.3).

On adding friction and pressure drag to inviscid flow, a new relationship can be developed as

$$\frac{L}{D} = {}^{c_p}\Big/\left[c_p\tan\theta + \left(\frac{A_w}{A_p}\right)\times {}^{c_f}\right] \quad \text{———— (2.16)}$$

Where, A_w = wetted area

A_p = planform area

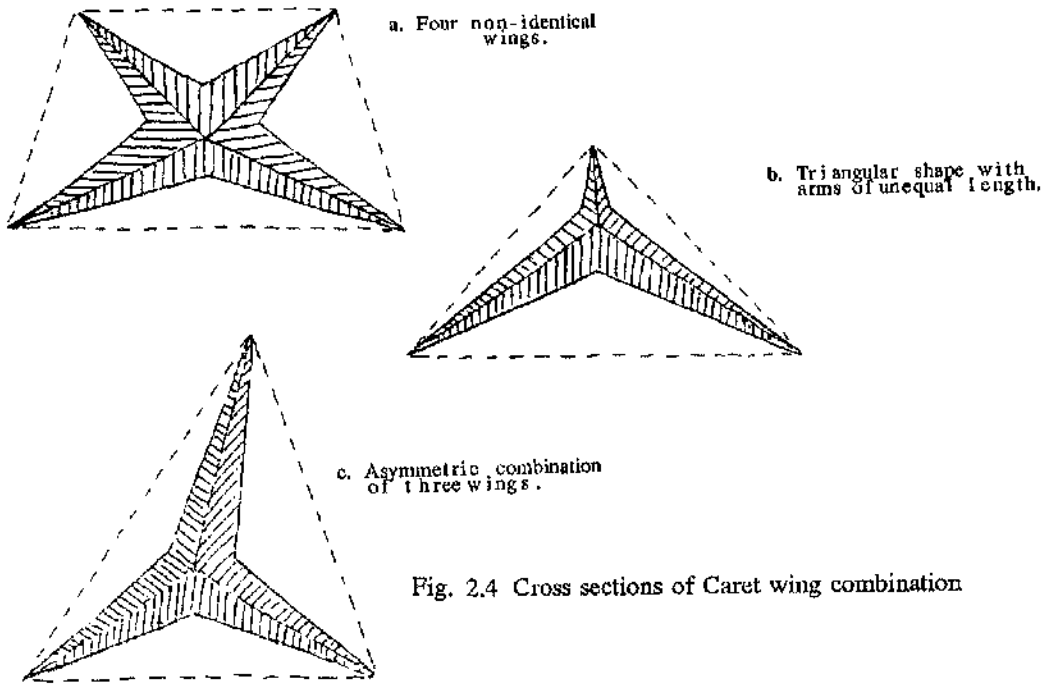

Fig. 2.4 Cross sections of Caret wing combination

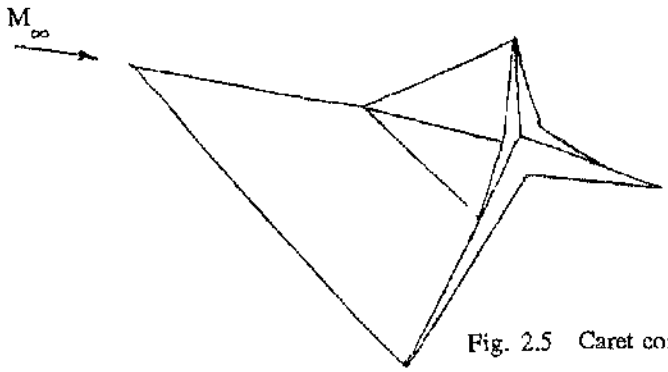

Fig. 2.5 Caret combination of different sizes.

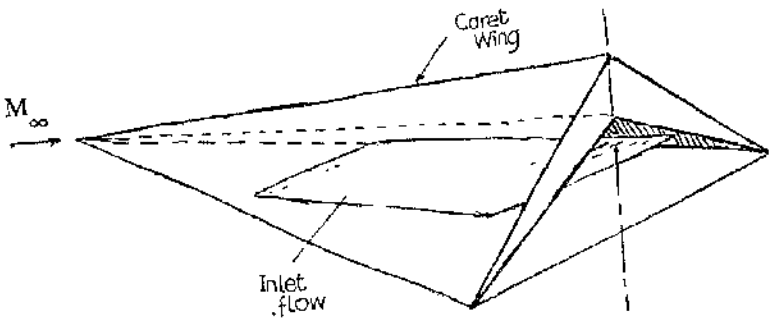

Fig. 2.6 Caret wing inlet

and, $$\frac{A_w}{A_p} = 2\sqrt{1+(\sin^2\beta/\tan^2\beta_l)}$$

where β_l = leading edge angle of caret wing planform (fig 2.3)

$$\frac{L}{D} = c_p \Big/ \left[c_p \tan\theta + 2\sqrt{1+(\sin^2\beta/\tan^2\beta_l)}\ .c_f\right]$$

and, by assumption that for small deflection angles pressure is proportional to the flow deflection, therefore

for $\theta << 0$, then $c_p \sim k\theta$, and $\tan\theta \sim \theta$, L/D can be written as

$$\frac{L}{D} = k\theta \Big/ \left[k\theta^2 + 2c_f\sqrt{1+(\sin^2\beta/\tan^2\beta_l)}\right] \quad \text{——— (2.17)}$$

where, k = proportionality constant.

The angle θ_{opt} for optimum L/D can be found by differentiating w.r.t θ and equating it to zero.

$$\text{Hence } \theta_{opt} = \left[\left(\frac{2c_f}{k}\right)\sqrt{1+(\sin^2\beta/\tan^2\beta_l)}\right]^{0.5} \quad \text{——— (2.18)}$$

and the maximum lift to drag ratio can be found from[38]

$$\frac{L}{D}_{max} = \frac{1}{4}\sqrt{\frac{2k}{c_f}}\left[1+\frac{\sin^2\beta}{\tan^2\beta_l}\right]^{-\frac{1}{4}} \quad \text{——— (2.19)}$$

2.3.1.c Combination of Caret Wings

In the previous section the simple theory for the caret wing is discussed. It suggests that the performance of caret wings can be readily evaluated and the effect of various design parameters can also be assessed using simple relations. Hence caret wing shapes can be connected together to yield many derivative forms which can be analysed easily. Some of the examples of these combinations are shown in fig(2.4). In this figure each element of the configuration is constructed in accordance with the rules for the construction of the caret wings.

This can be extended in order to provide a control surface as illustrated in (fig(2.5)).

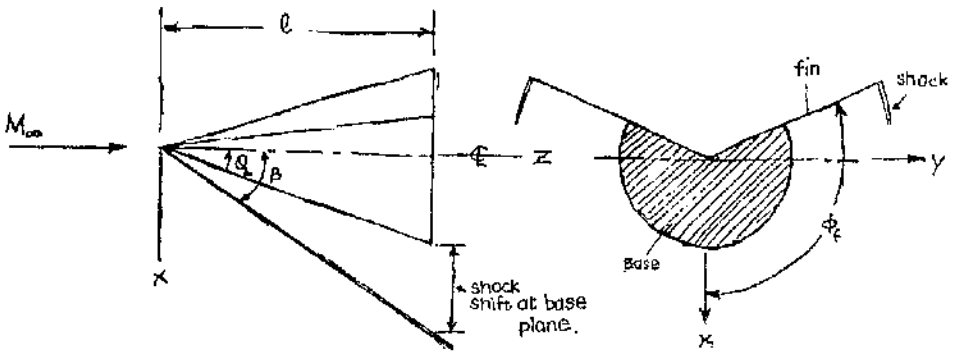

Fig. 2.7 Waveriders schematic basis is flow about a circular cone at $\alpha=0$.

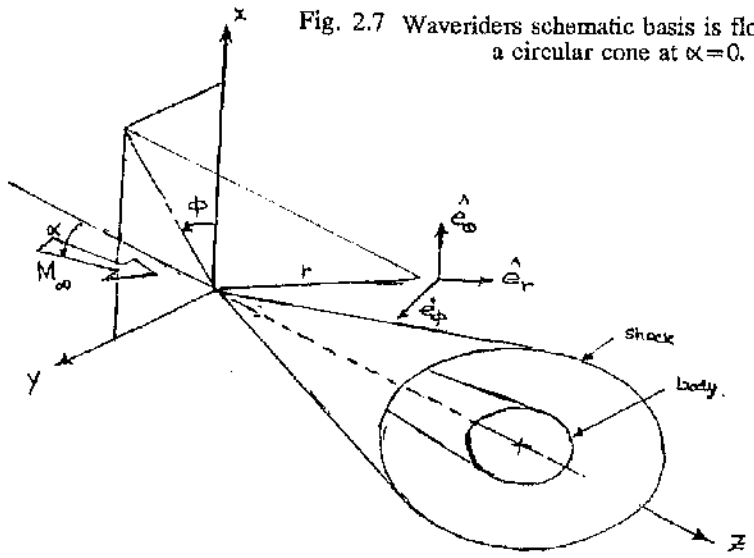

Fig. 2.8 Spherical co-ordinate system for conical flow waveriders.

Similarly the idea can be used to arrange caret wings to act as precompression inlets for air breathing engines to supply known uniform flow at its design condition. An example of it is shown in fig(2.6).

2.3.2 Waveriders derived from conical flowfield.

2.3.2.a Theory

The concept of a caret shape waverider to attain high lift can be extended to other shapes as long as they exhibit the designed flow pattern. For example any stream surface from the supersonic flow over an axisymmetric body can be used to generate a waverider with an attached shock wave along its complete leading edge. Roe [16] has derived optimum shapes using the same idea. Later, considering an inclined circular and elliptic cone, Rasmussen[24,77] and Kim[25,78] used the idea of a more generalised conical flow for deriving a waverider configuration. It is useful to provide derivation for a conical waverider in its simplest form, as follows.

2.3.2.b Waverider configuration derived from circular & elliptical cones.

Consider the supersonic flow about a circular cone at an angle of attack with an attached shock wave as referred to in figs(2.7) and (2.8)[24].

——→This waverider is extracted by truncating the cone and by adding fins.
——→The two fins are oriented at an angle ϕ_f relative to the x-axis where the angle can be less or greater than 90^o.
——→The fins are stream surfaces and extended outwards as far as the conical shock wave. These are used to confine the shock layer to the lower part of the body and for simplicity are assumed to be of negligible thickness. This approximation is good for optimization when $M_\infty \theta_c > 0.5$.

Now an approximate analytical solution for the flow field is developed based on the hypersonic small disturbance assumption to find out C_L & C_D and

other local properties.

Referring to fig(2.8) using a spherical co-ordinate system centered at the cone apex the velocity is

$$V = u\hat{e}_r + v\hat{e}_\theta + w\hat{e}_\phi$$

Since the flow is conical V,p,ρ... are constant along a ray and are independent of azimuthal angle ϕ,

Hence $w = 0$

and u, v depends only on θ.

Corresponding to this the exact jump conditions across the shock are

$$\frac{\rho_2}{\rho_\infty} = \frac{\gamma+1}{2} \frac{K_\beta^2}{1+[(\gamma-1)/2]K_\beta^2}$$

$$\frac{p_2}{p_\infty} = \frac{2}{\gamma+1}\left[\gamma K_\beta^2 - \left(\frac{\gamma-1}{2}\right)\right]$$

$$\frac{u_2}{a_\infty} = K_\beta \cot\beta$$

$$\frac{v_2}{a_\infty} = -\frac{2}{\gamma+1}\frac{1+[(\gamma-1)/2]K_\beta^2}{K_\beta} \qquad \text{——— (2.19a)}$$

where, $K_\beta = M_\infty \sin\beta$

Another useful approximation, which is reasonably accurate for hypersonic flow for this similarity relation for the shock location in terms of body angle θ_c is

$$K_\beta = \left(1+\frac{\gamma+1}{2}K_c^2\right)^{0.5} \qquad \text{where } K_c = M_\infty \sin\theta_c$$

or, vice versa K_b in terms of K_β

$$K_c^2 = (K_\beta^2 - 1)\times\frac{2}{\gamma+1}$$

Now for the different fluid properties in the conical flow shock layer

Density ——→ increases smoothly from ρ_2 at the shock to its value ρ_c at the body. For a slender body at hypersonic speeds, the magnitude of $(\rho_c-\rho_2)/\rho_2$ is quite small thus justifying the

assumption of a constant density shock layer. Also the shock layer is homentropic ($p \sim \rho^{\gamma}$).

Pressure ⟶ The change in pressure $(\frac{p_c - p_2}{p_2})$ is more significant than that of density but nevertheless it is still small.

Velocity Components ⟶ Component v at the shock is normal to it and zero at the body. However the magnitude of v_2/a_2 is well below unity because it is the normal component of the Mach number on the downstream side of the shock wave. So as a consequence $|v|$ is relatively small throughout the shock layer.

Component u is not small on the shock layer or zero on body.

Component w=0 because of the locally conical approximation.

The above statement can be elaborated more if one considers K_β to be of the order unity for different pressure, velocity and density relationships, and it can be shown that $\frac{\rho_2}{\rho_\infty}$, $\frac{p_2}{p_\infty}$ and $\frac{v_2}{a_\infty}$ are of the order of unity but $\frac{u_2}{a_\infty}$ is of the order β^{-1}(which is large compared to unity).

Now to determine a relationship for lift and drag, consider a small differential area ds in the base plane of the waverider, which in spherical co-ordinate is

$$ds = r^2 \sin^2\theta \, d\theta d\phi$$

where $r = \frac{\ell}{\cos\theta}$ and ℓ = length (refer fig(2.7))

$$ds = \ell^2 d\phi \, \frac{\sin\theta d\theta}{\cos^2\theta}$$

Since flow parameters change slowly along a streamline in the shock layer therefore integrals can be approximated by evaluating $\rho, p, v, \hat{e}_x$ just behind the shock where $\theta=\beta$ with V_2 given by $v.\hat{e}_z$

therefore $V_2 = u_2\hat{e}_r + v_2\hat{e}_\theta$

The basis vector transformation from cartesian to spherical are

$$\begin{bmatrix} \hat{e}_r \\ \hat{e}_\theta \\ \hat{e}_\phi \end{bmatrix} = \begin{bmatrix} \sin\theta\cos\phi & \sin\theta\sin\phi & \cos\theta \\ \cos\theta\cos\phi & \cos\theta\sin\phi & -\sin\theta \\ -\sin\phi & \cos\phi & 0 \end{bmatrix} \begin{bmatrix} \hat{e}_x \\ \hat{e}_y \\ \hat{e}_z \end{bmatrix}$$

Therefore taking dot product and putting $\theta = \beta$

$$V_2.\hat{e}_x = u_2\sin\beta\cos\phi + v_2\cos\beta\cos\phi$$

$$V_2.\hat{e}_z = u_2\cos\beta - v_2\sin\beta$$

Using the hypersonic similarity parameter (in terms of K_β (eqn.(2.19a))

$$V_2.\hat{e}_x = a_\infty\cos\beta\{M_\infty\sin\beta - \frac{2}{\gamma+1}\times\frac{1+[(\gamma-1)/2]K_\beta^2}{K_\beta}\}\cos\phi$$

$$= \frac{a_\infty\cos\beta}{K_\beta}\left[K_\beta^2 - \frac{2}{\gamma+1}\times\frac{1+[(\gamma-1)/2]K_\beta^2}{}\right]\cos\phi$$

And, for $K_c^2 = (K_\beta^2-1)\times\frac{2}{\gamma+1}$ on simplification,

$$V_2.\hat{e}_x = \frac{a_\infty\cos\beta}{K_\beta}K_c^2\cos\phi = V_\infty\cot\beta\sin^2\theta_c\cos\phi.$$

Similarly

$$V_2.\hat{e}_z = a_\infty\{M_\infty\cos^2\beta + \frac{2}{\gamma+1}\times\frac{1+[(\gamma-1)/2]K_\beta^2}{M_\infty}\}$$

$$= \frac{a_\infty}{M_\infty}\{M_\infty^2 - K_\beta^2 + \frac{2}{\gamma+1}K_\beta^2\} = \frac{a_\infty}{M_\infty}\{M_\infty^2 - \frac{2}{\gamma+1}(K_\beta^2 - 1)\}$$

$$= \frac{a_\infty}{M_\infty}\{M_\infty^2 - K_c^2\} = V_\infty\cos^2\theta_c$$

Now, lift is equal to the momentum behind the shock

hence $L = \rho_2 V_2\int ds$ and $\theta = \theta_c$

$$= \rho_\infty\frac{\gamma+1}{2}\frac{K_\beta^2}{1+[(\gamma-1)/2]K_\beta^2}\times V_\infty\cot\beta\sin^2\theta_c\times V_\infty\cos^2\theta_c$$

$$\times\frac{\ell^2\sin\beta}{\cos^2\beta}\int_{-\phi_f}^{\phi_f}\cos\phi d\phi\int_{\theta_c}^{\beta}d\theta$$

which by simplification gives

$$L = 2\gamma p_\infty \ell^2 K_c^2 \tan\beta \frac{\sin\phi_f}{1+K_c\{1+[(\gamma+1)/2]K_c^2\}^{1/2}} \quad \text{——— (2.20)}$$

where $\cos\theta_c = 1$ for a slender body.

Similarly drag can be calculated by making use of the relationship for drag

$$D = \{-(p_2-p_\infty)+\rho_2[V_\infty-(V_2.\hat{e}_x)](V_2.\hat{e}_x)\}S_{bsl} \quad \text{——— (2.21)}$$

Where S_{bsl} = shock layer base area

and $S_{bsl} = \ell^2(\tan^2\beta-\tan^2\theta_c)\phi_f \cong \ell^2(\beta^2-\theta_c^2)\phi_f$ ——— (2.22)

Using again the similarity relation (eq(2.19a)

$$\frac{p_2}{p_\infty} = \frac{2}{\gamma+1}(\gamma K_\beta^2 - \frac{\gamma-1}{2})$$

$$= \frac{2}{\gamma+1}(\gamma[1 + \frac{\gamma+1}{2}K_c^2] - \frac{\gamma-1}{2})$$

$$= 1 + \gamma K_c^2$$

or $p_2-p_\infty = \gamma p_\infty K_c^2$ ——— (2.23)

putting area S_{bsl} (eq(2.22)) and (p_2-p_∞) in eq(2.21), gives the following expression for drag

$$D = \frac{\gamma p_\infty K_c^4}{1+[(\gamma-1)/2]K_c^2} \times S_{bsl} = \gamma p_\infty \ell^2 \phi_f K_c^2 \theta_c^2 \quad \text{——— (2.24)}$$

and to determine the lift and drag coefficient, the planform area (S_p) is given by

$$S_p = \ell^2 \tan\beta \sin\phi_f \cong \ell^2 \beta \sin\phi_f$$

then, C_L & C_D are

$$C_L = 4\theta_c^2 \frac{\{1+[(\gamma+1)/2]K_c^2\}^{1/2}}{K_c+\{1+[(\gamma+1)/2]K_c^2\}^{1/2}} \quad \text{(2.25)}$$

$$C_D = \frac{2K_c\theta_c^3}{\{1+[(\gamma+1)/2]K_c^2\}^{1/2}} \times \frac{\phi_f}{\sin\phi_f} \quad \text{——— (2.26)}$$

and L/D ratio for a conical waverider is

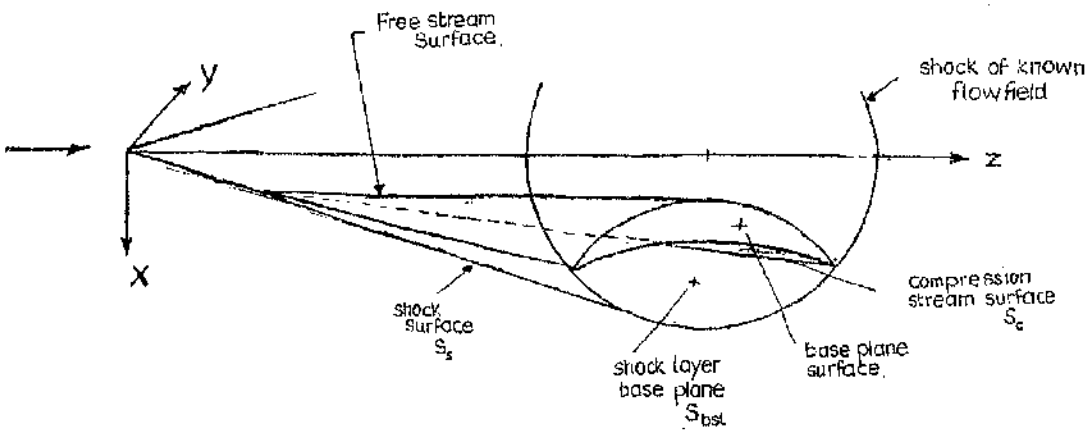

Fig. 2.9 Waverider configuration in cartesian co-ordinate system. [78]

$$\frac{L}{D} = 2M_{\infty}\frac{1+[(\gamma+1)/2]K_c^2}{K_c^2\left[K_c+\{1+[(\gamma+1)/2]K_c^2\}^{1/2}\right]}\frac{\sin\phi_f}{\phi_f} \quad \text{——— (2.27)}$$

This shows that, for a fixed value of K_c the ratio L/D will increase for an increase in Mach number but will slowly decrease with increase of fin angle ϕ_f.

2.3.2.c C_L & C_D for an arbitrary shape waverider.

In the last section an ideal conical waverider constructed by means of a cone with fins is considered. The same idea can be extended to a few other arbitrary shapes derived out of the conical flowfield. To demonstrate this consider a uniform, supersonic free stream flow aligned with the z-axis as shown in fig (2.9)[78].

Assume for the flow field that

——o The shock wave is of known shape.

——o The planar surface perpendicular to z intersects the shock wave along a closed curve.

——o The streamlines of the known flowfield defined from the shock-free stream intersection point constitute the compression surface of waverider.

Therefore for the waverider upper surface :

——o It is determined by freestream streamlines that pass through the curve for the leading edge of the body.

The whole waverider then consists of three planes.

——o The upper surface aligned with the free stream bearing a constant pressure p_{∞}.

——o A base plane perpendicular to free stream having an assumed pressure p_{∞}.

——o A compression surface, whose pressure need not to be constant.

The shock layer on which the body rides is also defined by three

surfaces.

—o The first surface is part of the shock wave downstream of the leading edge and has an area S_s. This is taken as the free stream side of the shock wave and terminates at the base plane.

—o The second surface is the compression surface of area S_c.

—o The third surface is the shock layer base plane with an area S_{bsl}(i.e., without vehicle base area S_b).

By applying the laws of conservation of mass and momentum for shock layer flow enclosed by these surfaces i.e.

$$\int_s \rho V.\hat{n} ds = 0 \qquad \text{——— (2.28)}$$

$$\int_s [\ \rho V(V.\hat{n})+p\hat{n}\ ]ds = 0 \qquad \text{——— (2.29)}$$

Here the integrals are surface integrals over all three areas
$S = S_s + S_c + S_{bsl}$ and $\hat{n}$ = outward unit normal vector

Also, since S is a closed surface area

therefore, $\int_S \hat{n} ds = 0$

Multiplying by p_∞ and subtracting from eq(2.29) gives

$$\int_S [\ \rho V(V.\hat{n})+(p-p_\infty)\hat{n}\ ]ds = 0 \qquad \text{——————— (2.30)}$$

On the three surfaces the following conditions exist,

On S_{bsl} $\quad \hat{n} = \hat{e}_z$

On S_c $\quad \hat{n} = \hat{n}_c$ $\quad$ and $V.\hat{n} = 0$

On S_s $\quad \hat{n} = \hat{n}_s$ $\quad$ and $V = V_\infty$, $p=p_\infty$, $\rho=\rho_\infty$

Therefore, equation (2.28) and (2.30) becomes

$$\int_{S_s} \rho_\infty (V_\infty.\hat{n}_s) ds + \int_{S_{bsl}} \rho V.\hat{e}_z ds = 0$$

$$\int_{S_c} (p-p_\infty)\hat{n}_c ds + \int_{S_{bsl}} [\rho V(V.\hat{e}_z)+(p-p_\infty)\hat{e}_z]ds + \int_{S_s} \rho_\infty V_\infty (V_\infty.\hat{n}_s) ds = 0 \qquad \text{– (2.31)}$$

The S_s integrals are eliminated to give

$$\int_{S_c}(p-p_\infty)\hat{n}_c\,ds=-\int_{S_{bsl}}[\rho\,(V-V_\infty)(V.\hat{e}_z)+(p-p_\infty)\hat{e}_z]ds \qquad \text{(2.32)}$$

The left hand side of equation (2.32) represents the force on the waverider due to excess pressure $(p-p_\infty)$ along the compression surface. Now assuming the flow is symmetric about the x-z plane, the sideways forces acting in the y direction cancel each other leaving the resultant force which can be resolved into lift and drag components.

$$L = -\hat{e}_x.\int_{S_c}(p - p_\infty)\hat{n}ds = \int_{S_{bsl}}\rho\,(V.\hat{e}_x)(V.\hat{e}_z)ds \qquad \text{(2.33)}$$

and for drag $\hat{e}_z.\hat{e}_z = 1$ and $V_\infty.\hat{e}_z=V_\infty$, therefore

$$D = \hat{e}_z.\int_{S_c}(p - p_\infty)\hat{n}ds = \int_{S_{bsl}}[\rho(V_\infty-V.\hat{e}_z)(V.\hat{e}_z) - (p-p_\infty)]ds \qquad \text{(2.34)}$$

The lift and drag coefficients in terms of planform area (S_p) can then be written as

$$C_L = \frac{2\,L}{\gamma p_\infty M_\infty^2 S_p} \qquad \text{(2.35)}$$

and,

$$C_D = \frac{2\,D}{\gamma p_\infty M_\infty^2 S_p} \qquad \text{(2.36)}$$

2.4 Viscosity and High Temperature effects on Waverider Design.

Waveriders have been considered as potential aerospace vehicles since the advent of Space Shuttle. However critical reviews of research around waveriders suggest that, during the theoretical development of these shapes,

different key factors of high speed flow or hypersonic flow have not been given proper consideration. These key factors can affect the designed flow characteristics and in turn body shape.

By virtue of its definition, the aerodynamic characteristics and performance of waveriders are usually well predicted by inviscid flow theory as they are designed in order to fit a known inviscid flow field. However for the designed configuration viscosity contributes to different flow phenomena such as boundary layer, skin friction, flow separation and heat transfer. Therefore factors like entropy layer, viscous interaction, low density flows, real gas effects and high temperature effects must be considered while designing and simulating the flow around waveriders.

2.4.1 Boundary Layer.

For the low speed flow of air around a body at normal densities the process of viscous dissipation and heat conduction are restricted to a relatively thin boundary layer near the surface of the body. This boundary layer may be considered as an entity distinct from the outer or external inviscid flow and hence can be neglected when the boundary layer thickness is small as compared to the shock layer thickness. The same is true for waveriders in that unless the boundary layer is very thick the displacement effect does not strongly influence the performance of waveriders, but under certain conditions it can be thick enough to change the effective geometry of the configuration. Furthermore flow could separate in the interior corner of the caret wing. When such a separated flow region is sufficiently large the shock wave pattern will be distorted and the pressure will not be the same as predicted by inviscid flow theory.

2.4.2 Skin Friction.

As configurations designed under waverider conditions are expected to have large surface area and hence large friction drag, therefore viscous effects due to skin friction drag must be accommodated in designing these shapes.

For example[4] for a caret wing operating at $\omega=4^{O}$ (where ω is the

design value of $(\beta-\theta)$) and W/S=30 $lb/_{ft^2}$ and h = 130,000 ft, it follows that $M_\infty = 10.9$ & $L/D_p = \cot\theta \cong \cot(6.8) \cong 8.4$, laminar friction drag on the lower surface only reduces this by 0.6 (or 7%) and if laminar flow is assumed for the upper surface, L/D remains above 7.5. Although these reductions in L/D are significant, they are less so at more conventional wing loadings. It is normally suggested that the upper surface drag can frequently be neglected while base drag is still a matter of question. If, for example, the base drag is included it could give values of L/D 10-15% less than predicted.

2.4.3 Flow Separation.

Consideration of the more significant phenomena of flow separation may be unnecessary for waverider considerations since they are designed to have low drag and high L/D ratio under specified conditions. But when the vehicle is manoeuvred, then at times the angle of attack may not match with the design condition resulting in local flow separation causing recirculating flow and which results in local effective changes in vehicle geometry or generate vortex formations. However, experimental work by Cole[29] suggest that uncertainties of this nature may not appear until twice the design incidence is exceeded.

2.4.4 Viscous interaction

Because of the high flow velocity in the hypersonic regime a large amount of kinetic energy is dissipated in the boundary layer thus causing an increase in temperature and viscosity and decrease in density resulting in an increase in boundary layer thickness (δ)

where, $$\frac{\delta}{\ell} \propto \frac{M_\infty^2}{\sqrt{Re_x}}.$$

Due to the increased thickness of the boundary layer a viscous-inviscid interaction phenomena takes place which complicates the boundary layer analysis and can also cause some first order effects on the surface pressure distribution. The relative importance of boundary layer on the outer flow can be estimated using the viscous interaction parameter

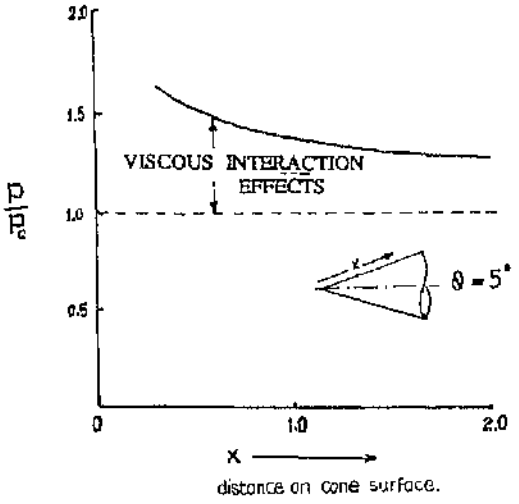

Fig. 2.10 Effect of pressure on surface of cone due to viscous interaction.

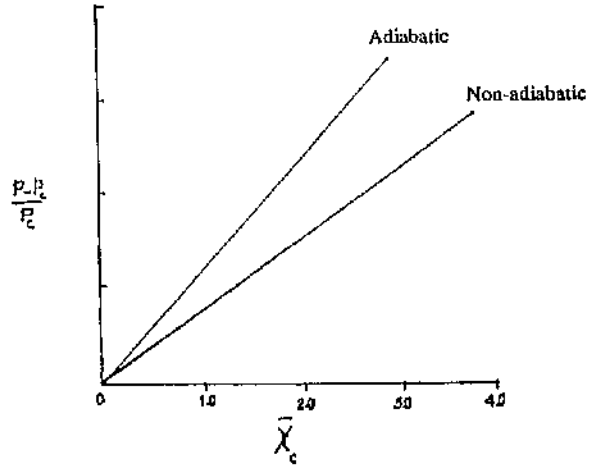

Fig. 2.11 Induced pressure vs interaction parameter.[13]

$$\bar{\chi} \propto \frac{M_\infty^3}{\sqrt{Re_\infty}}$$

For $\bar{\chi} \geq 1$, the surface pressure distribution may differ significantly from the inviscid prediction. Despite this all previous waverider designs are based upon inviscid flow. However it is difficult to achieve $\bar{\chi} < 1$, because all waverider configurations cater for vehicles flying at high altitude, where Re_∞ is small. Therefore when the interaction parameter is large ($\bar{\chi} \sim 3$) for example, the inviscid method must be abandoned or at minimum coupled with a boundary layer routine.

Fig(2.10) shows the effect on pressure over the surface of a cone due to viscous interaction at a free stream Mach number = 11 and Reynolds number = 1.88×10^5 per foot. It becomes even more clear from fig(2.11), in which the induced pressure increment is plotted against the interaction parameter $\bar{\chi}_c$ for a sharp cone,

where $\bar{\chi}_c \cong M_c^3 \sqrt{\frac{C}{Re_x}}$,

with $C = \frac{(\rho\mu)_w}{(\rho\mu)_c}$,

and w = wall conditions,

c = inviscid cone surface conditions,

Re_x = Reynolds number at a distance x from tip.

Also fig (2.11)[13] reveals that the variation between pressure and interaction parameter is linear. Theoretical results on this topic are obtained from Probstein's theory and Talbot's method. Probstein's theory[79] gives analytical results using a Taylor series expansion in the power of the slope of the boundary layer displacement thickness and Talbot's method[80] is an approximate graphical approach coupling the displacement thickness slope with the inviscid flow over a cone.

A correlation procedure that reflects the influence of its interaction parameter can be defined as

$$\frac{p}{p_\infty} = f(\bar{\chi}) = a_1 \bar{\chi} + \ldots\ldots$$

Here c_p can be related to interaction parameter as

$$c_p = \frac{2}{\gamma M_\infty^2}\left(\frac{p}{p_\infty} - 1\right)$$

i.e.,
$$c_p = \frac{2}{\gamma M_\infty^2} M_\infty^3 \sqrt{\frac{C}{Re_c}}$$

$$c_p \propto M_\infty \sqrt{\frac{C}{Re_c}} \equiv \bar{V}$$

Since lift and wave drag coefficients can be simply obtained by integrating c_p over the body surface, then C_D & C_L for the hypersonic case should correlate with this viscous interaction parameter $(\bar{V})$ defined above.

Data collected from the flight of the space shuttle has suggested a third viscous interaction parameter $\bar{V}'$ where values of C are evaluated at the reference enthalpy[39].

Hence $\bar{V}' = M_\infty^3 \sqrt{\frac{C'}{Re}}$ where $C' = \frac{(\rho\mu)''}{(\rho\mu)_\infty}$

and ρ', μ' are evaluated at a reference temperature within the boundary layer, defined as

$$\frac{T'}{T} = 0.468 + 0.532\frac{T_w}{T_\infty} + 0.195\left(\frac{\gamma-1}{2}\right)M_\infty^2$$

Although much has been done in solving viscous interaction by treating this as a coupled problem between boundary layer displacement thickness and a general approximate calculation of the outer inviscid flow, this is still an approximate and less accurate approach due to different constraints involved. The difference between inviscid and viscous flow (as modelled by the Navier-Stokes equations) predictions clearly demonstrates the substantial magnitude of the viscous interaction effect. The full shock layer calculations (NS Codes) accurately simulate viscous interaction effects and the results thus obtained are expected to be in good agreement with experiment.

For waveriders Bowcutt and Anderson[26] are the first to consider the

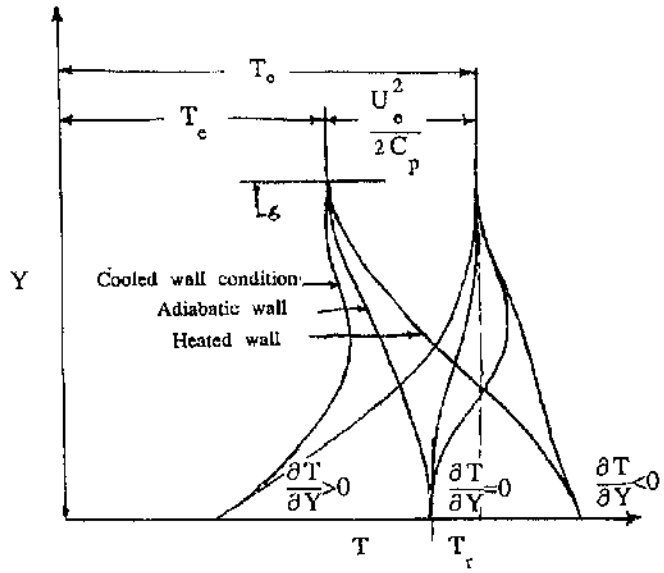

Fig. 2.12 Boundary-layer temperature distribution

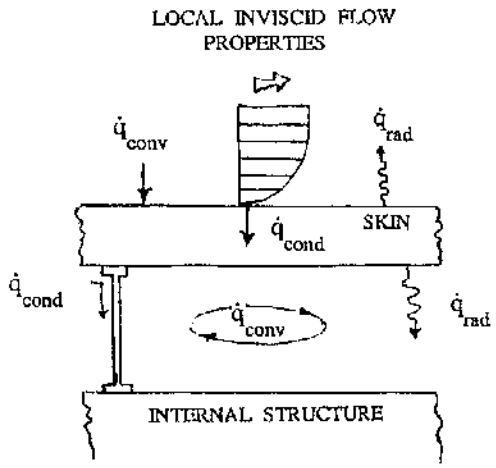

Fig. 2.13 Heat transfer modes.

detailed viscous effects for waverider design. They considered viscous interaction as a coupled problem and solved this by a boundary layer method. Their study revealed reasonable results but it is expected that these can be improved by applying a Navier-Stokes solution.

2.4.5 Heat Transfer & High Temperature effects.

A vehicle operating at supersonic conditions is heated by the gradient of temperature through the boundary layer that surrounds it. This temperature gradient is actually produced by the conversion of velocity into local gas enthalpy through flow deceleration in the boundary layer, as shown in fig(2.12).

For a body, having finite thickness, all three different modes of heat transfer occur in hypersonic flight (Fig(2.13)) i.e. conduction, convection and radiation. Each could have some influence on the other. Generally heat is transmitted first by convection and then conduction through a thin layer of gas film adjacent to the surface. Considering fig(2.13) taken as a small part of a body in high speed flow, the aerodynamic heating will increase the surface temperature of the skin and conduct through the skin with time. The high surface temperature will begin to radiate heat back to the atmosphere, as the heat pulse travels through the material to radiate the body interior.

Typical applications of waveriders in very high speed vehicles are re-entry space planes and missiles. Therefore at supersonic and hypersonic speed when the fluid becomes slow behind the shock wave and near the body much of kinetic energy is converted into internal energy. Especially during its hypersonic part of the trajectory this conversion process or energy phenomena can be so severe that chemical interaction of molecules such as dissociation and ionization takes place. Therefore factors due to high speed, resulting in high temperature must be accounted by considering at maximum phenomena such as

ionization
molecular vibration and dissociation
stagnation point heat transfer
chemical reaction

wall catalytic effect
radiation effect due to shock layer temperature.
variable γ.

All these phenomena mentioned above have their own unique importance towards proper data correlation and exact flow simulation e.g., stagnation point heat transfer can be best related by the Fay and Riddell[81] method. For chemical reaction, flight experience with the Space Shuttle has revealed its effect on pitching moment and it is believed that lack of modelling chemical reactions has resulted in under prediction of the required body flap deflection for trimming and stability.

Similarly it is observed that for the non-equilibrium flow over a body, the surface may act as catalyst for the recombination of atom and ions, hence increasing the heat transfer to the surface. It is clear that a non-catalytic surface such as glass can reduce the stagnation point heating by more than 50%.

As said earlier the main application of waveriders is concerned with very high speed vehicles, therefore, heat transfer can have an indirect effect on the design and performance of these shapes. So one must consider while designing, for heat transfer :

effect of leading edge sharpness or small bluntness.
material selection for leading edge.
effect of ablation and its performance on design.

Although for high speed, heating rate is large and has a prime importance especially while selecting materials used for the construction of space craft, it has also an influence on the flow attached to its leading edge. A waverider body requires sharp leading edges which have a high heat rate relative to the rest of surface. The overall effect on the heat transfer rate is however decreased compared to a conventional body.

A thorough knowledge of both the inviscid and viscous flow over the vehicle is required to evaluate reasonably well the aerodynamic heating. Generally for zero angle of attack this problem is not so difficult and can

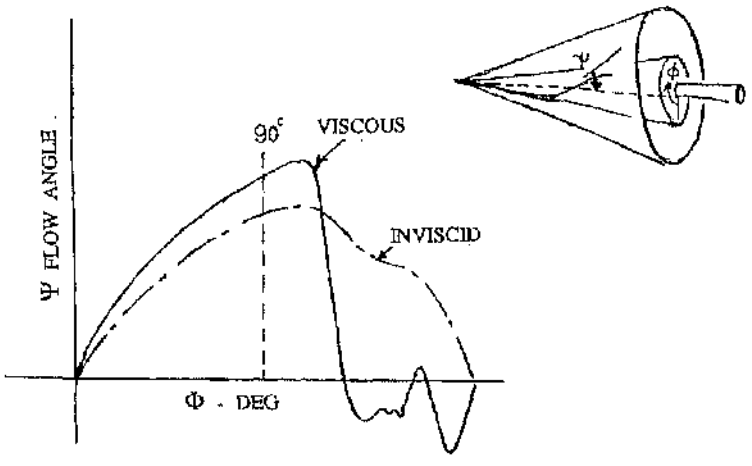

Fig. 2.14 Viscous influence on streamline turning.

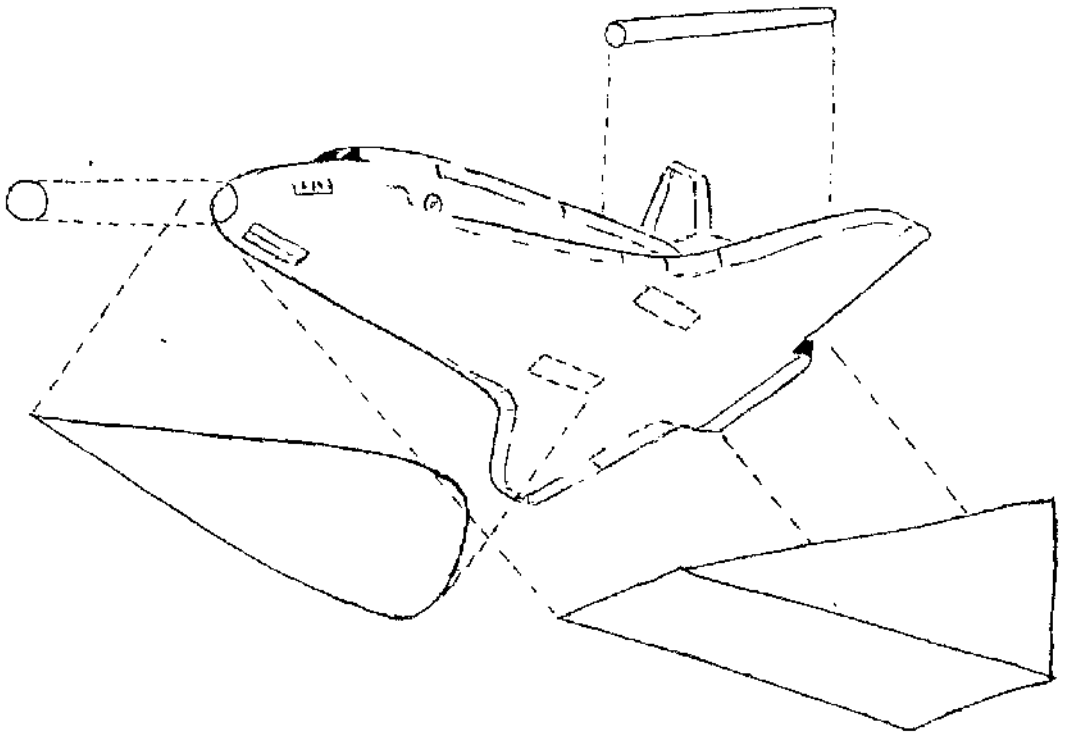

fig. 2.15 Sub-dividing technique applied to the Space Shuttle for prediction of heat transfer on different parts.

be solved using simple engineering methods. But as the angle of attack increases, pressure gradients are set up about the vehicle, which, in turn, cause streamlines to wrap about the vehicle seeking regions of low pressure. Boundary layers are therefore thinned in the regions of high pressure creating high heating. A skewing of streamline directions through the boundary layer is also produced since lower energy air near the surface turns more easily.

Fig(2.14) shows qualitative skewing of streamlines through the boundary layer, as observed in experiment. Failure to account for boundary layer thinning will lead to under prediction of heating. Lack of knowledge concerning streamlines and local flow properties along streamlines will lead to errors in predicting embedded phenomena, such as flow interference effects.

Although an accurate prediction of heat rate and simulation around any shape needs a full Navier Stokes solution, however, first hand approximation can be done through different methods. One such method for complex shapes is by considering the body as a combination of different geometrical configurations each of which is then evaluated separately. Wind tunnel data are then used to "correct" these initial estimates for the presence of any interaction effects between elements and for the geometrical complexity beyond the scope of the methods. In doing so, an important consideration is an understanding of the flow field around the body. This includes local flow properties of pressure, temperature, velocity and local flow direction in an inviscid stream about the body. A good application of this subdividing technique used in the development of Space Shuttle is shown in fig (2.15).

To approximate the heat transfer around waveriders or its combination with other shapes, a similar technique can be used. Also in waveriders although the heating is relatively reduced over the surface, it is severe on the leading edges. Therefore some of techniques used for prediction of heat rate on the leading edge of caret waveriders are discussed in next section.

2.5 Heat Transfer Over Caret Wing

In its basic form a caret wing configuration has a pure delta planform with a pointed apex and sharp corner along the lower ridge line.

Concerning the swept leading edges, it is suggested that internal conduction and surface radiation should allow these edges to be sharp (ie radius<3mm), even if the flow is attached to the both upper and lower surfaces.

Considering the leading edge temperature at re-entry, Nonweiler [40], has given a relation that for a solid metal member of optimized fineness ratio, heat from one side but radiating from both, leading edge temperature is equal to

$$T_{lc} = Cq^{\frac{2}{7}}(kA)^{-1/21}(\epsilon\ \sigma)^{\frac{-5}{21}}\cos^{\frac{1}{7}}\Lambda,$$

where constant C ranges from, $1.29 < C < 1.41$, for various profiles, and,

$\dot{q}$ = rate of heat transfer

σ = Stefans constant

ϵ = sum of surface emissivity (top plus bottom) so that $0 \leq \epsilon \leq 2$ and $\epsilon\sigma$ is of the order $10^{-10}\ \frac{kW}{m^2 K^4}$

k = thermal conductivity

A = cross-sectional area of the leading edge

Λ = sweep angle

Another relation for dealing with leading edge convective heating can be made by assuming the leading edge as a small cylinder lying in swept condition in the flow. By calculating the conditions at the stagnation point-line on this swept cylinder, the heating is

$$\dot{q} = A(\rho_s u_s)^{1-n}\left[\frac{\mu_s}{X}\right]^n (H_e - H_w)$$

where $p_s = \rho_\infty V_n^2 = \rho_\infty V^2 \cos^2\Lambda_e$

$$C_p T_s = H_s - \frac{V_t^2}{2} = \frac{V_\infty^2}{2} - \frac{V_\infty^2}{2}\sin^2\Lambda_c = \frac{V_\infty^2}{2}\cos^2\Lambda_e$$

$$\rho_s = \frac{p_s}{RT_s} = \frac{2\gamma}{\gamma-1}\rho_\infty$$

Λ_e = Effective Sweep angle = $\sin^{-1}(\sin\Lambda\cos\alpha)$

α_e = Effective angle of attack = $\tan^{-1}(\frac{\tan\alpha}{\cos\Lambda})$

The heat transfer beneath the caret wing can be considered equivalent to heat transfer beneath a flat plate at an angle of attack. For the caret wing case the strategy can be adopted in which α can be considered equivalent to the wedge angle(θ). Heat transfer is calculated by extending classical incompressible relations for skin friction to the compressible case[41] through the application of a "model" known as the Eckert reference (or intermediate) enthalpy method.

Here

$$q = \rho^* U_e C_p \frac{c_f}{2} k_k (T_r - T_w)$$

where,

$$T_r = \text{recovery temperature} = T_e + \frac{rU_e^2}{2C_p}$$

$$r = \text{recovery factor} = P_r^{0.5}$$

and parameters on the wedge can be written as

$$T_e = \frac{p_e}{\rho_e R},$$

T^* = reference temperature

$$= T_e + 0.5(T_w - T_e) + 0.22(T_r - T_e)$$

where, T_w = wall temperature

The incompressible laminar skin friction $c_f = \frac{0.664}{\sqrt{Re_s}}$ (Blasius relation)

$$\rho^* = \frac{p_e}{RT^*}$$

The viscosity at the reference point can be calculated (by the Sutherland relationship),

$$\mu^* = \frac{1.5T^{*\frac{3}{2}} \times 10^{-6}}{T^* + 120}$$

and, the Reynolds number at the reference value is given as

$$Re_s = \frac{1}{k_m} \frac{\rho_c^* U_e}{\mu^*} r$$

where, k_m = Mangler transformation, to transform the friction law from a 2-D to an axisymmetric case.

Another form of the same relation is introduced by Neumann[3],

$$St_\infty (Re_{\infty,x})^n = A\left(\frac{U_e p_e}{U_\infty p_\infty}\right)^{1-n} \left(\frac{T_\infty}{T^*}\right)^{1-2n} C^{*n} \left(\frac{H_r - H_w}{P_r^{2/3}(H_0 - H_w)}\right)$$

where n=0.5 and A=0.332 for Laminar Flow

and n=0.2 and A=0.0296 for Turbulent Flow

with $C^* = \frac{\mu^*}{T^*} \frac{T_\infty}{\mu_\infty}$

Another interesting relation for calculating heat transfer is by Tauber and co-worker is [84]

$$\dot{q} = C_K^N (V_s^2 - V^2)^N V^{M-2} \quad \text{with } V_s = 7.9 \text{ m/sec.}$$

where, C,N & M are given as :

for stagnation point : M=3, N=0.5, $C = 1.83\times10^{-8} r_n^{-\frac{1}{2}}(1-g_w)$,

flat plate laminar : M=3.2, N=0.5

$$C_1 = 2.53\times10^{-9}(\cos\phi)^{1/2}\sin\phi\ x^{-\frac{1}{2}}(1-g_w)$$

flat plate turbulent : for V≤ 3962 m/sec, M=3.37

$$C_2 = 3.89\times10^{-8}(\cos\phi)^{1.78}\sin\phi^{1.6}\ x_T^{-\frac{1}{5}}\left(\frac{T_w}{556}\right)^{-\frac{1}{4}}(1-1.11g_w)$$

for V > 3962 m/sec, M=3.7

$$C_2 = 2.20\times10^{-9}(\cos\phi)^{2.08}\sin\phi^{1.6}\ x_T^{-\frac{1}{5}}(1-1.11g_w)$$

where, $g_w = \frac{h_w}{h_0}$ and ϕ = local body angle relative to free stream.

FLOW SIMULATION AROUND WAVERIDER CONFIGURATIONS

3.1 Introduction.

Hypersonic flow is complex because of the inherent non-linearity in its modelling equations and due to the presence of shock waves. Although simplified methods are still much used for prediction they generally are rudimentary. A simple example of these is the estimation of the pressure distribution on a body at different angles of attack. For waveriders, different elementary methods can be used to estimate different aerodynamic forces but they cannot predict pressure distribution exactly especially when separated flows are present. This has prime importance towards accurately assessing skin friction and heat transfer coefficients.

The classical result from linearized, inviscid supersonic two dimensional theory,

$$c_p = \frac{2\theta}{\sqrt{M_\infty^2 - 1}} \qquad \text{(for small angles, } \theta\text{)} \qquad \text{——— (3.1)}$$

demonstrates that pressure is dependent on surface inclination. For this useful theory results are limited to small angles of attack but nevertheless it can give a starting point for more accurate solutions. Other methods in this context which produce more accurate results for initial estimation in hypersonic flow are —— Newtonian theory, modified Newtonian theory and Newton- Busemann theory. For the waverider at an angle of attack reasonable estimates for pressure distribution can be made in each case by using the respective relationships

$$c_p = 2\sin^2\theta \qquad \text{(Newtonian method)}$$

$$c_p = c_{p_{max}} \sin^2\theta \qquad \text{(modified Newtonian method)}$$

$$c_{p_i} = 2\sin^2\theta_i + 2\left[\frac{d\theta}{dy}\right]_i \sin\theta_i \int_0^{y_i} \cos\theta \, dy \qquad \text{(Newton Busemann theory)}$$

A third method can also be extended to consider the pressure at the body at point i equal to an equivalent cone or equivalent wedge with the

Table 3.1 Aerodynamic Prediction Methods [82]

Level	Type	Limitation	Complexity	Computer Time
O	Empirical	Qualitatively	Algebraic	Seconds
I	Linear	Small $\alpha M = 1$	Algebraic	Minutes
II	Inviscid	No separation	Differential	Hour
III	Navier Stokes	No restriction	Partial Differential	Hours

Table 3.2 Summary of Aerodynamic Prediction Methods[82]

Level	Type	No. of Terms	No. of Boundary Conditions	Restriction
III	Navier Stokes	77	27	None
	a) Parabolized		23	$\frac{\partial^2}{\partial x^2} = 0$
	b) Boundary layer		9	$\frac{v}{u} \ll 1$
II	Inviscid			
	a) Euler	15	12	$\mu = 0$
	b) Full potential	9	6	Weak shocks
I	Linear	3	6	$u = U_\infty + u'$

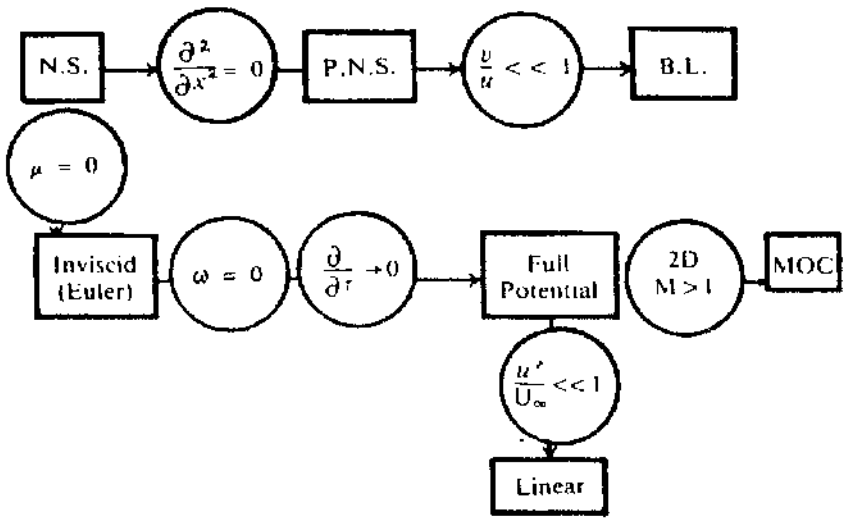

deflection θ_i. The equivalent wedge is used for a 2D body and equivalent cone for an axisymmetric body equal to a cone with semi angle θ_i. Other methods include the exact shock method.

The above are inviscid methods and more accuracy and correction for viscous effects are sought. Hypersonic similarity methods, hypersonic small disturbance theory or thin shock layer theory can be used[42]. For very high Mach numbers, Mach number independence can be applied because certain non-dimensional aerodynamic quantities like C_L, C_D and c_p become relatively independent of Mach number above a sufficiently high value of M_∞.

For inviscid flow more so-called exact solutions such as the classical method of characteristics can be applied. Also, the Euler equations can be solved using finite difference or finite element methods. Limitations and complexity for each prediction method are summarized in Table 3.1 and Table 3.2[82] and for any problem the aerodynamic approach towards final solution depends upon the accuracy required along with time and facilities available. Limitations for application of inviscid phenomena in hypersonic flow for waveriders is also briefly discussed in the previous chapter where the importance of the entropy layer, viscous interaction, high temperature, low density effects and real gas effects are pointed out.

Therefore whereas the simple methods are available for preliminary design work, an accurate prediction including viscous effects can only be obtained by applying the Navier-Stokes equations which provide an appropriate model for the flow around a body in a continuum flow.

Based on this strategy the Navier-Stokes Equations were applied to different waverider shapes to study viscous effects. Since the flow on typical waverider shapes is near conical, then it is appropriate to use the locally conical Navier-Stokes (LCNS) equations. The advantage of such an application is that it significantly reduces the requirement of computing resources both in terms of processor time and storage. So a LCNS solution [43],[44] was applied to predict the flow behaviour around waverider shapes. The study in this chapter used shapes which allowed simple grids to be used. More general waverider shapes are considered in the next chapter where more generalized coordinate transformations would be required.

The present chapter develops the equations and numerical techniques used. Results for the calculations of the flow over a family of caret wings, and a cone shape with anhedral wings at selected hypersonic flow conditions are presented. The cases are selected to illustrate the relevance of viscous effects in waverider design. The shapes chosen, in particular the choice of a 90° caret surface, were also controlled by the need for economic use of the computing resources that was necessary for this programme.

Before going into the details of numerical methods and solution schemes for the actual cases considered, off-design behaviour for cases which under ideal conditions (with inviscid assumptions) are expected to be on-design are first discussed.

3.2 Off Design Characteristics.

As discussed earlier at supersonic and hypersonic speed, with the presence of non-linearities and viscous effects the mathematical solution used to define this flow becomes very complex. In the past attempts were made to simplify these by manipulating the solution and simplifying the non-linear equation to the linear form. But as discussed these methods are not always sufficiently accurate. Although in the past especially in the 50's in support of the space race many of the advances were made by using this methodology and then improving the configurational design by long term wind tunnel testing. Nevertheless at each stage a more comprehensive solution which should embrace all the non-linearities is demanded, because wind tunnel experimentation has its own limitations as outlined earlier.

3.2.1 Off Design behaviour for Caret Wings.

An important problem at hypersonic speed involves shock boundary layer interaction and the problem becomes more complex when the flow around different airplane components interact with each other. For re-entry space planes, although the shapes like Appollo, Gemini and Mercury evolved, in order to contain the flow on the windward side, waverider shapes were suggested as an optimum design, for reasons which were discussed earlier.

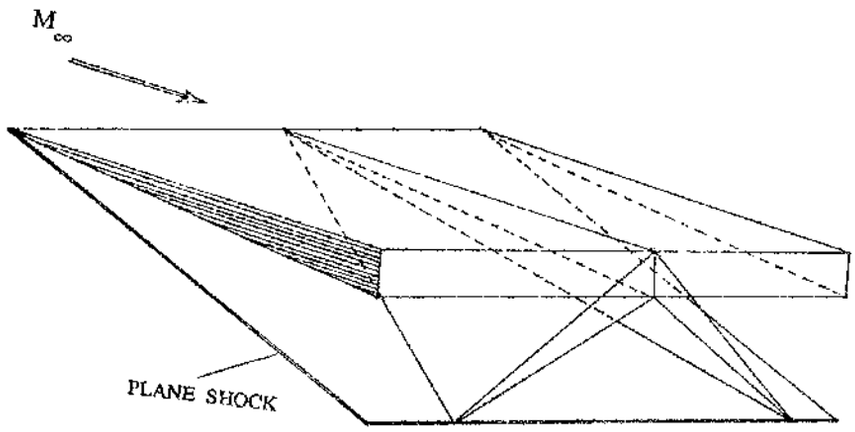

Fig. 3.1 Construction of caret wing from a single wedge flow.

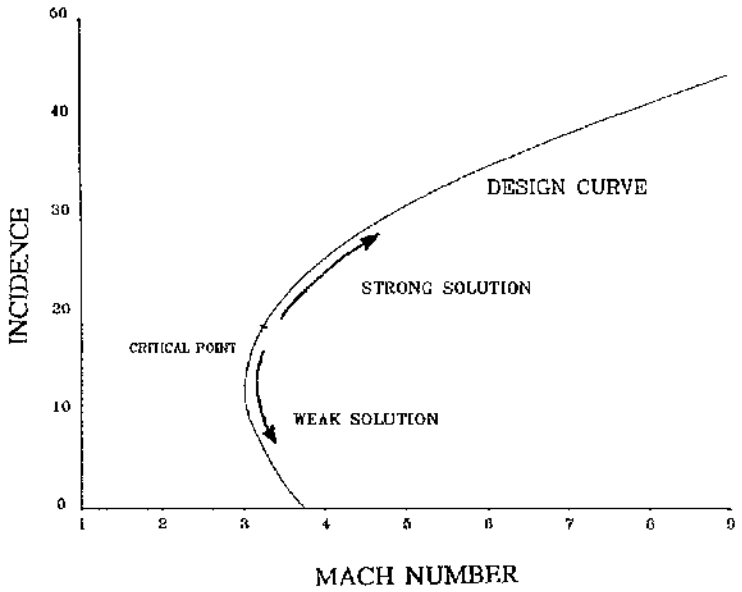

Fig. 3.2 On-design curve for a caret wing.

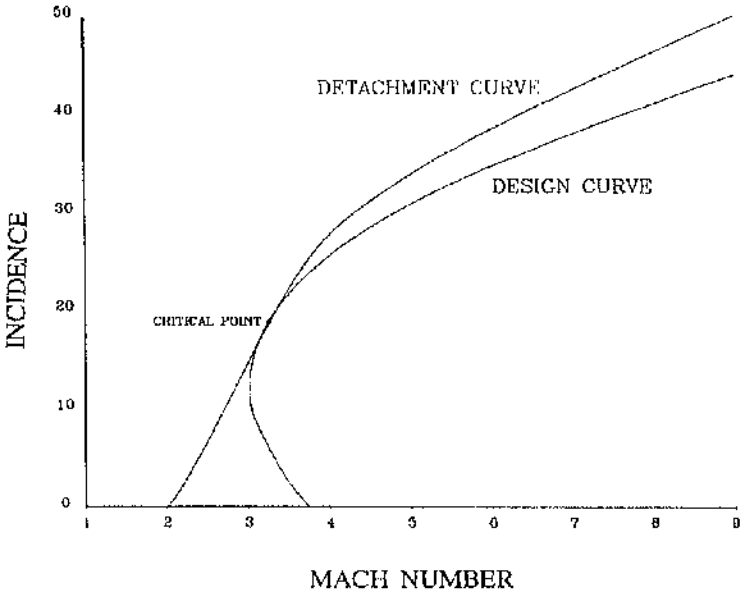

Fig. 3.3 Characteristic on-design and shock detachment curve for caret wing.

The idea of caret wings originally conceived by Nonweiler did give a boost to interest for lifting bodies and the idea was extended by Flower[15], Townend[4],[5] and Roe[16],[17] to consider its practicality for space plane shapes. Under ideal design conditions the waverider should exhibit the shock for which the streamline body is constructed but it is seen that viscous effects cause shock shapes to differ from those originally expected. For a given free stream Mach number and shock plane, the caret wing can be constructed by finding out the wedge angle (ridge angle) responsible for forming the shock on this plane (shock angle). An infinite number of Caret wings can then be constructed out of this flow but the definition of aspect ratio limits the shape of the wing (fig 3.1). Therefore one can say that M_{∞}, aspect ratio and shock angles are the basic parameters that define a caret wing.

A study of off-design behaviour has been carried out by Squire[22],[23] and Venn and Flower[45].

To understand the off-design behaviour for these wings first let us assume the on-design behaviour based on the complete inviscid shock wave solution. Two approaches can be used to construct the case, first by considering the flow for a yawed wedge or a flat plate in yaw and roll at some angle of attack. Although the two cases may seem different the concept is the same, that, the flow must be treated as for the body at a particular angle of attack with the leading edge lying in the shock plane.

For a caret wing the cross section parallel to the symmetric plane is equivalent to a 2-D wedge, therefore, one can construct a design curve for the flow around a wedge by using inviscid shock wave relationships. Hence for a particular wedge angle and shock angle (β), at different angles of incidence (α) a design curve can be calculated as shown in fig(3.2). This curve can be divided into two halves one for a strong solution and other corresponding to weak solution. For all normal cases the relevant solution is the weak one except when it is very near to the point where the strong and weak solutions are very close to each other. The design curve is only significant for a positive angle of incidence and has little meaning at negative angles when an expansion takes place.

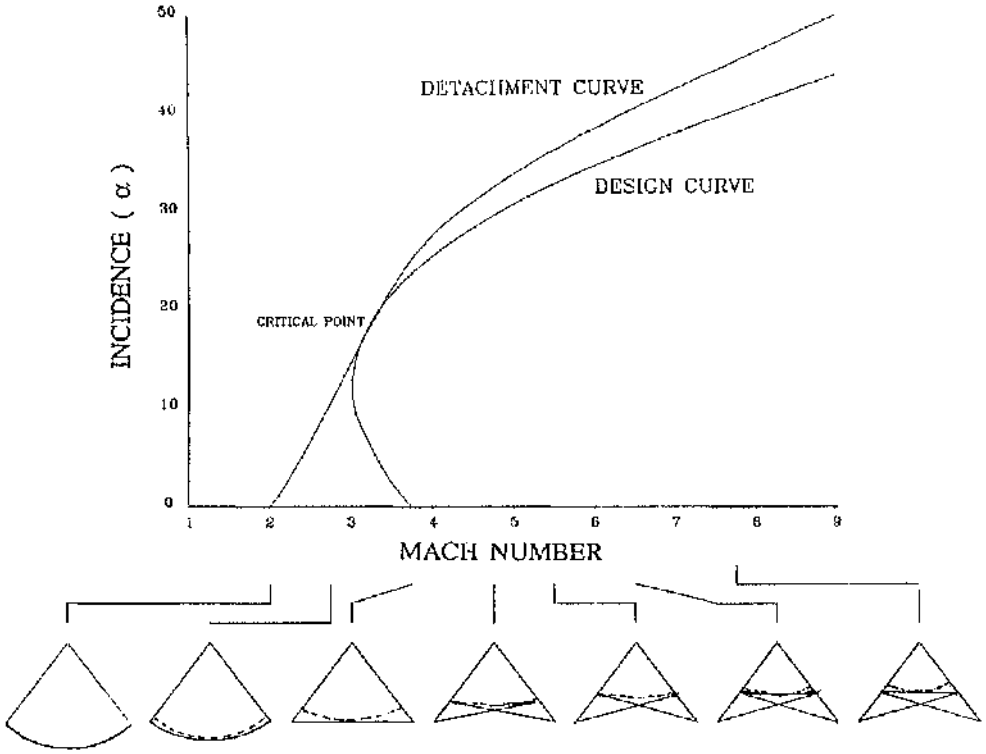

Fig. 3.4 Different final possible shock patterns (at zero incidence).

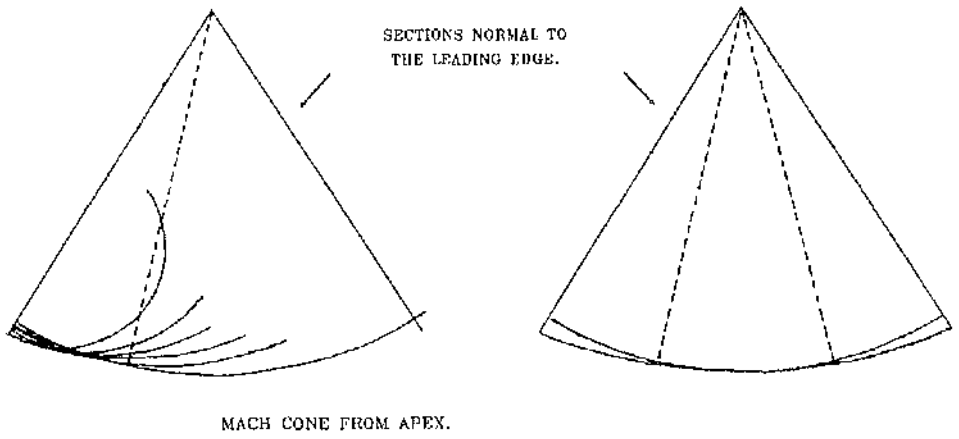

Fig. 3.5 Regions of influence.

Similarly a characteristic curve can be drawn by considering the flat plate at some angle of attack (α equivalent to wedge angle) in a roll and yawed orientation (where the yaw angle and roll angle together with the finite length of flat plate will determine the aspect ratio for the caret wing). So a family of design curves can be plotted corresponding to a range of possible design angles, where the flow remains attached and also for the same angles a curve where the flow is detached. Shock attachment and detachment curves touch each other at a critical point, at which the solution changes from weak to strong shown in fig(3.3).

For a fixed design angle, the design curve is independent of the aspect ratio but the detached flow curve is not. For any particular case the attached flow design curve remains fixed but the detached curve flow moves closer to it when decreasing the aspect ratio. Also for a decrease in aspect ratio the angle of incidence at the critical point is decreased.

Even for early studies in caret wing design, for the on-design case, doubts about the shock shapes existed. A few doubts were considered by Venn and Flower[45] who suggested that the final shock patterns emerging involved single, double and multiple shocks (fig 3.4). This study by Venn and Flower was mainly based on the extension of shock shapes emerging from Mach cones generated along a leading edge at zero incidence (fig 3.5) and different shock patterns are suggested by pointing out the 2D and 3D regions resulting from the complex reflection of waves and Mach cones.

These design curves and off-design shock shapes have been further elaborated by Squire[22,23] who, with the assumption that for low incidence the governing equations for flow at hypersonic speed can be linearized, continued attempts to develop the caret wing concept for reason of simplicity. Solutions for lifting bodies were proposed by Messiter and Hida [46,47] by using a first order correction to Newtonian Busemann theory. The resultant integral method was tested numerically, under these assumptions, by Squire[48] to calculate the pressure distribution and to derive shock shapes for Nonweiler's caret wings.

A comprehensive study of the off-design characteristics of waveriders emphasising the importance of viscous effects can be found in ref[48] and

49]. Off-design performance is discussed in ref[50].

The studies mentioned above so far revealed the off-design behaviour resulting from changes in incidence, Mach number or geometry. The final shock is a result of an initial multi shock (shock reflection etc.) system terminated by a smoothly curved final shock. The suggested theory corresponding to this is based on inviscid flow with hidden assumptions. Although certain shock patterns can be computed using these theories, in practice a further off-design behaviour is introduced due to the presence of a boundary layer, which causes the real shock shapes to differ in detail from those suggested.

Another important application, where the on design condition is sensitive to changing flow conditions in a similar way to the caret wing, is in the determination of the performance characteristics of ram jet inlets, propulsion unit inlets and supersonic diffusers.

Mohoney [51] has discussed these different possible off-design conditions for a ramjet inlet at $\alpha = 0^{\circ}$ in different modes where each mode is classified for different on, above and below design Mach numbers with further sub-critical, critical and super-critical operation of each according to the terminal normal shock position. In practical application, for a ramjet as well as for a caret wing, to have better performance, the concept of applying operational on-design conditions seems favourable and an optimum Mach number can be determined or adjusted by using shock wave relationships. But at high Mach number, in the presence of viscous effects the behaviour may differ significantly from prediction, the flow becoming more complex especially when the vehicle is flying at incidence. The foregoing study is an attempt to illustrate this off-design behaviour for simple shapes caused by the presence of viscous effects.

The present study of the waverider involving solutions of the Navier-Stokes equations is different from past studies in that, for final off-design shapes, viscous and inviscid effects come as part of the solution. Some interesting features of off-design behaviour on caret wings and idealized conical waveriders are reported in sect. (3.4.2) and (3.5.2) respectively.

3.3 Numerical Method and Solution Scheme.

Corresponding to three basic equations of fluid dynamics i.e.,

a. Conservation of mass.
b. Equation of momentum.
c. Conservation of energy.

there are two different approaches used for derivation. These are

1. Phenomenological approach;
2. Kinetic theory approach.

In the first approach, certain relations between stress and rate of strain, heat flux and temperature gradient are postulated and then the fluid dynamic equations are developed from the conservation laws, but the required constants of proportionality between stress and rate of strain and heat flux and temperature gradient (also called the transport coefficients) must be determined experimentally in this approach.

In the second approach computational fluid dynamics equations are obtained with the transport coefficients defined in terms of certain integral relations which involve the dynamics of colliding particles — then knowledge of interparticle forces are required in order to evaluate the collision integrals.

The theories by Schlichting[52] (for the former case) and Hirschfelder et al[83] (for the latter case) suggest that the two approaches will yield the same fluid dynamic equations if equivalent assumptions are made during their derivation. The complete set of these equations are known as the Navier-Stokes equations.

The system of Navier-Stokes equations supplemented by empirical laws for the dependence of viscosity and thermal conductivity with other flow variables and through a constitutive law defining the nature of the fluid, completely describe the relevant flow phenomena.

For the present study the Navier-Stokes equations are first written in conservation form and are then transformed into spherical form before applying the locally conical approximation.

Navier Stokes Equations in Cartesian Coordinates.

In conservation form the complete Navier-Stokes equations in three dimensions without external heat and body forces in Cartesian coordinates can be written[53] as

$$\frac{\partial U}{\partial t} + \frac{\partial E}{\partial x} + \frac{\partial F}{\partial y} + \frac{\partial G}{\partial z} = 0 \qquad \text{.....(3.2)}$$

where, dependent vector U and flux vectors E, F, G are given as

$$U = \begin{bmatrix} \rho \\ \rho u_x \\ \rho u_y \\ \rho u_z \\ \rho e \end{bmatrix} \qquad \text{.....(3.3)}$$

$$E = \begin{bmatrix} \rho u_x \\ \rho u_x^2 + p - \tau_{xx} \\ \rho u_y u_x - \tau_{yx} \\ \rho u_z u_x - \tau_{zx} \\ (\rho e + p)u_x + q_x - u_x\tau_{xx} - u_y\tau_{yx} - u_z\tau_{zx} \end{bmatrix} \qquad \text{..(3.4)}$$

$$F = \begin{bmatrix} \rho u_y \\ \rho u_x u_y - \tau_{xy} \\ \rho u_y^2 + p - \tau_{yy} \\ \rho u_z u_y - \tau_{zy} \\ (\rho e + p)u_y + q_y - u_x\tau_{xy} - u_y\tau_{yy} - u_z\tau_{zy} \end{bmatrix} \qquad \text{..(3.5)}$$

$$G = \begin{bmatrix} \rho u_z \\ \rho u_x u_z - \tau_{xz} \\ \rho u_y u_z - \tau_{yz} \\ \rho u_z^2 + p - \tau_{zz} \\ (\rho e + p)u_z + q_z - u_x\tau_{xz} - u_y\tau_{yz} - u_z\tau_{zz} \end{bmatrix} \quad ..(3.6)$$

Where shear stress terms are given as follows

$$\begin{aligned} \tau_{xx} &= \frac{2}{3}\mu\left(2\frac{\partial u_x}{\partial x} - \frac{\partial u_y}{\partial y} - \frac{\partial u_z}{\partial z}\right) \\ \tau_{yy} &= \frac{2}{3}\mu\left(2\frac{\partial u_y}{\partial y} - \frac{\partial u_x}{\partial x} - \frac{\partial u_z}{\partial z}\right) \\ \tau_{zz} &= \frac{2}{3}\mu\left(2\frac{\partial u_z}{\partial z} - \frac{\partial u_y}{\partial y} - \frac{\partial u_x}{\partial x}\right) \qquad \text{..... (3.7)} \\ \tau_{xy} &= \tau_{yx} = \mu\left(\frac{\partial u_x}{\partial y} + \frac{\partial u_y}{\partial x}\right) \\ \tau_{xz} &= \tau_{zx} = \mu\left(\frac{\partial u_x}{\partial z} + \frac{\partial u_z}{\partial x}\right) \\ \tau_{yz} &= \tau_{zy} = \mu\left(\frac{\partial u_y}{\partial z} + \frac{\partial u_z}{\partial y}\right) \end{aligned}$$

A perfect gas is assumed with the standard constants for the equation of state ,

$$p = \rho RT$$

where, the gas constant for perfect air, the medium of interest, R = 287 m^2/sec^2 K and temperature T are related in the form.

$$T = (\gamma - 1)\,[e - |V|^2/2]/R \qquad \text{.....(3.8)}$$

for the ratio of specific heats $\gamma = 1.4$.

To express heat transfer, the Fourier's law of heat transfer by conduction is assumed. Therefore heat flux in each direction can be given as

$$\begin{aligned} q_x &= -k\frac{\partial T}{\partial x} \\ q_y &= -k\frac{\partial T}{\partial y} \qquad \text{... . ..(3.9)} \\ q_z &= -k\frac{\partial T}{\partial z} \end{aligned}$$

Viscosity is calculated by the Sutherland formula.

$$\mu = 1.458 \frac{T^{\frac{3}{2}}}{T + 110.4} \times 10^{-6} \text{ kg/m sec} \quad \text{.....(3.10)}$$

For a hypersonic space vehicle, the presence of 3 dimensional viscous effects require a solution of the complete Navier-Stokes equations for the flow over the whole body. Unlike the flow for a low speed vehicle where the viscous effects are important only in a localized region, viscous effects in high speed flows become significant for the whole body. But as a full Navier-Stokes solution may be difficult to apply, to model the flow around the full body, therefore, the equivalence principle (or subdividing technique (see fig(2.15)) can be used as an alternative provided interference and interaction effects are accounted for in arriving at final conclusions. Another way is to reduce the Navier-Stokes equations with appropriate assumptions while retaining the viscous terms, such as used in the parabolized form of the Navier-Stokes equations or the locally conical Navier-Stokes equations.

Locally Conical Navier Stokes Solution

As the flow around the majority of high speed planes and missiles is approximately conical in nature, it is a reasonable assumption that for the present case study, the numerical method used is based on the locally conical Navier-Stokes Equations (LCNS). The method uses the 3-D , unsteady, compressible Navier Stokes equations for viscous laminar flow written in a weak conservation form in a spherical coordinate system (as shown in appendix 3) simplified by making use of assumptions that for these vehicle shapes the gradients are much smaller in the radial than in the cross flow direction. The result is the locally conical Navier-Stokes equations in non dimensionalised form as follows

$$\frac{\partial U}{\partial \iota} + \frac{\partial F}{\partial \theta} + \frac{\partial G}{\partial \varphi} + H = 0 \qquad \text{.....(3.11)}$$

where

$$U = \sin\theta \begin{bmatrix} \rho \\ \rho u_r \\ \rho u_\theta \\ \rho u_\varphi \\ \rho e \end{bmatrix} \qquad \text{.....(3.12)}$$

$$F = \sin\theta \begin{bmatrix} \rho u_\theta \\ \rho u_r u_\theta - \tau_{r\theta} \\ \rho u_\theta^2 + p - \tau_{\theta\theta} \\ \rho u_\varphi u_\theta - \tau_{\varphi\theta} \\ (\rho e + p)u_\theta + q_\theta - u_r\tau_{r\theta} - u_\theta\tau_{\theta\theta} - u_\varphi\tau_{\varphi\theta} \end{bmatrix} \qquad \text{..(3.13)}$$

$$G = \begin{bmatrix} \rho u_\varphi \\ \rho u_r u_\varphi - \tau_{r\varphi} \\ \rho u_\theta u_\varphi - \tau_{\theta\varphi} \\ \rho u_\varphi^2 + p - \tau_{\varphi\varphi} \\ (\rho e + p)u_\varphi + q_\varphi - u_r\tau_{r\varphi} - u_\theta\tau_{\theta\varphi} - u_\varphi\tau_{\varphi\varphi} \end{bmatrix} \qquad \text{..(3.14)}$$

$$H = \sin\theta \begin{bmatrix} 2\rho u_r \\ 2\rho u_r^2 - \rho u_\theta^2 - \rho u_\varphi^2 - \tau_{rr} + \tau_{\theta\theta} + \tau_{\varphi\varphi} \\ 3\rho u_r u_\theta - \mathrm{ctg}\theta(\rho u_\varphi^2 + p) + \mathrm{ctg}\theta\,\tau_{\varphi\varphi} - 2\tau_{r\theta} \\ 3\rho u_r u_\varphi + \mathrm{ctg}\theta\,\rho u_\theta u_\varphi - \mathrm{ctg}\theta\,\tau_{\theta\varphi} - 2\tau_{r\varphi} \\ 2u_r(\rho e + p) - u_r\tau_{rr} - u_\theta\tau_{r\theta} - u_\varphi\tau_{r\varphi} \end{bmatrix} \qquad \text{.(3.15)}$$

where the shear stress terms are given as follows

$$\tau_{rr} = -\frac{2}{3}\frac{1}{\mathrm{Re}_{\infty,r}}\left(2u_r + \frac{\partial u}{\partial\theta}\theta + \mathrm{ctg}u_\theta + \frac{1}{\sin\theta}\frac{\partial u_\varphi}{\partial\varphi}\right)$$

$$\tau_{\theta\theta} = 2\mu/\mathrm{Re}_{\infty,r}\left(\frac{\partial u_\theta}{\partial\theta} + u_r\right) + \tau_{rr}$$

$$\tau_{\varphi\varphi} = 2\mu/\mathrm{Re}_{\infty,r}\left(\frac{1}{\sin\theta}\frac{\partial u_\varphi}{\partial\varphi} + u_r + u_\theta\mathrm{cotg}\theta\right) + \tau_{rr} \qquad \text{.....(3.16)}$$

$$\tau_{r\theta} = \tau_{\theta r} = \mu/Re_{\infty,r}\,(-u_\theta + \frac{\partial u_r}{\partial \theta})$$

$$\tau_{\theta\varphi} = \tau_{\varphi\theta} = \mu/Re_{\infty,r}\,(\frac{\partial u_\varphi}{\partial \theta} - \cot g\theta\, u_\varphi + \frac{1}{\sin\theta}\frac{\partial u_\theta}{\partial \varphi})$$

$$\tau_{r\varphi} = \tau_{\varphi r} = \mu/Re_{\infty,r}(\frac{1}{\sin\theta}\frac{\partial u_r}{\partial \varphi} - u_\varphi),$$

and, heat flux is defined as.

$$q_\theta = -\frac{\mu}{2Re_{\infty,r}Pr}\frac{\partial T}{\partial \theta} \qquad \text{.....(3.17)}$$

$$q_\varphi = -\frac{\mu}{2\sin\theta Re_{\infty,r}Pr}\frac{\partial T}{\partial \varphi}\ .$$

Viscosity is calculated by the Sutherland formula.

For the solution of the equations a time marching MacCormack two step implicit finite difference scheme is employed using the following predictor and corrector scheme to equation (3.11) :

Predictor :

$$\Delta U^n_{i,j} = -\Delta t(\Delta_+ F^n_{i,j}/\Delta\theta + \Delta_+ G^n_{i,j}/\Delta\varphi + H^n_{i,j})$$

$$[\,I - (\Delta t/\Delta\theta)\Delta_+ |A^n|\,][\,I - (\Delta t/\Delta\varphi)\Delta_+ |B^n|\,]\,\delta U^{\overline{n+1}}_{i,j} = \Delta U^n_{i,j}$$

$$U^{\overline{n+1}}_{i,j} = U^n_{i,j} + \delta U^{\overline{n+1}}_{i,j}$$

Corrector :

$$\Delta U^{\overline{n+1}}_{i,j} = -\Delta t(\Delta_- F^{\overline{n+1}}_{i,j}/\Delta\theta + \Delta_- G^{\overline{n+1}}_{i,j}/\Delta\theta + H^{\overline{n+1}}_{i,j})$$

$$[\,I - (\Delta t/\Delta\theta)\Delta_- |A^{\overline{n+1}}|\,][\,I + (\Delta t/\Delta\varphi)\Delta_- |B^{\overline{n+1}}|\,]\delta U^{n+1}_{i,j} = \Delta U^{\overline{n+1}}_{i,j}$$

$$U^{n+1}_{i,j} = (1/2)(U^n_{i,j} + U^{\overline{n+1}}_{i,j} + \delta U^{n+1}_{i,j})$$

Although shock waves are captured automatically through this procedure, oscillations in flow parameters are very prominent near shock wave discontinuities. Therefore to dampen these oscillations a modified adaptive artificial viscosity (AAV) term in conservative form is applied. This term is significant to the calculation only near the shock wave. It has very little effect inside the boundary layer. It has also been observed that for an accurate viscous solution, the AAV must be switched off near the wall,

otherwise residues near the wall cannot be reduced further after two or three orders of reduction have been achieved.

The AAV in the θ direction used here has the form :

$$D_{\theta i,j} = d_{\theta i+1/2,j} - d_{\theta i-1/2,j}$$

with

$$d_{\theta i+1/2,j} = C_{\theta i+1/2,j}\ \varepsilon_{i+1/2,j}(U_{i+1,j} - U_{i,j})$$

where

$$C_{\theta i+1/2,j} = k_o|u_\theta + c|/\Delta\theta_i$$

and the sensor of the shock wave in the θ direction, $\nu_{\theta i,j}$ is

$$\nu_{\theta i,j} = \left|\frac{p_{i+1,j} - 2p_{i,j} + p_{i-1,j}}{p_{i+1,j} + 2p_{i,j} + p_{i-1,j}}\right|$$

$$\bar{\nu}_{\theta i+1/2,j} = \max\ (\nu_{\theta i+1/2,j}, \nu_{\theta i+1,j}, \nu_{\theta i,j}, \nu_{\theta i-1,j})$$

$$\varepsilon_{\theta i+1/2,j} = \min\ [k_1, k_2 \max\ (0\ ,\ \bar{\nu}_{\theta i+1/2,j} - k_3)]$$

where constants

$$k_o = 0.1,\ k_1 = 0.5,\ k_2 = 1 \text{ and } k_3 = 0.1$$

The artificial viscosity for the φ direction can be described similarly.

The numerical solution gives the fluid properties of temperature, pressure, the three velocity components, density (ρ), Mach number(M), pitot pressure (p_o) and heat rate (Q) values in non-dimensionalised form on a computational surface at a distance r from the tip. The computation surface consist of a 65 × 65 grid stretched in the θ and φ direction as shown in fig 3.7 for the caret wings and 65 × 90 as shown in fig 3.16 for conical wave riders. In N-S equations values are non-dimensionalised by

$$u_r^* = \frac{u_r}{|V|_\infty} \qquad u_\theta^* = \frac{u_\theta}{|V|_\infty} \qquad u_\varphi^* = \frac{u_\varphi}{|V|_\infty}$$

$$\rho^* = \frac{\rho}{\rho_\infty} \qquad P^* = \frac{P}{\rho_\infty |V|_\infty^2} \qquad \mu^* = \frac{\mu}{\mu_\infty}$$

$$e^* = \frac{e}{|V|_\infty^2} \qquad T^* = \frac{T}{T_o - T_\infty}$$

where the nondimensionalised variables are denoted by an asterisk.

3.4 Caret Waveriders.

3.4.1 Geometry of models and flow conditions.

The configurations for the caret wings consist of two 8° wedges intersecting each other at 90° with different sweep angles. To get the inviscid flow design condition for simulation for each configuration an inverse approach was used. For each case the free stream velocity should be such as to exhibit the shock pattern for the particular caret wing case. Conditions for caret wing simulations are shown in table (3.3). Here the free stream Mach number was calculated using the oblique shock relation for the deflection angle in terms of the free stream Mach number and wave angle

$$\theta = \beta - \tan^{-1}\left[\frac{}{\sin\beta\cos\beta}\left(\frac{\gamma-1}{\gamma+1}\sin^2\beta + \frac{2}{\gamma+1}\frac{1}{M_1^2}\right)\right]$$

where θ = Wedge angle corresponding to the intersection

β = Shock angle corresponding to the design caret wing conditions.

TABLE : 3.3

Flow conditions for simulation (Caret wings).

T_∞ = 38.73 K
ρ_∞ = 6.16076×10^{-3} Kg/m^3
P_∞ = 68.48 Pa
T_w = 43 K
r = distance from nose = 10 cm
a = velocity of sound = 124.74 m/s
width or span of the wedge=0.05 m
(except for 75 case where s= 0.025 m)

	Reynolds number	χ	Mach number	wing sweep
CASE S30M144	48841	.013	1.44	30
CASE S45M174	58806	.0216	1.74	45
CASE S60M251	84737	.0542	2.51	60
CASE S75M493	166618	.2926	4.93	75

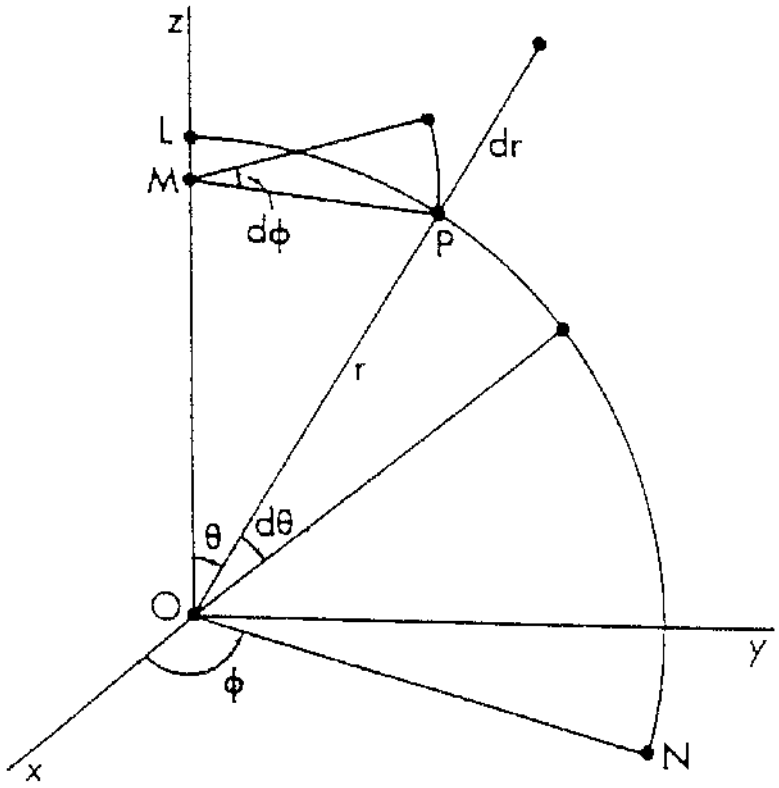

Fig. 3.6 Coordinate transformation (Spherical and Cartesian).

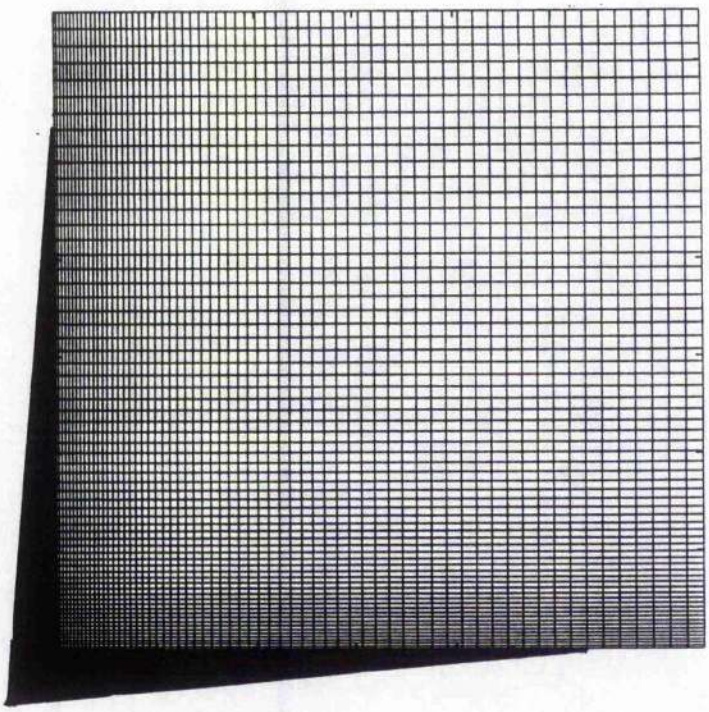

Fig. 3.7 Grid used for caret wings (65×65).

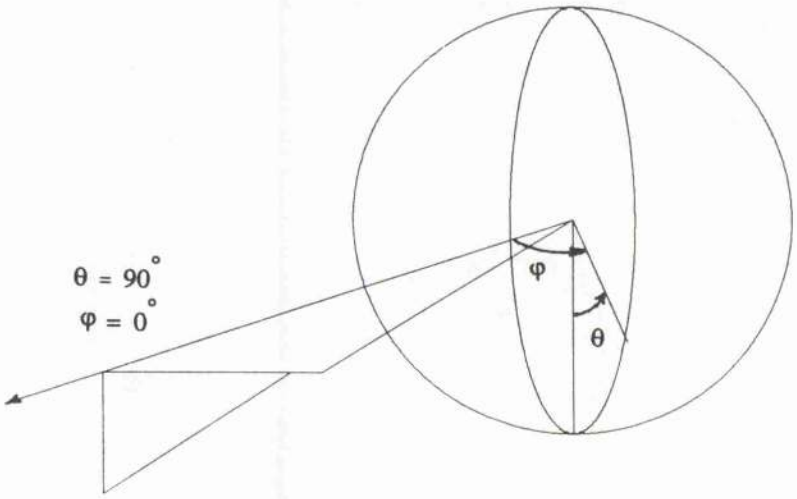

Fig. 3.8 Caret wing in spherical coordinate.

The position for the computed station is located through the Reynolds number by

$$Re_{\infty,r} = \frac{\rho_\infty U_\infty r}{\mu_\infty}$$

A perfect gas is assumed for simulation.

For either case the following boundary conditions are used :

On the wall : $U_r = U_\theta = U_\varphi = 0$; and $T = T_w$ = constant,

at the outer boundary : free stream conditions,

on the symmetric planes : reflection conditions.

For numerical simulation, in each case with different sweep angles, the caret model was placed in spherical coordinates as shown in fig 3.8, such that the corner coincides with the $\theta = 90^\circ$ and $\varphi = 0^\circ$ coordinate extending towards the r direction. The nose tip of caret wing is placed at the origin of the spherical coordinate system. The incoming flow direction is parallel to the upper surface in each case and the wedge angle with respect to incoming flow is β. Velocity vectors for the incoming flow in Cartesian co-ordinates can be transformed to those in spherical coordinates through the following coordinate transformation (ref fig 3.6).

$$\begin{bmatrix} e_r \\ e_\theta \\ e_\varphi \end{bmatrix} = \begin{bmatrix} \sin\theta\cos\varphi & \sin\theta\sin\varphi & \cos\theta \\ \cos\theta\cos\varphi & \cos\theta\sin\varphi & -\sin\theta \\ -\sin\varphi & \cos\varphi & 0 \end{bmatrix} \begin{bmatrix} e_x \\ e_y \\ e_z \end{bmatrix}$$

3.4.2 Results and discussion.

As the theoretical procedure suggests, to generate a waverider flow for a fixed caret wing shape, there exists only one combination of M_∞ and θ, which can reveal this pattern and the inviscid flow beneath the caret shapes can be calculated such that it is equivalent to a 2-D wedge flow. Therefore inviscid shock wave theory was used to provide the initial input values for the LCNS equations. Results thus obtained numerically are compared with theoretical values to determine the effects of viscous interaction on shock wave and flow properties.

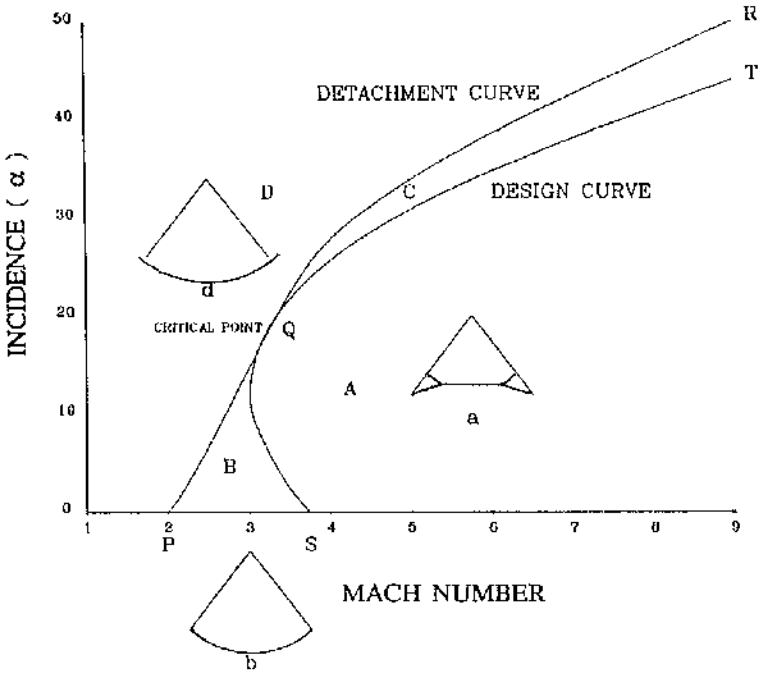

Fig. 3.9 Flow regions on caret wings.

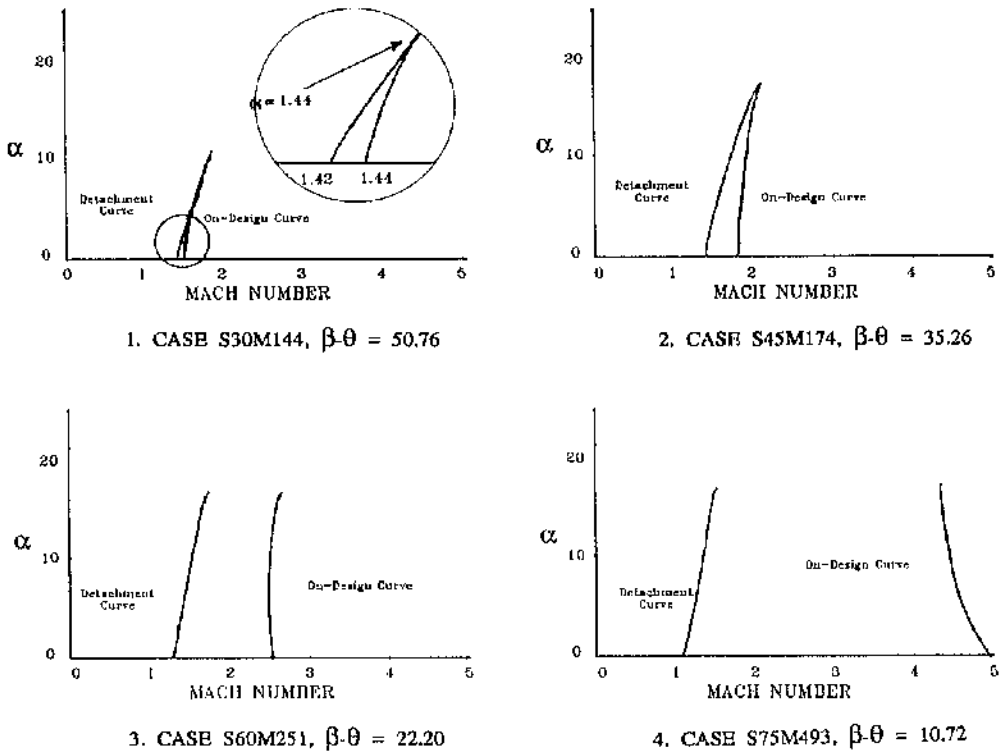

Fig. 3.10 Likely off-design conditions for caret wings.

Before further discussion about viscous effects around these shapes, it is necessary to review some off-design characteristics of caret wings. Fig(3.9) shows a few likely off-design conditions for caret gliders, where the flow around a particular type of caret wing can be described within certain boundaries. In fig(3.9) these flow regions are illustrated in the M-α plane. Here line SQT corresponds to on-design conditions, in which a two dimensional shock lies in the plane of the leading edge and the lower surface of the caret wing is a stream surface. In the region SQP (or region B) the shock wave is slightly curved but still attached to the leading edge. To the right of SQT, in region A, the flow takes up the complex shock pattern as shown in fig(3.9). Curve PQR in the figure describes the shock detachment from the leading edge and beyond this in region D the shock is completely detached. The shock pattern under RQT (or region C) is less likely to happen but if present it is similar to region D.

In figure(3.10) these regions are shown for each of the cases considered. Here the line on the right corresponds to the on-design conditions i.e., line SQT in fig(3.9) and the line on the left shows the limit of the detached shock wave (line PQR). The symbol α in figures (3.9 and 3.10) relates the deflection of the upper surface of the caret wing with respect to the free stream flow. Figures 3.10(1) and 3.10(2) illustrate that the shock waves are very strong and only a small variation in flow parameters may show up as a major change in shock shape. In 3.10(1), for the 30° sweep-back angle, region B is very small and is shown enlarged. It can be seen from the enlarged portion that for a wedge angle of 9.76° at a Mach number of 1.44 the shock wave is on-design and at Mach number of 1.42 it becomes detached. Fig 3.10(2) shows another case of a strong shock wave at an on-design configuration. Here again an on-design shock is more close to the detached shock line and influenced by it. However for the other two cases of sweep-back 60° and 75° shown in fig 3.10(3) and 3.10(4) the on-design lines are far away from the detached region, therefore although viscous effects may be higher for these cases due to high Mach numbers, the weak shock shapes generated are less likely to be affected.

Keeping these regions in mind a similar comparison can be made for the numerical results. Fig (3.11 to 3.14) shows the contour plots for different

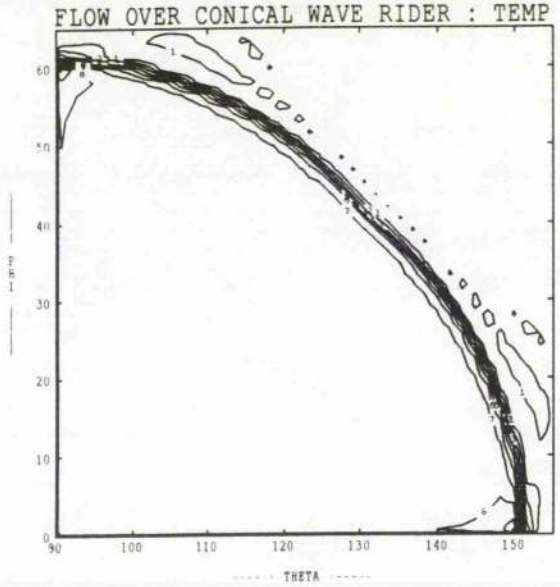

CONTOUR KEY	
1	0.2500E+01
2	0.2570E+01
3	0.2640E+01
4	0.2710E+01
5	0.2780E+01
6	0.2850E+01
7	0.2920E+01
8	0.2990E+01
9	0.3060E+01
10	0.3130E+01
11	0.3200E+01

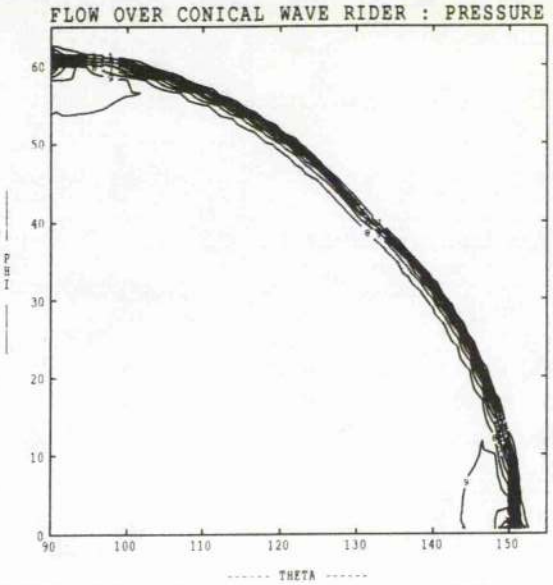

CONTOUR KEY	
1	0.4000E+00
2	0.4300E+00
3	0.4600E+00
4	0.4900E+00
5	0.5200E+00
6	0.5500E+00
7	0.5800E+00
8	0.6100E+00
9	0.6400E+00
10	0.6700E+00
11	0.7000E+00
12	0.7300E+00
13	0.7600E+00
14	0.7900E+00

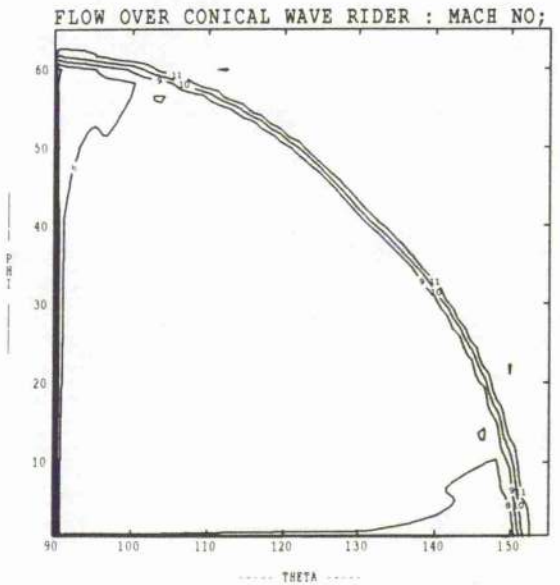

CONTOUR KEY	
1	0.0000E+00
2	0.1350E+00
3	0.2700E+00
4	0.4050E+00
5	0.5400E+00
6	0.6750E+00
7	0.8100E+00
8	0.9450E+00
9	0.1080E+01
10	0.1215E+01
11	0.1350E+01

Fig. 3.11 Case S30M144

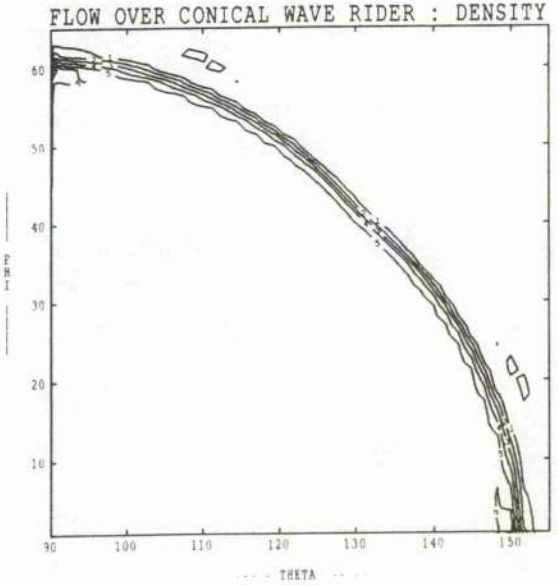

CONTOUR KEY	
1	0.1050E+01
2	0.1150E+01
3	0.1250E+01
4	0.1350E+01
5	0.1450E+01
6	0.1550E+01
7	0.1650E+01
8	0.1750E+01
9	0.1850E+01
10	0.1950E+01
11	0.2050E+01

Fig. 3.11 Case S30M144

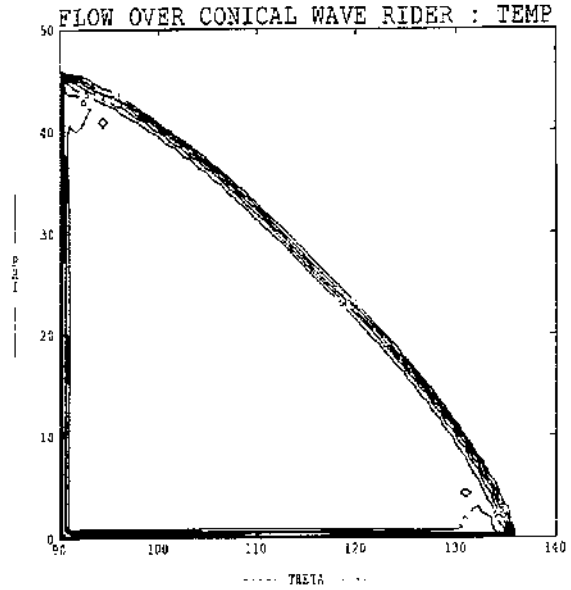

CONTOUR KEY	
1	0.1680E+01
2	0.1720E+01
3	0.1760E+01
4	0.1800E+01
5	0.1840E+01
6	0.1880E+01
7	0.1920E+01
8	0.1960E+01
9	0.2000E+01

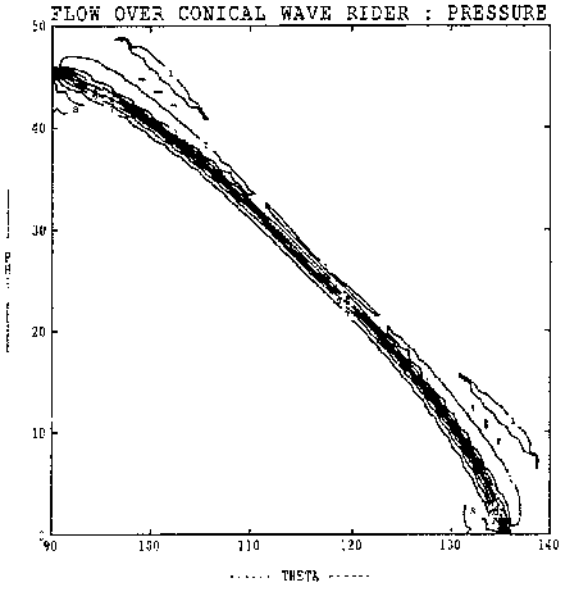

CONTOUR KEY	
1	0.2300E+00
2	0.2500E+00
3	0.2700E+00
4	0.2900E+00
5	0.3100E+00
6	0.3300E+00
7	0.3500E+00
8	0.3700E+00
9	0.3900E+00

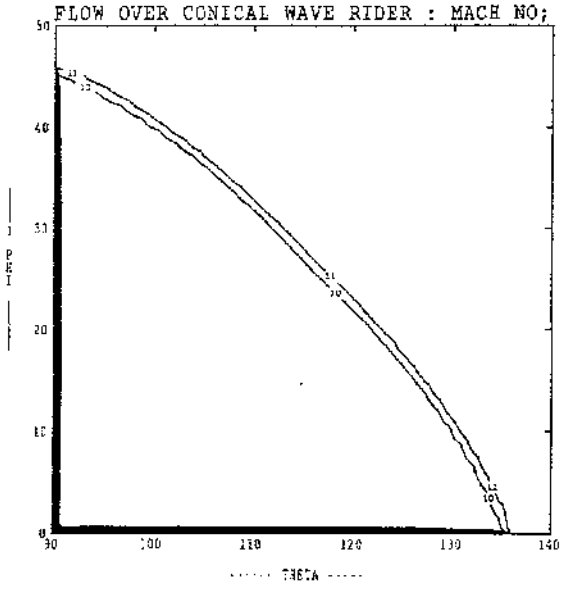

CONTOUR KEY	
1	0.0000E+00
2	0.1700E+00
3	0.3400E+00
4	0.5100E+00
5	0.6800E+00
6	0.8500E+00
7	0.1020E+01
8	0.1190E+01
9	0.1360E+01
10	0.1530E+01
11	0.1700E+01

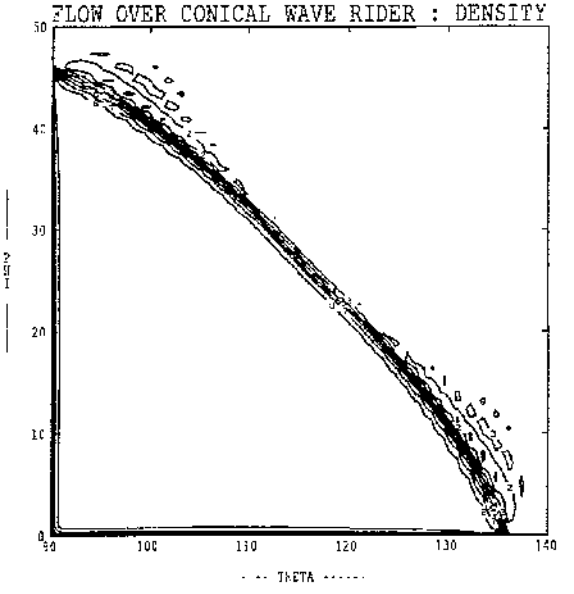

CONTOUR KEY	
1	0.9100E+00
2	0.9700E+00
3	0.1030E+01
4	0.1090E+01
5	0.1150E+01
6	0.1210E+01
7	0.1270E+01
8	0.1330E+01
9	0.1390E+01
10	0.1450E+01
11	0.1510E+01

Fig. 3.12 Case S45M174

Fig. 3.12 Case S45M174

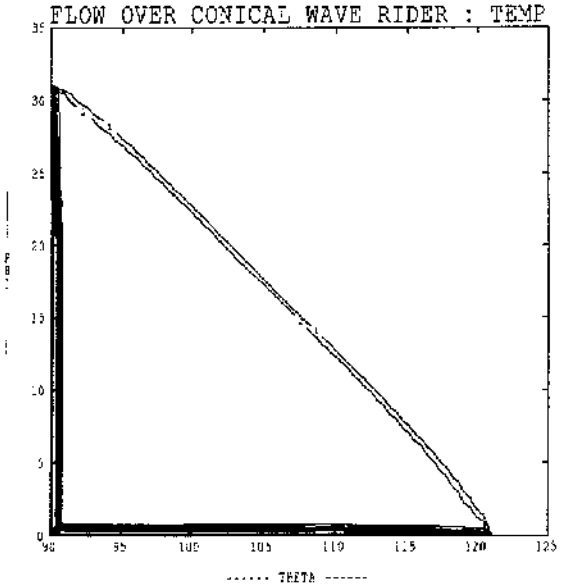

CONTOUR KEY	
1	0.8590E+00
2	0.8765E+00
3	0.9036E+00
4	0.9295E+00
5	0.9560E+00
6	0.9825E+00
7	0.1009E+01
8	0.1035E+01
9	0.1062E+01
10	0.1088E+01
11	0.1115E+01

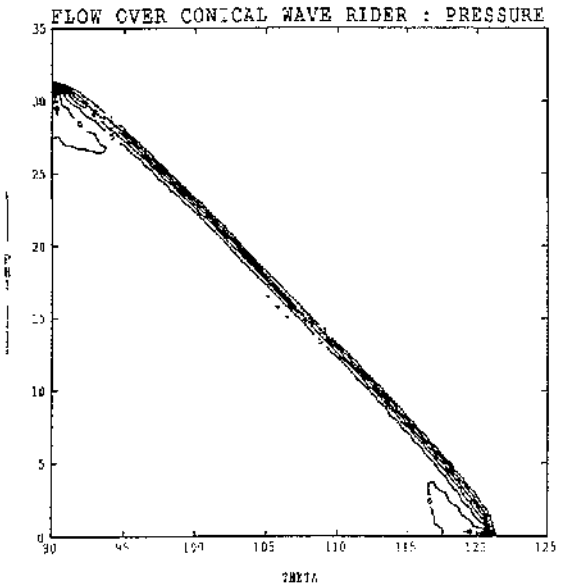

CONTOUR KEY	
1	0.1260E+00
2	0.1330E+00
3	0.1400E+00
4	0.1500E+00
5	0.1600E+00
6	0.1700E+00
7	0.1800E+00
8	0.1900E+00
9	0.2000E+00

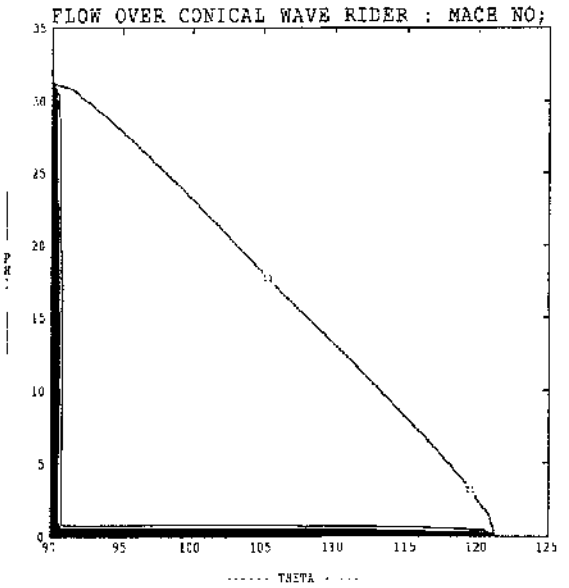

CONTOUR KEY	
1	0.5320E-01
2	0.2902E+00
3	0.5302E+00
4	0.7701E+00
5	0.1010E+01
6	0.1250E+01
7	0.1490E+01
8	0.1730E+01
9	0.1970E+01
10	0.2210E+01
11	0.2450E+01

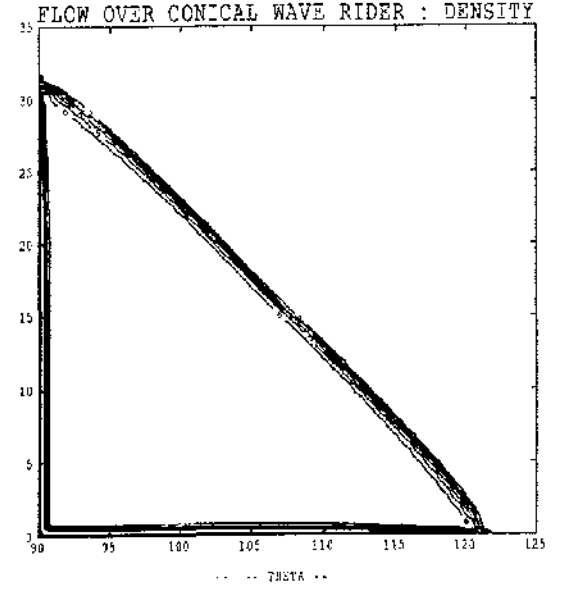

CONTOUR KEY	
1	0.1050E+01
2	0.1100E+01
3	0.1150E+01
4	0.1200E+01
5	0.1250E+01
6	0.1300E+01
7	0.1350E+01
8	0.1400E+01
9	0.1450E+01
10	0.1500E+01
11	0.1550E+01

Fig. 3.13 Case S60M251

Fig. 3.13 Case S60M251

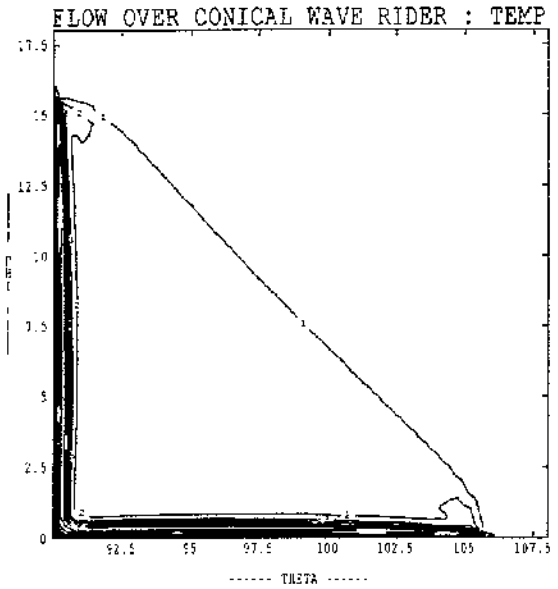

CONTOUR KEY	
1	0.2130E+00
2	0.2430E+00
3	0.2730E+00
4	0.3030E+00
5	0.3330E+00
6	0.3600E+00
7	0.3900E+00
8	0.4200E+00
9	0.4500E+00
10	0.4800E+00
11	0.5100E+00

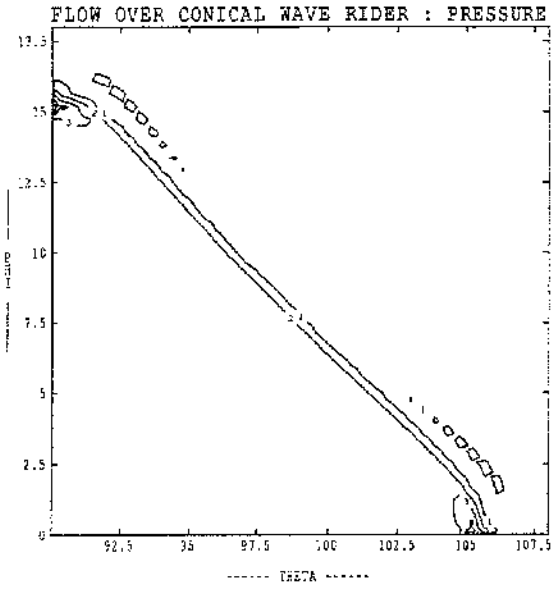

CONTOUR KEY	
1	0.3000E-01
2	0.4000E-01
3	0.5000E-01
4	0.6000E-01
5	0.7000E-01
6	0.8000E-01
7	0.9000E-01
8	0.1000E+00

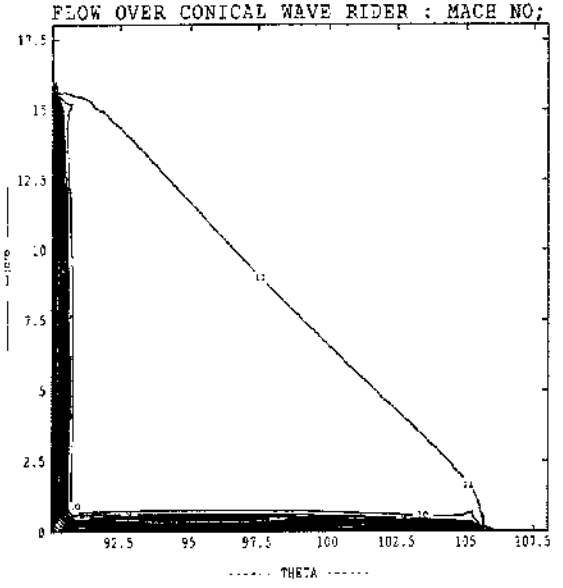

CONTOUR KEY	
1	0.2130E+00
2	0.6730E+00
3	0.1133E+01
4	0.1593E+01
5	0.2053E+01
6	0.2513E+01
7	0.2973E+01
8	0.3433E+01
9	0.3893E+01
10	0.4353E+01
11	0.4813E+01

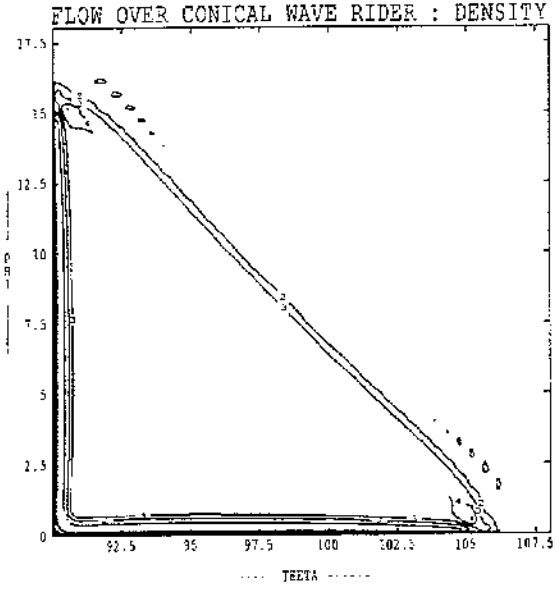

CONTOUR KEY	
1	0.8270E-00
2	0.1027E+01
3	0.1227E+01
4	0.1427E+01
5	0.1627E+01
6	0.1827E+01
7	0.2027E+01
8	0.2227E+01
9	0.2427E+01
10	0.2627E+01
11	0.2827E+01

Fig. 3.14 Case S75M493

Fig. 3.14 Case S75M493

TABLE 3.4

CASE S30M144

	Pressure (Pa)	Temperature (K)	Density (kg/m^3)	Mach number
Theory	115.37	45.139	.0089053	1.0422
Numerical	125.26	47.61	.0091672	0.9688

CASE S45M174

	Pressure	Temperature	Density	Mach number
Theory	102.466	43.539	.0082	1.4653
Numerical	104.81	45.066	.00844	1.44

CASE S60M251

	Pressure	Temperature	Density	Mach number
Theory	98.67	43.05	.007986	2.2731
Numerical	99.70	43.68	.008156	2.249

CASES75M493

	Pressure	Temperature	Density	Mach number
Theory	97.35	42.48	.007910	4.63
Numerical	104.5	44.143	.008421	4.55

S75 M493
wedge sweep angle
design Mach number

flow parameters for each shape of the caret wing. For caret wings the results were based on a fixed aspect ratio with different sweep-back and corresponding wedge angle. Fig 3.11 illustrates the results for a 30° sweep angle. The design wedge angle and the shock angle were 9.76° and 60.53° respectively for this low Mach number case. Table 3.4 shows the theoretical and computational values outside the boundary layer for each case. These differences in values suggest the effect of viscous interaction e.g., for the 30° case the numerical values for pressure, temperature and density are higher than the inviscid values which correspond to a smaller Mach number than expected. Referring to fig 3.10 it is seen that the Mach number fell short of the on-design Mach number thus pushing the off-design behaviour towards region B. Therefore an attached curved shock wave is expected. A similar behaviour for the shock can be observed in fig 3.11.

The results for the 45° sweep are also summarized in table 3.4. A similar observation can be made here for having a higher pressure than theoretical for the design wedge and shock angle values of 8° and 43.26° respectively. For this later case, the temperature as well as density is high and the corresponding Mach number is low. Contour plots displaying all these parameters including viscous effects are given in fig 3.12.

The effect of viscous flow over sweep angles 60° and 75° cases is illustrated in figs 3.13 and 3.14. Comparison of the data from table 3.4 for these cases seems to reveal the same behaviour. Pressure and other values are slightly higher than theoretical e.g., for the 60° case, behind the shock wave, theoretical values for pressure, temperature and density are 98.67 Pa, 43.05 K, .007986 kg/m^3 as compared to numerical values of 99.7 Pa, 43.68 K, and 0.008156 kg/m^3, whereas the Mach number for numerical solution (M = 2.249) is lower than the theoretical Mach number (M = 2.2731). A similar observation can be made for the 75° swept caret wedge.

It can be seen from fig.3.13 and 3.14 that the shock waves are more close to their on-design patterns at high sweep angles and at high Mach numbers. This is because in the latter cases, the wedge angles (θ = 5.67 for 60° and 0 = 2.944 for 75°) are small. These correspond to weaker shock solutions, resulting in little significant effect on the shock behaviour. However due to a higher Mach number then a thicker boundary layer is

developed near the surface thus differentiating it from the inviscid phenomena. Practically speaking, in the presence of the boundary layer, a proper theoretical quantitative prediction of supersonic flow is difficult because in the presence of the boundary layer, the flow becomes complex and the best solution can be achieved by solving the full Navier Stokes equations. The difference of values for different flow parameters in computational and theoretical results for the caret wings suggests that for a final design study, viscous effects must be included at all design stages and must not be ignored as these effects are significant even if values of χ (table 3.3) are very small.

In reality, the presence of boundary layer thickness changes the effective geometrical shape of the caret wave-rider. Comparison of the computational contour plots (figure 3.11 to 3.14) with different curves in figure 3.10(1-4) shows that: for 30° and 45° sweep angles, off-design behaviour due to viscous effects shifts the shock pattern into region B; for 60° the on-design condition is retained; and for 75° region A behaviour is shown. Based on these observations it is suggested that for the final design of caret wings, to achieve the on-design behaviour including viscous effects, the operating Mach number should be adjusted or angle of attack changed or these effects included while generating the effective shape of the body.

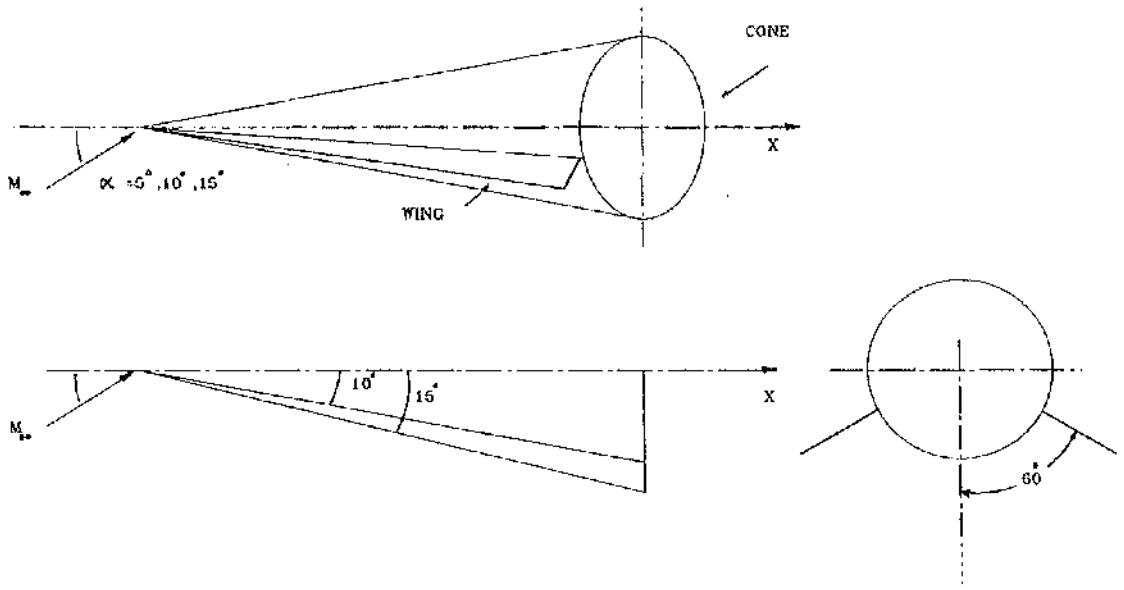

Fig. 3.15 Conical waverider model.

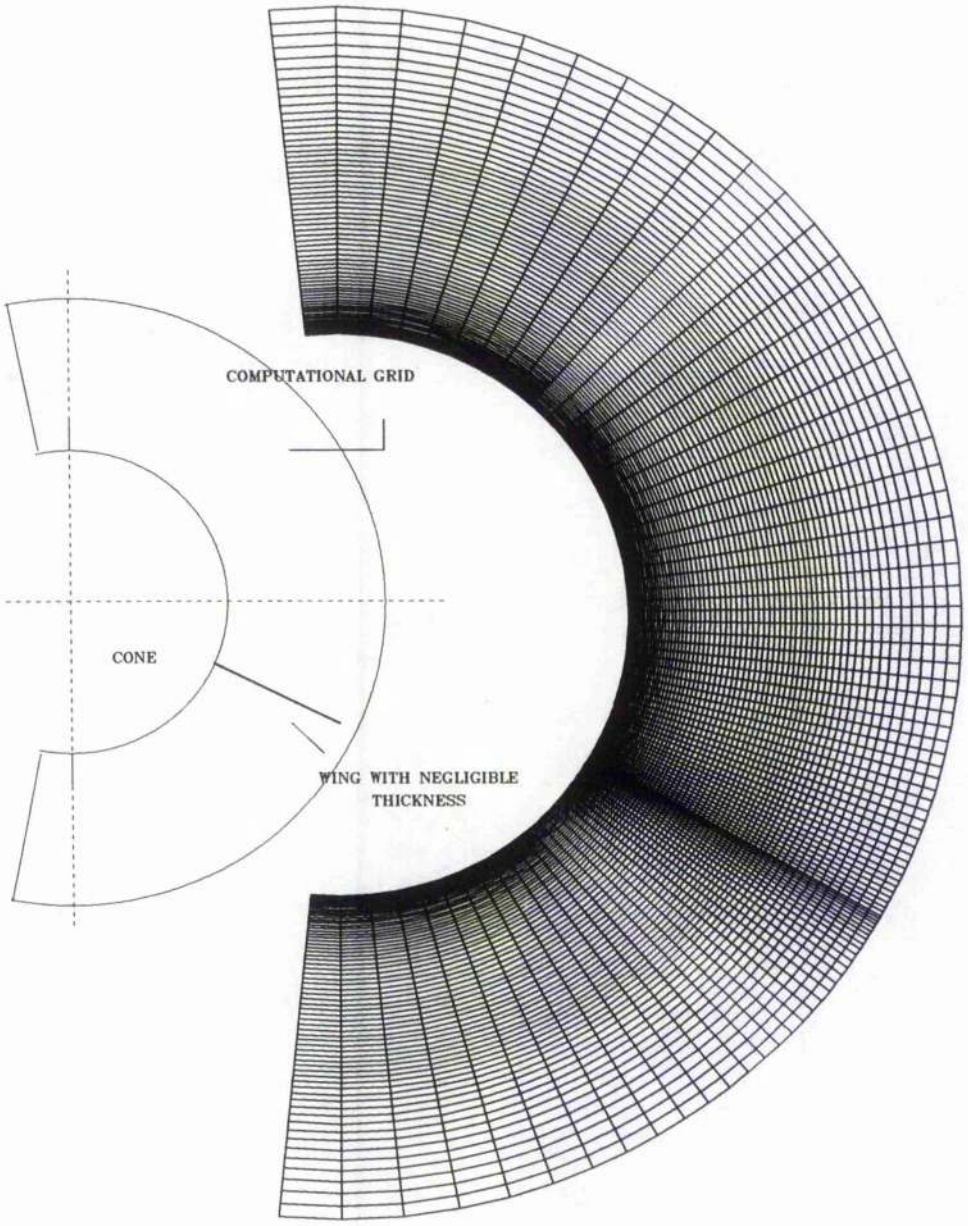

Fig. 3.16 Grid used for simulation.

3.5 Conical Waveriders.

3.5.1 Geometry of Models and Flow Conditions.

For caret wings the simulated data were compared with theoretical values because unfortunately no experimental data appeared available to validate the results for the different shapes studied. Also it was considered that there was less support for its usage by its critics resulting in the cone-delta-wing being considered more advantageous[54],[55] and likely to be used than a caret wing. Therefore a cone-delta-wing shown in fig(3.15) was chosen. For this configuration, experimental data [56] was available to validate simulation.

TABLE : 3.5

Flow conditions for simulations (cone-delta wing)

Cone angle = 20°
Location of wings = 30° anhedral
Sweep back angle = $\Lambda = 75$
$T_{\infty} = 64.69$ K
$T_w = 293$ K
$T_o = 500$ K
$P_o = 100$ psi $= 689.5\times10^3$ N/m^2 (Pa)
$P_{\infty} = 537.41$ N/m^2
$\rho_{\infty} = 0.028945$ kg/m^3
$U_{\infty} = 935.08$ m/s
M_{∞} = Mach number = 5.8
α = angle of attack = 5°, 10°, 15°
$\chi = .6172$
Re = Reynolds number = 991179

The model chosen consisted of a 20° cone with wings of negligible thickness with a sweep angle of 75° located at 60° from the plane of symmetry giving 30° wing anhedral. Flow conditions used for simulation are shown in table(3.5).

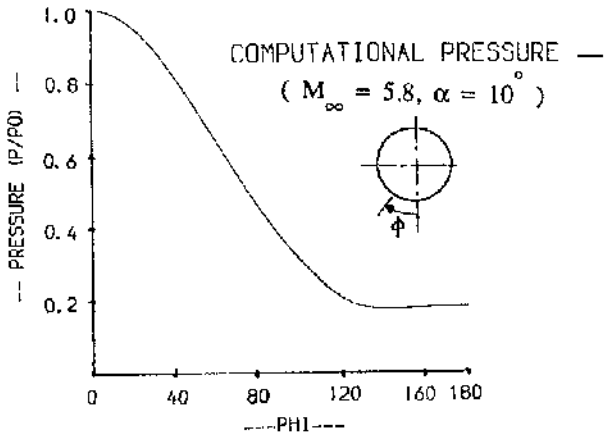

Fig. 3.17 Pressure distribution on cone surface.

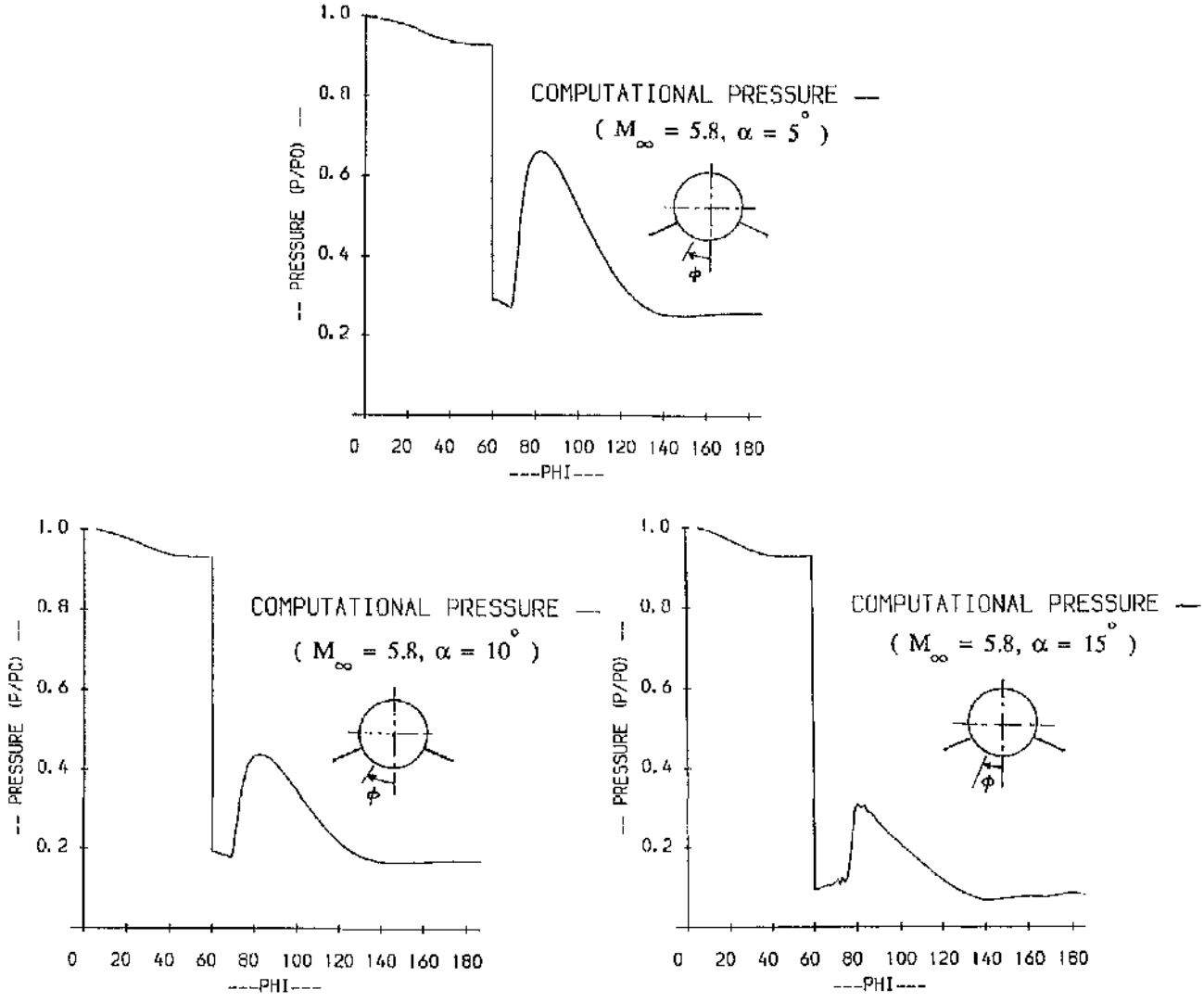

Fig. 3.18 Pressure distribution on cone surface (wing-cone waverider).

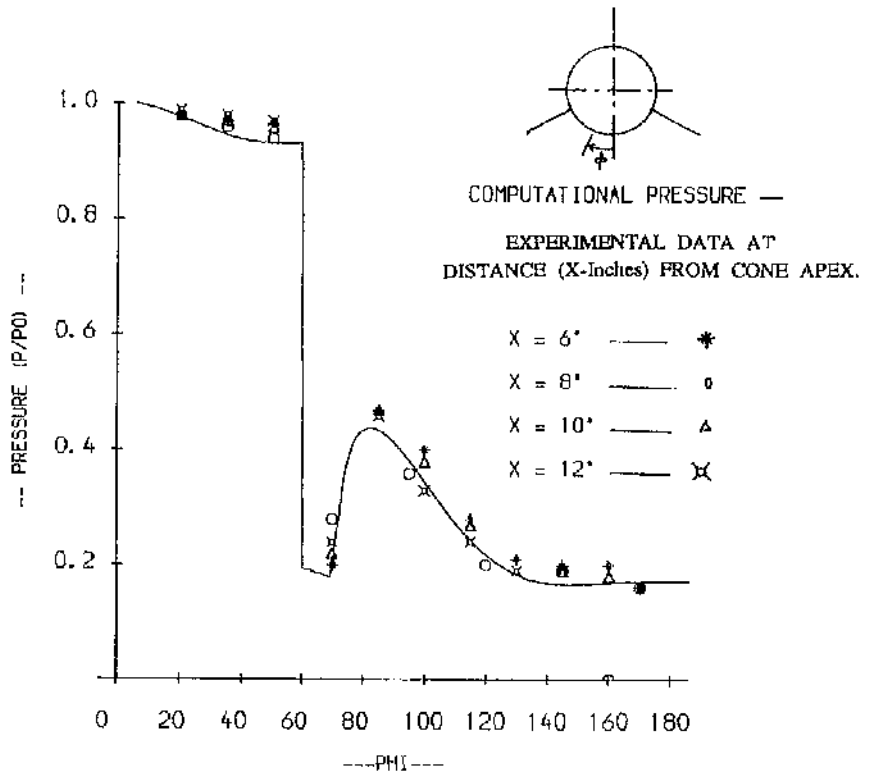

Fig. 3.19 Computational and experimental pressure on cone surface. (wing-cone waverider)

(Flow simulation around simple cone at $\alpha = 10^{\circ}$).

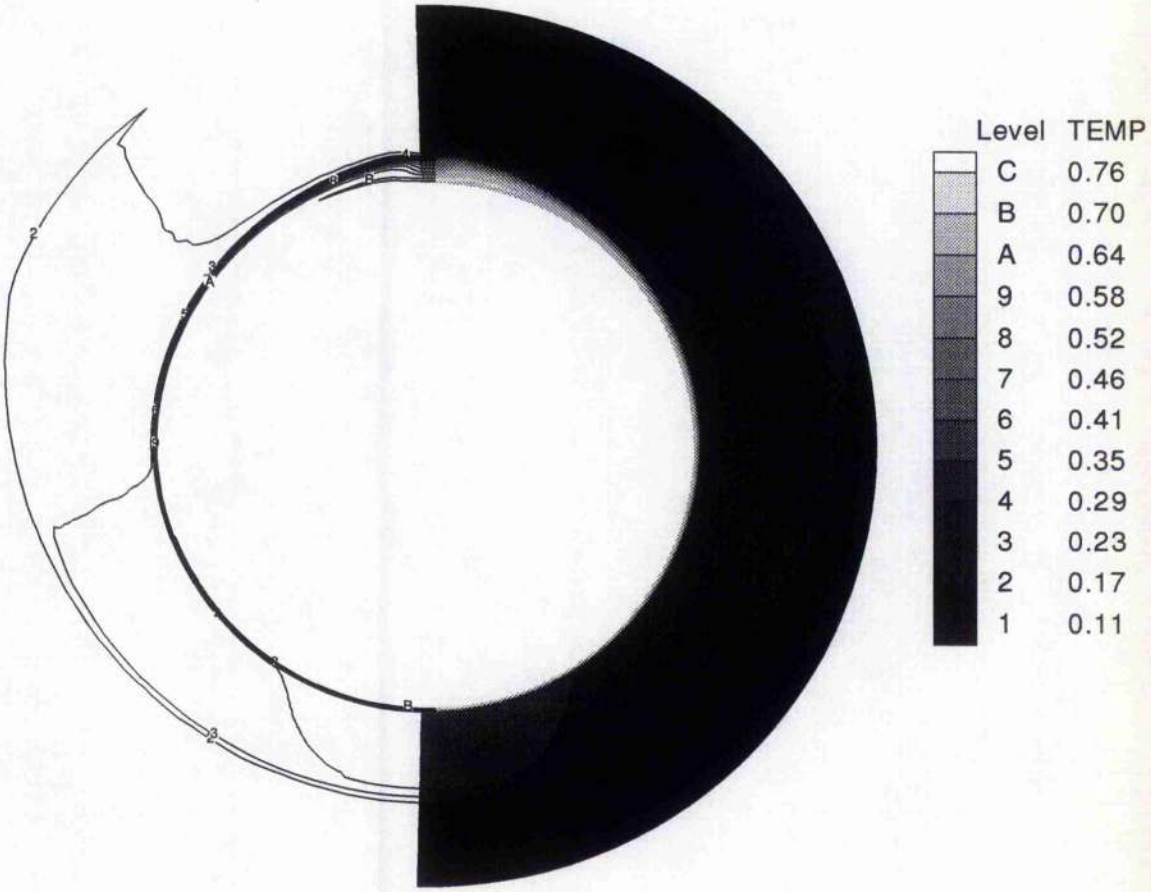

TEMPERATURE

Fig. 3.20a Flowfield contours, $\alpha = 10^{\circ}$, $M_{\infty} = 5.8$ (cone).

(Flow simulation around a simple cone at $\alpha = 10^{\circ}$).

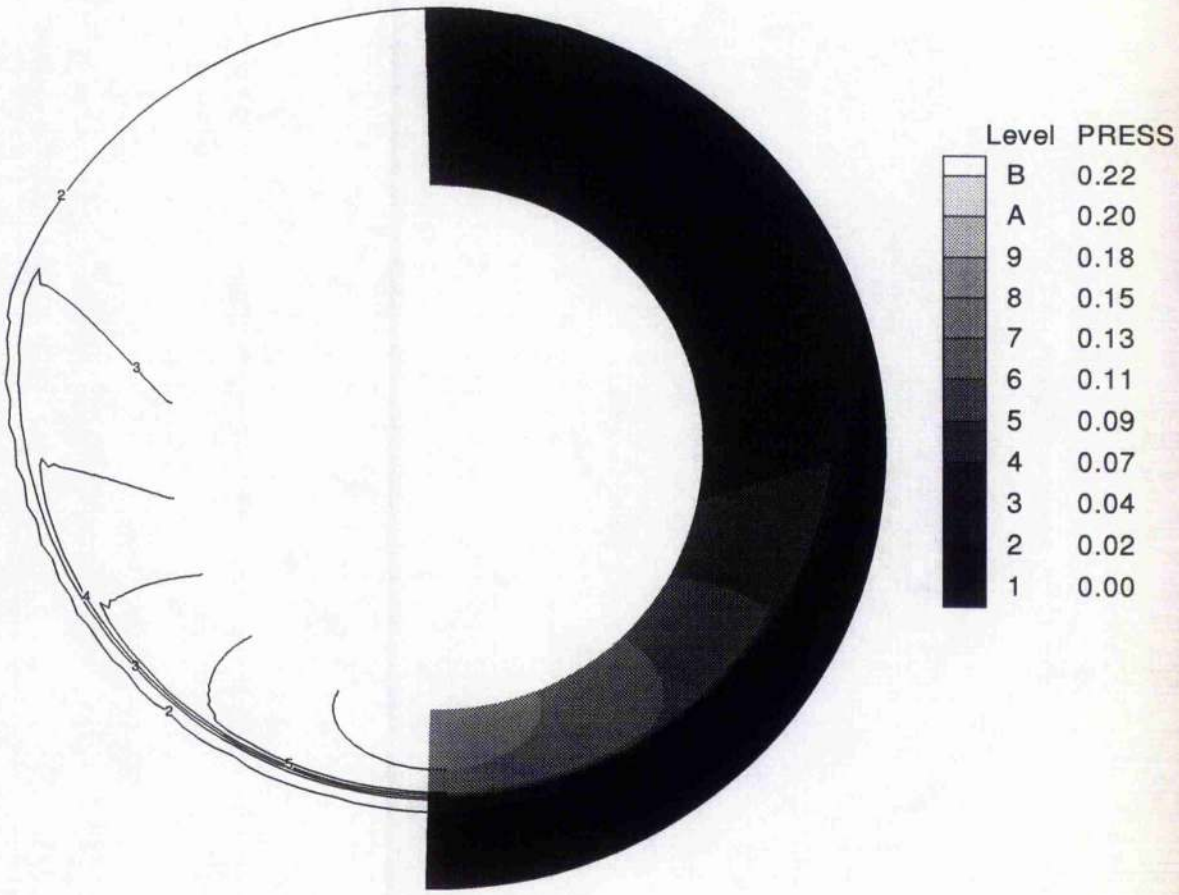

PRESSURE

Fig. 3.20b Flowfield contours, $\alpha = 10^{\circ}$, $M_{\infty} = 5.8$ (cone).

(Flow simulation around a simple cone at $\alpha = 10^{\circ}$).

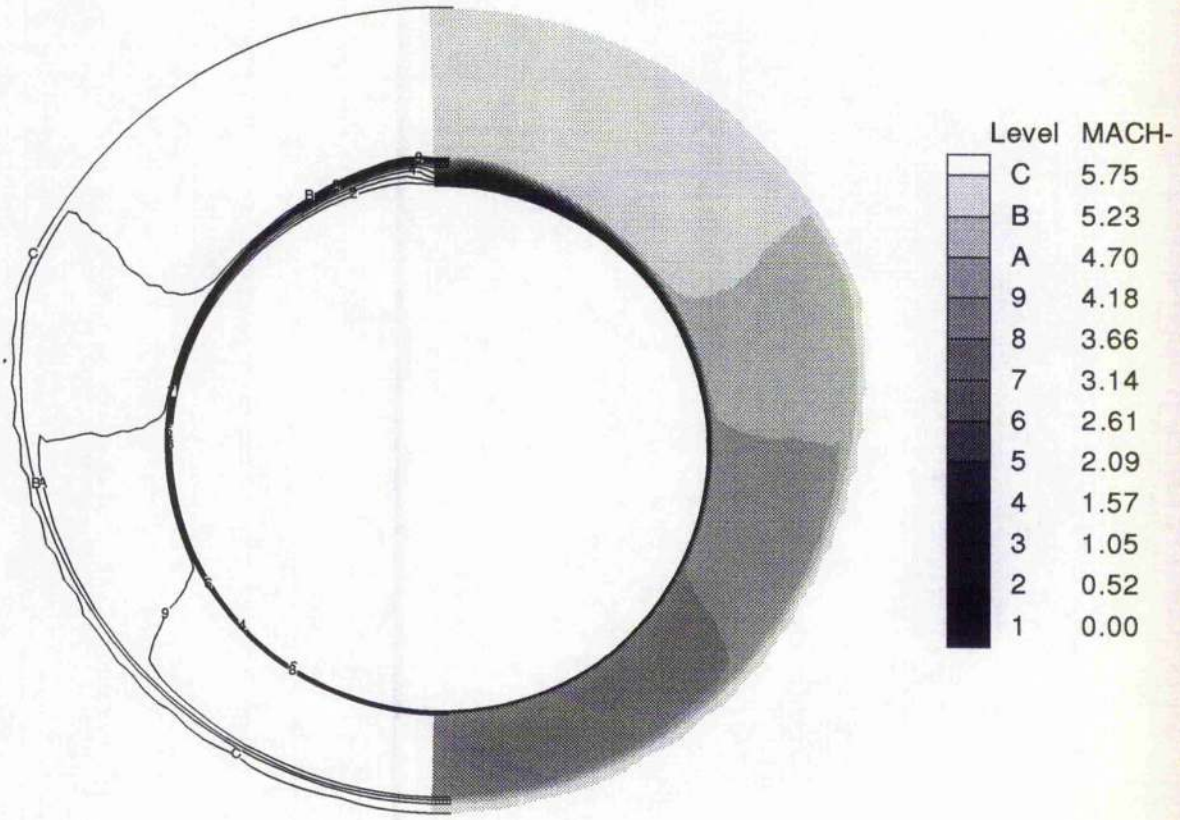

MACH NUMBER

Fig. 3.20c Flowfield contours, $\alpha = 10^{\circ}$, $M_{\infty} = 5.8$ (cone).

(Flow simulation around a simple cone at $\alpha = 10^{\circ}$).

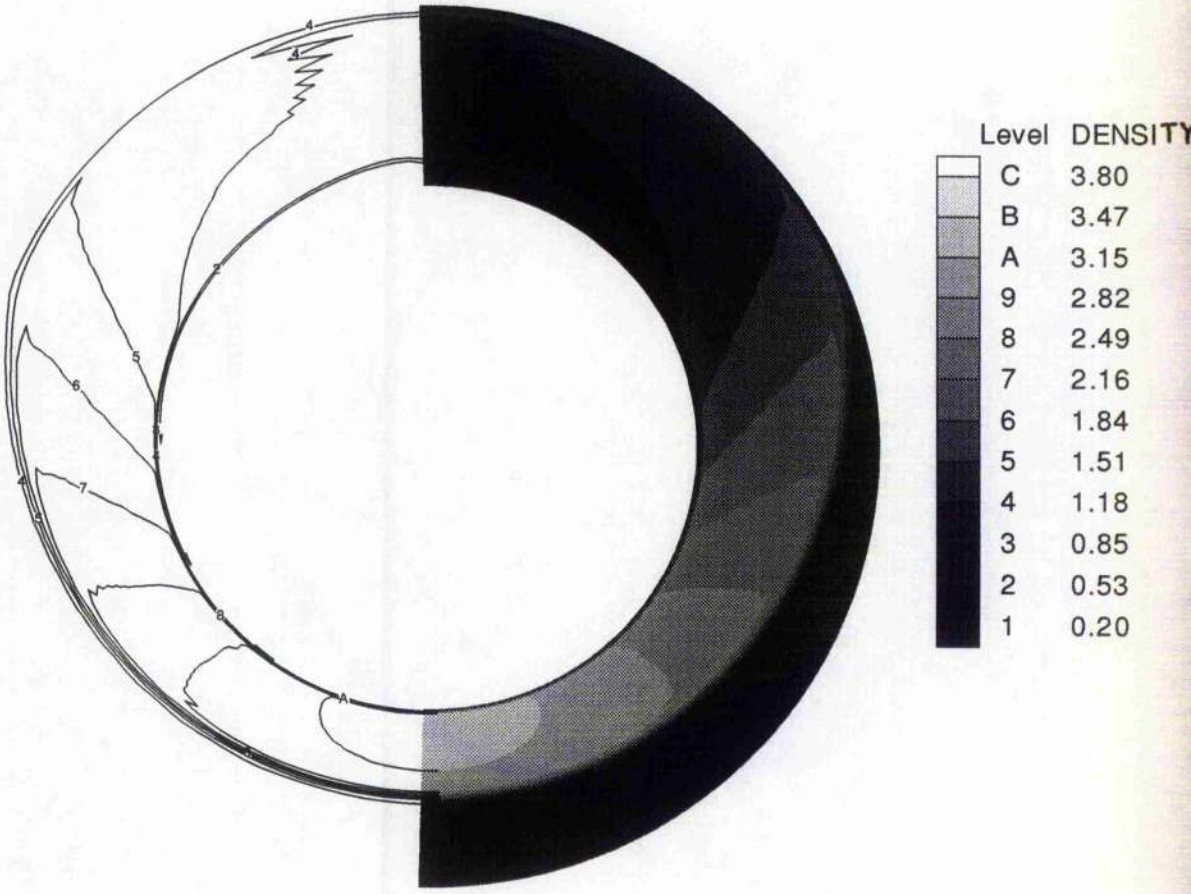

DENSITY

Fig. 3.20d Flowfield contours, $\alpha = 10^{\circ}$, $M_{\infty} = 5.8$ (cone).

3.5.2 Results and Discussions.

Results are presented for M = 5.8 and a Reynolds number of 0.991×10^6 with different angles of attack (5°,10°,15°). Contour plots at the station considered are also obtained for basic fluid properties e.g., pressure, temperature, density, Mach number and velocity to enable detailed insight of the fluid behaviour. The program was also run for different Reynolds numbers and it was observed that the pressure distribution is essentially independent of it. Results obtained are compared with experimental data for validation. Pressure results are also obtained for a simple cone at an angle of attack ($\alpha=10^\circ$) (ref fig. 3.17) to observe the difference without the presence of anhedral wing.

Fig(3.18) shows the pressure distribution on the cone surface for the wing-cone configuration at $\alpha = 5^\circ, 10^\circ$ and 15°. The pressure distribution demonstrates the advantage of anhedral interference due to the wing. In the windward region it remains almost constant on the surface of the cone from 0° to 60°. On the upper portion of the cone just above the wing a low pressure in the vortical region is observed. Further around the cone surface, the flow behaves similar to that over a simple cone without anhedral wings. Fig(3.19) also reveals the comparison between computational and experimental data at $\alpha=10^\circ$ which shows that the values agree quite well around the whole body.

Figures (3.21,3.23 and 3.25) show the contour plots of four flow parameters around the configuration at three different angles of attack. Each plot gives details of the flow field for the single fluid property. To observe the differences and advantages of a wing-cone combination, results for a simple cone are also shown in fig(3.20). Importance is given to the flow between the compressed surface and the shock wave. To reduce computing time results are restricted to a certain computational domain and do not cover the full expansion region. To cover the full expansion region computational domain may be extended. The general features for these flow simulations confirm that high constant pressure is achieved through capture of flow on the windward surface due to anhedral which also gives enhanced lift to the body.

(wing-cone waverider).

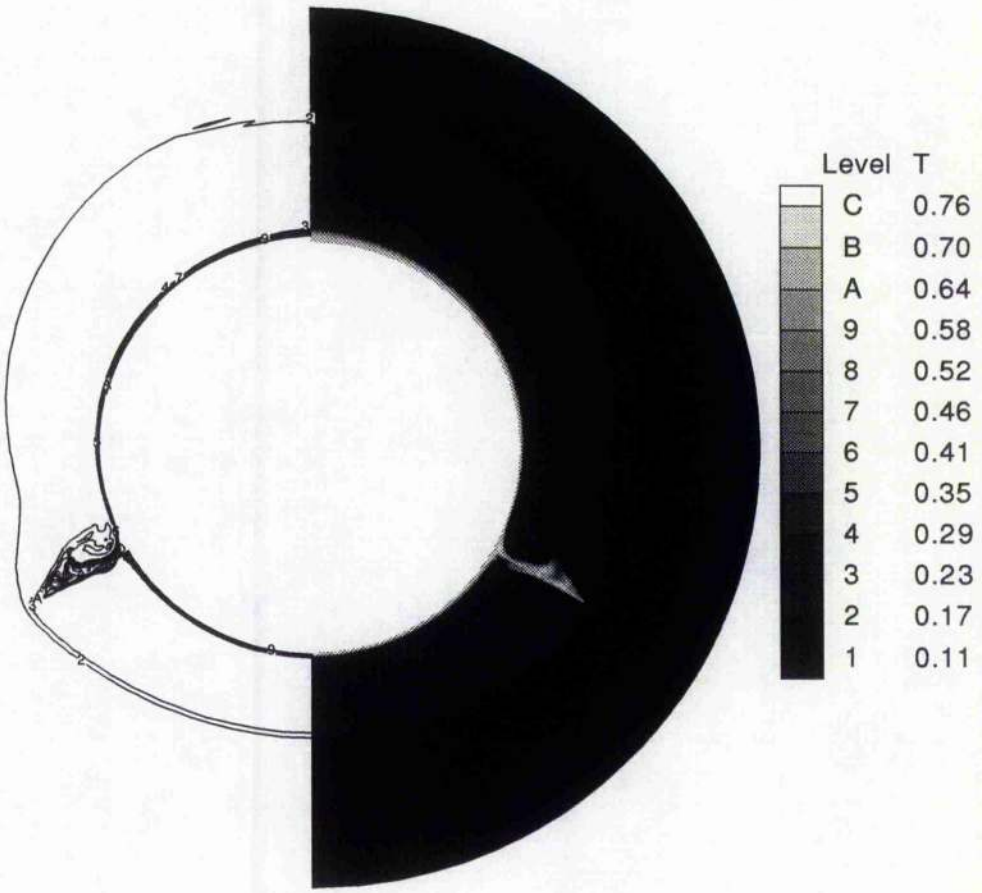

TEMPERATURE

Fig. 3.21a Flowfield contours, $\alpha = 5^{\circ}$, $M_{\infty} = 5.8$.

(wing-cone waverider).

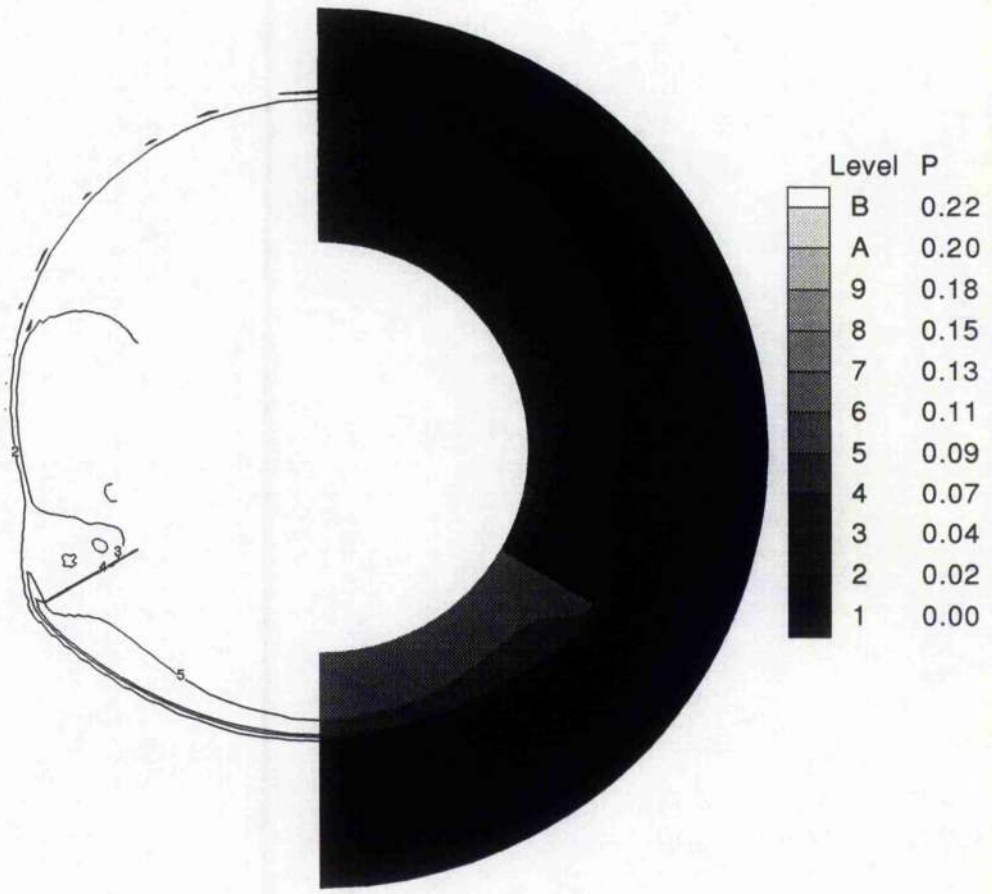

PRESSURE

Fig. 3.21b Flowfield contours, $\alpha = 5^{\circ}$, $M_{\infty} = 5.8$.

(wing-cone waverider).

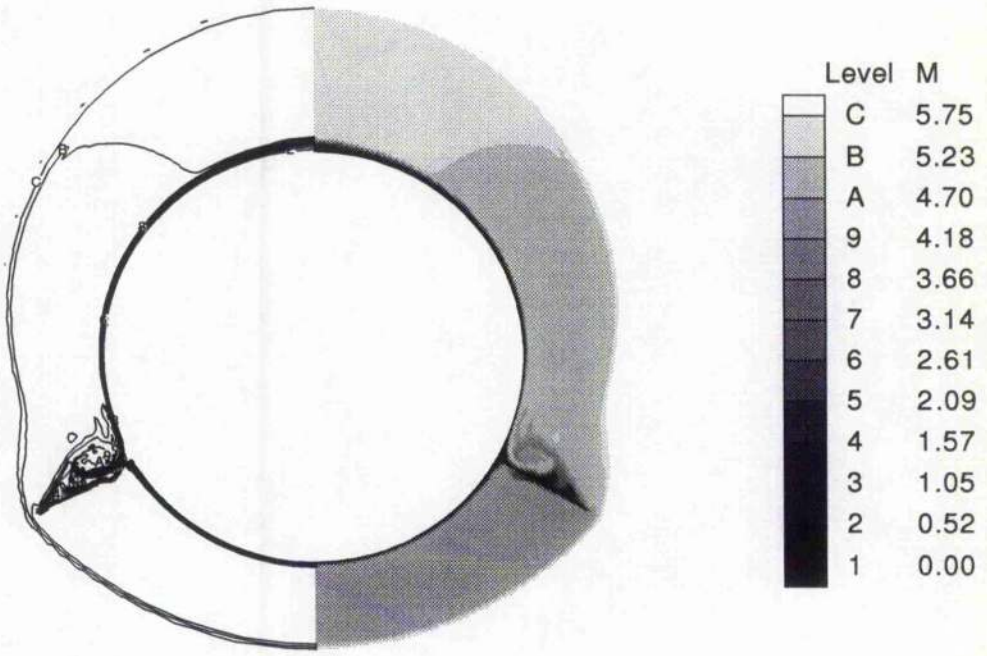

MACH NUMBER

Fig. 3.21c Flowfield contours, $\alpha = 5^{\circ}$, $M_{\infty} = 5.8$.

(wing-cone waverider).

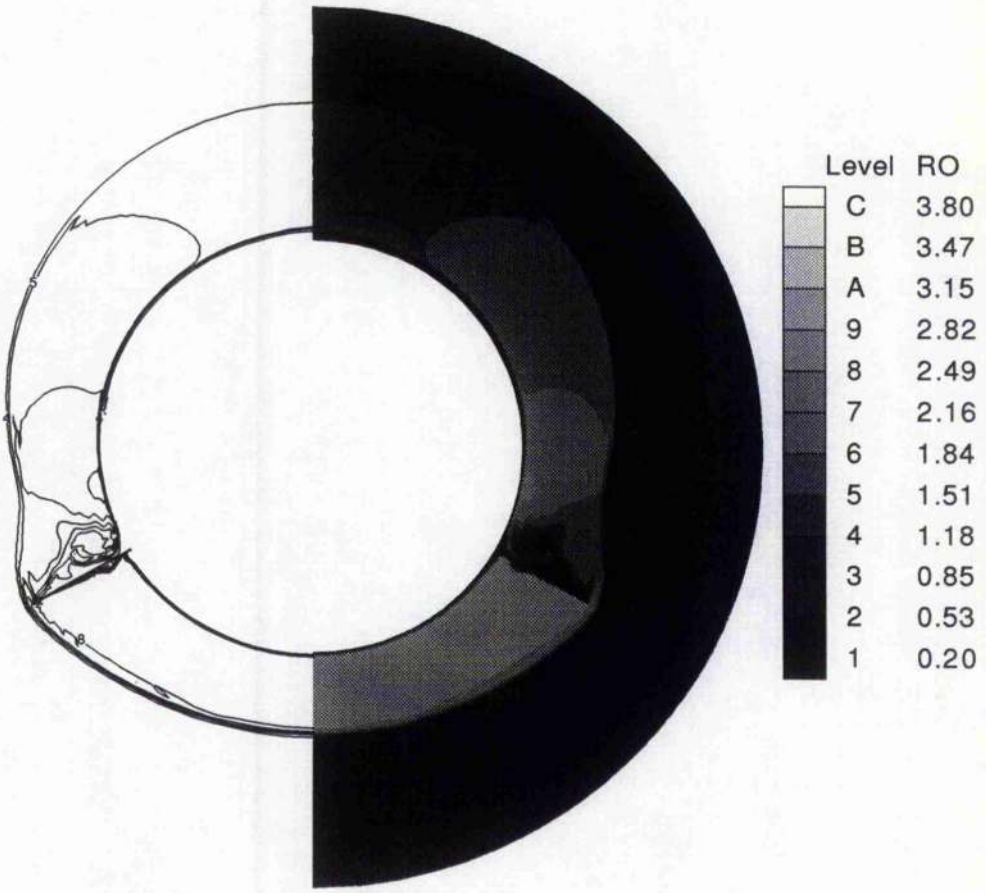

DENSITY

Fig. 3.21d Flowfield contours, $\alpha = 5^{\circ}$, $M_{\infty} = 5.8$.

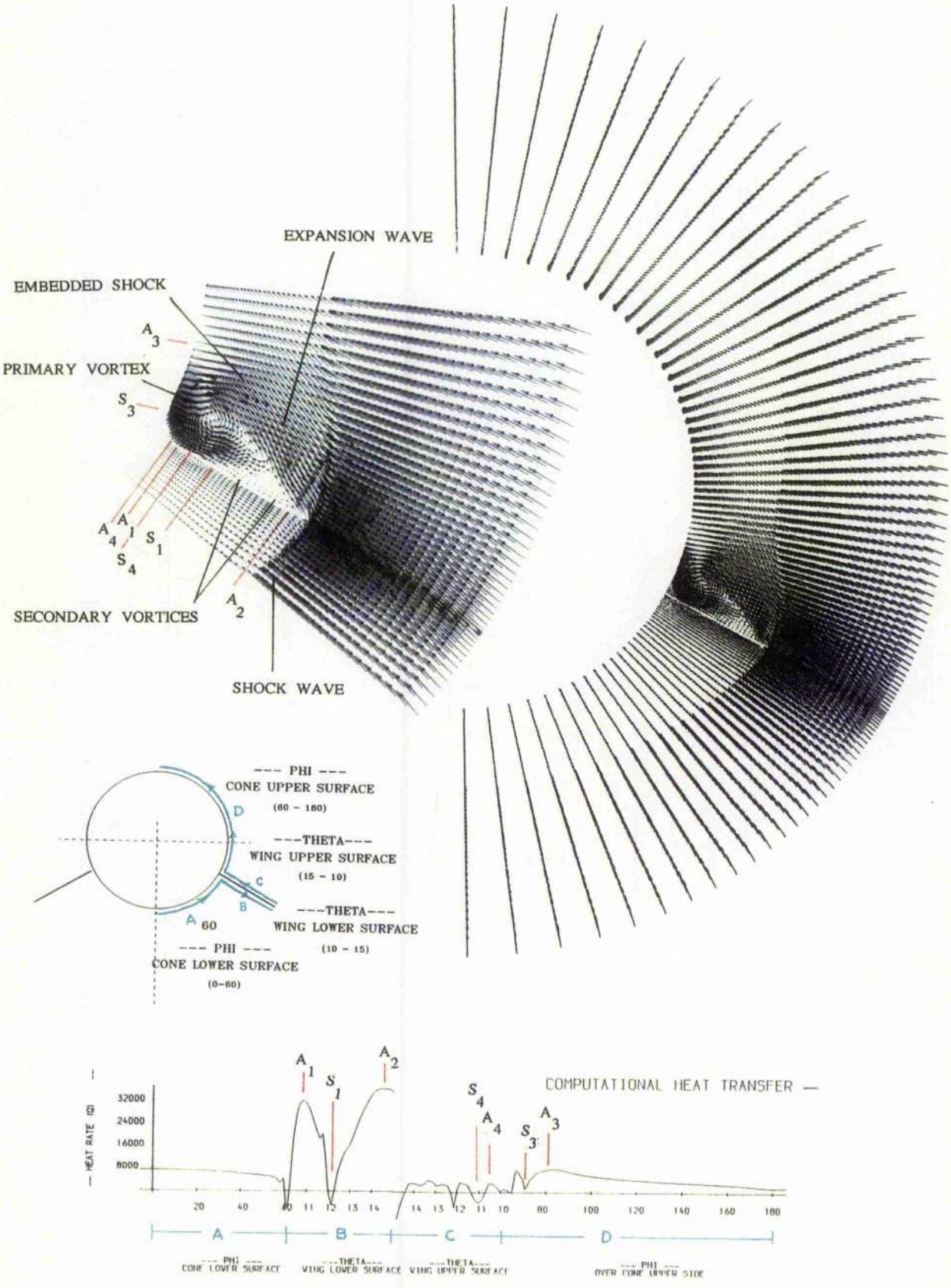

Fig. 3.22 Velocity vectors, $\alpha = 5^{\circ}$, $M_{\infty} = 5.8$ (wing-cone waverider).

The effect of the angle of attack on the fluid behaviour around the body is illustrated in figs (3.21 to 3.27). In the foregoing figures, what appears to be flow changes in front of the shock wave are purely due to changes in grid spacing and difficulties in communicating this highly resolved data. There are indeed constant conditions calculated upstream of shock. Figs (3.22,3.24,3.26) show the resultant velocity vector plots at 5°, 10° and 15° angles of attack respectively.

In fig(3.22) for $\alpha=5^{\circ}$, the shock layer due to the cone and wing creating the high pressure can be seen very clearly. On the upper surface of the wing near the corner the separated flow forms a strong vortex. Generally on the windward side a uniformly high pressure can be observed on the cone and wing lower surfaces with no particular flow features except for a small vortex near the junction which does however create a localized heating on reattachment. On the upper surface, apart from the primary vortex, a bow shock wave, an expansion wave and two other small secondary vortices also appear. Referring to the cross flow velocity vector plots the above regions can be marked and identified and heat transfer over the surface can be related to this flow picture e.g., the above mentioned small vortex on the windward side can be seen separating near the wing-cone junction and attaching itself at A_1, causing a high local heating. It further separates at point S_1. It can also be observed that the flow is attached to the lower side of the wing near the leading edge at A_2. It is interesting to note here that the localized heating at A_1 (fig 3.27) is as severe as near the leading edge. On the upper surface of the wing the primary vortex separates at S_3 and reattaches to the cone surface at A_3. On the wing surface this vortex separates at S_4 and attaches at A_4. The corresponding behaviour for these reattachments and separations can also be observed in the heat distribution where all peaks relate to attachment points and crests to separation points. Zero heat transfer rates are shown in fig(3.27) in the vicinity of the wing leading edge. These are considered to be in error because the grid sizing at the sharp leading edges is insufficiently fine in order to be able to capture accurately the flow processes and thus to obtain accurate heat transfer information.

Near the leading edge, the effect of the expansion wave on the cone shock wave is also shown. It is observed that for a low angle of attack

(wing-cone waverider).

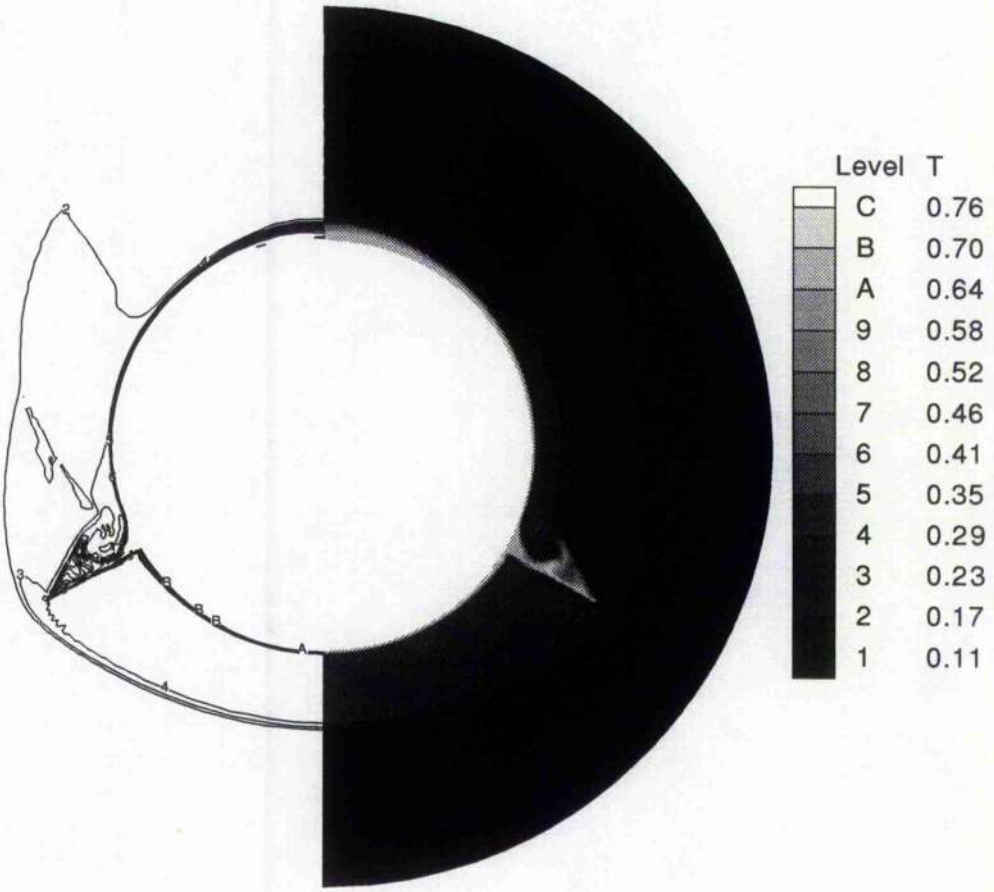

TEMPERATURE

Fig. 3.23a Flowfield contours, $\alpha = 10^{\circ}$, $M_{\infty} = 5.8$.

(wing-cone waverider).

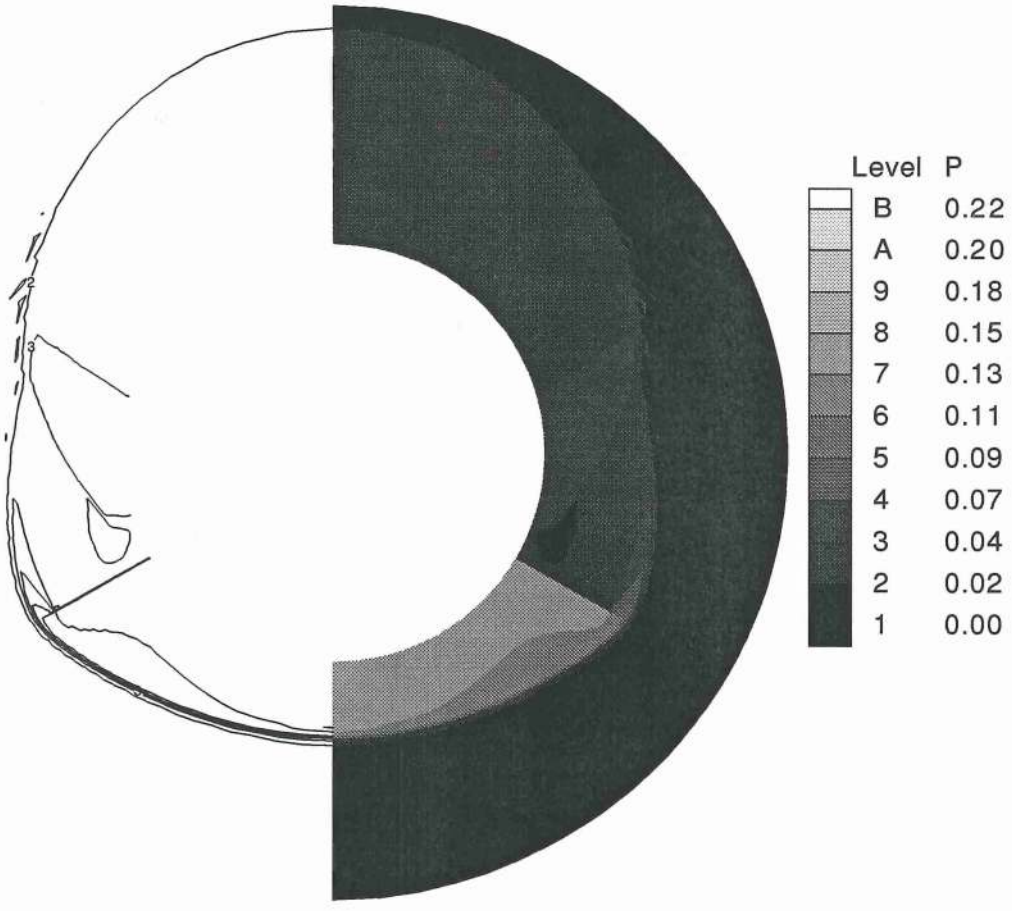

PRESSURE

Fig. 3.23b Flowfield contours, $\alpha = 10^{\circ}$, $M_{\infty} = 5.8$.

(wing-cone waverider).

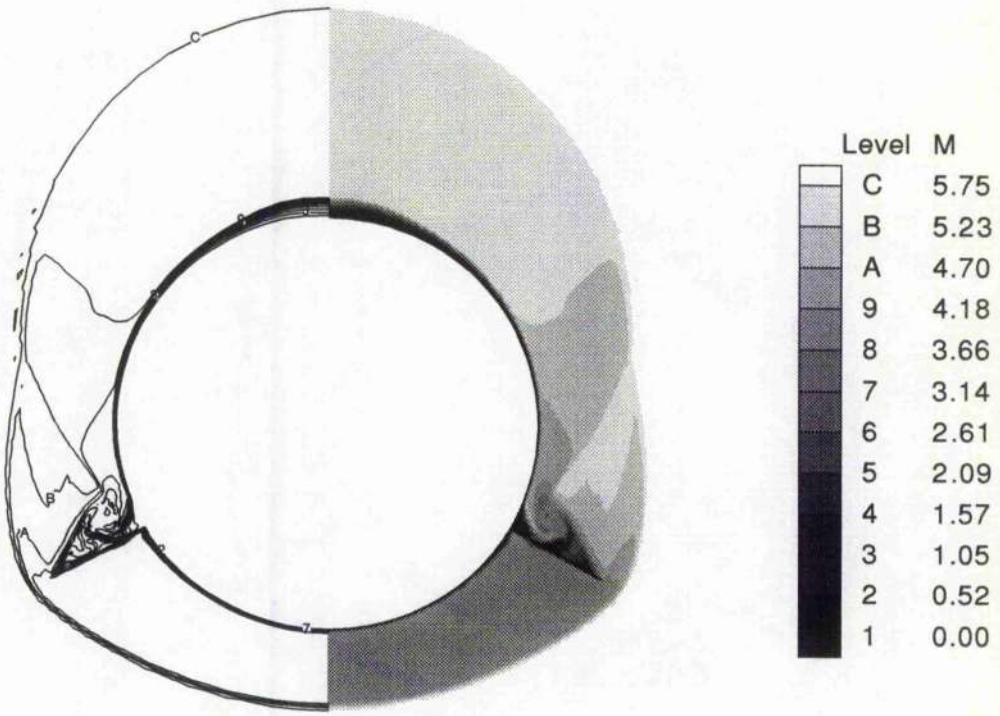

MACH NUMBER

Fig. 3.23c Flowfield contours, $\alpha = 10^{\circ}$, $M_{\infty} = 5.8$.

(wing-cone waverider).

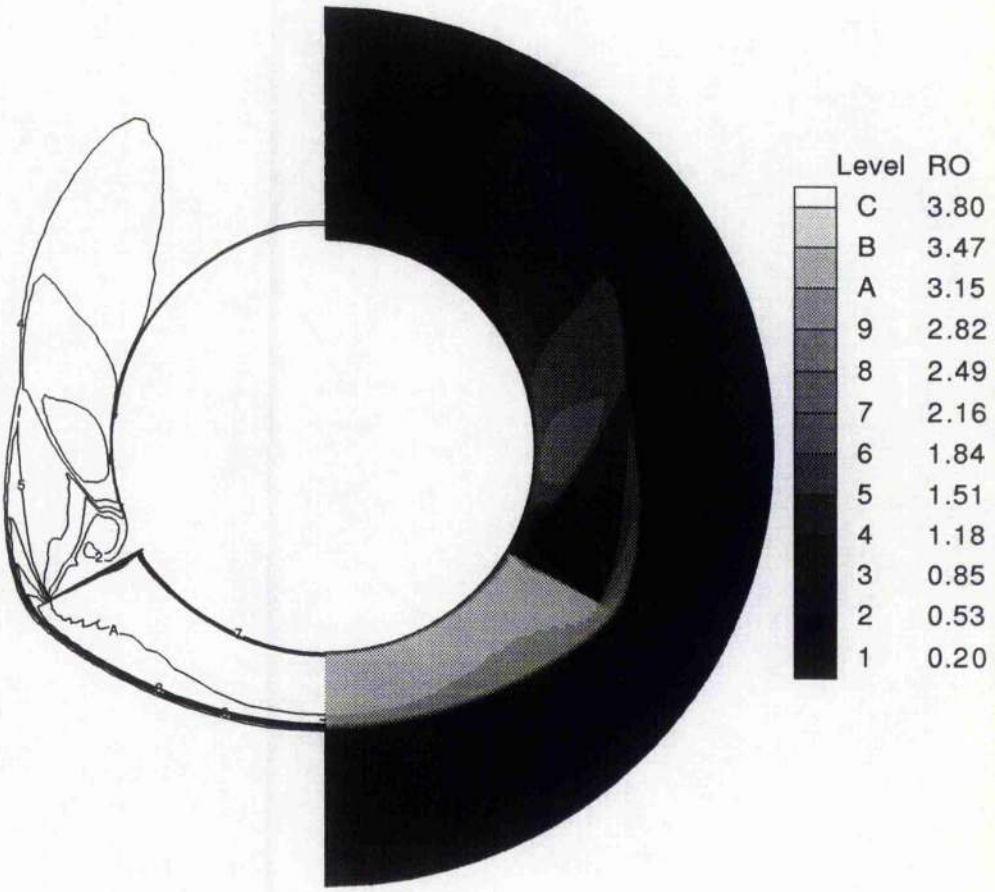

DENSITY

Fig. 3.23d Flowfield contours, $\alpha = 10^{\circ}$, $M_{\infty} = 5.8$.

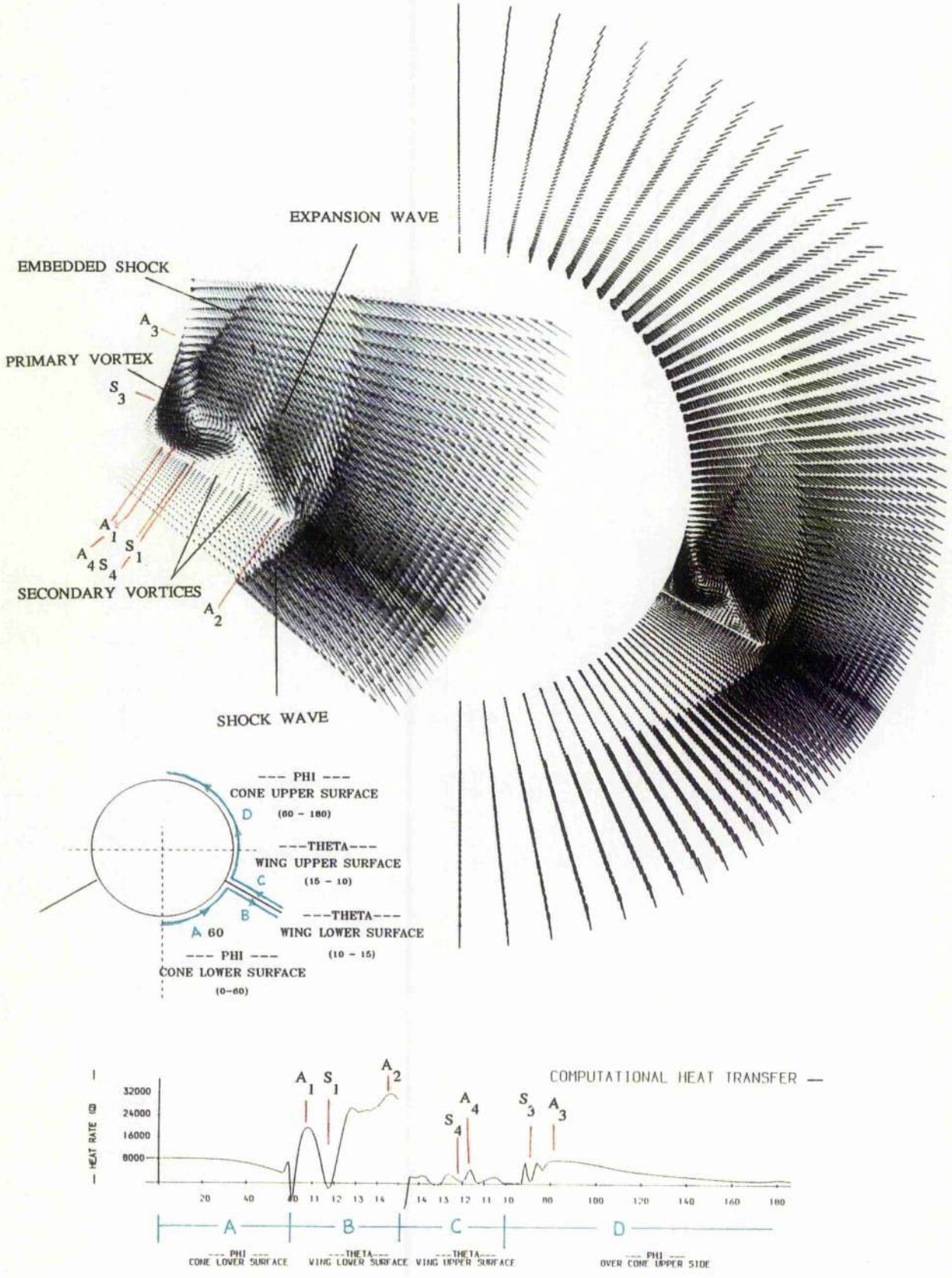

Fig. 3.24 Velocity vectors, $\alpha = 10^{\circ}$, $M_{\infty} = 5.8$ (wing-cone waverider).

(wing-cone waverider).

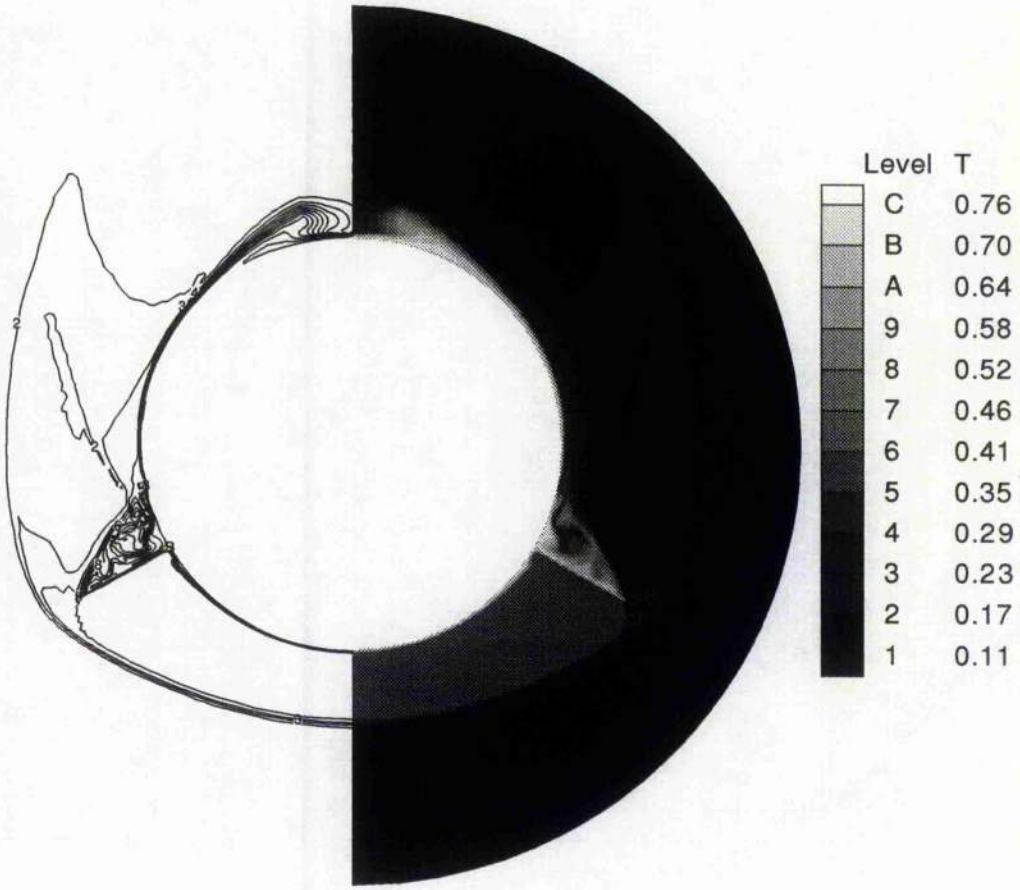

TEMPERATURE

Fig. 3.25a Flowfield contours, $\alpha = 15^{\circ}$, $M_{\infty} = 5.8$.

(wing-cone waverider).

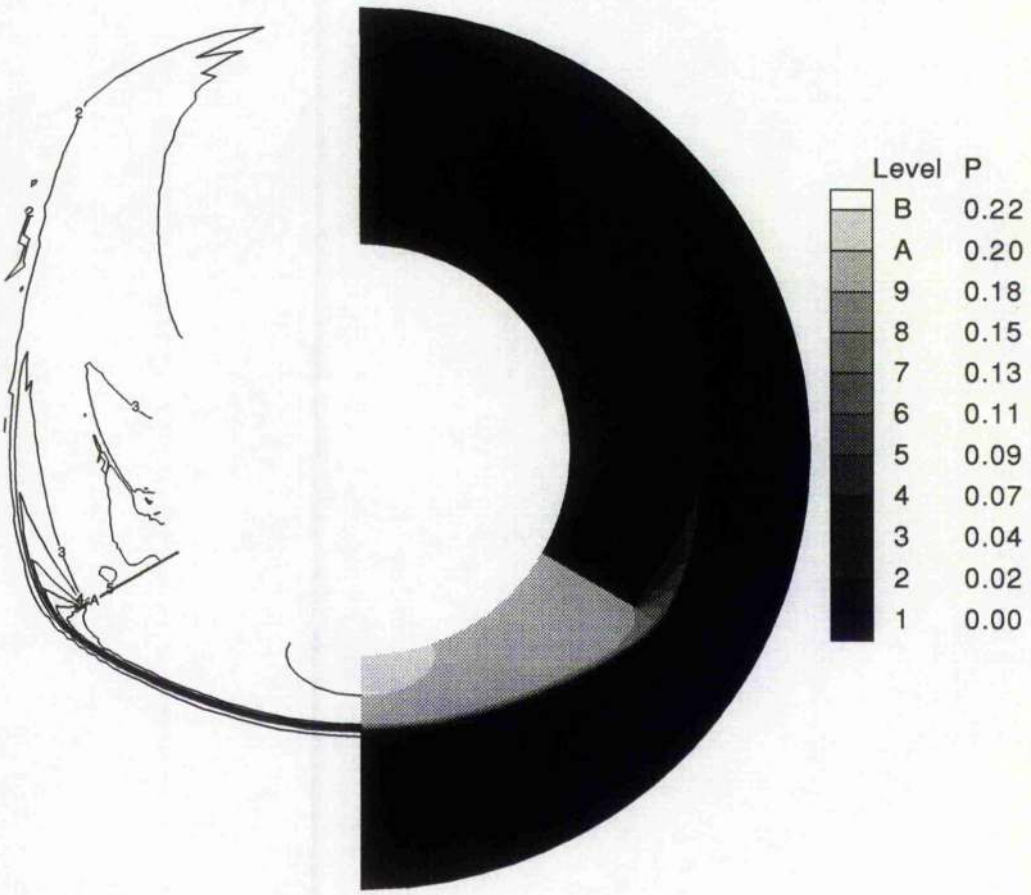

PRESSURE

Fig. 3.25b Flowfield contours, $\alpha = 15^{\circ}$, $M_{\infty} = 5.8$.

(wing-cone waverider).

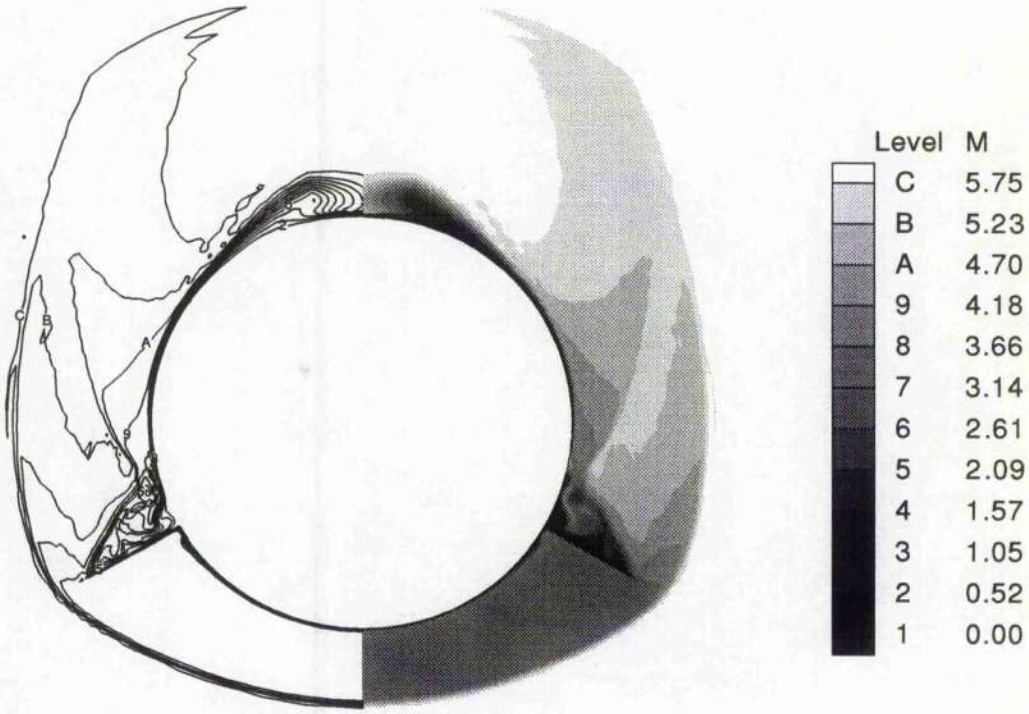

MACH NUMBER

Fig. 3.25c Flowfield contours, $\alpha = 15^{\circ}$, $M_{\infty} = 5.8$.

(wing-cone waverider).

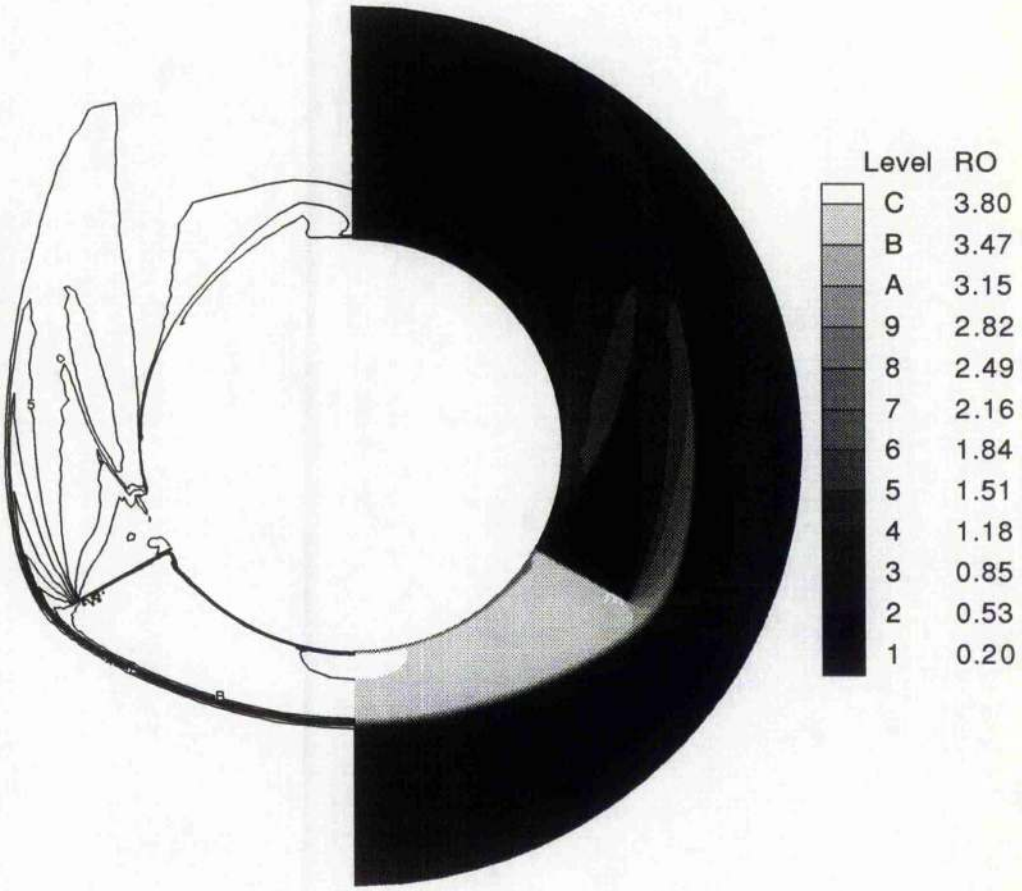

DENSITY

Fig. 3.25d Flowfield contours, $\alpha = 15^{\circ}$, $M_{\infty} = 5.8$.

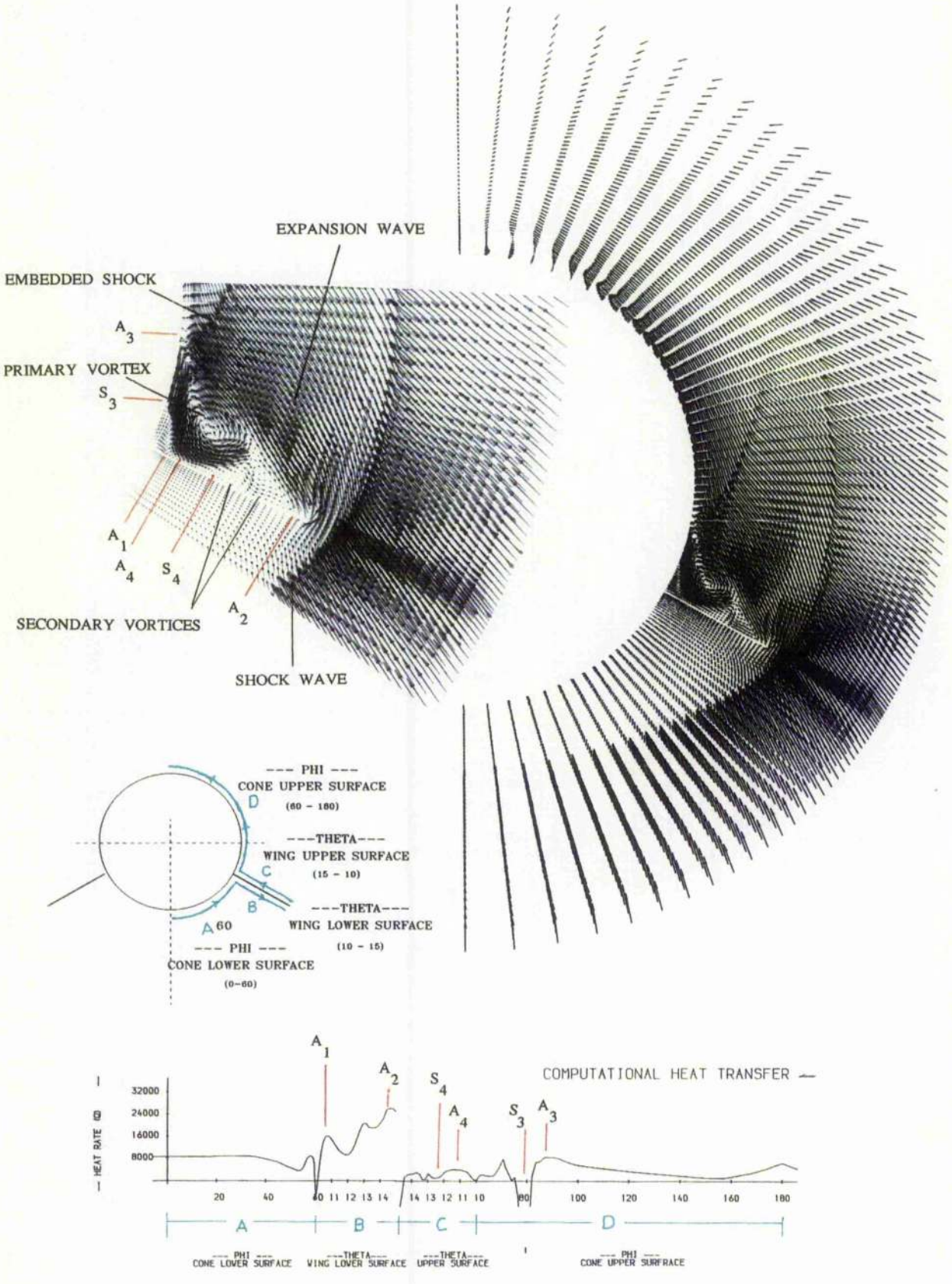

Fig. 3.26 Velocity vectors, $\alpha = 15^{\circ}$, $M_{\infty} = 5.8$ (wing-cone waverider).

these effects diminish after a few degrees and furthermore only a cone shock can be seen. The local variation and behaviour in any fluid parameter such as density, pressure, temperature and Mach number due to the above phenomena at each point are illustrated in figs 3.21(a-d).

Fig 3.24 reveals the effect on the fluid due to an increase in α to 10°. Here, on the windward side, the cone shock can be seen moving close to the cone surface. All the features explained earlier are present with a slight change. On the wing-cone under surface a high pressure can be detected. Near the wing-cone junction a small vortex due to a cone wing boundary layer interaction is present however the intensity of it is reduced at attachment A_1, but the local high heat rate remains present. Near the leading edge the shock is slightly detached and on the upper portion where the expansion wave merges with the primary vortex an embedded shock originates. On increasing the angle of attack the pressure increases on the windward side but decreases on the leeward side (fig 3.18). At the high angle of attack case two secondary vortices are more visible. Referring to this discussion, the effect on temperature, pressure, density and Mach number at $\alpha = 10^{\circ}$ can be deduced from fig 3.23.

Fig 3.26 in conjunction with fig 3.25 illustrates the further propagation of flow phenomena at 15° angle of attack. At this much higher angle the flow still retains its major properties and a constant high pressure exists on the wing-cone surface in the windward side behind a strong shock. The shock wave can be seen detached from the leading edge. On the upper surface the cone shock becomes weak and merges into an expansion wave. Other distinct characteristics of the flow such as primary and secondary vortices, and the embedded shock are shown clearly in fig 3.25. A boundary layer is developed on the cone surface which reattaches around the primary vortex and separates at about 160° from the plane of symmetry. The effect of the flow on the surface at reattachment points can be assessed by observing the heat transfer distributions in fig 3.27. Care again should be taken about the inaccuracies near the wing leading edge noted earlier. Individual flow parameters for this case are summarized in fig 3.25.

Fig 3.28 shows the numerical results for C_L and C_D at different angles of attacks. Results are obtained by integrating the pressure data over the

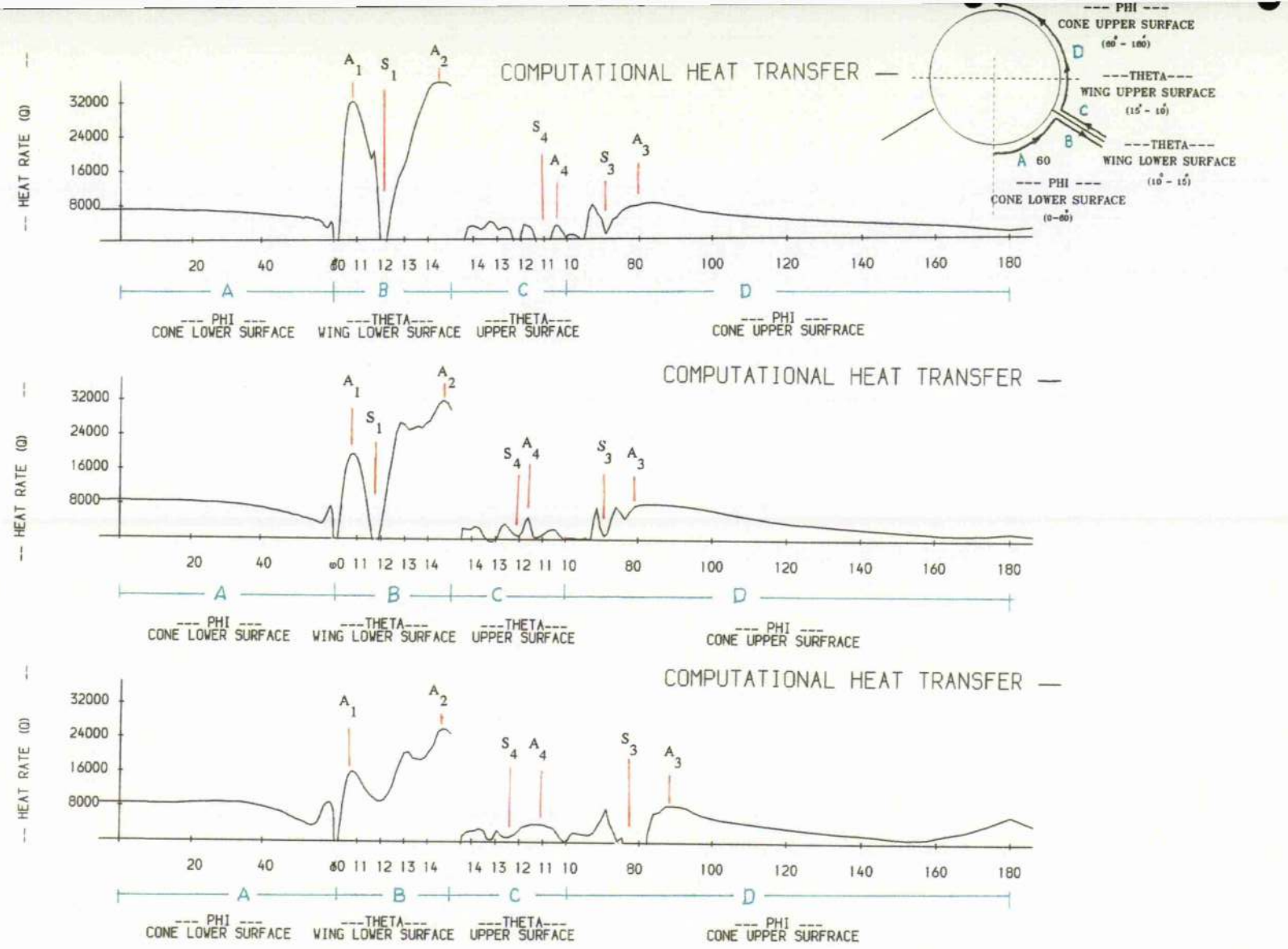

Fig. 3.27 Heat transfer over wing-cone waveriders.

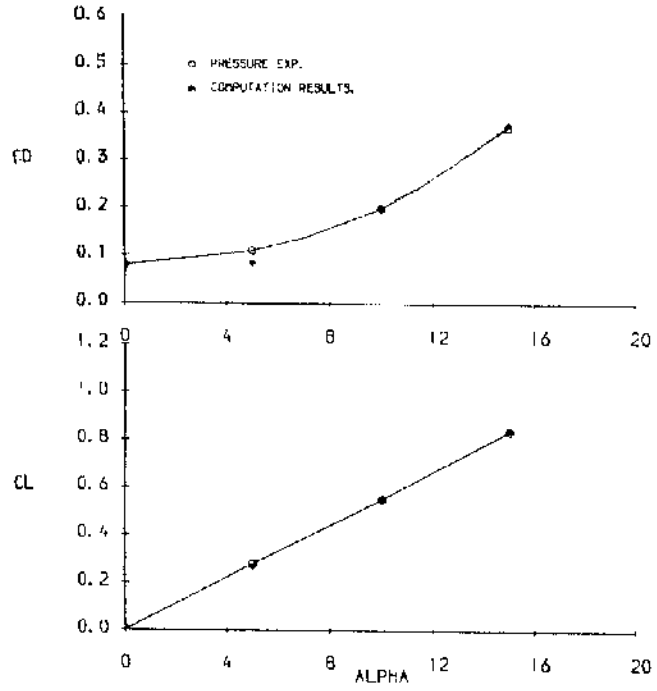

Fig. 3.28 Lift and drag coefficients vs angle of attack.

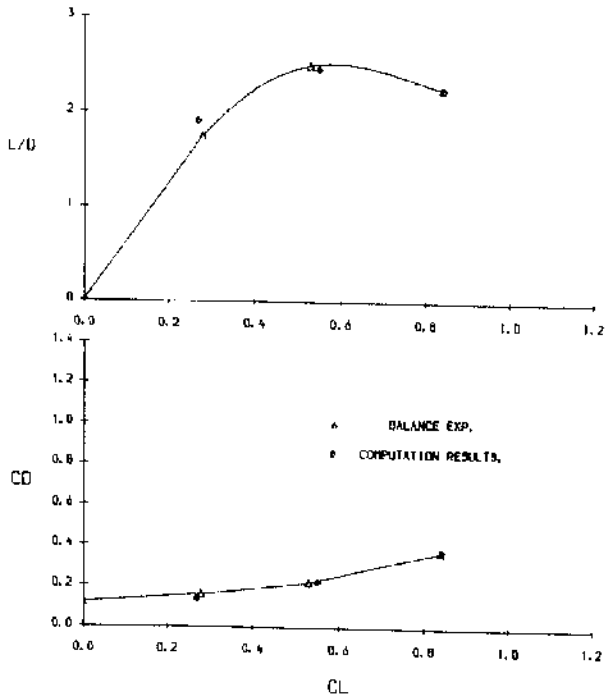

Fig. 3.29 Drag coefficient and lift-drag ratio vs lift coefficient.

surface. Comparison of these results with experimental values are quite good. Results are also presented for C_L vs C_D and C_L vs L/D. In fig 3.29 C_D is the total drag coefficient which, apart from pressure drag, includes viscous and base drag. Viscous drag is calculated from skin friction values through the Eckert reference enthalpy method and the base drag coefficient is taken as 0.04 at $\alpha = 0^{\circ}$ and zero at $\alpha=15^{\circ}$. The calculations are based on the result from one station only. Results are reasonably accurate and a further improvement in accuracy will arise from by using data resulting from the implementation of calculations at different stations. Similarly for a better prediction of skin friction drag, which is 15% of original drag at $\alpha=0^{\circ}$, the more accurate values for shear stress should be used at each station. Also, for the base drag which is shown to be 33% of the total drag, a complete Navier Stokes solution around the full body is required for proper prediction.

FLOW AROUND ARBITRARY SHAPE WAVERIDERS.

4.1 Introduction

The last chapter concerned the flow over idealized waveriders exemplified by the caret wing and the cone-wing combination. The calculated phenomena for these shapes revealed interesting results at zero incidence and at different angle of attacks. These calculations have limited applicability for practical aircraft shapes, but nevertheless provide some initial understanding of the problems concerned with the inclusion of viscous effects.

For the construction of more general shapes, the same approach may be extended to bodies derived from two dimensional flows with shocks. Such an approach was attempted in part by Townend[4,5], Flower[15] & Pike[57]. The advantage of this approach is that it opens up a wider choice of body shape to the designer of hypersonic vehicles. This will allow different stability and volumetric constraints to be removed more easily.

For the waverider concept, there are a multitude of possible configurations which produce the same shock shape but a compromise needs to be made to produce a high contained pressure, hence high lift, whilst retaining favourable volumetric and stability characteristics. Apart from developing the configuration from a wedge flow (caret wing), conical flow has also been used as a basis to construct waverider shapes. Jones, Wood[20,58], Jones, Moore, Pike and Roe[21] provides examples of the latter. In the recent past Rasmussen[24] and Anderson[26,31] and their co-workers have extended these ideas to the design of high speed lifting vehicles.

The study presented in this chapter is based on this approach except that even more general shapes are constructed using both conical and wedge flow fields. A numerical approach has been developed to construct these waveriders. Comparisons have been made to evaluate the advantages and disadvantages of each type of configuration generated. Results are discussed in the light of numerical predictions and from experimental results on conical and wedge derived waveriders.

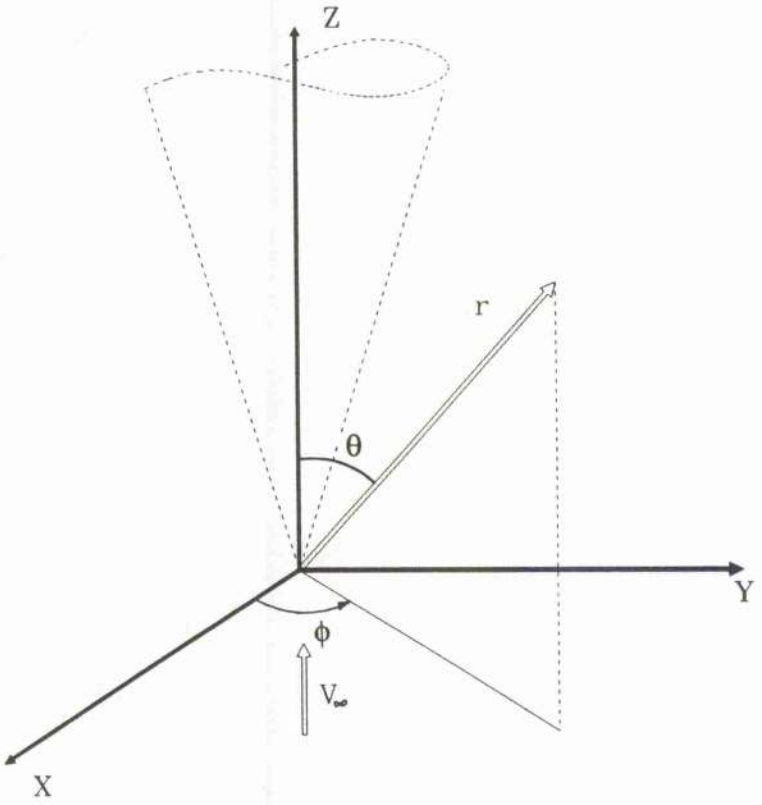

Fig. 4.1 Cone system in spherical coordinates.

4.2 Numerical Method and Solution Scheme.

It is appropriate to use conical flow as the basic flow for waveriders, since not only do hypersonic vehicles and missiles have a cylindrical shape, but also conical flow has been well documented in the literature. The work by Taylor and Maccoll[59] is the first such calculation for the flow around a cone and is used as a basis in this approach.

When applying the conical flow calculations to a waverider, the Mach number of the free stream and the cone vertex angle are such that the resulting shock wave is attached to the cone vertex and may be represented by a right circular cone, co-axial with the cone inserted in the flow. The flow can be seen to be symmetric around the cone axis.

The configuration is illustrated in fig (4.1). Now since the Z-axis is the axis of symmetry, for an axisymmetric or quasi 2-Dimensional flow,

$$\frac{\partial}{\partial \phi} \equiv 0 \qquad \text{(Axisymmetric flow)} \qquad ...(4.1)$$

$$\frac{\partial}{\partial r} \equiv 0 \qquad \text{(Conical flow)} \qquad ...(4.2)$$

and thus, when the flow is independent of ϕ, provided the semi vertex angle is not greater than the shock detachment angle, there will be a conical shock wave attached to the apex of the cone.

Therefore, the continuity equation can now be written as

$$\nabla.\rho V = 0$$

or, in polar co-ordinates,

$$\nabla.(\rho V) = \frac{1}{r^2}\frac{\partial}{\partial r}(r^2 \rho V_r) + \frac{1}{r\sin\theta}\frac{\partial}{\partial \theta}(\rho V_\theta \sin\theta) + \frac{1}{r\sin\theta}\frac{\partial}{\partial \theta}(\rho V_\phi) = 0$$

Evaluating the derivative and applying (4.1) and (4.2)

$$\text{then} \quad \nabla.(\rho V) = 2\rho V_r + (\rho V_\theta \cot\theta) + \rho \frac{\partial V}{\partial \theta}\theta + V_\theta \frac{\partial \rho}{\partial 0} = 0 \qquad ...(4.3)$$

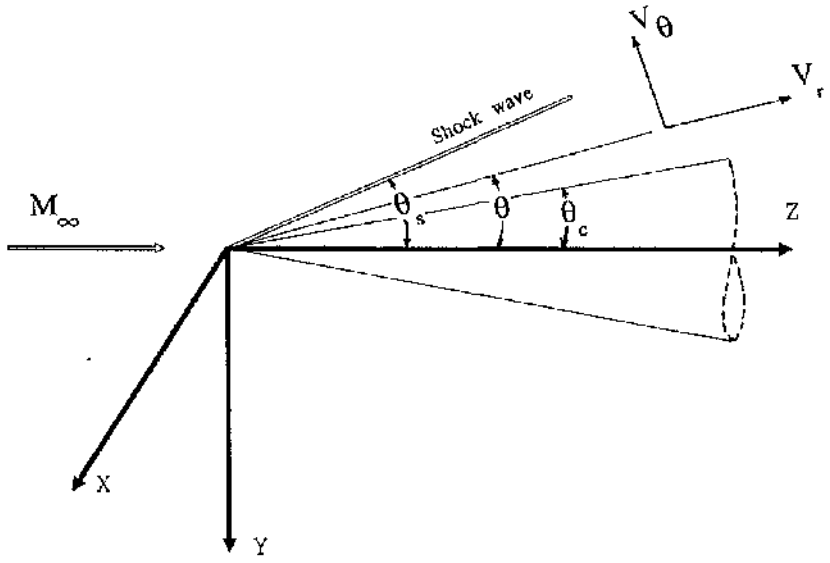

Fig. 4.2 Spherical coordinate system for the shock and the cone.

For the conical flow shown in fig (4.2), analytic treatment requires basic assumptions of existence of continuity, irrotationality and adiabatic flow. It is assumed that the velocity vector along any ray from the cone vertex, lying between the cone and shock wave is constant. A similar assumption is implied for other flow properties such as pressure, density and temperature.

For the attached supersonic flow over a cone, the streamline increases from θ' just downstream of the shock to θ_c when it comes close to the surface far downstream. Since the shock wave surface is conical and of uniform strength, the following assumptions can be used :

(1) The increase in entropy across the shock is same for all streamlines, thus $\Delta S = 0$ in the shock layer;

(2) The flow is adiabatic and steady, therefore, $\Delta H_o = 0 = H_2 - H_1$ where, H_1 is the enthalpy before the shock and H_2 is the enthalpy after the shock;

(3) For irrotational conical flow, $\nabla \times V = 0$,

therefore,
$$\nabla \times V = \frac{1}{r^2 \sin\theta} \begin{vmatrix} e_r & e_\theta & (r\sin\theta)\, e_\phi \\ \partial/\partial_r & \partial/\partial_\theta & \partial/\partial_\phi \\ V_r & rV_\theta & r\sin\theta V_\phi \end{vmatrix} = 0. \quad (4.4)$$

On applying axisymmetric ($\partial/\partial\phi \equiv 0$) and conical flow ($\partial/\partial r \equiv 0$) conditions to the above equation, this simplifies to

$$V_0 = \frac{\partial V_r}{\partial \theta} = 0 \qquad \ldots(4.5)$$

In order to carry out the analytical treatment of the flow between the cone and the shock, the following Taylor Maccoll equation is used

$$(6U'^2 - 1 + U^2)U'' = 2U(1-U^2) + (1-U^2)U'\cot\theta - 7UU'^2 - U'^3\cot\theta \quad \ldots(4.6)$$

where, U is the non-dimensional velocity, (V_r / V_{max}) and primes denote first and second derivative w.r.t θ.

The derivation of this equation is given in Appendix 4.

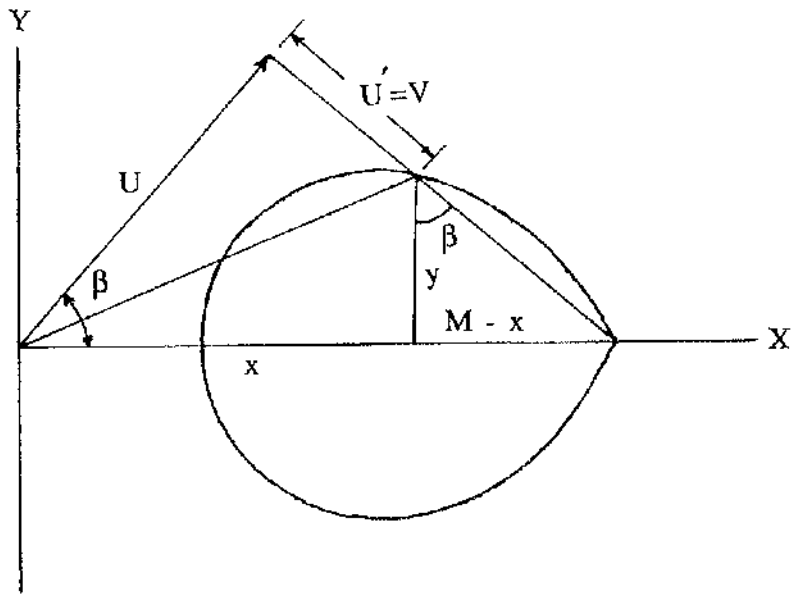

Fig 4.3 Shock polar diagram for conical flow.

Equation(4.6) is a 2nd order non-linear ordinary differential equation. A numerical solution of the equation with appropriate boundary conditions is thus normally required to carry out non-trivial cases.

4.3 Boundary Conditions.

The above non-linear differential equation is only valid between the cone body surface ($\theta = \theta_c = \theta_b$) and the shock angle ($\theta=\theta_s$). Two boundary conditions are required for a solution. These conditions can be provided by firstly specifying the upstream Mach number (M_∞) and shock angle θ_s.

The first boundary condition selected is therefore at the body surface at $\theta=\theta_b$. Here on the cone surface V_θ must vanish, as at the cone surface there is no flow in or out of its surface,

and thus, $$\frac{dU}{d\theta} = \frac{dV_r}{d\theta} = 0 \qquad \text{at } \theta=\theta_b. \qquad .....(4.7)$$

The second boundary condition occurs at the shock wave, where shock angle β is determined by the free stream mach number (M_∞) and the cone angle (θ_b). Hence a relation between θ, V_r, $\frac{dV_r}{d\theta}$ ($=V_r'$) at $\theta = \beta$ is required.

The second boundary condition can be found through an analytic approach by referring to the shock polar equation using the shock polar diagram (fig.4.3). This is

$$\tan\theta = -\frac{1}{6}\frac{(1 - U^2)}{UU'} \qquad \text{at } \theta = \beta \qquad .....(4.8)$$

Equation (4.7) and (4.8) are appropriate as boundary conditions for the solution of equation (4.6). Their application, however is limited since there is no direct method available for accurately determining the shock angle β for cone flow. For wedge flow, the streamline angle for the flow behind the shock is equal to θ_b, so the computation of β through the shock polar is easy. For the flow around the cone, solution is possible in the following two ways :

(1) Assign M_∞ and β, and determine V_r and V_θ at the shock and then calculate θ_b for which $U=0$;

or,

(2) Assign V_r along θ_b and determine β and hence the Mach number from equation (4.8).

This can be accomplished by carrying out the successive differentiation of equation (4.6) and by obtaining the Taylor series for V_r and V_θ respectively in the form [85]

$$\frac{V_r}{V_b} = 1 - h^2 + a_1 h^3 - a_2 h^4 + a_3 h^5 - \ldots\ldots \quad ..(4.9)$$

and,
$$\frac{V_\theta}{V_b} = -2h + 3a_1 h^2 - 4a_2 h^3 + 5a_3 h^4 - \ldots\ldots \quad ..(4.10)$$

where,

$$a_1 = \frac{1}{3}\cot\theta_b$$

$$a_2 = \frac{1}{12}\left[3\cot^2\theta_b + \frac{20V_b^2}{1-V_b^2}\right]$$

$$a_3 = \frac{\cot\theta_b}{5}\left[\cot^2\theta_b + \frac{193}{12}\times\left(\frac{0.03627 + V_b^2}{1-V_b^2}\right)\right]$$

and, V_b = Velocity at cone body.

In between θ_b and the shock angle β at any particular value h from the body the direction of streamline at that point can be found using the relation

$$\theta_{fs} = \theta_b + h - \tan^{-1}\left[-\frac{V_\theta}{V_r}\right] \quad ....(4.11)$$

However for the present study, the first approach is used, whereby the free stream Mach number and shock angle are supplied. Thus by applying the reverse process the corresponding cone angle can be found. This can be accomplished by solving equation (4.6) sequentially starting from the shock wave and moving towards the body. Once an angle has been reached at which V_θ is zero, this defines the corresponding cone or body angle.

Properties just behind the shock wave are calculated using the oblique shock wave theory. Since the pressure distribution is required to determine lift and drag, thus the pressure is calculated numerically at each point along the flow field.

4.4 Basic Configuration Construction.

In the previous chapter two types of waveriders derived using simple approaches were discussed. The first was the caret wing derived through a wedge flow field and the second was the idealized conical waverider where a winglet is attached to the cone to provide an anhedral shape thus containing the high pressure on the leeward side.

The results for these idealized waveriders are interesting but these configurations however are not practical because if the winglets are infinitesimally thin then these will have a sharp ridge on the upper surface and they are not actually blended with the main body. Also these idealized shapes have increased wetted area which produces additional unwanted viscous drag at hypersonic speed. However some practical shapes can be constructed from these simple flow fields whereby the bodies thus generated may not have conical shapes.

This idea is extended to generate more general shapes. Continuing the above discussion, once the cone has been defined for a particular conical flow shock angle and Mach number, one can construct a shape of a body out of this flow field such that the shock remains attached to the leading edge of the body and its lower surface is defined by a stream surface of the flow behind the shock.

Given the planform area and volume constraints the top surface is first defined. For the cases discussed here the top surface is defined by a plane developed by extending the parabola in the body base plane

$$Y = AX^2 + R,$$

in the upstream direction. A and R can be adjusted for area and volume requirements and are predefined parameters.

Fig.(4.4) shows one such shape placed in the flow field in Cartesian

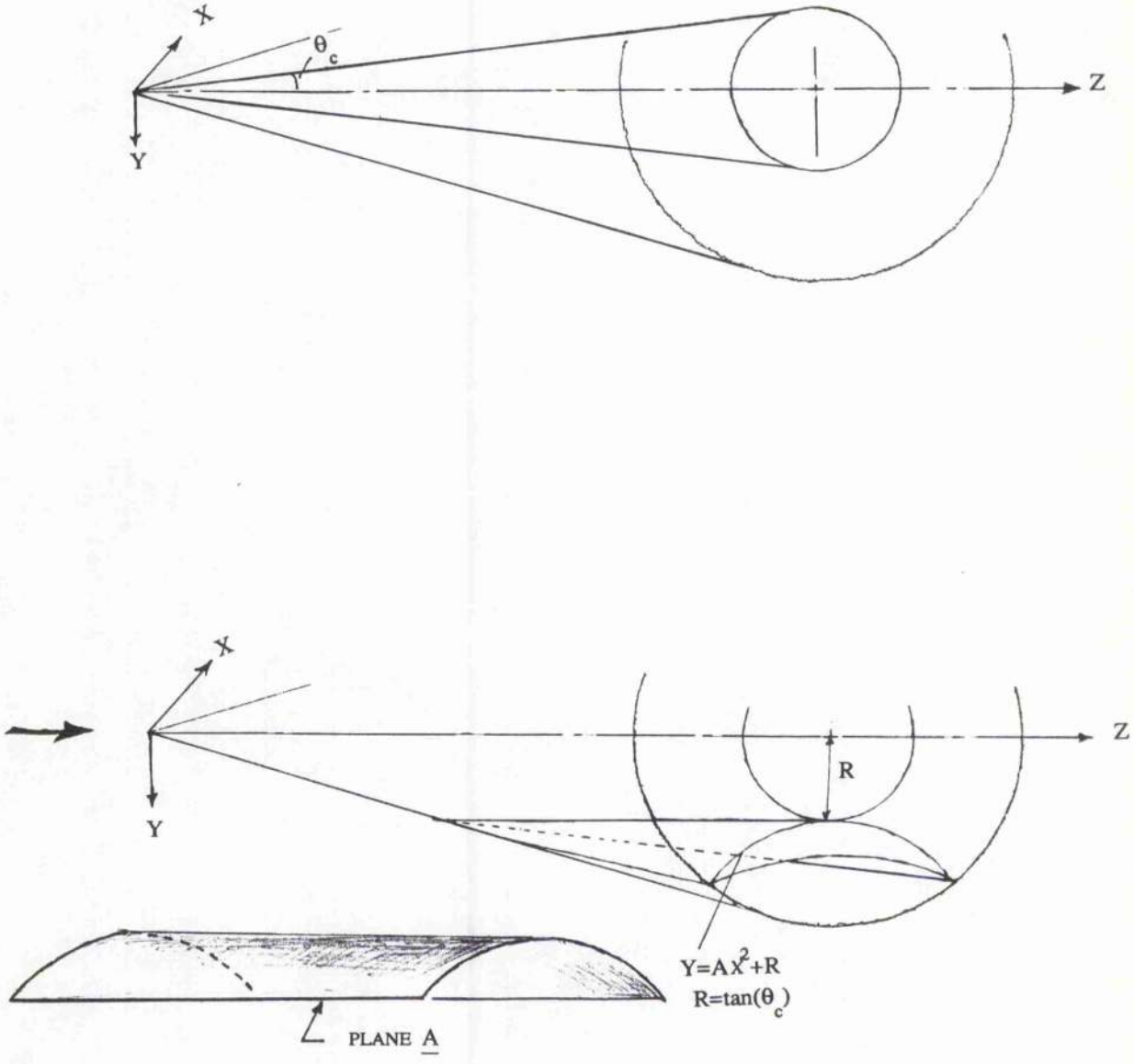

Fig 4.4 Construction of waveriders generated from conical flow.

coordinates. The outer cone represents the conical shock corresponding to the flow around the inner cone at the design Mach number. Plane A shown in fig.(4.4) represents the upper surface of this waverider. The upper surface becomes a stream surface in the free stream and on extension upstream where it cuts the shock cone defines the leading edge of the waverider.

The leading edge is thus merely the intersection of the projection of upper free stream surface with the shock cone. Mathematically the shock cone for the known shock angle θ_s in Cartesian coordinates can be defined as

$$X^2 + Y^2 = Z^2 \tan\theta_s^2$$

From fig(4.4) the upper surface of the waverider at a distance R from the center line, extended in Z plane is

$$Y = AX^2 + R$$

which on extending towards the shock cone, cuts the shock cone at some point thus defining the leading edge of the waverider. For the lower surface, to have the shock remaining attached to the leading edge and exhibiting waverider characteristics it must be constructed by a surface defined by the streamlines. Thus once the leading edge has been determined, the lower surface can be constructed by tracing the streamlines from this edge until it reaches the trailing edge. The direction of streamlines at any point can be found from equation (4.11), as the velocity vectors along different rays between the body and the shock are already known (from the Taylor Maccoll solution). It is important to note that the direction of streamlines θ_{fs} may differ along the body length towards the trailing edge but each streamline lies in a plane of constant azimuthal angle ϕ. For the current study along the lower compression surface at each cross-section (z-axis) each streamline is defined by

$$Y = AX^2 + BX + C$$

where, A,B and C are calculated numerically.

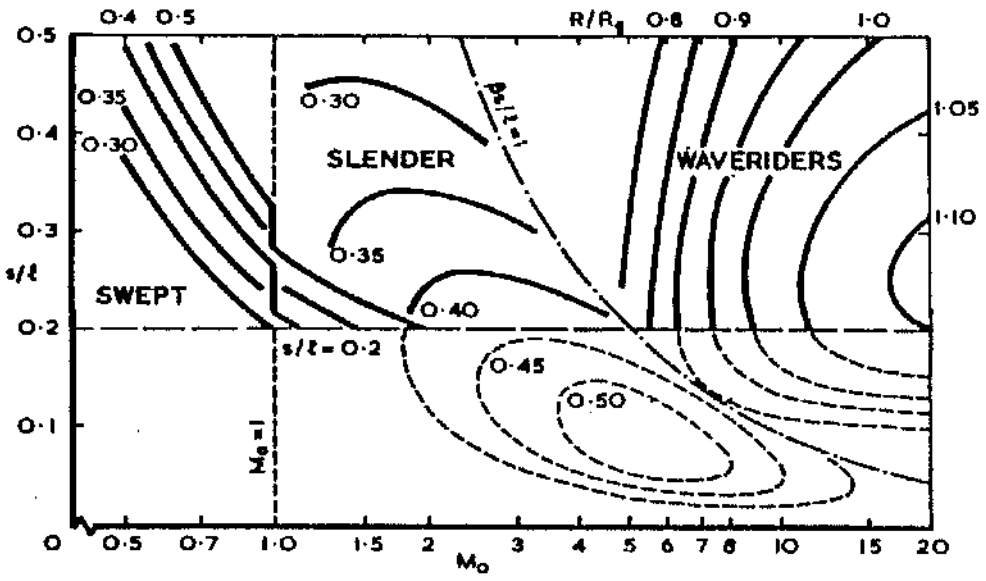

Fig 4.5 Shapes of planes for different sonic regimes. [Kuchemann] [31]

4.5 Results and Discussion.

The aerodynamic efficiency of waveriders results from a combination of favourable features. Comparing the application of a waverider to a conventional subsonic and supersonic aircraft their respective missions demand a different shape. In contrast to the subsonic airplane, supersonic airplanes are designed around a principle of the slender wing. The main idea behind this is to maintain a simple well behaved flow around the whole body at all flight conditions. A stage by stage analysis of these shapes for different Mach number regimes has been developed by Kuchemann[31]. For the supersonic case this is achieved by choosing a leading edge sweep such that flow remains subsonic along most of the leading edge. When the M_n (Mach number normal to the leading edge) is subsonic, the flow over the wing is shock free except at the trailing edge. This means that the analysis is accomplished using subsonic flow assumptions.

The foregoing is applicable for low supersonic cases but for very high speed (i.e. hypersonic flow) it is suggested[31] that the shape of the wing be slender(fig(4.5)). Then to achieve a high L/D as well other prominant aerodynamic characteristics at low speed one must employ variable geometry on the slender wing or use a fixed wing and accept a supersonic flow normal to the leading edge.

As mentioned earlier, because of a high level of activity in manned-space missions and hypersonic transport the ideas on waveriders are currently of great interest. For constructing a wing shape from a system of shock waves a number of direct and indirect methods have been developed. These start from the simple case of the caret and idealized cone derived waveriders (discussed in chapter 3) to more general shapes derived out of conical flow as well as power law bodies. Different theories have been developed to support and to calculate the flow for each case.

4.5.1 Conical VS Wedge derived Waveriders.

The literature on waveriders generally favours shapes developed from conical flowfields, since it has been considered that shapes derived from

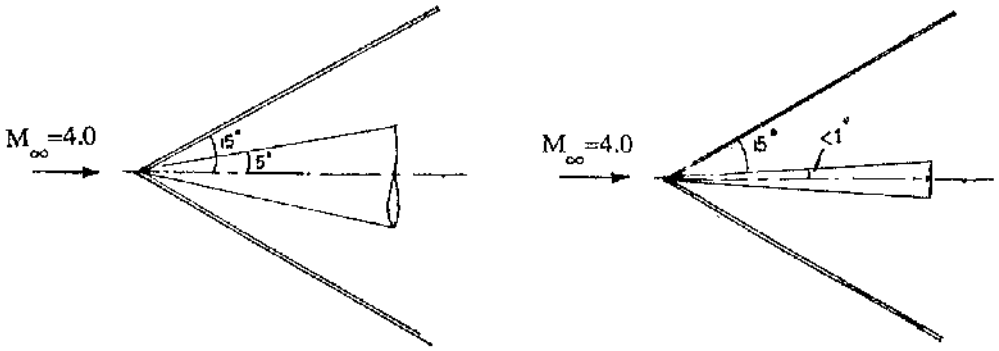

a: Equal Shock Angle.

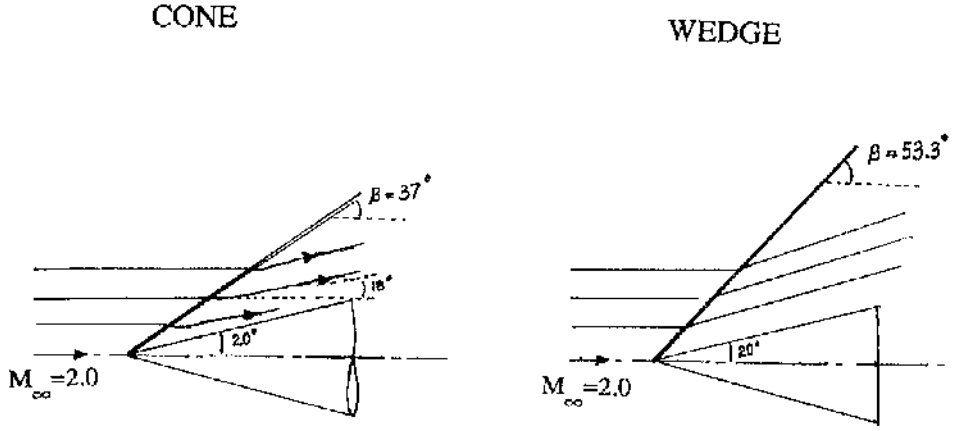

b: Equal Body Angle.

Fig 4.6 Comparison Cone Vs Wedge Flow.

wedge flows are impractical. If however volume constraints are relaxed, then it is argued in this section that there are some considerable advantages in using wedge flow as the starting point.

To start consider the hypersonic flow over a cone and a wedge at zero incidence as illustrated in fig(4.6). For a given free stream Mach number of 4 and a shock angle of 15° it can be seen that a sharp wedge of half angle equivalent to less than one degree is required as compared to a half cone angle of 5° for the same shock flow. Thus in the case of the wedge although the surface of the body required for a particular shock is small compared to the conical flow counter part, if the volume of the shape is not important then the resulting shock is farther from the body. Conversely, for a free stream Mach number of 2 acting on a surface angle of 20° for both the wedge and cone, the shock angle for the wedge is higher (i.e. 53.3°) compared to the cone (37°).

For wedge flow, more accurate and simple solutions are possible than for cone flow therefore the theoretical construction of lifting shapes is easier. For the supersonic flow over a wedge, the oblique shock theory is an exact solution of the flow field, thus no simplifying assumptions need be made. To summarize, attached shock flow over the wedge has the following features:

- straight shock wave surface from the nose;
- uniform flow downstream of the shock, with streamlines parallel to wedge surfaces;
- uniform pressure distribution behind the oblique shock.

Similarly, the features of the attached shock flow over a cone are:

- the direction of the streamline changes and is curved rather than straight;
- pressure changes along a streamline;
- furthermore the shock wave on the cone is weaker than the corresponding wedge and the cone surface pressure is less.

There is an infinite number of choices of waverider shapes that can be derived from these basic flow fields which requires few assumptions and

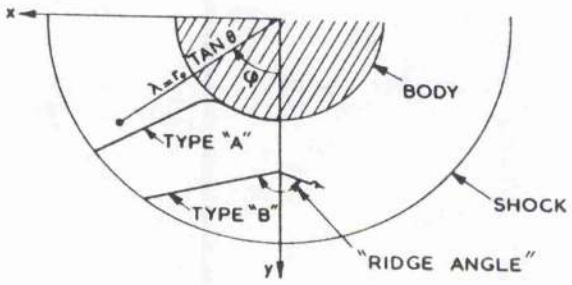

Fig 4.7 Rear view of a Conical waverider.

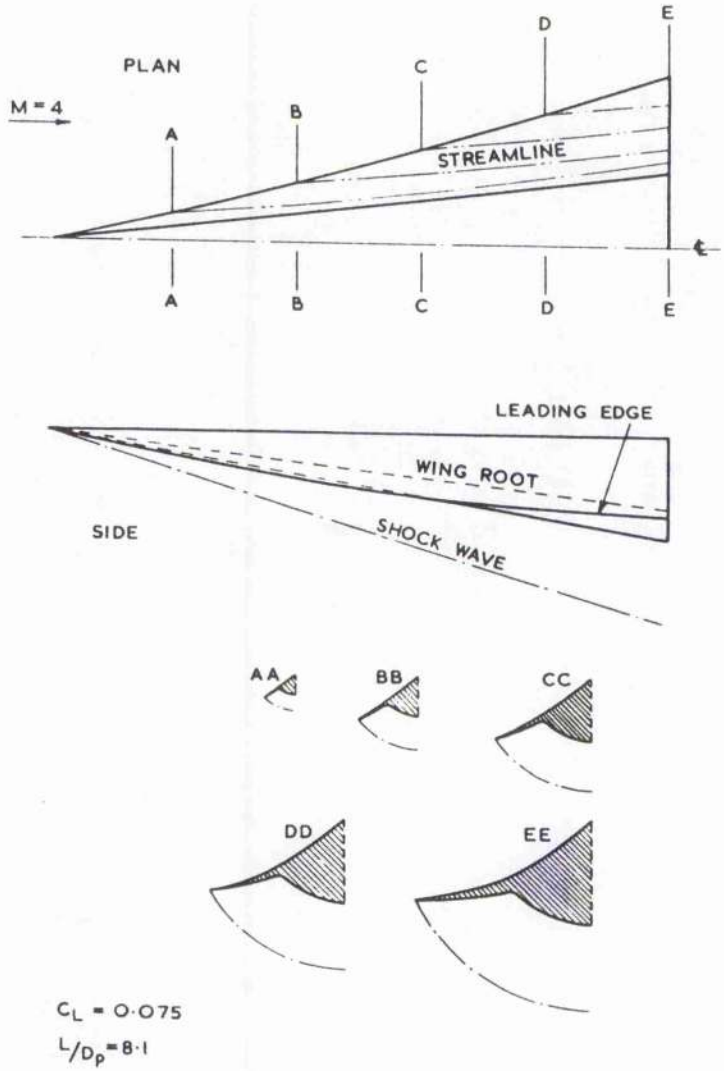

Fig 4.8 a. Type A Configuration

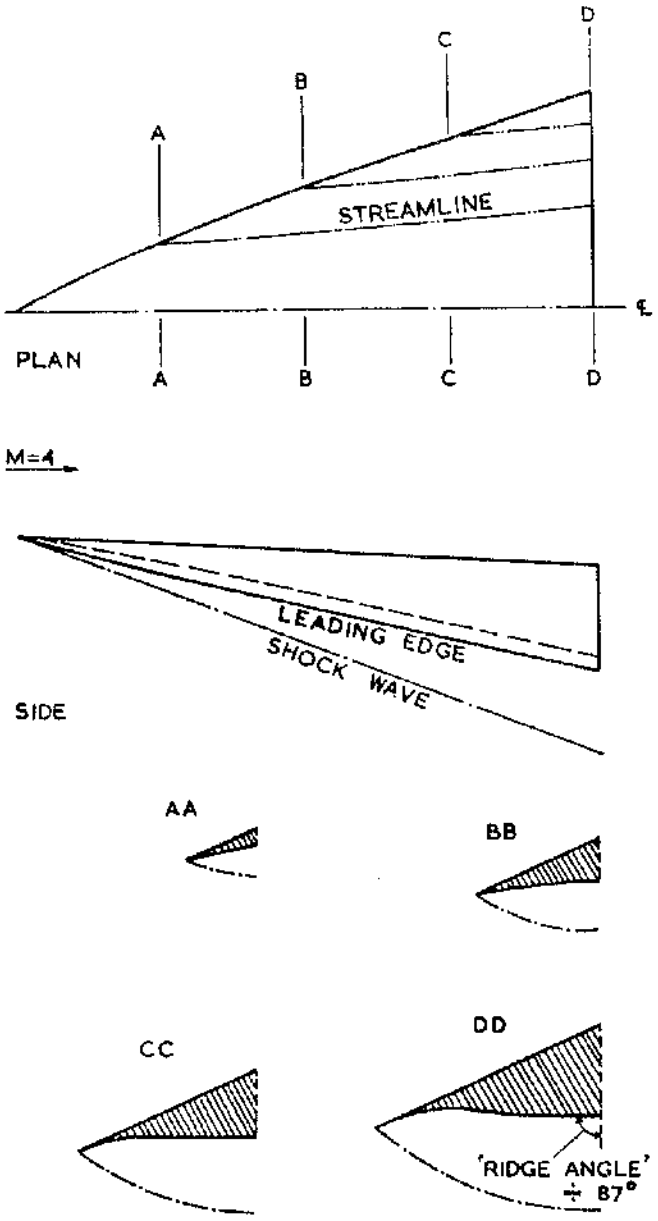

$C_L = 0{\cdot}146$

$L/D = 5{\cdot}3$

Fig 4.8 b. Type B Configuration

exploit particular properties. Due to the perceived limitations of caret waveriders, support has always been in favour of constructing shapes out of a conical flow field and the construction of more general shapes out of wedge flow appears not to have been tried. In the present study some of the advantages of waveriders constructed through wedge flow field are highlighted. These advantages are explored theoretically as well through inspection of experimental results gathered from the literature.

Fig(4.7) illustrates the rear view of a conical waverider in which the top surface is defined by a free stream surface $f(X,Y)$, which on extending towards the conical shock, describes the leading edge of the waverider, where it cuts this shock. The top surface can be any function of $f(X,Y)$ extending in the Z direction. The leading edge of the lifting surface can be given in spherical coordinates as

$$\theta = \theta_s$$
$$\phi = F(r).$$

The lower surface is defined by the streamlines of the conical flow field passing through the leading edge. For any streamline its direction may differ in the θ direction but it does remain in a ray of constant ϕ. Different top surface shapes have been suggested. Following the caret wings of Nonweiler derived from wedge flow, the type 'A' and 'B'(see below for definition) surfaces by Jones and Woods[20] can be seen as the pioneering equivalent work in conical flow lifting shapes. The power law bodies of Cole[29] and optimum shapes by Bowcutt and Anderson[26] and the parabolic shape top surfaces by Rasmussen[30] can be considered as an extension of the same idea.

The type 'A' configuration is formed when the leading edge extends to the apex of the original cone. In this case distinction can be made between the wing and the body i.e., part of the cone which supports the shock defines the body whereas streamlines originating from the leading edge define the wing. In type 'B' configurations for lifting surface, their apex lies behind the apex of the original cone and the surface thus does not include any part of the circular cone which supports the conical shock, thus θ is always greater than θ_c. For a type 'B' surface, distinction between the cone and wing cannot be made (fig 4.8).

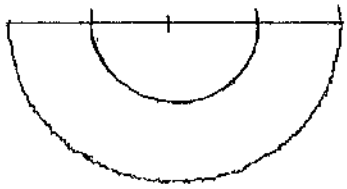

Fig 4.9 Type 'A' Configuration (with maximum possible volume).

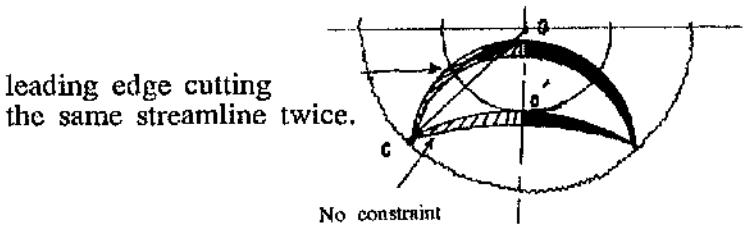

Fig 4.10 Some constraints while defining the upper surface.

For the inlets of hypersonic scram jets, another kind of waverider can be defined where the projection of the leading edge is derived inversely such that the shock wave is a straight line and the rear view exhibits a straight trailing edge.

Aircraft designers generally consider volume to be more usable when it is deployed in the vicinity of the plane of symmetry of the aircraft. Furthermore this should be of a cylindrical form. A waverider derived from a conical flow field naturally has the feature of the major part of the volume centrally placed with little volume away from the plane of symmetry.

The prime advantage of constructing a waverider from conical flow rather than a wedge flow has been their more usable volume as compared to the thinner waverider derived from wedge flow. Fig(4.9) shows the type 'A' configuration (after Jones) which provides the maximum volume for a conical flow waverider. It can be seen that this volume always remains close to the centre. If the requirement is that the volume is to be distributed laterally then conical flow waveriders have their limitations. An obvious method of achieving this volume distribution, is to provide more curvature to the leading edge curve OC as shown in the end view fig(4.10). However now the flow becomes more complex because a number of points on the curve OC are cutting the same leading edge twice along a particular conical streamline thus making it more complex to define. The complexity can be observed in many of the shapes suggested in the literature [21,24,26,39] where this particular constraint is ignored. This problem is similarly present for the more general type 'B' or optimized shapes, because, even if the shape is defined for a particular Mach number at zero incidence, then if operating slightly off-design, the same limitations as shown in fig(4.10) will be exhibited. This constraint can be removed by deriving more general shapes out of a wedge flow field where the choice of upper surface curvature or shape is not limited.

It is evident that waverider shapes generated from wedge flow fields provide volume distributed evenly across the span, whereas those generated from cone flow fields provide more volume around the plane of symmetry. This even distribution is considered generally to be a disadvantage and thus it

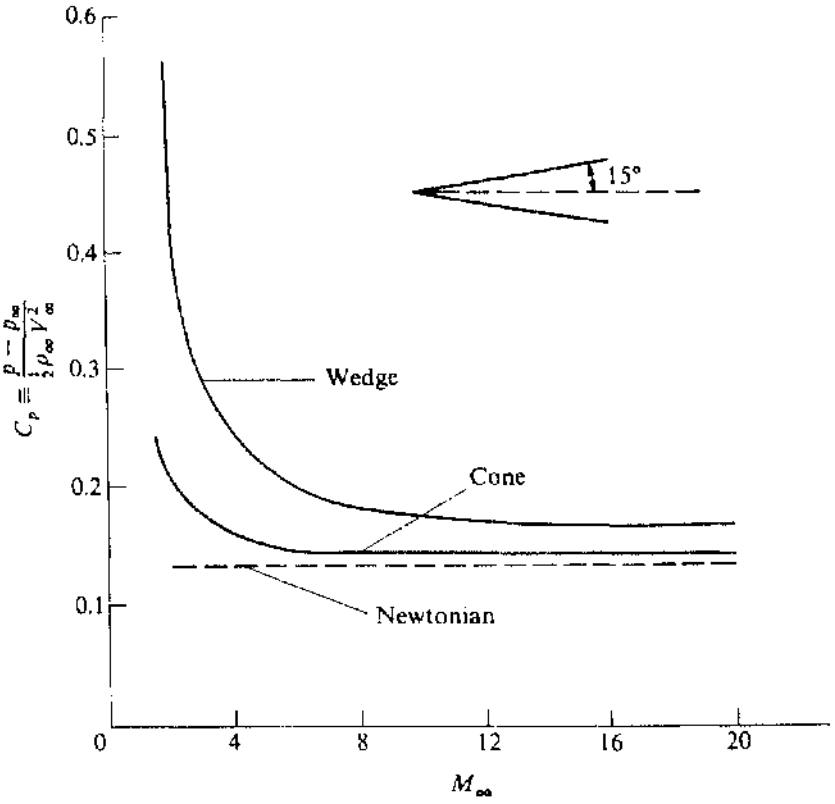

Fig 4.11 Pressure coefficient for a sharp cone and wedge with equal body angles(exact results).

must be weighed against the favourable characteristics of the former which involve low Mach number and off-design performance.

The basic characteristics for which waveriders are favoured for hypersonic space planes is that the high pressure due to contained flow on the lower side can produce higher lift than conventional wings at high speed. Fig(4.11) exhibits the exact results for the pressure coefficient on a sharp wedge and sharp cone at 15° surface angle to the flow. It can be seen that the pressure coefficient for the wedge is higher than that for the cone. This difference is very significant at lower Mach numbers. For example at M=4, the pressure coefficient over the wedge (C_{pw}) is 0.24615 as compared to 0.16153 for the cone, i.e a difference of 52%. For high Mach numbers this difference is reduced, for example at M=16 it gives a 19% higher pressure for the wedge (C_{pw} = 0.1692) than the corresponding cone (C_{pc} = 0.1423).

Thus, if these pressures can be achieved by containing the flow, more lift will be generated by a waverider of the wedge derived flowfield rather than of the conical flowfield.

Another advantage of waveriders constructed through a wedge flowfield is the complexity of defining the streamline path for a conical flow compared with wedge flow. Hence since the tracing of the streamlines is accurate and easy, then the definition of the lower surface is likely to lead to better accuracy.

The primary objective then, of the design of waveriders is to design a shape with high lift. To achieve this, a shape is required in which the high pressure is contained under the lower surface. This is obtained by using a known simple supersonic or hypersonic flow field and then choosing a portion of a stream surface to construct the basic lifting body. For this basic body, lift and drag characteristics can be found by using the knowledge of the flowfield and exploiting the above principle that high pressure remains contained in the space between the shock wave and the lower surface. For the ideal case there is then no spillage from the leading edge.

In practice the term waverider can be applied to any shape designed on these principles. The lift for all these shapes is primarily produced by

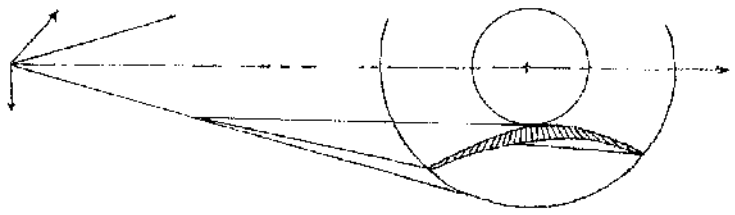

(ON-DESIGN)
Waverider configuration shown in conical flow field.

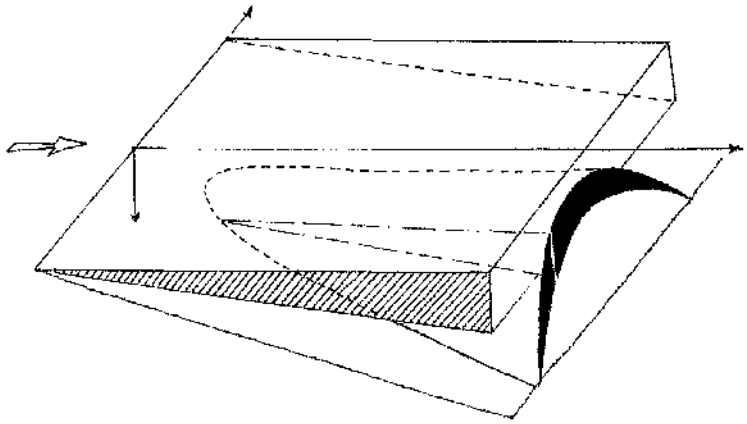

(ON-DESIGN)
Waverider configuration shown in wedge flow field.

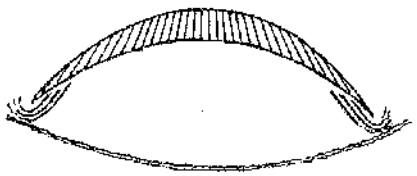

(CONICAL FLOW)	(WEDGE FLOW)
* Less resistance to spillage.	* More resistance to spillage.
* Less contribution towards lift & earlier stall as compared to a similar condition of a wedge derived shape.	* Maintains lift contribution still at higher off-design (e.g., at higher α values).

Fig. 4.12 Advantages of using wedge flowfield than conical flowfield for deriving waverider shapes *(at off-design conditions)*.

the high pressure on the under surface of the shock system. Efficient lift has been obtained from the use of two dimensional or axisymmetric flow fields of known characteristics where the lower surface of the body is a stream surface carrying the shock wave system as defined above. This favourable condition of contained flow will be achieved at one Mach number condition, and the discussion has been carried out neglecting viscous effects. An important practical consideration is the behaviour of the containment at off-design conditions as produced by operating at different Mach numbers and including the viscous effects that are particularly large at large Mach numbers.

Fig(4.12) summarises graphically the basic differences between the characteristics of conical and wedge derived waveriders at slightly off-design condition. For a wedge derived waverider on the under surface, streamlines are spaced parallel to each other and to the Z-X plane. On the other hand for a conical shape waverider every streamline is placed in a constant azimuthal angle ϕ and concentration of the flow is more towards the leading edge than in the center, hence, the contribution towards lift is comparatively limited. Also it can be argued that it is likely that the spillage will be less for a wedge shape than a conical shape for a condition away from the design case. Hence the loss of containment in off-design conditions is likely to be less for a wedge flow than for a conical flow derived shape.

4.5.2 Experimentation with waveriders.

Experimental evidence of the production of more lift through caret wings than conventional delta wings was obtained [48,60,61,62] in the sixties. These studies suggested that a higher value of C_L can be reached even for low flow deflection angles (θ) ($<30^\circ$) and low Mach numbers ($M_\infty <$ 9). The C_L values achieved for caret wings are greater than 10% than those for delta wings. At slightly higher Mach numbers with greater sweep (76°) for delta and caret wing, experimental data was obtained by Rao[63], Carr[19] and Davies[64]. Rao[63] and Carr[19] tested flat wings and caret wings for $4^\circ \leq \omega \leq 10^\circ$ (where ω = design angle which equals (β-θ)) with sharp leading edges. Their results showed that at ω = 9.8 and free stream Mach

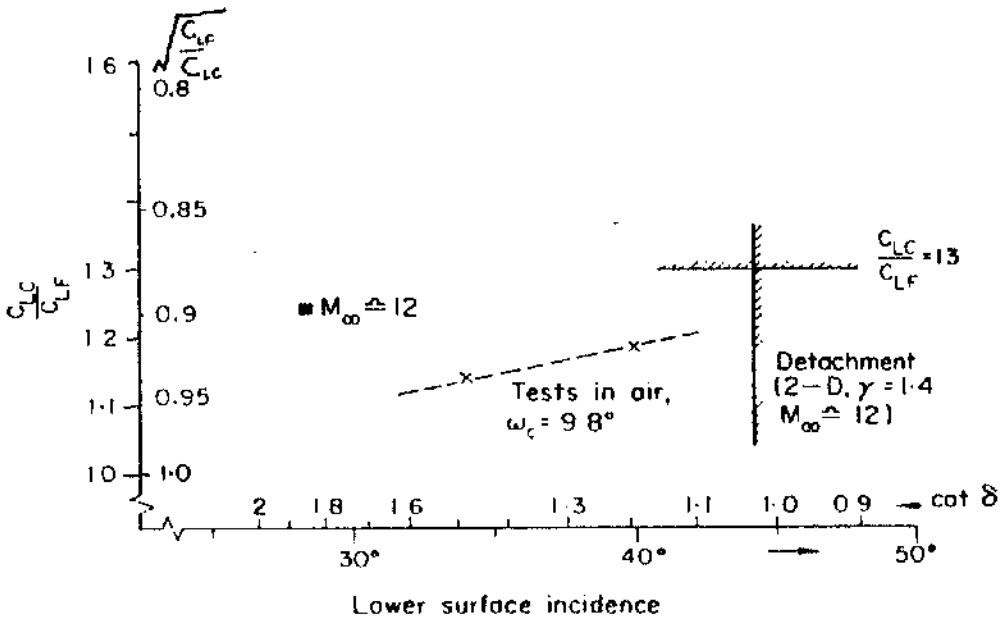

Fig. 4.13 Experimental data for flat and caret wings at high incidence and high Mach numbers.

number (M_∞=12) at the design condition (θ=34°), the caret wing had 10% extra lift than the delta wing. Increasing the deflection angle to 40° causes the additional lift to nearly double to 20%.

The data of Rao[63] had an interesting feature. Experiments were performed for angles of attack of 45° or more for the flow field environment at which two dimensional theory predicts a detached shock wave. The flow field did exhibit some instability but surprisingly C_L was still increasing with increasing incidence angle. Furthermore the ratio of C_L's at 60° incidence was even higher than that measured at lower angles fig (4.13).

Models tested by Davies[64] were of a more practical nature. One of the models with a flat bottom delta had a semi-span to length ratio (s/l) of 0.11 representing the basic shape of the U.S.A.F. NASA Hyper 3 reentry vehicle and the second was a modification of the delta wing by constructing a recess on the underneath surface with ω = 5° (where $\omega = \beta - \theta$), thus representing an equivalent caret wing. These models were tested at M_∞=12 and incidence 58° and 60°. During the experiment it was observed that the flat delta wing failed even to reach the Newtonian value and the C_L obtained was 0.65. On the other hand apart from some limitations the recessed wing revealed an extra 10% C_L as well as a reduction of 5% of heat transfer on the under surface of caret wing.

A comparative study by Squire[18] predicted the performance characteristics of these wings at different angles of attack at high Mach numbers at off-design conditions. For slightly lower values of ω than design, a lower value of C_L would be obtained. For example if a caret wing of ω = 13° is designed for M_∞=15 and γ=1.4, at incidence of 40°, it would give $\frac{C_{LC}}{C_{FC}}$ (caret wing to flat delta wing) ratio of 1.21, where as if ω is reduced to 5° this ratio reduces to 1.1.

Studies by Roe[65] and Squire[66] revealed that the degree of anhedral is a very important factor providing two advantages. First it helps to retain the lift and also its careful design allows moderate concavity. So by careful design the central sections of the under surface can be allowed to be filled in thus generating more usable volume. Furthermore such a

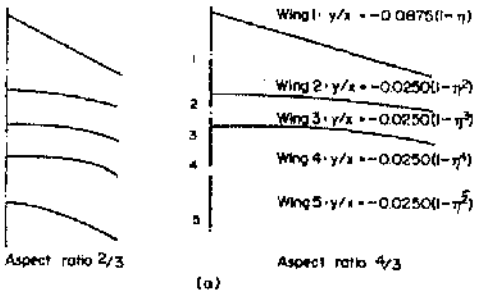

Fig. 4.14 Delta wings with nonuniform anhedral distribution. (Data due to Squire
(a) Anhedral distributions of Squire's delta wings 1-5.

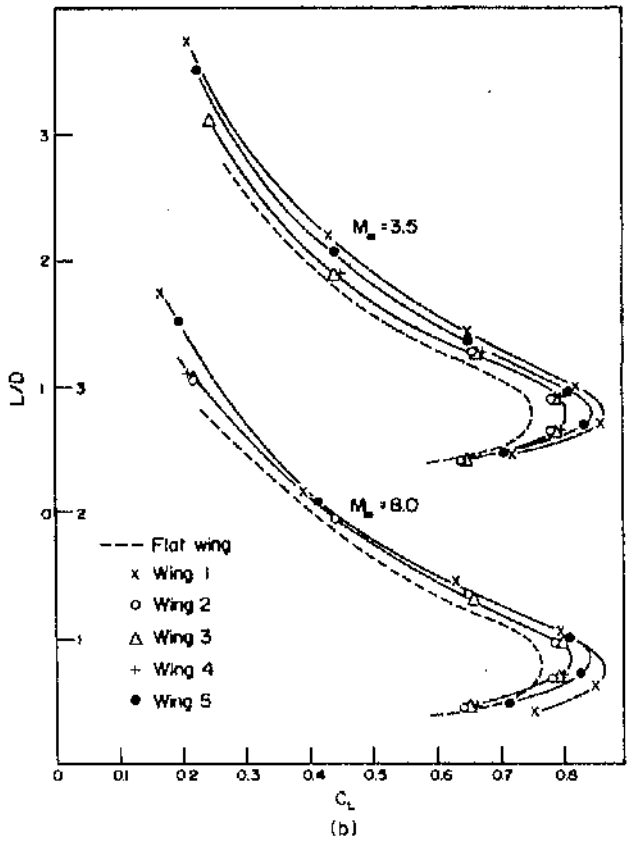

(b) Variation of C_L with C_L/C_D, wings 1-5. Aspects ratio 2/3.

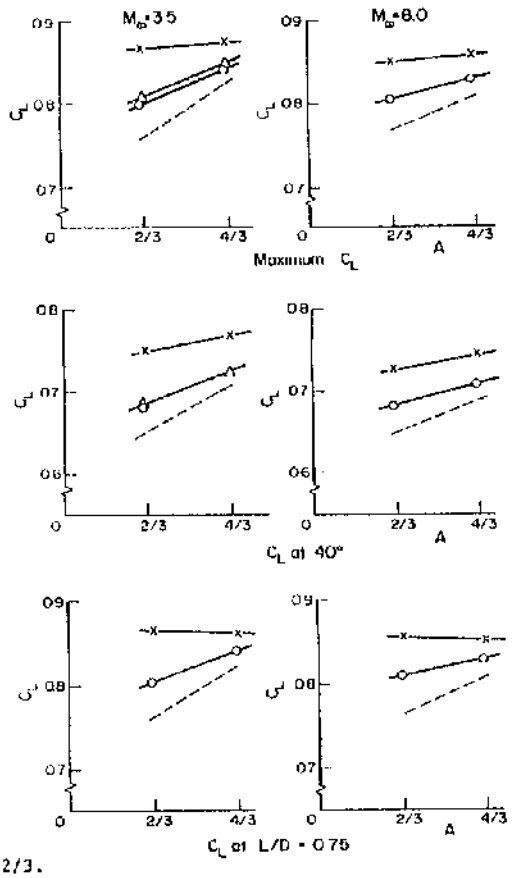

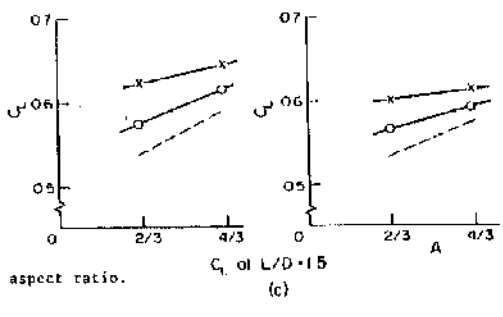

(c) Effects of aspect ratio.

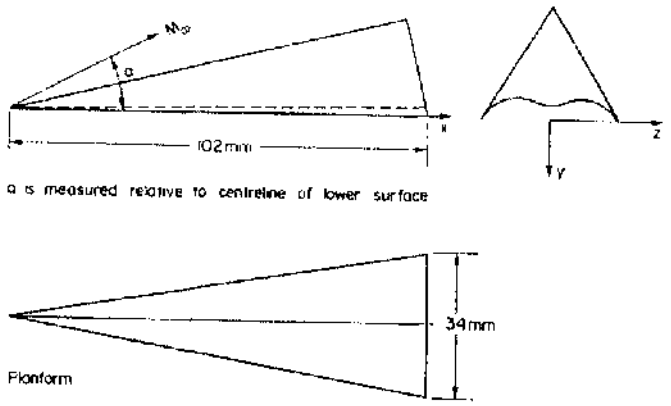

Fig(4.15)a. Squire's "wavy wing" ($\int l/l \approx 0.17$)

Fig(4.15)b. Wings with similar performance, at M_∞=3.5, L/D ≈ 1.62, C_L=0.62

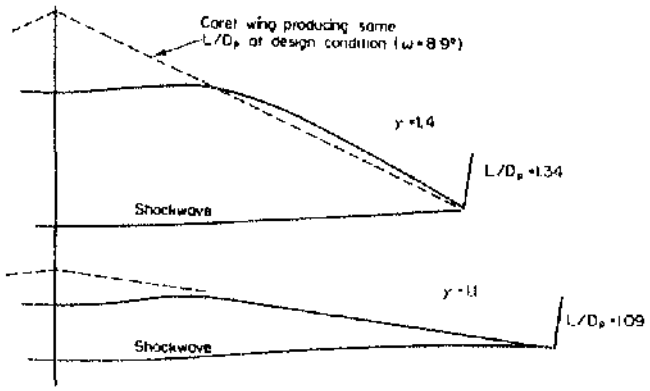

Fig(4.15)c. Optimized wings for infinite Mach number & $\int l/l \approx 1/3$.

modification may force the shock wave outward in the plane of symmetry at some other point along the span by generating extra local lift thus improving overall C_L. The principal work in this field is attributed to L.C. Squire[66], Roe[65,67] and Davies[68].

Squire studied the performance and behaviour of a delta wing to changes in aspect ratio and anhedral distribution. The study was carried out at Mach numbers ranging from 3.5 and 8 and at angles of attack up to 60°. Fig(4.14 a) shows some of the resultant anhedral distributed wings designed by Squire with aspect ratios of 2/3 to 4/3. Fig(4.14 b,c) compares some of these results with a simple delta wing and caret wing. Results confirm that significantly higher values of C_L and small improvements in L/D at constant C_L can be obtained by changing anhedral. Increases in the aspect ratio decrease C_L slightly.

Another advantage of these anhedral surfaces is that modification near the plane of symmetry can be made to improve the volume characteristics of lifting vehicles. Hence wavy wings were suggested by Squire[66] to improve configurations for practical use. Fig(4.15) illustrates a number of wings with similar performance at M_∞=3.5 and demonstrates the advantages of wavy wings over the caret version. Although for the Squire shapes[66] (fig 4.15a,b) at low Mach number, a marginal increase in C_L was quoted for a wavy wing, Roe[68] suggests that for very high Mach number at ($M_\infty = \infty$) a form of wavy wing can offer the same L/D_p (D_p = pressure induced drag) as a caret wing while showing a reduction in concavity but an increase of Y_s i.e., shock distance from the compressed surface (hence shock wave movement) and therefore C_L(fig.4.15c). For example for γ=1.4 and $M_\infty=\infty$, C_L for caret and wavy wings are 0.72 and 0.71 respectively whereas for a flat delta wing it is only 0.58.

Options for designing anhedral shapes, whilst not altering the basic flow field, are not restrictive. Many irregular curves theoretically produce the same shock shape. Furthermore the slope of this shock plane, according to Roe[17], can be fixed by the required design Mach number and lift coefficient mathematically as

$$\sin^2\theta = \frac{1}{M_\infty^2} + \frac{2\ C_L}{(\gamma+1)}$$

Interestingly the resulting shapes derived from this shock plane are affine transformations of each other and look similar either from the top or front view. However for such shapes derived from these planes a necessary relationship between aspect ratio and friction drag has to be satisfied. For the case of high aspect ratio, a small anhedral is required and vice versa. Also an increase in wetted area means an increase in friction drag. A particular difficulty arises if a surface is to be designed from wedge flow for low Mach numbers, high C_L and relatively low aspect ratio.

This preliminary study reveals that there exist advantages in designing a waverider from a wedge flow field with only a few disadvantages, and that a wide choice of shapes is available.

As discussed earlier, to construct more general and realistic shapes other flow fields should be considered for waverider shapes using the same principle. In this context Jones[69] first extended the idea of using the flow over an unyawed cone. The advantages of such waverider shapes were more usable volume, less anhedral and less friction drag. Initial experimental data for these shapes was limited, so drawing conclusions was difficult, however, experimental findings by Houwink and Richards[54] and Reggiori[56] did point out that even by adding thin anhedral wings to prevent spillage from the cone, a substantially better performance (high C_L and L/D) can be obtained even at high angles of attack.

Ideas for deriving these shapes have developed more recently and during the 1970's and 1980's most of the general shapes were derived from conical flow fields. The use of a simple cone flow as the basic field however, has its own disadvantages. In this case the streamlines of the flow are concave with a positive pressure gradient along them. Thus any surface constructed from this flow field will have, even for a well developed case, the centre of pressure and volume far rearwards, which was one of the reasons for which caret wings were rejected as practical shapes. An experimental study of the applicability of using simple idealized cone waverider configurations with varying anhedral angles for a hypersonic transport aerospace plane has been

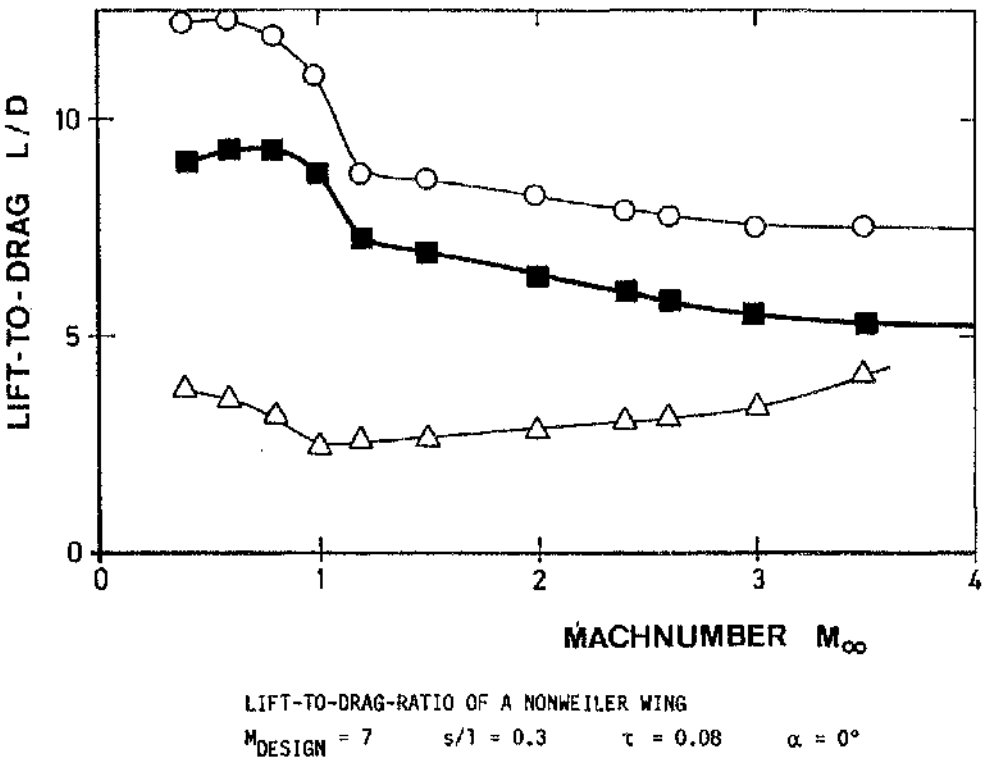

Fig 4.16 L/D at different Mach numbers.

made out by Hozumi[70].

The theoretical treatment of cases from more general conical flow fields shapes has been carried out quite extensively using a variety of different theories and assumptions, in which support has been claimed by favourable comparison with experimental results. But the only report where wedge (caret wings) and conical (Jones wings) generated shapes are treated simultaneously is that by Ganzer et al, ref[71]. In this case a variety of investigations have been made at the Technical University of Berlin around simple delta, double delta and waverider configurations with special treatment of vortex formation. Special attention was given to the effect of Mach number, sweep angle, angle of attack and leading edge shape as well as overall general shape as each parameter in turn affects the location, structure and origin of the main leading edge vortices.

Both models used were designed on the basis of a caret wing constructed from 2-dimensional wedge flow and a Jones waverider based on conical flow. Configurations used were characterized by design Mach number, span to length ratio (s/l) and volume parameter (τ = V/F, where F = $S^{3/2}$). Both models were designed for a free stream Mach number of M_∞=7.0. Resultant models used for experimentation had s/l= 0.3 and τ= 0.08 for the caret wing and s/l= 0.28 and τ = 0.0883 for the Jones waverider respectively.

For the caret wing it was observed that if the operating Mach number is reduced below the design Mach number the shock wave bulges and then detaches from the wing. A similar phenomenon was observed when the angle of attack is increased. Flow around the leading edge occurs with separation resulting in a rolling up of the flow into spiral vortex sheets. A low pressure is observed on the upper surface below the vortex. These vortices contribute additional lift and therefore increase overall lift-to-drag ratio. Fig(4.16)[71] illustrates L/D ratio at different Mach numbers below the design value. It was further observed that at subsonic speed for caret wing, the low pressure due to leading edge vortices provides roughly half of the total lift.

Lift and drag are calculated from the measured pressure distribution. A strong upstream influence of the base flow is shown to exist on the lower

surface of the wing resulting in some uncertainties in the results.

Unlike the caret wing, the Jones waverider was based on a conical flow. At the design conditions the shock wave was expected to be conical and remain attached to the leading edge. This wing appears more practical due to its small dihedral and extra volume but the experiment revealed that the flow field at slightly off-design conditions is very complex and is basically non-conical in nature. For the pressure distribution over the Jones waverider, unlike the caret wing where the pressure distribution is almost constant at supersonic conditions, a pressure variation was observed on the lower surface due to non-conicity of the body. Overall flow behaviour was however close to predictions. A closely predicted flow was also obtained by Pike[72] for conical flow waveriders at M=4 derived from cone angles of 11° and 16°. Here the causes of error are mainly attributed to experimental environment such as model shape, tunnel calibration etc.

Experimental data for conical constructed waveriders at hypersonic flow is limited. The above mentioned experiments were carried out in the low supersonic and supersonic range up to a Mach number of 4. Some off-design behaviour is also believed to have been caused by viscous effects. As the thickness of the boundary layer changes the effective shape of the geometry, then a need to revise the body shape due to these effects is required. Bowcutt and Anderson[26] have communicated some of these shapes in which viscous effects were included in the final optimized shapes.

The models for these final optimized shapes were treated experimentally by Jones and Vanhoy[73] at the University of Maryland at subsonic speeds. Two models were constructed. One of a Mach six optimized waverider and the other a sharp delta wing with approximately the same length and span. Results showed a small primary vortex and a secondary vortex on the upper surface originating from the leading edge for both delta and waverider shapes, which enhance the final lift. The only difference was found at a very high angle of attack when the flow over the waverider tends to separate near the nose, contrary to the delta wing which has a fuller planform shape. However other characteristics such as lift were the same for both configurations, until $(C_L)_{max}$ was achieved.

WAVERIDERS

(Constructed through Conical Flow field)

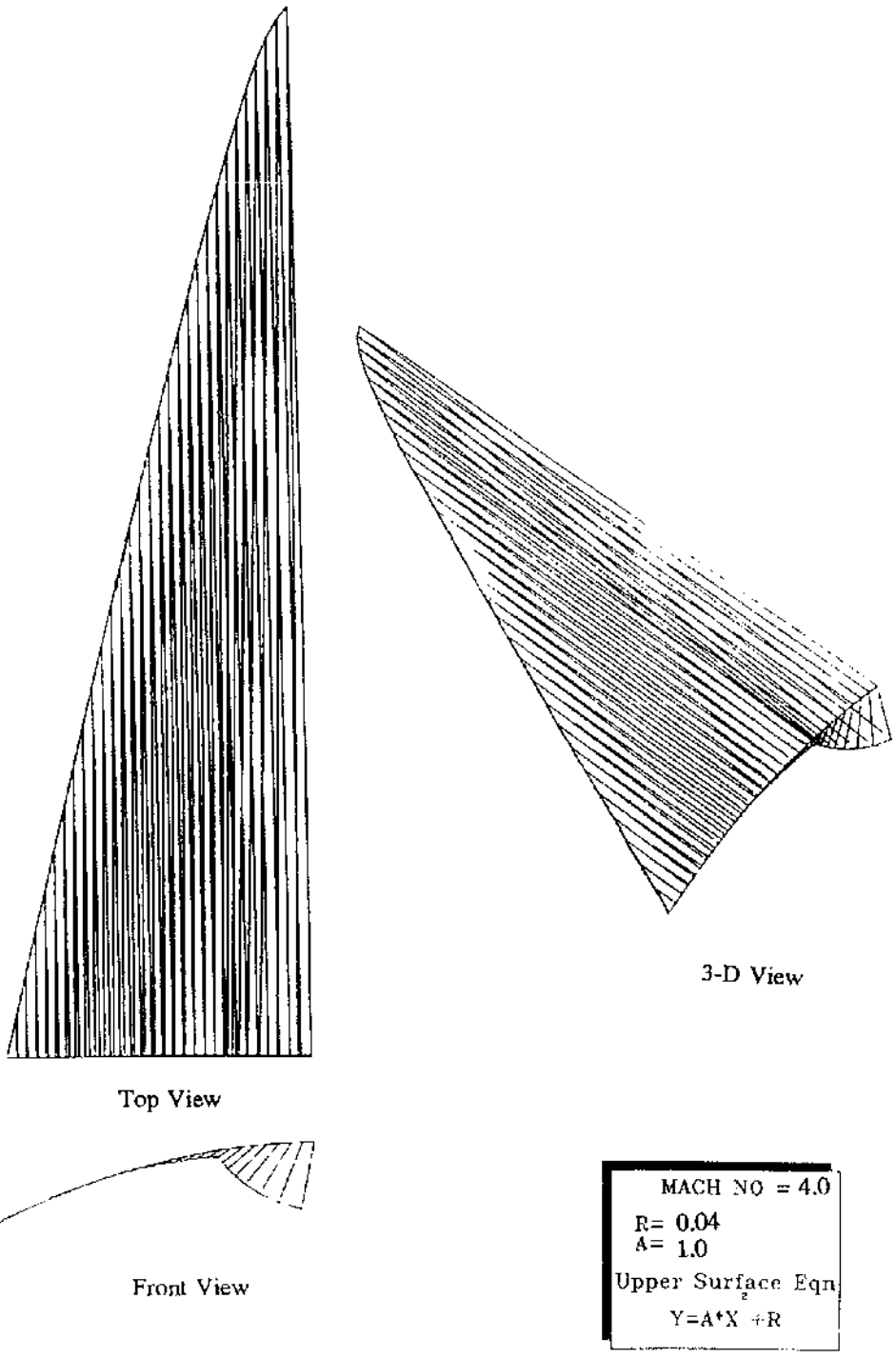

Fig 4.17 Perspective views of a general conical derived waverider (with inclusion of cone body at Mach 4.00)

WAVERIDERS
(Constructed through Conical Flow field)

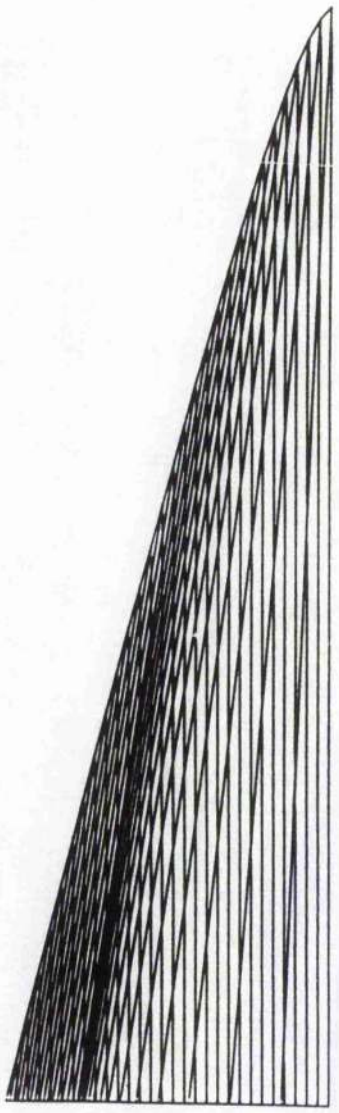

Top View

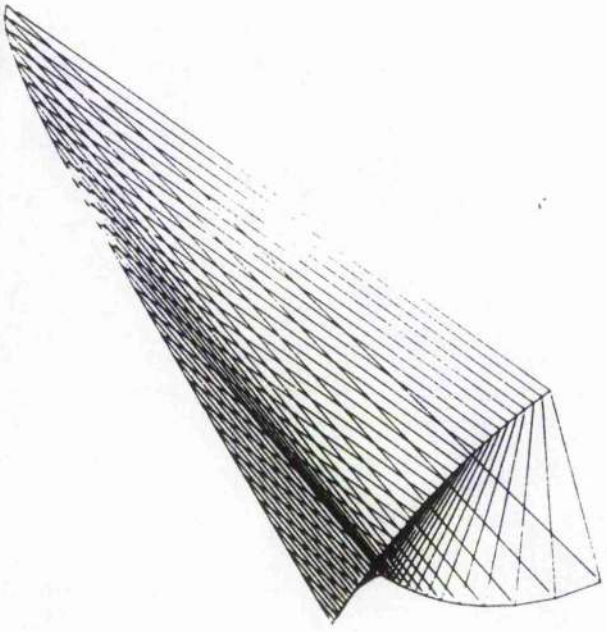

3-D View

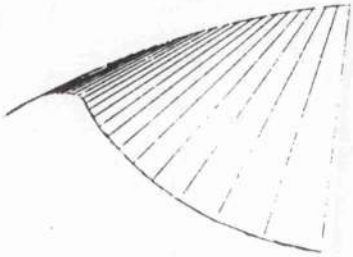

Front View

MACH NO =8.0
R= 0.04
A= 1.0
Upper Surface Eqn
$Y=A*X^2+R$

Fig 4.18 Perspective views of a general conical derived waverider (with inclusion of cone body at Mach 8.00)

WAVERIDERS

(Constructed through Conical Flow field)

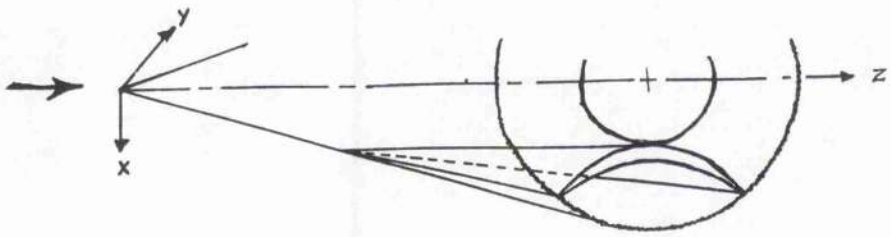

Waverider configuration shown in conical flow field.

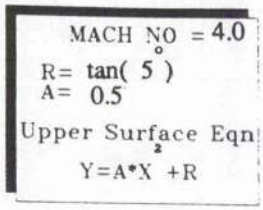

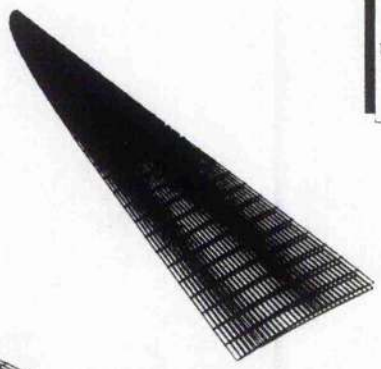

Waverider configuration 3-D

Top View

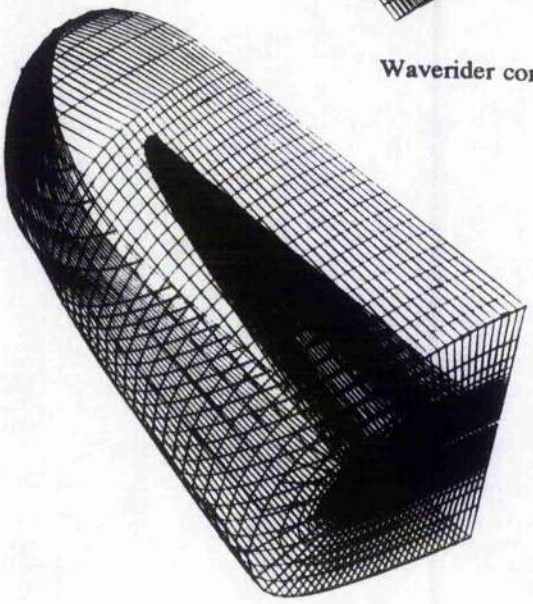

3-D View shown with computational grid (27 60 17)

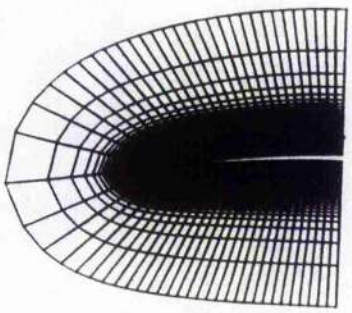

Cross sectional view with grid

Fig. 4.19 Perspective views of a general conical derived waverider (with exclusion of cone body at Mach 4.00).

Ref.[74] describes experiments on these optimised waveriders at M=4 and 6 for a range of incidences between -16° and 14°. Initial results showed that the maximum lift-to-drag ratio was 13% lower than predicted for the Mach 4 case and 6% lower for the Mach 6 case. The difference between the measured and the predicted values was cited to have been caused by the slight detachment of the shock due to off-design behaviour at the design Mach number and angle of attack.

Experimental results on caret wings at hypersonic speeds can also be found in ref[75] and [76].

In the light of the above discussion including theoretical support and experimental review it is suggested that where the caret wing has disadvantages, conical waveriders also have limitations. Although in the past most attention was given to conical derived shapes, it is clear that under certain conditions advantages for wedge derived shapes cannot be ignored. In the present study more general waverider shapes have been derived in a similar fashion from conical as well as wedge flow fields.

Fig(4.17) illustrates a derived inviscid conical flow waverider at a free stream Mach number of 4. Here the upper free stream parabolic surface is placed at R=0.04 with a constant A=1.0 such that the basic shape includes part of the cone (i.e., Jones "A" type). Keeping other parameters constant and increasing the free stream Mach number to 8 demands an increase in the half cone radius thus providing extra usable volume. This is shown in fig(4.18).

The flow around these type A shapes is more complex. If part of the cone is not to be included in the shape, the upper ridge of the waverider can be arranged to be limited to $R_1 > L\tan\theta_c$, where L=cone chord. In this case, the top ridge line always lies beneath the cone body as shown in fig(4.19).

4.5.3 Effect of the leading edge shape for Waveriders.

The general shape of the waverider for conical flow, if the top ridge does not coincide with the cone apex, is non-conical and it may exhibit

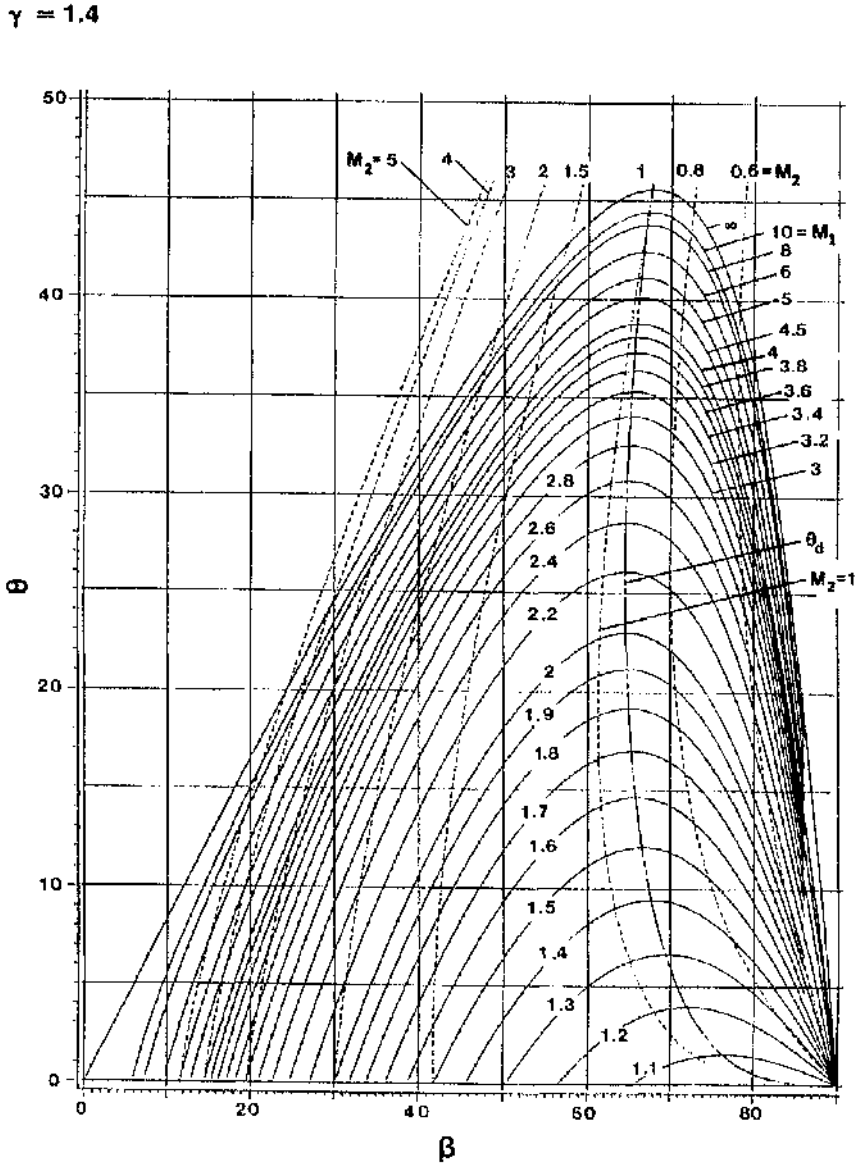

Fig 4.20 Mach number (M) vs Body angle (θ) and Shock angle (β)[34].

complex flow phenomena. As discussed earlier for conical flow derived shapes, streamlines lie in the constant azimuthal angle ϕ and the usable volume advantage can only be achieved if part of the basic cone is included in the shape. The advantages of selecting waveriders as lifting shapes is attributed to their flow simplicity by using shapes defined inversely from a 2-dimensional flow (conical or wedge) as a basis of their construction. Initial treatment through inviscid assumptions of these shapes has demonstrated attractive characteristics and the oblique shock wave relations can be used to carry out initial predictions. Treating the wedge derived shape is more simple resulting in probable higher accuracy whereas treating a curved shock as a plane oblique shock wave, to be used as an approximation for cone derived shapes, is reasonable only as long as its radius of curvature is large compared to the thickness of the shock layer.

The problem reduces to a 2-dimensional one along the leading edge for an attached flow behind the oblique shock wave. As there is no tangential force experienced along the wave front and to fulfill the continuity condition $v_{1t} = v_{2t}$, the flow can be reduced to a one dimensional problem, with a uniform velocity parallel to the wave front superimposed. In the process of flow crossing the discontinuity (shock wave), the normal component of the velocity changes suddenly. As there is no change in the tangential component and direction of the flow, the flow is compressed and turns towards the shock wave. The shock relationships shown in (Appendix I) reveal the different changes in the state variables behind and in front of the shock wave. All these relationships can be applied simply and they show that most of the ratios of these variables are expressed as a simple function of the shock angle and free stream velocity. Pressure, density and temperature ratios across the shock in terms of M_∞ and shock angle (β) are graphically presented in fig(4.20)[34].

To investigate the influence of leading edge shape consider now the flows around waveriders derived from both wedge and cone flowfields. Consider a slice with a negligible thickness (i.e in a 2D sense) from each flow aligned along their respective streamlines. For the wedge derived waverider the slice will lie in the X-Y plane parallel to the free stream flow and will resemble the flow over an approximate 2-D wedge. For the slice of the cone derived waverider the streamline direction will not align with

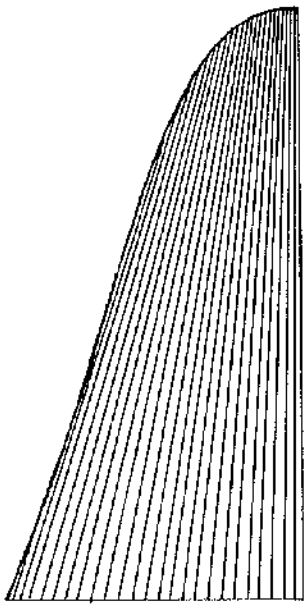

Fig. 4.21
Conical derived waverider.

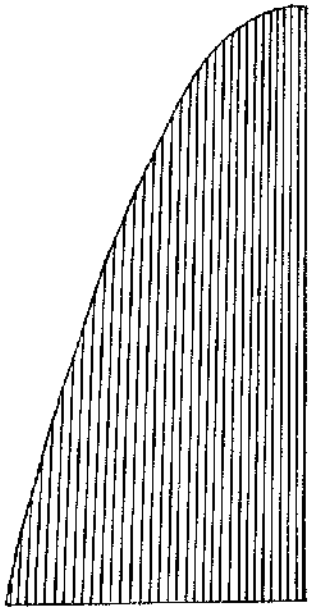

Fig. 4.22
Wedge derived waverider.

Top view for two waveriders derived from same free stream surfaces and flow conditions.

the free stream flow, but will lie in a constant azimuthal angle ϕ. However it will closely resemble a 2D wedge placed in the flow with a slight roll and yaw.

Since both of these general derived waveriders shapes are constructed through the same free stream flow conditions (and assuming that the upper free stream surface is also the same in each case) then it is useful to understand which particular part of the waverider defines the shape of the lower streamline flow and resultant shock shape. It is useful to explore which of the two general waverider shapes, illustrated in fig(4.21) and fig(4.22) and constructed for a particular free stream flow, will produce the highest lift.

Wind tunnel tests will give the definitive answer. However an initial answer is possible if the leading edge shape is known. Both of these waveriders look the same, thus it is not obvious at first glance to say which is more efficient. With closer inspection, however if only the leading edge shapes can be defined, then an answer can be found, as the shape of the leading edge in terms of planform and local wedge angle to the flow is found to be the only parameter which influences the lower streamline flow from wedge- to conical- derived.

For conical flow, when a free stream surface (e.g.,$y=Ax^2+R$) cuts the shock cone ($x^2+y^2=Z^2\tan\beta^2$, $\theta_s=\beta$), the shape of the leading edge curvature projected on the X-Z plane (as shown in fig(4.21)) can be shown mathematically as

$$Z = \left\{ \left[(Ax^2+R)^2 + x^2 \right] \cot^2\beta \right\}^{1/2} \qquad ...(4.12)$$

For the wedge derived shape where the equation for the shock plane is $Y\cos\beta - Z\sin\beta$, which on intersecting the same free stream surface reveals the equation for the leading edge line in the X-Z plane as

$$(Ax^2+ R)\cos\beta - Z\sin\beta = 0 \qquad ...(4.13)$$

or, $$Z = (Ax^2+R)\cot\beta$$

This is shown in fig (4.22).

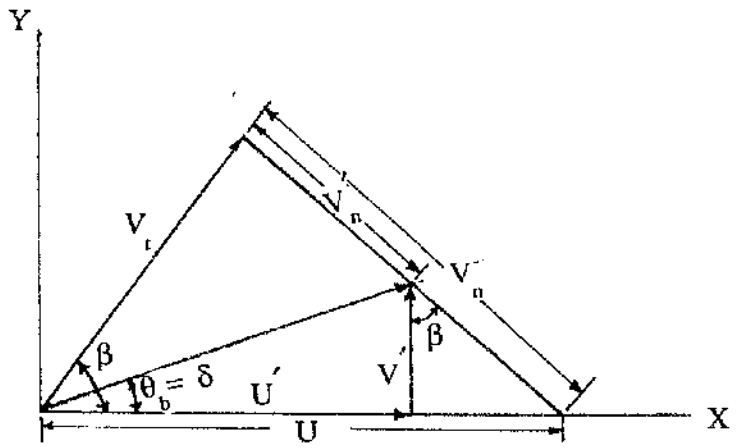

Fig(4.23). Velocity vector across the shock (shock polar).

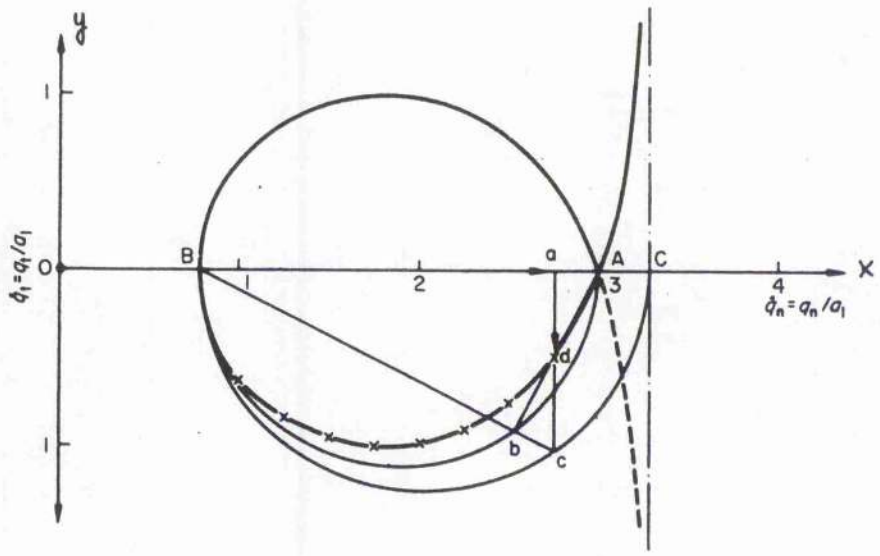

Fig 4.24 Construction of shock polar.

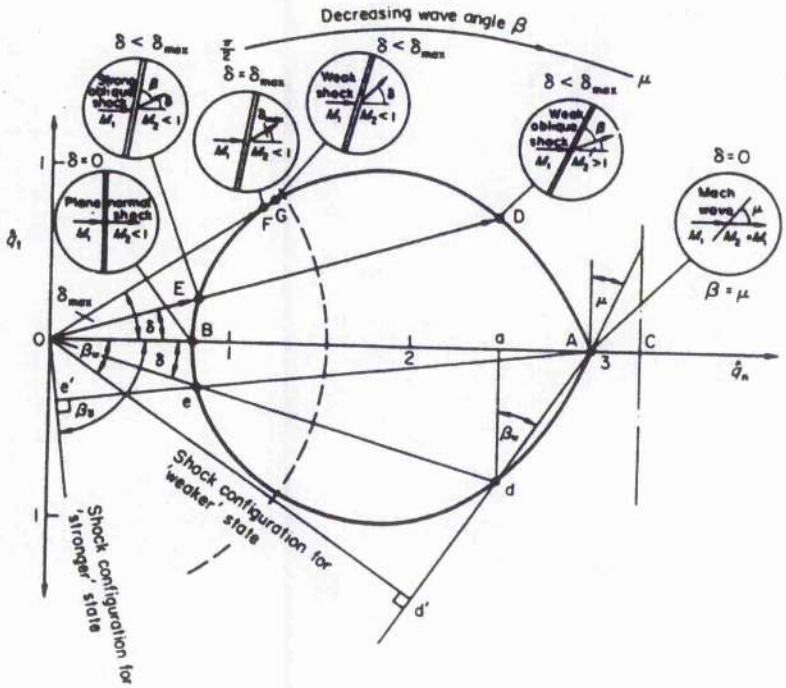

Fig 4.25 Shock polar with operational range. [86]

In order to retain the streamline flow along the free stream direction and thus to contain the flow to optimise lift, a change in leading edge shape may provide extra advantage but the ultimate shape (for extra usable volume) is derived simply by increasing the θ (body deflection angle or wedge angle) along the leading edge to the shock detachment value. These limits can be defined with the help of the shock polar (fig 4.23).

The shock polars illustrated in figs(4.24) and (4.25) provide the different possible flows downstream of an attached shock wave. The important flows to be considered in these figures are those pertinent to the line lying between point A and B (in fig(4.24)). All flows, physically possible, are represented on the closed shock curve. Here the point A is the limiting value which represents an infinitesimal disturbance producing the Mach wave inclined at μ (fig(4.25)) to free stream. Relevant to waveriders, are points on the curve from point F towards A which represents all cases of attached flow on the cone. The line connecting OF, which is tangent to the curve, corresponds to the maximum deflection of the flow.

The angle, θ_{max}, which defines the maximum limit to have the flow attached to the leading edge, can also be found mathematically by differentiating equation(2.7) with respect to β and equating to zero. The result found thus is [86]

$$\sin^2\beta_{max} = \frac{1}{\gamma M_1^2}\left[\frac{\gamma+1}{4}M_1^2 - 1 + \sqrt{(\gamma+1)\left(1+\frac{\gamma-1}{2}M_1^2+\frac{\gamma+1}{16}M_1^4\right)}\right]$$

which substituting in equation (A5.9a) gives θ_{max}. It follows that θ_{max} is theoretically the angle above which the flow is detached. For all points to the right of a point G, which is close to F, the downstream flow is supersonic (attached) and to the left (detached) subsonic.

Since the flow over a waverider, in its ideal on-design case, is part of a wedge flow, the oblique shock polar diagram can be used to explore the increase in the local deflection angle to enhance the usable volume of the waverider as well to provide an indication of the angle of attack limit for operation.

4.6 Cases for Mach 6.00 & Mach 8.00 Waveriders.

The discussion on oblique shock polars developed in the last few pages was applied to the flow over waveriders in order to compare the performance of conical and wedge-derived waveriders. Flowfield conditions used for simulation are shown in table 4.1. Tables 4.2 and 4.3 show the results obtained for two particular free stream flows. To simplify the comparison, it is assumed that the flow for the conical-flow waverider causes a conical streamline flow underneath its surface, as it would for an idealized conical derived waverider. Correspondingly, for the wedge-derived case, the streamline behaviour is equivalent to that obtained from a simple two dimensional wedge placed in the flow.

TABLE : 4.1
Flow conditions for simulation

T_∞ = 64.69 K
ρ_∞ = 0.028945 kg/m^3
P_∞ = 537.41 N/m^2
T_w = 300 K
U_∞ = 935.08 m/s
M_∞ = 6.00 and 8.00
P_o = 689.5 × 10^3 N/m^2
T_o = 500 K

For both conical and wedge-derived waveriders a parabolic shape upper free stream surface given by $Y=AX^2+R$, (in which A=0.5 & $R=Tan\theta_c$) was used. For both cone and wedge-derived shapes, parameters "A" and "R" for each free stream Mach number remain the same. In the procedure, an upper surface trailing edge is first specified from which the free stream is extended towards the shock plane. Where it intersects the respective shock planes defines the leading edge. From the leading edge, the waverider compression surface is defined by the streamlines of the shock layer from the leading edge envelope to the base plane. The definition for this differs for the

cone-and wedge-derived flow approximately. For all cone constructed shapes only type 'B'waveriders (i.e where the originating cone surface is not part of the waverider shape) are considered. For each waverider, it follows that the ridge of the under surface lies at $R=\tan\theta_c$.

Viscous effects are included in the study assuming it is only two dimensional planar flow. Also it is assumed that the flow is totally laminar over the whole body and there is no turbulent or transitional flow.

For the free stream surface, as it has a constant pressure (p_∞), therefore, the flow on this surface is considered equal to a flat plate boundary layer flow. A local skin friction co-efficient $(c_f)_{local}$ is calculated at some distance ℓ from the leading edge by the Blasius formula :

$$c_f = \frac{\tau_w}{q_\infty} \frac{0.664}{(Re_\ell)^{0.5}}$$

where,

$$Re_\ell = \frac{\rho_\infty V_\infty}{\mu_\infty} (z-z_{le}).$$

For the lower surface local skin friction co-efficients are evaluated using conditions behind the shock wave.

The results for Mach number 6 and 8 are included in tables 4.2 and 4.3 which exhibit the change in lift, drag, L/D and wetted area respectively. It can be seen from the table that for the conical waveriders, although a high lift can be achieved by these shapes, under similar conditions a general wedge constructed waverider provides even higher lift.

Table (4.2) shows the data obtained for two general conical constructed shape waveriders for free stream Mach number 6.00 and 8.00 for a shock angle(β) of 15°. For M=6.00 a basic cone with a half cone angle of 10.73° is required to produce this shock angle whereas a θ_c of 12.08° corresponds to the Mach 8.00 case. A lift of 49.32 N can be achieved for the Mach 6.00 general conical derived waverider shape. For the high Mach number the lift increases to 64.14 N for which the planform area also reduces to 0.038 because of the shift of R(top ridge point shift from Y-axis) as a result of

the increase in cone angle. The friction drag for the Mach number 6.00 case is 1.722 N which increases to 2.566 N for a Mach number of 8.00. This reduces the overall L/D to 4.55 from 5.394, a reduction of 15.64%.

TABLE : 4.2

General conical derived shape waverider.

Mach No: M_∞	Shock angle β	Cone angle θ_c	L.Edge Stream l. angle θ_{sl}	Lift L	Drag (Pressure) D	Drag (Friction)	L/D	S_w
				N	N	N		m^2
6.00	15.0°	10.73°	7.18°	49.32	7.42	1.722	5.394	0.1296
8.00	15.0°	12.08°	9.41°	64.14	11.51	2.566	4.555	0.07575

TABLE : 4.3

General wedge derived shape waverider.

Mach No: M_∞	Shock angle β	Cone angle θ_c	L.Edge Stream l. angle θ_{sl}	Lift L	Drag (Pressure) D	Drag (Friction)	L/D	S_w
				N	N	N		m^2
6.00	15.0°	-	7.18°	136.84	17.24	3.78	6.51	0.3476
8.00	15.0°	-	9.41°	167.20	27.73	5.753	4.99	0.2132

One of the prime objectives of the present study was to explore some of the advantages for these general wedge derived shapes over the conically derived ones. For the similar freestream conditions as used for the conical derived flowfield, the general waverider shapes are derived for the wedge. Data due to these are shown in table 4.3.

Results from the wedge derived shapes reveal that a considerably higher value of lift and L/D can be obtained compared with conic-derived shapes, due to the comparatively high contained pressure on their under surface than for the corresponding conically derived waveriders. Fig (4.26) shows the pressure distribution underneath both (conical and wedge derived) shapes. This shows that for general cone derived shapes the pressure is lower near

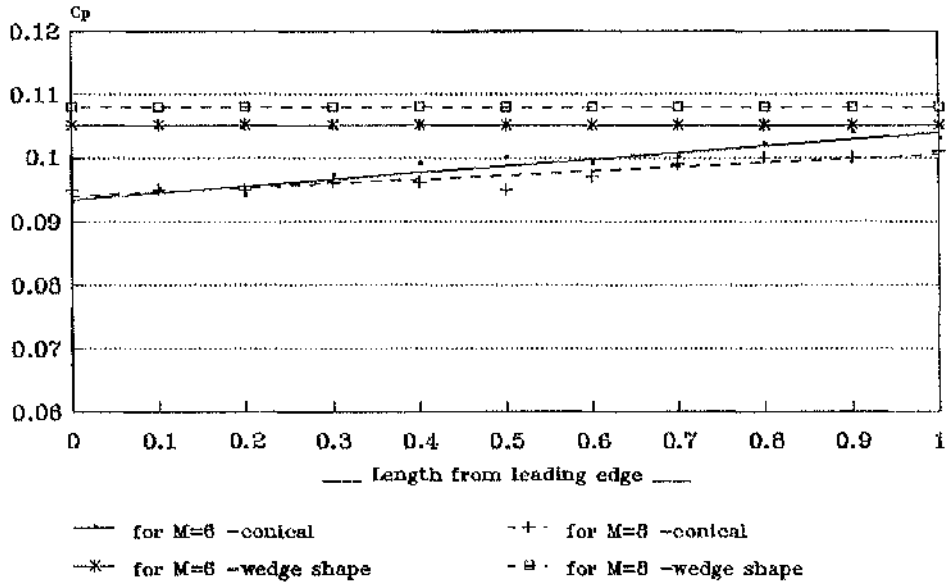

Fig 4.26 Pressure distribution along a cross-section of conical and wedge derived waveriders. (at M_∞ = 6.00 and M_∞ = 8.00)

CONICAL VS WEDGE DERIVED WAVERIDERS

Effect of change in L,D & L/D.

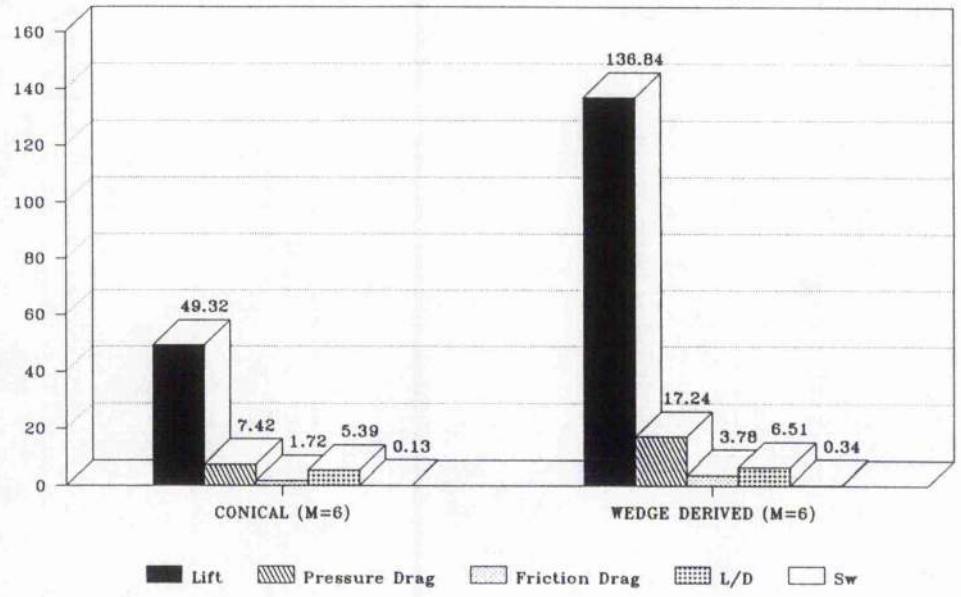

* For Mach number and shock angle const.

Fig(4.27a)

CONICAL VS WEDGE DERIVED WAVERIDERS

Effect of change in L,D & L/D.

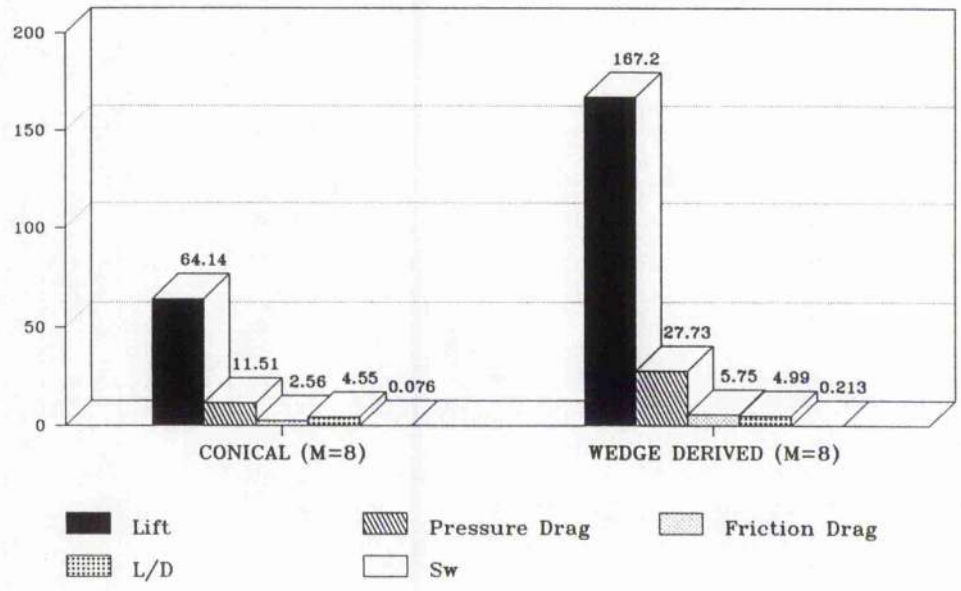

* For Mach number and shock angle const.

Fig(4.27b)

the leading edge and increases gradually to the trailing edge. Even at the highest value it is still smaller than the corresponding wedge derived shape. For the Mach 6.00 case near the leading edge, the contained pressure for the conical case, is 1296 N/m^2 as compared to 1422 N/m^2 for a wedge derived shape, an extra 9.7%. Near the trailing edge it is 1407 N/m^2 for the conical but still less than the wedge constructed shape at 1422 N/m^2. This difference increases for the high Mach number case, where compared to 2598 N/m^2 (pressure for the wedge- shape), for the conic- derived shape the pressure is 2297 N/m^2 near the leading edge and 2434 N/m^2 near the trailing edge.

Table 4.3, shows that a lift of 136.84 N is predicted for the Mach number 6 case with a pressure drag of 17.24. The L/D ratio has an increasing trend for inviscid flow equal to $1/\tan\theta_h$ but the presence of viscous effects reverses the trend reducing it to 6.51 with friction drag equal to 3.78 N. For a free stream Mach number of 8.00 lift, pressure drag and friction drag increases respectively to 167.2, 27.73 and 5.7537 N. Also a comparatively high L/D ratio can be observed (4.99) corresponding to the respective cone derived waverider (4.55).

Regarding the criticism against wedge derived waverider shapes of having sharp leading edges it is important to note that at the leading edge where the waverider rides on the shock plane, the initial streamline angle at the leading edge is the same ($\theta_{sl}=7.18^{\circ}$ for $M_{\infty}=6.00$) and ($\theta_{sl}=9.41^{\circ}$ for $M_{\infty}=8.00$) for both conical and wedge derived waveriders. For conically derived waveriders, a slightly higher volume is achieved at low Mach numbers rather than at high Mach numbers due to a higher deflection of local streamlines, but this effect diminishes at higher Mach numbers. In contrast, for the wedge derived shapes an increase in Mach number will not only increase volume but also lift and L/D ratio. Comparison is shown in fig(4.27a) and fig(4.27b) for both cases.

The increase in wetted area for wedge constructed shapes makes the understanding of the foregoing point difficult. The data in the second row of table 4.4, obtained for wedge flowfield waveriders for Mach number 6.00 with lift equals the corresponding conic waverider, helps clarify this point. The result clearly show that for the same free stream conditions and

CONICAL VS WEDGE DERIVED WAVERIDERS

Effect on other parameters while keeping lift constant.

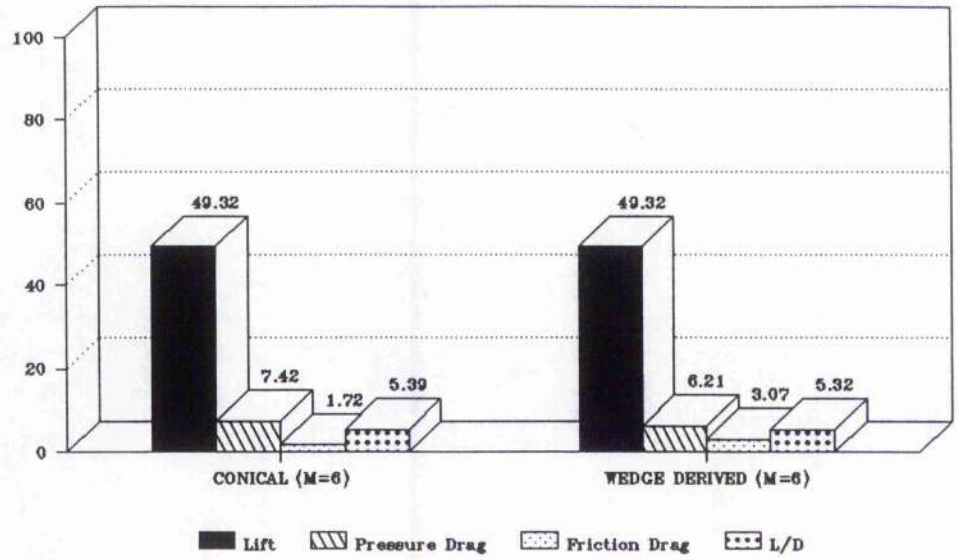

* For M, shock angle & lift constant.

Fig(4.27c)

CONICAL VS WEDGE DERIVED WAVERIDERS

Effect on other parameters while keeping lift & Sp constant & ajdusting Mach no.

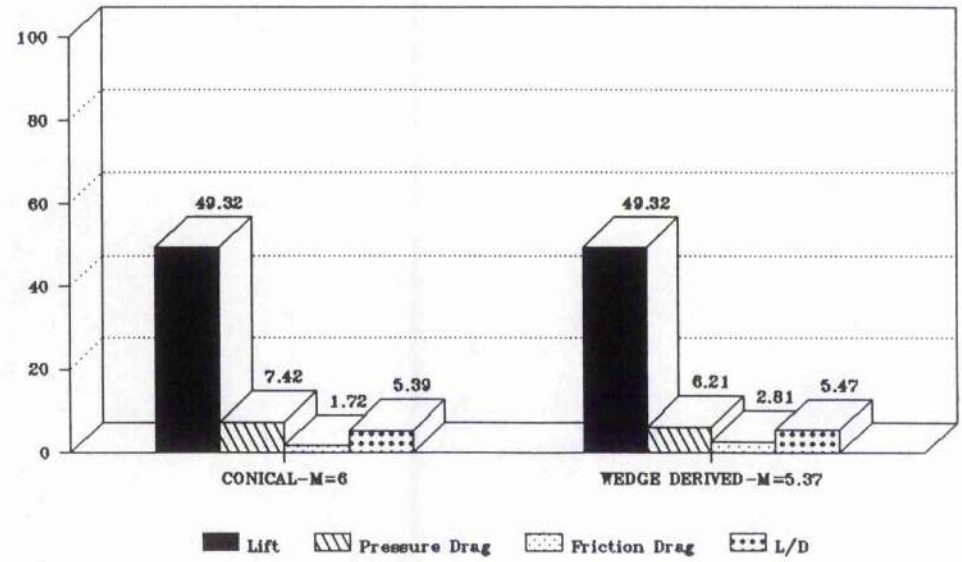

* For shock angle & lift constant.

Fig(4.27d)

a similar top surface shape, to produce the same lift, a 23.65% lesser planform area than the conical derived shape is required. It can also be observed that there is a decrease in pressure drag (D_p=6.213 N). An increase in friction drag (D_f=3.07) is also noted due to the increase in wetted area which results in a decrease of the final L/D ratio (fig 4.27c).

TABLE : 4.4

Comparison of performance

of conically derived and wedge derived waveriders

(for lift kept constant)

Mach No: M_∞	Shock angle β	Cone angle θ_c	L.Edge Stream l. angle θ_{sl}	Lift L	Drag (Pressure) D	Drag (Friction)	L/D	S_w	S_p
				N	N	N		m^2	m^2
6.00	15.0°	10.73	7.18°	49.32	7.42	1.722	5.394	0.1296	.073
6.00	15.0°	wedge	7.18°	49.32	6.213	3.078	5.32	0.2612	.055

TABLE : 4.5

Comparison of performance

of general conically derived and wedge derived waveriders

[(with conic- lift equals wedge- derived waverider lift and $S_p)_{conic} = S_p)_{wedge}$]

Mach No: M_∞	Shock angle β	Cone angle θ_c	L.Edge Stream l. angle θ_{sl}	Lift L	Drag (Pressure) D	Drag (Friction)	L/D	S_w	S_p
				N	N	N		m^2	
6.00	15.0°	-	7.18°	49.32	7.42	1.722	5.394	0.1296	.073
5.376	15.0°	wedge	7.18°	49.32	6.213	2.812	5.47	0.330	.073

Furthermore interesting results can be observed in table 4.5, where, in the second row data is obtained for wedge derived shapes optimized for planform area equivalent to the conical derived waverider. The values here indicate that to achieve the same lift as that of the conical-derived shape, a lesser free stream Mach number (of 5.376 - for wedge) is required (instead

WAVERIDERS

(Constructed through Wedge Flow field)

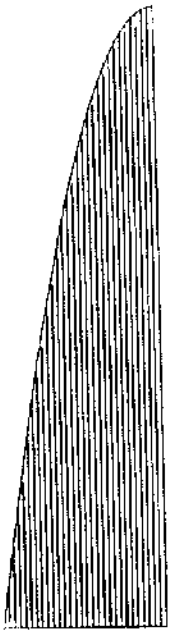

Top View

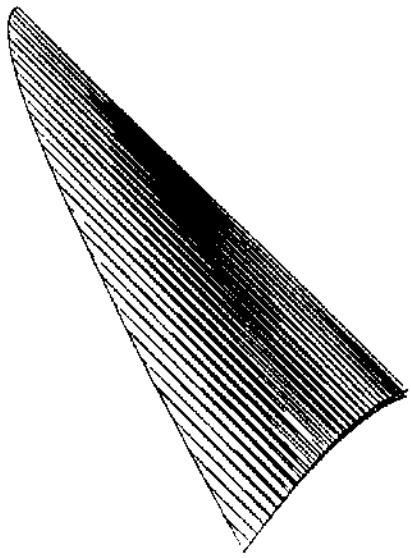

waverider configuration 3-D

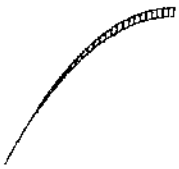

Front View

MACH NO = 4.0
R= 0.0875
A= 0.5
Upper Surface Eqn
$Y=A*X^2+R$

Fig 4.28 Perspective views of a general wedge derived waverider (For Mach No:4.00)

WAVERIDERS
(Constructed through Wedge Flow field)

Top View

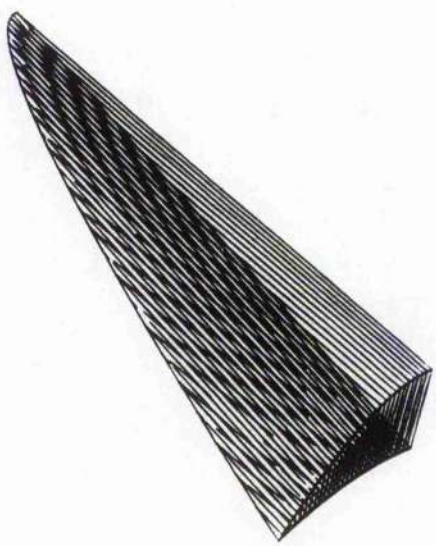

waverider configuration 3-D

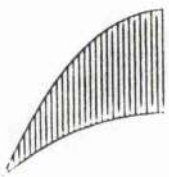

Front View

MACH NO = 8.0
R= 0.0875
A= 0.5
Upper Surface Eqn
$Y=A*X^2+R$

Fig 4.29 Perspective views of a general wedge derived waverider (For Mach No:8.00)

WAVERIDERS
(Constructed through Wedge Flow field)

Top View

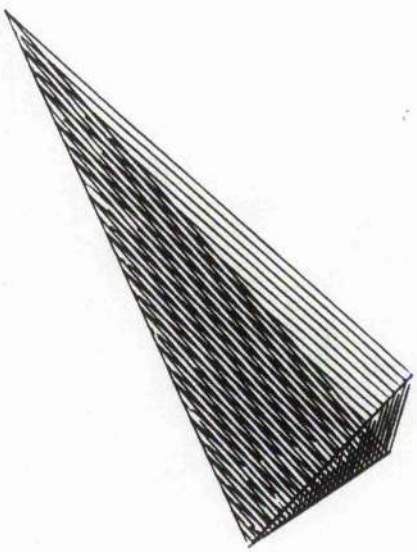

waverider configuration 3-D

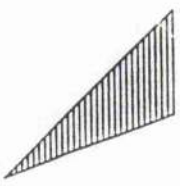

Front View

MACH NO = 8.0
R= 0.0875
A= 0.5
Upper Surface Eqn
Y=A*X +R

Fig. 4.30 Perspective views of an ideal general wedge derived waverider (Caret Wing)-(For Mach No:8.00).

of 6.00 - for conical derived). Also it results in an increase in L/D ratio to 5.47 (fig 4.27d).

An increase in wetted area for wedge constructed shapes may be seen to be the cause of a reduction of the total L/D ratio due to a comparative increase in friction drag. The friction drag included in the study is calculated with an assumption of weak interaction and it is used merely to get the initial estimate of viscous drag. The friction drag is not discussed in detail because the program has been developed to provide the basic input shape for a full Navier Stokes solution which shall include the detailed viscous effects for the final results automatically. An optimum shape can thus be generated by keeping a few parameters constant at a time.

Views of derived general wedge shape waveriders at Mach number = 4.00 and 8.00 are shown in fig(4.28) and fig(4.29) respectively. Changing the top free stream surface to a straight plane an ideal caret wing as shown in fig(4.30) can be constructed.

In order to treat these shapes using a full solution of the Navier Stokes equations, a computational grid is generated. Fig(4.31) and fig(4.32) shows a conical and caret wing placed in the computational grid. This will be useful for further research in the topic.

In the view of above discussion it is appropriate to say that great advantage can be achieved through small changes in the leading edge shape and secondly the limitation often referred to in wedge derived shapes of having little usable volume can also be overcome to a certain extent by using a shock angle close to the maximum value before detachment. A shape derived from such a shock corresponds to an optimum volume distribution. Also, for waveriders, a number of geometrical parameters vary for each change in free stream condition, which complicates the drawing of definitive conclusions. Thus in order to demonstrate the practicality of any waverider an optimization of the shape must be done by studying the relationships between these different parameters.

WAVERIDERS

(Constructed through Conical Flow field)

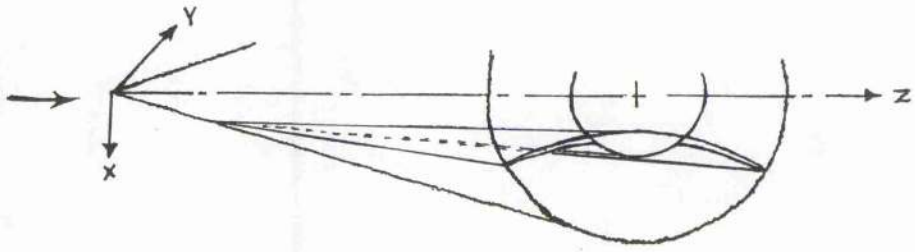

Waverider configuration shown in conical flow field.

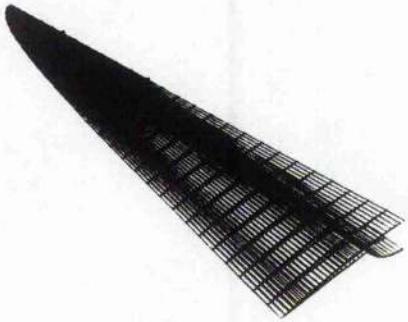

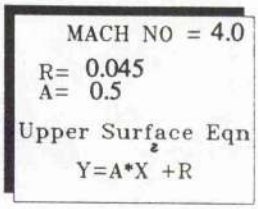

Waverider configuration 3-D

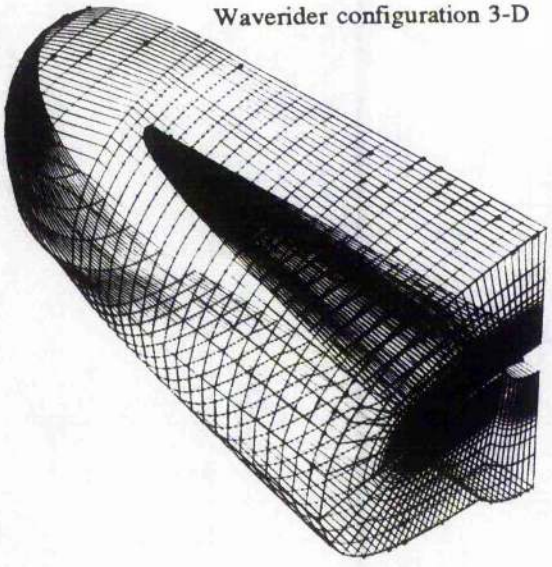

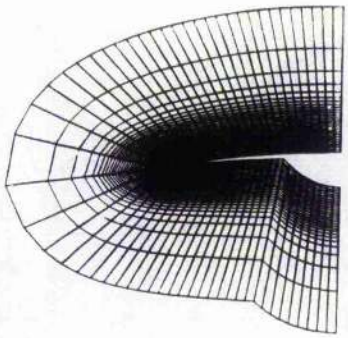

Cross sectional view with grid

3-D View shown with computational grid (27x60x30)

Fig. 4.31 Perspective views of a general conical derived waverider with computational grid.
(with inclusion of cone body at Mach 4.00).

WAVERIDERS

(Constructed through Wedge Flow field)

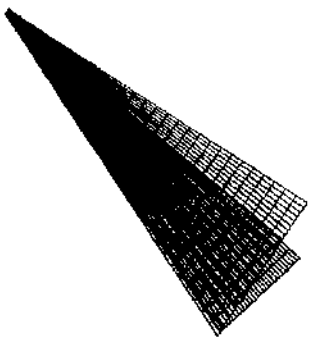

3-D View

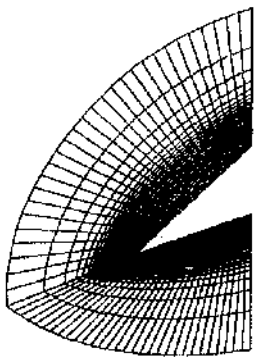

Cross sectional view with grid

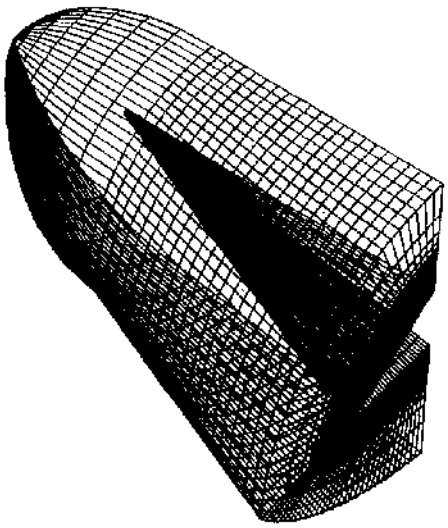

3-D View shown with computational grid (27x60x17)

MACH NO = 8.0
R= 0.0875
A= 0.5
Upper Surface Eqn
z
Y=A*X +R

Fig 4.32 Perspective views of an ideal general wedge derived waverider in computational Grid. (Caret Wing)-(For Mach No:8.00)

CONCLUSIONS AND FUTURE WORK

Following the success of the Space Shuttle, a strong enthusiasm has been observed for further development of hypersonic vehicles. The existence of research vehicle progammes such as X-30, HOPE and HOTOL etc. demonstrates that hypersonic vehicle design is an important technology driver for the next century, in which the objective is that the cost of placing payloads into space will be reduced considerably. As a result of such developments it is expected that to place a normal payload in low earth orbit will cost considerably less than at present. The Space Shuttle is considered as a system of limited flexibility and suffers from excessive downtime between missions. It is clearly not efficient in delivering payloads and personnel to space stations.

For global flights and space missions in the atmospheric phase of the flight, traditional wing-body and slender body configurations have aerodynamic limitations since the high Mach numbers involved result in a loss in efficiency due to wing leading-edges being forced to be supersonic. The waverider type configuration which naturally operates with a supersonic leading edge provides an alternative and as a result spaceplane shapes with a blend of waverider and traditional concepts have been considered in vehicle design.

The waverider has been slow to be accepted, however because to date limited resources have been made available to adequately prove the concept. Techniques in numerical modelling using computational fluid dynamics (CFD) approaches have been limited in computing power for such cases and experimental techniques have been expensive and do not always provide adequate simulation. For example, since in the past there has not been available a sufficient computational capability, studies have been concentrated on idealised waverider shapes at design conditions whilst often ignoring some important flow physics. One of the objectives of the present study was to point out and investigate the effect of removing some of these constraints especially those associated with viscous effects and to consider the best configurations to operate well in near off-design conditions.

In the literature, some work has indeed been reported on the effect of

including viscous flows, but this has been generally done by using boundary layer corrections to the inviscid computation. At hypersonic speeds, especially at high altitudes however viscous interaction with the shock layer becomes important (i.e. $\chi>>1$) and the boundary layer approximation is no longer accurate. Furthermore for off-design conditions, the main flow is no longer simple since complex viscous dominated vortex flows and shock interactions are present and these can contribute substantially to the prediction of overall forces.

Viscous effects from these applications can only be reliably predicted using solutions of the Navier-Stokes equations, which, with models for turbulence and high temperature effects will embrace all of the necessary physics envisaged for flight within the atmosphere (when mean free paths of molecules are small). Now, with the availability of large computers, and the development of efficient computational techniques, Navier-Stokes solvers are becoming practical to apply.

Numerical solution of the full 3-d Navier-Stokes equations currently require particularly large computer resources. Fortunately, for the flow over waverider-type shapes it can be countenanced that a reduced set of Navier-Stokes (NS) equations, would be sufficient for modelling the flow thus making the computer resource required less substantial. For example, thin-layer NS equations which still enable counter-stream separations should be sufficient to tackle the majority of on-design and off-design cases. For sharp nose shapes with streamwise oriented separated regions such as produced by slender wings and bodies, successful efficient solutions should be attainable using the parabolised NS equations. It can be speculated that for the earlier conceived waverider shapes such as the caret shape and for wing-cone combinations in which the flow is nearly conical that the locally conical NS (LCNS) should provide adequate modelling.

A computer code solving the LCNS equations was used to predict the flow over examples of the latter shapes. The range of numerical studies included 4 cases of caret wing optimised for flight at Mach numbers of 1.44, 1.74, 2.51 and 4.93(section 3.4) and 3 cases of a wing cone configuration at Mach 10 at incidences of 5, 10, and 15 degrees(section 3.5). This computational study revealed that :

* viscous effects have significant influence over the flow field even at low Mach number cases and reduce the lift expected from inviscid on-design calculations;
* however, even with substantial viscous interaction, enhanced lift over their conventional counterparts was achieved through the contained flow beneath the waverider shapes tested - this was true even for the cone-wing configurations at high incidence;
* the good comparison between the computations and experimental results demonstrated that modelling these flows over idealised waverider shapes using LCNS equations is reasonably adequate - it also provided considerable detail of the flow that assisted the understanding of the aerodynamics of the configurations;
* the presence of viscous regions changes the effective shape of the body so that the flows are no longer the original simple flow fields (i.e. creates off-design flow cases). It is possible however to restore approximately the desired ideal simple flowfield by altering the Mach number or the angle of incidence - such changes can arrange for the shock to re-attach to the vehicle leading edge.

Existing studies have shown that it is not necessary, however to be constrained to these caret or cone-wing configurations. It is possible to generate more generalised shapes. Most work on generalised waverider shapes to date has been done by imaginatively deriving shapes from flows generated by cones. A numerical method based on the Taylor-McColl theory was developed in this work to assist the generation of such generalised shapes and to help the analysis of the on-design cases of these shapes. However, also in this work, it was recognized that configurations derived from flows generated from wedges have been much neglected in the literature. Thus a numerical method was also developed using oblique shock theory to generate and investigate these later configurations.

A comparative study of examples of cone-derived and wedge derived generalised waveriders was carried out in this research. In this study it was demonstrated:

* that wedge-derived waveriders provided higher lift than the

cone-derived counterparts at the same incidence;

* that wedge derived waveriders were less sensitive to off-design operation - containment of flow was improved in off-design operation over cone derived generalised shapes;
* the leading edge shape and its lower surface orientation to the flow for the two equivalent waveriders are different but not easy to differentiate without careful examination;
* high payload volume for wedge derived waveriders, which had been thought only possible with cone-derived shapes, can be achieved by using the basic flow field from a wedge at high angles of attack up to its shock detachment angle;
* with the use of the shock polar diagram, further refined optimised shapes can be achieved by using a variable leading edge geometry.

It has also been observed from the numerical studies that extra lift can also be generated by arranging for the upper surface to generate vortex lift.

This research has demonstrated that advanced CFD techniques incorporating the Navier-Stokes equations provide a powerful tool to explore in detail waverider aerodynamics in on-design and off-design operation. Such techniques are suitable to deal with the upper surface vortex flows as well as the complex shock interactions that may occur. However this demonstration was done using only a lower order mathematical model (LCNS) mainly because of resource limitations at the time of study. This limited the studies of the effect of viscous flows on configurations to caret and wing-cone configurations. Becoming available now are improved computing facilities and efficient numerical algorithms to tackle higher order reduced, but adequate, models such as PNS which include the ability to predict turbulence and high temperature effects. Since these computer codes can be run just as easily on complex shapes as on simplified ones, such as done in this study, then the flow over the generalised waverider shapes derived from wedge or cone flows can be tackled. This is further enabled since there exist suitable grid generators for Navier-Stokes solvers on such shapes. Future research involves a systematic programme using in turn the configuration design codes, grid generators and CFD codes to explore more in depth the performance of generalised cone- and wedge-derived waverider shapes in hypersonic flows with realistic flow physics.

APPENDIX 1

NORMAL SHOCK WAVE RELATIONSHIPS.

Changes in the flow variables across a shock are obtained by considering the conservation of mass, momentum and energy across the shock front, which is assumed to be infinitesimal thickness.

By conservation of mass

$$\rho_1 U_1 = \rho_2 U_2$$

by conservation of momentum

$$p_1+\rho_1 U_1^2 = p_2+\rho_2 U_2^2$$

and, by conservation of energy

$$h_1+U_{1/2}^2 = h_2+U_{2/2}^2$$

where 1 refers to conditions upstream and 2 refers to conditions downstream. Entropy S also must increase across the shock

$\therefore \quad \Delta S = S_2-S_1>0$

Other relations are as following

$$\text{Temp ratio} = \frac{T_2}{T_1} = \left[\frac{a_2}{a_1}\right]^2$$

$$\frac{T_2}{T_1} = \frac{\left[2\gamma M_1^2-(\gamma-1)\right]\left[(\gamma-1)M_1^2+2\right]}{(\gamma+1)^2 M_1^2} \longrightarrow \frac{2\gamma(\gamma-1)M_1^2}{(\gamma+1)^2}$$

Pressure ratio

$$\frac{p_2}{p_1} = 1+\frac{2\gamma}{\gamma+1}(M_1^2-1) \longrightarrow \frac{2\gamma}{\gamma+1} M_1^2$$

The density, velocity and dynamic head ratios are

$$\frac{\rho_2}{\rho_1} = \frac{U_1}{U_2} = \frac{q_1}{q_2} = \frac{\gamma+1}{(\gamma-1)+(2/M_1^2)} \longrightarrow \frac{\gamma+1}{\gamma-1} \quad \text{as } M_1 \longrightarrow \infty$$

The Mach number behind shock can be calculated by

$$M_2 = \frac{U_2}{a_2} = \left[\frac{(\gamma - 1)M_1^2+2}{2\gamma M_1^2 - (\gamma - 1)}\right]^{1/2} \longrightarrow \sqrt{\frac{\gamma-1}{2\gamma}} \quad \text{as } M_1 \longrightarrow \infty$$

Pressure coefficient

$$c_p = \frac{p_2 - p_1}{\frac{1}{2}\rho_1 U_1^2} = \frac{4}{\gamma+1}\left[1-\frac{1}{M_1^2}\right] \longrightarrow \frac{4}{\gamma+1} \quad \text{as } M_1 \longrightarrow \infty$$

note : When temperature and pressure ratios across the normal shock increases (with M_1^2) the density, the velocity, the dynamic head ratio, Mach number behind the shock and the pressure co-efficient reach limiting values for large M_1 as shown.

APPENDIX 2

OBLIQUE SHOCK WAVE RELATIONSHIPS.

A requirement for an oblique shock is that the tangential component of the velocity is unaltered, where as the normal component obeys the relationship for a normal shock.

The change of temperature, pressure and density across an oblique shock may be simply obtained from equations (for normal shock waves) by replacing M_1 by $M_1 \sin\beta$, where β is shock angle.

Therefore following relationships are obtained again

$$\frac{T_2}{T_1} = \frac{\left[2\gamma M_1^2 \sin^2\beta - (\gamma-1)\right]\left[(\gamma-1)M_1^2\sin^2\beta + 2\right]}{(\gamma+1)^2 M_1^2 \sin^2\beta} \longrightarrow \frac{2\gamma(\gamma-1)M_1^2\sin^2\beta}{(\gamma+1)^2}$$

$$\frac{\rho_2}{\rho_1} = \frac{(\gamma+1)M_1^2\sin^2\beta}{(\gamma-1)M_1^2\sin^2\beta + 2} \longrightarrow \frac{\gamma+1}{\gamma-1}$$

The Mach number behind the shock is given by,

$$M_2^2 = \left\{\frac{(\gamma-1)M_1^2\sin^2\beta + 2}{2\gamma M_1^2 \sin^2\beta - (\gamma-1)}\right\} \times \frac{1}{\sin^2(\beta-\theta)}$$

and, pressure co-efficient

$$c_p = \frac{p_2 - p_1}{\frac{1}{2}\rho_1 U_1^2} = \frac{4}{\gamma+1}\left\{\sin^2\beta - \frac{1}{M_1^2}\right\} \longrightarrow \frac{4}{\gamma+1}\sin^2\beta$$

In addition the velocity component U_2 and V_2 behind the shock are given by

$$\frac{U_2}{U_1} = 1 - \frac{2(M_1^2\sin^2\beta - 1)}{(\gamma+1)M_1^2} \longrightarrow 1 - \frac{2\sin^2\beta}{\gamma+1}$$

$$\frac{V_2}{U_1} = \frac{2(M_1^2 \sin^2 \beta - 1)\cot\beta}{(\gamma+1)M_1^2} \longrightarrow \frac{\sin 2\beta}{\gamma+1}$$

As in case of a normal shock, the temperature and pressure ratio for an oblique shock increases for large Mach numbers, with the square of the Mach numbers (more precisely, with $M_1^2 \sin^2\beta$) where as the other ratios reach limiting values which are independent of Mach number and are function either of γ only, or of γ and shock angle β. $M_1 \sin\beta$ is the normal component, M_n of the incident Mach number M_1.

APPENDIX 3

NAVIER STOKES EQUATIONS (in spherical co-ordinates).

By transforming the Cartesian coordinate into the spherical form, the Navier-Stokes equations in spherical form can be written. A simple coordinate transformation relationships can be used i.e.,

$$\begin{aligned} x &= r \sin\theta \cos\varphi & r &> 0 \\ y &= r \sin\theta \sin\varphi & 0 &\le 0 \le \pi \\ z &= r \cos\varphi & 0 &\le \varphi \le 2\pi \end{aligned}$$

and the resulting equations in spherical coordinates are written in conservation form as

$$\frac{\partial U}{\partial t} + \frac{\partial E}{\partial r} + \frac{\partial F}{\partial \theta} + \frac{\partial G}{\partial \varphi} + H = 0 \qquad \text{.....(A3.1)}$$

where

$$U = r^2 \sin\theta \begin{bmatrix} \rho \\ \rho u_r \\ \rho u_\theta \\ \rho u_\varphi \\ \rho e \end{bmatrix} \qquad \text{.....(A3.2)}$$

$$E = r^2 \sin\theta \begin{bmatrix} \rho u_r \\ \rho u_r^2 + p - \tau_{rr} \\ \rho u_\theta u_r - \tau_{\theta r} \\ \rho u_\varphi u_r - \tau_{\varphi r} \\ (\rho e + p) u_r + q_r - u_r \tau_{rr} - u_\theta \tau_{\theta r} - u_\varphi \tau_{\varphi r} \end{bmatrix} \qquad \text{..(A3.3)}$$

$$F = r \sin\theta \begin{bmatrix} \rho u_\theta \\ \rho u_r u_\theta - \tau_{r\theta} \\ \rho u_\theta^2 + p - \tau_{\theta\theta} \\ \rho u_\varphi u_\theta - \tau_{\varphi\theta} \\ (\rho e + p) u_\theta + q_\theta - u_r \tau_{r\theta} - u_\theta \tau_{\theta\theta} - u_\varphi \tau_{\varphi\theta} \end{bmatrix} \qquad \text{..(A3.4)}$$

$$G = \begin{bmatrix} \rho u_\varphi \\ \rho u_r u_\varphi - \tau_{r\varphi} \\ \rho u_\theta u_\varphi - \tau_{\theta\varphi} \\ \rho u_\varphi^2 + p - \tau_{\varphi\varphi} \\ (\rho e + p) u_\varphi + q_\varphi - u_r \tau_{r\varphi} - u_\theta \tau_{0\varphi} - u_\varphi \tau_{\varphi\varphi} \end{bmatrix} \quad ..(A3.5)$$

$$H = r \sin\theta \begin{bmatrix} 0 \\ -2p - \rho u_\theta^2 - \rho u_\varphi^2 + \tau_{\theta\theta} + \tau_{\varphi\varphi} \\ \rho u_r u_\theta - ctg\theta\ (\rho u_\varphi^2 + p - \tau_{\varphi\varphi}) - \tau_{r\theta} \\ \rho u_r u_\theta + ctg\theta\ \rho u_\theta u_\varphi - ctg\theta\ \tau_{\theta\varphi} - \tau_{r\varphi} \\ 0 \end{bmatrix} \quad .(A3.6)$$

Where shear stress terms are given as follows

$$\tau_{rr} = 2\mu \frac{\partial u_r}{\partial r} - \frac{2}{3}\mu \text{ div } V$$

$$\tau_{\theta\theta} = 2\mu \left(\frac{1}{r}\frac{\partial u_\theta}{\partial \theta} + \frac{u_r}{r}\right) - \frac{2}{3}\mu \text{ div } V$$

$$\tau_{\varphi\varphi} = 2\mu \left(\frac{1}{r\sin\theta}\frac{\partial u_\varphi}{\partial \varphi} + \frac{u_r}{r} + \frac{u_\theta ctg\theta}{r}\right) - \frac{2}{3}\mu \text{ div } V \quad .....(A3.7)$$

$$\tau_{r\theta} = \tau_{\theta r} = \mu \left[r\frac{\partial}{\partial r}\left(\frac{u_\theta}{r}\right) + \frac{1}{r}\frac{\partial u_r}{\partial \theta} \right]$$

$$\tau_{\theta\varphi} = \tau_{\varphi\theta} = \mu \left[\frac{\sin\theta}{r}\frac{\partial}{\partial \theta}\left(\frac{u_\varphi}{\sin\theta}\right) + \frac{1}{r\sin\theta}\frac{\partial u_\theta}{\partial \varphi}\right]$$

$$\tau_{r\varphi} = \tau_{\varphi r} = \mu \left[\frac{1}{r\sin\theta}\frac{\partial u_r}{\partial \varphi} + r\frac{\partial}{\partial r}\left(\frac{u_\varphi}{r}\right)\right]$$

$$\text{div } V = \frac{1}{r^2 \sin\theta}\left[\frac{\partial}{\partial r}(r^2 \sin\theta u_r) + \frac{\partial}{\partial \theta}(r\sin\theta u_\theta) + \frac{\partial}{\partial \varphi}(r u_\varphi)\right]$$

and heat flux is defined as,

$$q_r = -k\frac{\partial T}{\partial r}$$

$$q_\theta = -k\frac{1}{r}\frac{\partial T}{\partial \theta} \quad .....(A3.8)$$

$$q_\varphi = -k\frac{1}{r\sin\theta}\frac{\partial T}{\partial \varphi}$$

APPENDIX 4

TAYLOR MACCOLL CONICAL FLOW RELATIONSHIP

For an axisymmetric or quasi 2-Dimensional flow

$$\frac{\partial}{\partial \phi} \equiv 0 \qquad \text{(Axisymmetric flow)} \qquad ...(A4.1)$$

$$\frac{\partial}{\partial r} \equiv 0 \qquad \text{(Conical flow)} \qquad ...(A4.2)$$

and thus, when the flow is independent of ϕ, provided the semi vertex angle is not greater than the shock detachment angle, there will be a conical shock wave attached to the apex of the cone.

Therefore, the continuity equation can now be written as

$$\nabla.\rho V = 0$$

or, in polar co-ordinates,

$$\nabla.(\rho V) = \frac{1}{r^2}\frac{\partial}{\partial r}(r^2 \rho V_r) + \frac{1}{r\sin\theta}\frac{\partial}{\partial \theta}(\rho V_\theta \sin\theta) + \frac{1}{r\sin\theta}\frac{\partial}{\partial \theta}(\rho V_\phi) = 0$$

Evaluating the derivative and applying (A4.1) and (A4.2)

$$\text{then} \quad \nabla.(\rho V) = 2\rho V_r + (\rho V_\theta \cot\theta) + \rho \frac{\partial V}{\partial \theta}\theta + V_\theta \frac{\partial \rho}{\partial \theta} = 0 \qquad ...(A4.3)$$

For the attached supersonic flow over a cone, the streamline increases from θ' just downstream of the shock to θ_c when it comes close to the surface far downstream. Since the shock wave surface is conical and of uniform strength, the following assumptions can be used :

(1) The increase in entropy across the shock is same for all streamlines, thus $\Delta S = 0$ in the shock layer;

(2) The flow is adiabatic and steady, therefore, $\Delta H_o = 0 = H_2 - H_1$ where, H_1 is the enthalpy before the shock and H_2 is the enthalpy after the shock;

(3) For irrotational conical flow, $\nabla \times V = 0$,

$$\text{therefore,} \quad \nabla\times V = \frac{1}{r^2\sin\theta}\begin{vmatrix} e_r & e_\theta & (r\sin\theta)\,e_\phi \\ \partial/\partial_r & \partial/\partial_\theta & \partial/\partial_\phi \\ V_r & rV_\theta & r\sin\theta V_\phi \end{vmatrix} = 0. \quad \text{(A4.4)}$$

On applying axisymmetric ($\partial/\partial\phi\equiv 0$) and conical flow ($\partial/\partial r\equiv 0$) conditions to the above equation, this simplifies to

$$V_\theta = \frac{\partial V_r}{\partial \theta} = 0 \qquad \text{...(A4.5)}$$

In order to carry out the analytical treatment of the flow between the cone and the shock,

$$dp = -\rho V dV$$

where, $V = \sqrt{V_r^2 - V_\theta^2}$

and $dp = -\rho(V_r dV_r + V_\theta dV_\theta)$ ....(A4.6)

also under the isentropic conditions,

$$dp/d\rho = \partial p/\partial\rho)_s = a^2$$

or, $$dp/\rho = -\frac{1}{a^2}(V_r dV_r + V_\theta dV_\theta) \qquad \text{....(A4.7)}$$

For energy conversation, $H_\circ = H + \frac{V^2}{2}$ = constant, and we can define a reference reference velocity (V_{max}), which is the maximum theoretical velocity obtained from a fixed reservoir condition. When $V=V_{max}$ the flow has expanded to zero enthalpy, hence H = 0.

For a perfect gas, $H_\circ = C_p T + \frac{V^2}{2}$ = Constant

and also for an inviscid adiabatic steady flow with no body forces the total enthalpy is constant along a given streamline.

i.e $$H_\circ = \text{Constant} = \frac{\gamma}{\gamma-1} RT + \frac{V^2}{2} = \frac{a^2}{\gamma-1} + \frac{V^2}{2} = \frac{V_{max}^2}{2}.$$

and

$$a^2 = (V_{max}^2 - V^2)\frac{\gamma-1}{2} \quad \text{where,} \quad V^2 = V_r^2 + V_\theta^2 \qquad \text{...(A4.8)}$$

substituting (A4.8) in (A4.7) gives Euler's form for studying conical flow.

$$dp/\rho = -\frac{2}{\gamma-1}\frac{(V_r dV_r + V_\theta dV_\theta)}{(V^2_{max} - V_r^2 - V_\theta^2)} \qquad (A4.9)$$

Equations (A4.3), (A4.5) and (A4.9) are three equations with three dependent variables ρ, V_r and V_θ. Since these equations describe axisymmetric conical flow conditions, there exists only one independent variable i.e., θ and hence they can be written in ordinary differential form as,

$$2V_r + (V_\theta \cot\theta) + \frac{dV_\theta}{d\theta} + V_\theta \frac{d\rho}{d\theta}\frac{1}{\rho} = 0 \qquad ...(A4.10)$$

and, $$V_\theta = \frac{dV_r}{d\theta}$$

$$dp/d\theta = -\frac{2}{\gamma-1}\rho\frac{(V_r\frac{dV_r}{d\theta} + V_\theta\frac{dV_\theta}{d\theta})}{(V^2_{max} - V_r^2 - V_\theta^2)} \qquad ....(A4.11)$$

putting (A4.11) into (A4.10)

$$2V_r + (V_\theta\cot\theta) + \frac{dV_\theta}{d\theta} + -\frac{2}{\gamma-1}V_\theta\frac{(V_r\frac{dV_r}{d\theta} + V_\theta\frac{dV_\theta}{d\theta})}{(V^2_{max} - V_r^2 - V_\theta^2)}$$

or, $$\frac{\gamma-1}{2}(V^2_{max} - V_r^2 - V_\theta^2)(2V_r + V_\theta\cot\theta + \frac{dV_\theta}{d\theta}) - V_\theta(V_r\frac{dV_r}{d\theta} + V_\theta\frac{dV_\theta}{d\theta}) \quad ...(A4.12)$$

putting value of $V_\theta = \frac{dV_r}{d\theta}$ in the above equation gives,

$$= \frac{\gamma-1}{2}\left\{2h + V^2 - V_r^2 - \left[\frac{dV_r}{d\theta}\right]^2\right\}\left\{2V_r + \frac{dV_r}{d\theta}\cot\theta + \frac{d^2V_r}{d\theta}\right\}$$

$$- \frac{dV_r}{d\theta}\left(V_r\frac{dV_r}{d\theta} + \frac{dV_r}{d\theta}\frac{d^2V_r}{d\theta^2}\right) = 0 \qquad ...(A4.12a)$$

eqn(A4.12a) is the conical form of the Taylor Maccoll equation, and can be further transformed into non-dimensionalised form as

$$= \frac{\gamma-1}{2}\left\{1 - V_r^2 - \left[\frac{dV_r'}{d\theta}\right]^2\right\}\left\{2V_r' + \frac{dV_r'}{d\theta}\cot\theta + \frac{d^2V_r'}{d\theta}\right\}$$

$$-\frac{dV_r'}{d\theta}\left(V_r'\frac{dV_r'}{d\theta}+\frac{dV_r'}{d\theta}\frac{d^2V_r'}{d\theta^2}\right)=0 \qquad \text{...(A4.12b)}$$

where $V'=\dfrac{V}{V_{max}}$

and is a function of Mach number $\left[V'=f(M)\right]$ only, so

$$V'=\frac{V}{V_{max}}=\left[\frac{2}{(\gamma-1)M^2}+1\right]^{-1/2}$$

equation (A4.12b) can be more simplified by putting $\gamma=\frac{7}{5}$ and $V'=\frac{dV_r'}{d\theta}=U'$, and the Taylor Maccoll equation can be expressed in another form as

$$(6U'^2-1+U^2)U''=2U(1-U^2)+(1-U^2)U'\cot\theta-7UU'^2-U'^3\cot\theta \quad \text{...(A4.13)}$$

APPENDIX 5

The Shock Polar Diagram

A shock polar is the locus of equations satisfied by the components u_2 and v_2 of the velocity behind the shock. The curve is then the exit vector velocity curve uniquely determined by the particular free stream velocity and covers all the possible exit flows down stream of an attached shock wave.

Along the stream lines for a steady flow the velocity and pressure can be expressed as (Bernoulli's eqn.)

$$VdV + \frac{dp}{\rho} = 0 \qquad \text{...(A5.1)}$$

and, as flow is adiabatic, therefore, introducing $\rho = \frac{\rho_1 \cdot p^{\frac{1}{\gamma}}}{p_1^{\frac{1}{\gamma}}}$

in above equation it can be written as ,

$$\frac{V^2 - V_1^2}{2} + \frac{\gamma}{\gamma-1} \frac{p_1^{1/\gamma}}{\rho_1} \left(p^{\frac{\gamma-1}{1}} - p_1^{\frac{\gamma-1}{1}} \right) = 0$$

or,

$$\frac{1}{2} V^2 + \frac{\gamma}{\gamma-1} \frac{p}{\rho} = \frac{1}{2} V_1^2 + \frac{\gamma}{\gamma-1} \frac{p_1}{\rho_1} \qquad \text{...(A5.2)}$$

which shows that for a given mass of gas sum of kinetic and potential energy along a stream line remains constant provided $\frac{p}{\rho^{\gamma}}$ = const. By substituting and simplifying terms of normal and tangential components (fig(A5-1)) it results in

$$V_n'(6V_n^2 + 6C^{*2} - V_t^2) = V_n(6V_n'^2 + 6C^{*2} - V_t^2)$$

or, in factored form

$$(V_n - V_n')(6V_n V_n' - 6C^{*2} + V_t^2) = 0$$

where primes denotes values behind the shock. And, as $(V_n - V_n') \neq 0$, therefore,

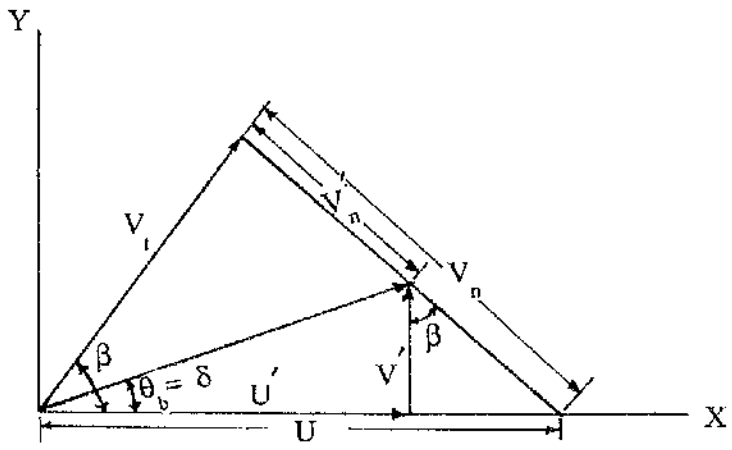

Fig (5-I) Velocity vector across the shock (shock polar).

$$V_n V_n' = C^{*2} + \frac{V_t^2}{6}) = 0 \qquad \text{...(A5.3)}$$

By substituting the following velocity values from rectangular coordinates (U,V and U', V') in above relationship (ref fig A-I)

$$V_t = V_t' = U\cos\beta$$
$$V_n = U\sin\beta$$

and, $$V_n' = U\sin\beta - \frac{V'}{\cos\beta}$$

A general relationship is obtained as follows.

$$U^2\sin^2\beta - UV'\tan\beta = C^{*2} - \frac{1}{6}U^2\cos^2\beta. \qquad \text{...(A5.4)}$$

Now if β is to be eliminated, from fig(A5-I), putting

$\beta = \tan^{-1}\left\{\frac{U - U'}{V'}\right\}$, further simplification reveals that

$$V'^2(C^{*2} + \frac{5}{6}U^2 - UU') = (U-U')^2(UU' - C^{*2}). \qquad \text{...(A5.5)}$$

In non-dimensionalized form if (V'/C^* & U'/C^*) are considered as variables x and y, and the whole equation is divided by C^{*2}, then, the equation for the resultant shock polar becomes

$$y^2(1 + \frac{5}{6}M^{*2} - M^*x) = (M^* - x)^2(M^*x - 1). \qquad \text{...(A5.6)}$$

At any arbitrary point

$$\tan\theta = \frac{y}{x}, \text{ and } \tan\beta = \left\{\frac{U - U'}{V'}\right\} = \frac{M^* - x}{y}. \qquad \text{...(A5.7)}$$

Here y and x are merely the exit radial and tangential velocities expressed in terms of polar components. The reference or datum line aligns itself to the free stream velocity direction V_1. The resultant shock polar equation (A5.6) is uniquely determined by free stream Mach number. For any free stream Mach number there is only one unique shock polar curve. For y=0, possible solutions are $x = M^*$ and $x = \frac{1}{M^*}$. There is a third possible solution when $x = \frac{1}{M^*} + \frac{5}{6}M^*$, but this has no physical significance because then y becomes infinity and the line becomes only a vertical asymptote of the

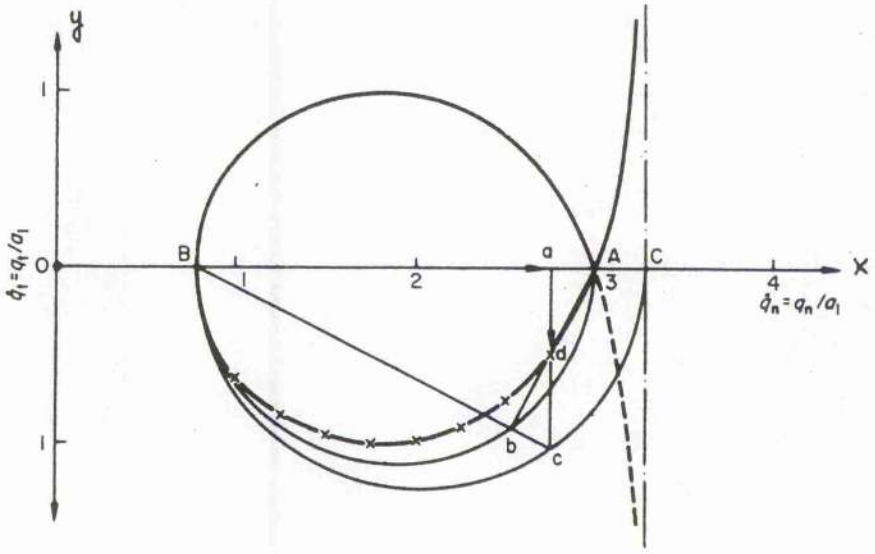

Fig (5-II) Construction of shock polar.

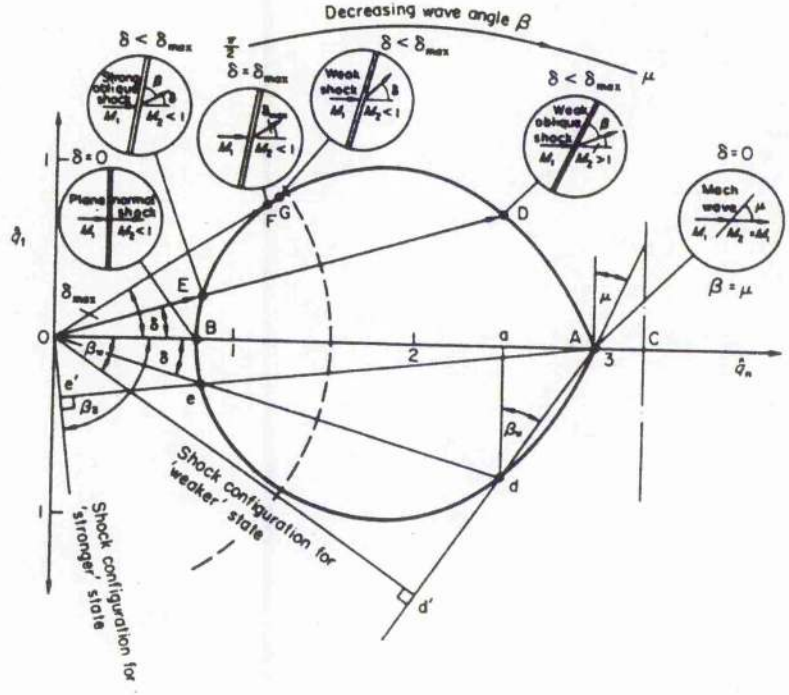

Fig (5-III) Shock polar with operational range.

curve. Furthermore this interval $M^* < x < \frac{1}{M^*} + \frac{5}{6}M^*$, is not physically possible since it implies that the exit flow is greater than the inlet flow. All these three points for M>1 can be seen in fig(A5-II) where pt A corresponds to $x = \frac{1}{M^*}$and, B and C corresponds to $x = \frac{1}{M^*}$ for y=0 and $x = \frac{1}{M^*} + \frac{5}{6}M^*$ for y= ∞. From the fig(A5-II) it also appears that the main significant point of the shock polar is between point A and B. All different physically possible flows can be represented on the closed shock portion of the curve.

Considering figure (A5-III) point A can be seen as a limiting value for an exit flow velocity which corresponds to a free stream subjected to an infinitesimal disturbance and which produces the Mach wave inclined at μ to the free stream but produces no deflection to the stream and no change to the exit velocity.

In the intermediate region, for example at point D, the polar cuts the curve at point E, and physically represents the flow through a particular oblique shock, the inlet stream of direction and magnitude given by OA being deflected through an angle θ to give a flow of magnitude and direction given by vector OD (or od). The ordinates of OD gives normal and tangential exit velocity components. Corresponding wave angle β_w(for weak shock) can be shown as

$$\tan\beta_w = \frac{M_1^* - x}{y} = \frac{(OA)-(oa)}{(ad)} = \frac{(aA)}{(ad)} \qquad ...(A5.8)$$

A similar approach can be adopted for point E where ordinates correspond to normal and tangential components for a strong solution. The orientation of β_s (for the strong solution) suggests that the wave is nearly normal to the flow. Thus in this case the velocity drop for the same flow deflection (OD) for (OE) is much greater, and is normally subsonic.

To achieve the maximum deflection angle for flow attached to the leading edge, differentiation of equation (2.7) reveals [86]

$$\sin^2\beta_{max} = \frac{1}{\gamma M_1^2}\left[\frac{\gamma+1}{4}M_1^2 - 1 + \sqrt{(\gamma+1)\left(1+\frac{\gamma-1}{2}M_1^2 + \frac{\gamma+1}{16}M_1^4\right)}\right] ...(A5.9)$$

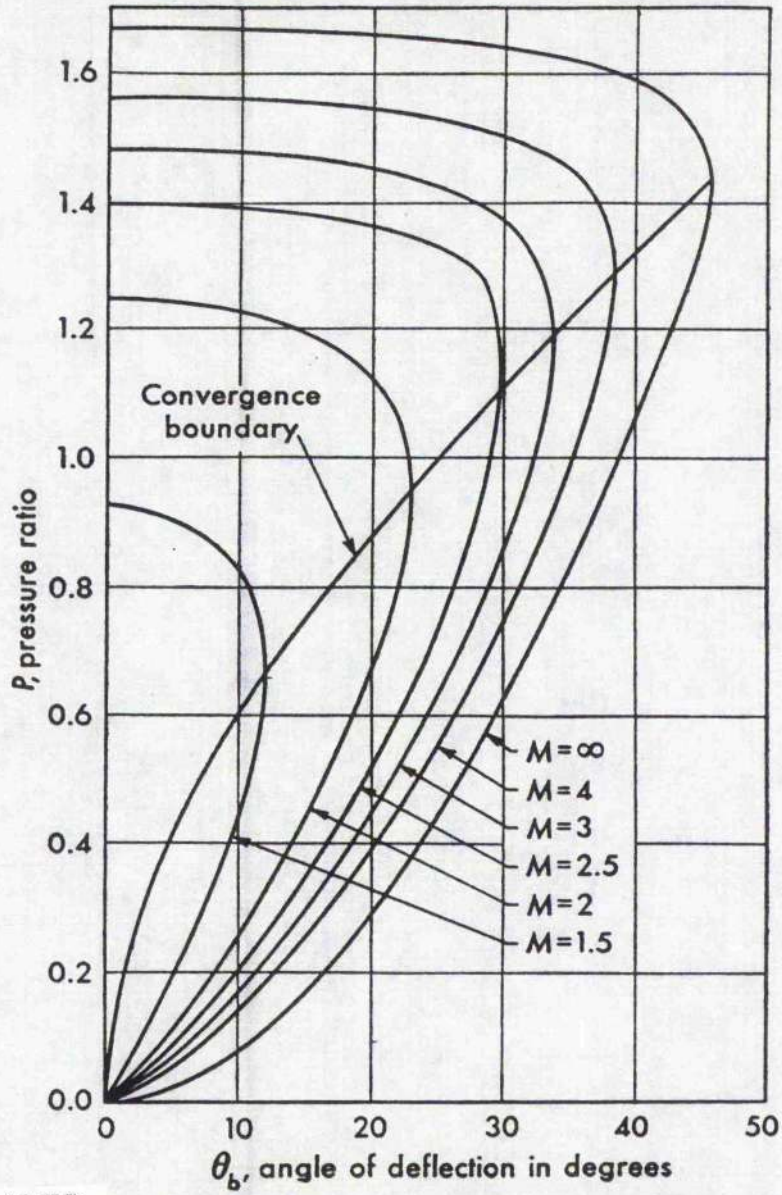

Fig (5-IV) Maximum attainable pressure for a particular flow. (area of interest is from origin to convergence boundary)[85]

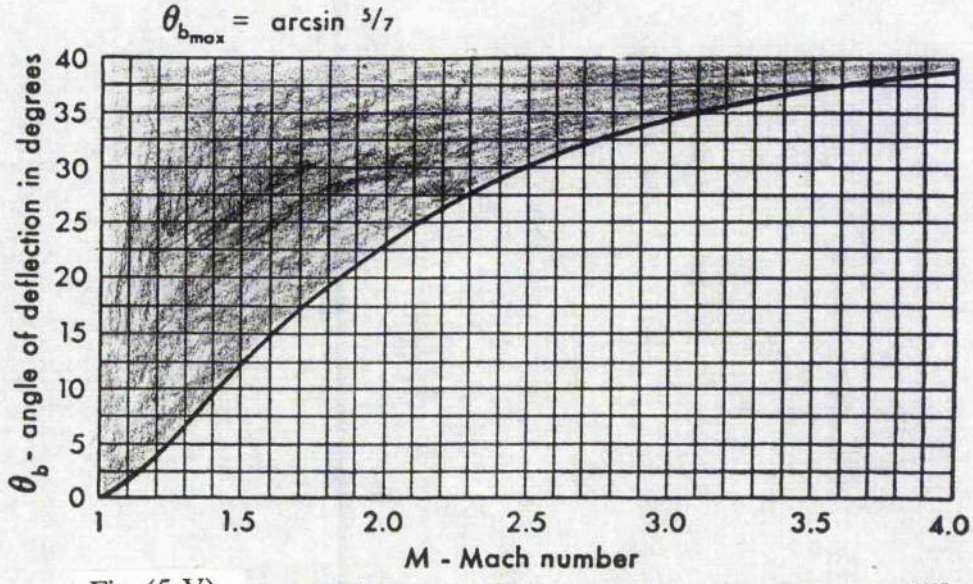

Fig (5-V) Regions of attached and detached shock wave.[85]

which, substituting in, $$\frac{\tan\beta}{\tan(\beta-\theta)} = \frac{(\gamma+1)M_1^2 \sin^2\beta}{2+(\gamma-1)M_1^2\sin^2\beta} \quad ...(A5.9a)$$

results in θ_{max}.

To assist the study of waverider shapes based on wedge flows a relationship to find out the optimum value of θ_b to gain maximum pressure with an attached shock is sought. It is noticed that a significant number of variables along the wave front can be expressed as a product of $M\sin\beta$. Using the general relationship for β, θ_b and M and by introducing the parameter c_p expressed in terms of the above, β can be eliminated. The final result is given as

$$\cot\theta_b = \left[\frac{6M^2}{5M^2\left(\frac{3}{5}c_p + \frac{1}{M^2}\right)-5} - 1\right]\tan\beta \quad ...(A5.10)$$

or alternatively

$$c_p^2\left[3M^2c_p + 5 - 5M^2\right] = \left[5 + 3M^2c_p\right]\left[c_p - 2\right]^2\tan^2\theta_b \quad ...(A5.11)$$

The coefficient of pressure, c_p for different Mach numbers given by eqn.(A5.11) is plotted in figure (A5-IV). Here the locus of points for any Mach number for infinite slope of c_p is determined, which marks the maximum value of pressure, which can be obtained for a particular value of M with an attached shock wave [85]. Under this condition, the equation reduces to

$$9M^2c_p^2 - 2(5M^2-5 + 7\sin^2\theta_b M^2)c_p + 4\sin^2\theta_b(3M^2-5) = 0 \quad ...(A5.12)$$

By putting $\sin^2\theta_b = K$, in order to determine the boundary, locus boundary and eliminating M between (A5.11) and (A5.12), we get

$$4(7c_p^2 - 14c_p + 12)K^2 - 4c_p(6c_p^2 - 11c_p + 10)K + 3c_p^4 = 0 \quad ...(A5.13)$$

Solving the simple quadratic equation

$$\text{then } K = c_p\,\frac{6c_p^2 - 11c_p + 10 - \sqrt{5}\sqrt{3c_p^4 - 18c_p^3 + 41c_p^2 - 44c_p + 20}}{2(7c_p^2 - 14c_p + 12)} \quad ...(A5.14)$$

This equation is illustrated in fig(A5-V) which gives the maximum value of c_p attained for particular M with an attached shock wave.

For designing the optimum wedge derived shapes for a particular value of M a useful idea is to plot all these intersection points as Mach numbers versus body angle (wedge angle θ_b) as shown in fig(A5-V). Now the upper coloured portion shows the detached shock condition and the lower half shows the attached shock to the leading edge with the values close to the curve promising maximum lower surface pressure. An equation for the curve can be derived by considering the maximum boundary of β-θ graph i.e., by considering for $M \longrightarrow \infty$ in β-0-M relationship ($\theta=\theta_b$),

$$\cot\theta_b = \left[\frac{6}{5\sin^2\beta} - 1\right]\tan\beta$$

and finding the maximum of this curve in equation (A5.10), resulting in

$$7M^4\sin^4\beta-(10-6M^2)M^2\sin^2\beta-(6M^2+5) = 0 \qquad ...(A5.15)$$

Because, for our design of waverider, body shape is more important, therefore, from (A5.10) and (A5.15) β can be eliminated to get the results in terms of θ_b, which is the final equation for the curve in fig(A5-V), and the resultant equation is as following.

$$\sin^2\theta_b = \frac{25}{98M^2}\times\frac{9M^6-80M^4-2M^2-170+\sqrt{3}\,(3M^4+4M^2+20)^{\frac{3}{2}}}{9M^4+5M^2+25} \qquad ...(A5.16)$$

REFERENCES

1. R.M.William, "National Aero Space Plane : technology for America's future.", Aerospace America, Nov 1986, Pg 18-22.
2. I.R.Yates, "Future Aerospace projects for engineering the future for UK Ltd.", Aerospace Dynamics, No 24, 1988,Pg 14-27.
3. R.D.Neumann, "Defining the aero thermodynamic methodology-II." Proceedings of joint Europe-US short course on hypersonic, University of Texas at Austin, Nov-1987.
4. L.H. Townend. "Some design aspects of Space Shuttle Orbiter." Progress in Aerospace Sciences, vol.13, 1972, pp. 81-135
5. L.H. Townend. "Research and design for lifting re-entry vehicles.", Progress in Aerospace Sciences, vol.18, 1979, pp. 1-80.
6. T.R.F. Nonweiler. "Aerodynamic problems of manned space vehicles", J.R. Aero. Society, vol 65, Sep 59.
7. T.R.F. Nonweiler. "Delta wings of shapes amenable to shock wave theory", J.R. Aero.Society, vol 67, Jan 63.
8. John D. Anderson Jr., "Fundamentals of aerodynamics", McGraw-Hill Book Company.
9. J. Lukasiewicz, "Experimental methods of hypersonics", Marcel Dekker Inc., New York, 1973, Pg 1-23,185-195
10. J. Jodge, "Computational fluid dynamics", Aerospace America, November 1989, Pg 6-11.
11. A. Jameson, "The evolution of computational methods in aerodynamics.", Journal of Applied Mechanics, Vol 50, December 1983, pg 1052-1070.
12. Paul Kutler, "A perspective of theoretical and applied computational fluid dynamics.", AIAA Journal, Vol 23, No 3, Pg 328-341.
13. Luis R. Miranda, "Application of computational aerodynamics to air plane design", J. Aircraft, Vol 21, No 6, June 1984, Pg 355-370.
14. John E. Allen, "Aerodynamics - The science of air in motion", Granada, London, 1982, Pg 158-159.
15. J.W. Flower. "Configurations for high supersonic speeds derived from simple shock wave and expansion.", J.R. Aero. Society, vol 67, 1963, p287.

16. P.L. Roe."Optimum shapes", Lecture Series -- Aerodynamic Problems of Hypersonic vehicles, R.A.E. Bedford, England, Lecture 2, January 1970.

17. P.L. Roe. "Theory of waveriders", Lecture Series -- Aerodynamics Problems of Hypersonic vehicles, R.A.E. Bedford, England, Lecture 3, January 1970.

18. L.C. Squire. "A comparison for the lift of flat delta wing and waveriders at high angle of incidence and high Mach number.", Ingenieur-Archiv 40, 1971, pg 339-352.

19. C.J.Carr, "Force measurements on caret and delta wings over the incidence range $27^{\circ} \leq \alpha \leq 55^{\circ}$ at M_{∞}=12.2.", I.C. Aero Report 71-22, Oct 1971, Imperial College London.

20. J.G. Jones and B.A. Woods, "A method for designing lifting configurations for high supersonic speeds using the flowfields of non-lifting cones.", R.A.E. Aero Report 2674, 1963.

21. J.G. Jones, K.C. Moore, J. Pike and P.L. Roe. "A method for designing lifting configurations for high supersonic speeds, using axisymmetric flow fields.", Ingenieur Archiv, 1968, pg56 - 72.

22. Squire,L.C., "Calculated pressure distributions and shock shapes on conical wings with attached shock waves" Aero. Quart, XIX (1968), P.31

23. Squire,L.C., "Calculated pressure distributions and shock shapes on thick conical wings at high supersonic speeds.", Aero. Quart, XVIII (1967), P.185

24. Maurice L. Rasmussen. "Waverider configurations derived from inclined circular and elliptic cones.", J.Spacecraft and Rockets, vol 17, no 6, Nov-Dec 1980, Pg537-545.

25. B.S.Kim, M.L.Rasmussen and M.C.Jischke, "Optimization of waverider configurations generated from axisymmetric conical flows.", AIAA paper No; 82-1299, 1982.

26. Kevin G. Bowcutt, John D. Anderson & Diego Capriotti. "Numerical optimization of conical flow wave riders", Proceedings of the Conference for Aerodynamics of Hypersonic Lifting Vehicles, AGARD CP-428, 1987., 1987.

27. M.L.Rasmussen, M.C.Jischke and D.C.Daniel, "Experimental forces and moments on cone derived waveriders for M_{∞}=3 to 5.", Journal of

Spacecraft and Rockets, Vol 19, No.6, 1982, Pg 592-598.

28. M.C.Jischke, M.L.Rasmussen and D.C.Daniel, "Experimental surface pressures on cone derived waveriders from M_{∞}=3 to 5.", Journal of Spacecraft and Rockets, Vol 20, No.6, 1983, Pg 539-545.
29. J.D.Cole and T.F.Zien, "A class of three dimensional optimum hypersonic wings.", AIAA Journal, Vol 7, No.2, Feb 1969, pg 264-271.
30. M.L.Rasmussen and H.Xiaohai, "Analysis of cone derived waveriders by hypersonic small disturbance theory.", Paper presented at 1st hypersonic waverider symposium, University of Maryland, USA, Oct 17-19,1990.
31. Kuchemann D., "The Acrodynamic design of aircraft", Pergamon Press, Oxford, 1978, pg 448-514.
32. Wallace D. Hayes & Ronald F. Probstein, "Hypersonic flow theory", Academic Press, London, 1959.
33. William H. Dorrance, "Viscous hypersonic flow", McGrawHill Company, New York.
34. G. Emanuel, "Gasdynamics: theory and application.", AIAA, New York, 1986
35. R.Truitt, "Hypersonic aerodynamics", Ronald Press Co., New York, 1959.
36. R.N. Cox & L.F. Crabtree, "Elements of hypersonic aerodynamics", Academic Press, New York, 1965.
37. Ronald F. Probstein, "Introduction to hypersonic flow", Academic Press, New York, 1961.
38. L.H. Schindel, "Waveriders", Progress in Astronautics & Aeronautics, vol. 104, pg 199-242, AIAA Education Series, Washington USA.
39. John D.Anderson Jr., "A survey of modern research in hypersonic aerodynamics", AIAA Paper No. 84-1578.
40. T.R.F.Nonweiler, H.Y.Wong and S.R.Aggarwal, "The role of heat conduction in leading edge heating.", Ingenieur-Archiv, 1970.
41. R.D.Neumann and J.R.Hayes, "Introduction to aerodynamic heating analysis of supersonic missiles.", AIAA book on missile aerodynamics, 1986, pg 421-481.
42. John D. Anderson Jr., "Hypersonic and high temperature gas

dynamics.", McGraw-Hill Book Company, New York, 1989.

43. N. Qin and Richards B.E., "Simulation of hypersonic flow around a cone-delta-wing combination by an implicit method with multigrid acceleration.",Lecture Notes in Physics,vol 287, 1987.
44. N. Qin., "Towards numerical simulation of hypersonic flow around space plane shapes", PhD. Thesis, Department of Aerospace Engineering, University of Glasgow., 1987.
45. J.Ven. and J.W. Flower, "Shock patterns for simple caret wings", Journal of Royal Aeronautics Society, Vol 74, 1970, Pg 339-348
46. A.F.Messiter, "Lift of cylinder wings according to Newtonian theory", AIAA Journal, Vol. 1, Pg. 794, 1963.
47. K. Hida, "Thickness effects on the force of cylinder wings in hypersonic flow.", AIAA Journal, Vol 3, Pg. 427,1965.
48. L.C. Squire, "Calculations of the pressure distribution on lifting conical wings with applications to the off-design behaviour of waverider.", AGARD Conference Proceedings held at Royal Aeonautical Soc. London, Paper 11, 1968.
49. C.T. Nardo, "Aerodynamic characteristics of 2-D waverider configurations", AIAA Journal, Vol 10, Sep. 1972, P 1258.
50. Lyle N. Long, "The off-design performance of hypersonic Waveriders". Proceedings of the Conference for Aerodynamics of Hypersonic lifting Vehicles., AGARD CP428, 1987, Paper 26.
51. John J. Mahoney, "Inlets for supersonic missiles", AIAA Education Series, Washington D.C., 1990.
52. H.Schlichting, "Boundary layer theory.", Pergamon Press, London, 1955, Pg .
53. Dale A. Anderson, John C. Tanehill, Richard H. Pletcher, "Computational fluid dynamics & heat transfer", Hemisphere Publishing Corporation, New York, 1984, Pg 496.
54. R.Houwink and B.E.Richards, "Experimental study of a high lift re-entry vehicle configuration." AIAA Journal 11,5, pg749-751, May 1973.
55. B.E.Richard and R. Houwink, "An experimental study of space vehicle configurations with high lift during re-entry." VKI Technical Note 117, March 1976.
56. Reggiori, A. "Lift and drag of a wing-cone configuration in

hypersonic flow.", AIAA Journal, vol 9, No. 4, 1971.

57. J.Pike, "Efficient waveriders from known axisymmetric flow fields.", Paper presented at 1st Hypersonic Waverider Symposium, University of Maryland, Oct 17-19, 1990.
58. J.G. Jones & B.A. Woods, "The design of compression surfaces for high supersonic speeds using conical flow fields", R & M No:3539, Her Majesties Stationary Office, London, 1968.
59. G.I. Taylor & J.W. Maccoll, "The air pressure on a cone moving at high speed", Proc. Roy. Society. (London), A139, 278-311,1933.
60. T. Opatowski, "Lift, Drag and Pitching moment measurements on a 20° cone, a flat delta and cone-delta wing at mach number 8.3", A.R.C.C.P., 908 (1966).
61. T. Opatowski, "An experimental study of the flow around and the forces developed by the hypersonic lifting vehicles", University of London, PhD. Thesis, Sept,1967.
62. D.H.Peckham, "Pressure disribution measurements on a series of slender delta body shapes at mach number 6.85 and 8.60", R.A.E. Technical note Aero 2952 (1964).
63. D.M.Rao,"Comparative study of flat delta and caret wing models at M=12 and high incidence angles."
64. L.Davies, R.F.Cash, J.D.Regan, J.E.G.Townsend and A.Catley, "Experiments on flat delta wings and waveriders upto angles of incidence and Mach numbers suitable for lifting re-entry." Paper presented at the English International Shock tube Symposium, 5-8 July 1971, London.
65. P.L. Roe, "A simple treatment of the attached sock layer on delta wing.", R.A.E. Technical Report TR 70246, (Dec 1970).
66. Squire,L.C., "The effects of recessed lower surface shape on the lift and drag of conical wings at high incidence and high Mach numbers." Aero. Q.26,1,1-10, February 1975.
67. Roe P.L., "Aerodynamic problems of hypersonic aircraft." AGARD LS42, 1972.
68. Davies L., Roe P.L., Stollery J.L. and Townend L.H., "Configuration design for high lift re-entry.", AIAA Paper 72-132, 1972.
69. Jones J.G., "A method for finding lifting configurations for high

supersonic speeds using the flowfields of non-lifting cones.", R.A.E., R2674, 1963.

70. K.Hozumi and S.Watanaba, "A study of aerodynamic performance of waveriders.", Paper presented at 1st Hypersonic Waverider Symposium, University of Maryland, Oct 17-19, 1990.
71. U.Ganzer and S.Joachim, "Vortex formation over delta, double delta and waverider configurations at supersonic speeds.", AGARD CP-428, Paper 25, Bristol U.K., April 6-9,1987.
72. J.Pike, "Experimental results from three cone-flow waveriders.", AGARD Conference Proceedings held at Royal Aeonautical Soc. London, Paper 12, 1968.
73. Everett Jones and David Vanhoy, "Low speed wind tunnel testing of a Mach 6 viscous optimized waverider.", Paper presented at 1st Hypersonic Waverider Symposium, University of Maryland, Oct 17-19, 1990.
74. Steven X.S.Bauer, Peter F.Covell, Dana K.Forrest and Brian E.McGrath, "Preliminary assessment of Mach 4 and Mach 6 waverider." Paper presented at 1st Hypersonic Waverider Symposium, University of Maryland, Oct 17-19, 1990.
75. K.Kipke, "Experimental investigations of waveriders in the Mach number range from 8 to 12.", AGARD Conference Proceedings held at Royal Aeonautical Soc. London, Paper 13, 1968.
76. J. Stollery, "A review of force measurements on delta and caret wings made at the imperial college.", Paper presented at 1st Hypersonic Waverider Symposium, University of Maryland, Oct 17-19, 1990.
77. M.L.Rasmussen, "On hypersonic flow past unyawed cone.", AIAA Journal, Vol 5, Aug 1967, pg 1495-1497.
78. B.S.Kim, "Optimization of waverider configurations generated from non-axisymmetric flows past a nearly circular cone.", PhD dissertation, University of Oklahama, Norman, 1983.
79. R.F.Probstein, "Interacting hypersonic laminar boundary layer flow over a cone.", Division of engineering, Brown University technical report AF 2798/1, March 1955.
80. L.Talbot, T.Koga, and P.M.Sherman., "Hypersonic viscous flow over slender cones.", NACA TN 4327, September 1958.

81. J.A.Fay and F.R.Riddell., "Theory of stagnation point heat transfer in dissociated air.", Journal of the Aeronautical Sciences, Vol. 2, Feb 1958, pg 73-85.

82. W.H.Hankey, "Re-entry aerodynamics.", AIAA, New York, 1988, Pg 59-61.

83. J.O.Hirschfelder, C.F.Curtiss, and R.B.Baird, "Molecular theory of gases and liquids.", Wiley Press, New York, 1954.

84. M.E.Tauber, and G.P.Meness, "Aerothermodynamics of transatmospheric vehicles.", AIAA Paper 86-1257,1986.

85. E.R.C.Miles, "Supersonic aerodynamics.", Dover publications, New York, 1950, pg 143-217.

86. E.L.Houghton, and N.B.Carruthers, "Aerodynamic for engineering students.", Edward Arnold Publishers, London, 1970, pg 359-385.